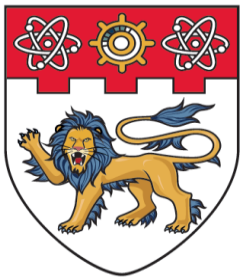

NANYANG TECHNOLOGICAL UNIVERSITY
SINGAPORE

WEARABLE AND FUNCTIONAL MICRONEEDLE SKIN PATCH PLATFORMS WITH 3D PRINTING FOR TRANSDERMAL DRUG DELIVERY

TAY JIE HAO

SCHOOL OF CHEMISTRY, CHEMICAL ENGINEERING AND BIOTECHNOLOGY

2022

WEARABLE AND FUNCTIONAL MICRONEEDLE SKIN PATCH PLATFORMS WITH 3D PRINTING FOR TRANSDERMAL DRUG DELIVERY

TAY JIE HAO

SCHOOL OF CHEMISTRY, CHEMICAL ENGINEERING AND BIOTECHNOLOGY

A thesis submitted to the Nanyang Technological University

in partial fulfilment of the requirement for the degree of

Doctor of Philosophy

2022

Statement of Originality

I hereby certify that the work embodied in this thesis is the result of original research, is free of plagiarized materials, and has not been submitted for a higher degree to any other University or Institution.

12th Dec 2022

. . . . . .

Date

. . . . . .

Tay Jie Hao

Supervisor Declaration Statement

I have reviewed the content and presentation style of this thesis and declare it is free of plagiarism and of sufficient grammatical clarity to be examined. To the best of my knowledge, the research and writing are those of the candidate except as acknowledged in the Author Attribution Statement. I confirm that the investigations were conducted in accord with the ethics policies and integrity standards of Nanyang Technological University and that the research data are presented honestly and without prejudice.

12th Dec 2022

. . . . . .

Date

. . . . . .

Song Juha

Authorship Attribution Statement

This thesis contains material from two publications submitted and two technical disclosures (TD) filed in the following institutes in which I am listed as main author or co-inventor.

Chapter 3 is submitted as Tay, J. H.; Lim, Y. H.; Tan, W. S.; Zhao, Y.; Xu, C.; Ramamurty, U.; Song, J., Hyaluronic acid-silica hybrid microneedles for enhanced penetration efficiency and drug delivery capability. (Under review)

The contributions of the co-authors are as follows:

- Song J., Xu C. and Ramamurty U. provided the initial project direction and drafted the manuscript contents.
- I designed and performed the experiments, data analysis and edited the manuscript.
- Lim Y. H. and Tan W. S. assisted on material procurements and microneedles fabrication.
- Ramamurty U. and Zhao Y. designed and supervised the nanoindentation tests and data processing.

Chapter 4 is submitted as Tay, J. H.; Lim, Y. H.; Tan, W. S.; Zheng, M.; Xu, C.; Song, J., Bioinspired flexible microneedle patches for Improved adaptability and functionality. (Under review). The proposed highly flexible MN patch has also filed patent as Song, J.; Tay, J. H.; Lim, Y. H.; Tan, W. S.; Zheng, M., & Xu, C. (2021). *Design And Fabrication Method Of Flexible And Adaptive Microneedle Patches Thereof* (NTU Ref No. 2021-528). Intellectual Property Office of Singapore.

The contributions of the co-authors are as follows:

- Song J. provided initial design direction and edited the patent content.

- Xu C. and Zheng M. designed and supervised the *in vivo* evaluation of proposed MN patch
- Lim Y. H. and I designed the patch, performed the experiments and data analysis.
- Tan W. S., Lim Y. H. and I finalized the patch design and 3D printed the base substrate.

Chapter 5's highly flexible MN-based glucose sensor is filed as Song, J.; Tan W. S.; Tay, J. H.; Lim, Y. H.; Zheng, M, & Xu, C. (2021). *A Highly Flexible Microneedle Patch System With An Integrated Glucose Sensor And A Method of Fabrication Thereof* (NTU Ref No. 2021-529). Intellectual Property Office of Singapore.

- Song J. and Xu C. provided initial design direction and edited the patent content.
- Tan W. S. and Zheng M. designed and performed the flexible base substrate fabrication.
- Xu C. and Zheng M. designed the MN material and evaluation method.
- Lim Y. H. and I performed MN fabrication and glucose sensor assembling.
- Tan W. S. and I performed the glucose sensor functionality evaluation and data analysis.

12th Dec 2022

. . . . . .

Date

. . . . . .

Tay Jie Hao

Acknowledgements

First and foremost, I would like to express my sincere gratitude to my supervisor Prof Song Juha for offering me the opportunity to start my PhD journey after my undergraduate study. Throughout these years, she has shown great patience, motivation, enthusiasm and innovative ideas which inspired me to think and perform more towards a good researcher. She has also offered many wonderful opportunities for me to learn multi-disciplinary knowledge which has improved my engineering thinking. Her invaluable guidance helped me to overcome many challenging periods during my research works and throughout my thesis writing period.

Next, I would like to thank School of Chemistry, Chemical Engineering and Biotechnology in NTU for the research scholarship. My PhD journey would have been impossible without financial support from NTU Research Scholarship. Besides that, a special thanks to administrative and technical staffs Miss Ren Jie , Miss Yong Siew Wai Terri, Dr Yu Shucong and Dr Wang Xiujuan for their kind and patience help whenever I encounter administrative issues.

I am also thankful to all current and previous group members for their kind help. Dr Zhang Wenyu gave me many insightful suggestions about chemical analysis and research logics. Dr. Pan Houwen Matthew and Dr. Chen Shengyang contributed a lot on lab maintenance and patiently guided me with lab works. Dr. Tan Wen See supported many procurement processes for my purchase and selflessly shared her immense knowledge on 3D printing. Dr Shi Qian, Dr Aravind Kumar Jayasankar and Dr Lee Yilin Amelia always allocates their free time to assist my simulation problem. A special thanks to Miss Lim Yu Han for the encouragement and help during the toughest period that we have worked together. Dr Zhao Yakai, Han Win Tun Allan, Muhammad Aidil Bin Juhari, Chong Shi Hui Lydia, Zheng Mengjia, Lee Junghyun, Han Rui Yuan, all assisted me throughout these years.

Finally, I would like to thank my family and friends who always support me during my PhD study.

Table of Contents

Table Captions

Figure Captions

Figure 2-2. Examples of pressure-actuated device designed for hollow MN drug delivery system. A. Experiment setup of hollow MN attached to FITC-loaded syringe [27]. B. Illustration of hollow MN integrated modified syringe [29] C. Digitally controlled hollow MN injection system (DC-hMN-iSystem)[30]. D. Hollow Micro-Structured Transdermal System (hMTS) and respective components [31]. Retrieved from Review [28]

Figure 2-3. A. SEM images of solid silicon MN. (i) 3 x 6 array of solid Si MNs with SiO_2 layer for wet etching. (ii) Final solid Si MNs after 165 minutes etching [23]. Scale bars = 400µm. B. In plane stainless steel MNs for skin insertion. (i) Optical micrograph of 50 MNs array. (ii) SEM of a section of 50 MNs array [24]. Scale bar = 200µm. C. *Ex vivo and in vivo* swelling behavior of "super swelling" MN. (i) Schematics of experimental setup to evaluate *in vivo* cargo delivery on rat. (ii) False color image of the MNs swelling profile over 3 hours period using OCT on *ex vivo* porcine skin. Scale bar = 300µm (iii) Optical morphology of super swelling MN upon removal from rat skin after 24 hours insertion, showing that all MNs remained intact [27]. D. Coated MN drug delivery system. (i) Zosano-Pharma (ZP) with MNs in applicator ring. (iI) ZP-patch press fit onto applicator. (iii) Schematics of rhGH dip coating using roller drum [32]. (iv) SEM front view of individual rhGH coated MN [33]. Scale bar = 200µm. E. Drug loaded dissolving MNs with different shapes. (i) Optical image of bevel-tip MN and (ii) tapered-cone MNs made of PLGA and calcein encapsulation. Scale bar = 250µm. (iii) PLA microparticles exposed from the PLGA MN tip. Scale bar = 50µm. (iv) 20x10 array of PLGA MNs [47].

Figure 2-4. Hierarchy of MN system in the perspective of Individual tip design and MN assembly design. Parameters of individual MN design should be well aligned such that the MN can penetrate human skin with low insertion force. Design of MN assembly should ensure uniform and consistent performance of assembled tips, which includes parameters like MN alignment (orientation of

neighboring MN) and base substrate design. Optimization of these levels form the final MN patch.

Figure 2-5. MN geometrical studies on shape effect. A. Common MN shape designs where studies showed that strength, drug loading capacity and penetration depth can be affected by MN shape [65]. B. SEM image of fabricated arrowhead cGel-cHA MN tip with PLA support shaft [74]. C. Fracture test result (force-displacement) of pyramidal cylindrical and bevel-tip SU-8 MNs. D. COMSOL FEM model of 3x3 MNs array under 5N axial force from the base in terms of (i) buckling mode and (ii) surface von Mises stress. (iii) Effect of facets in polygon on fracture strength, presented in von Mises stress (GPa) and critical load factors.[72]

Figure 2-6. Geometrical studies on aspect ratio, tip sharpness and array density. A. Experimental and numerical predicted failure force of MN: (i) with D_{tip} = 25μm and D_{base} = 200μm, as a function of MN length and end fixity factor K(0.5, 0.7 and 1.0).[76] (ii) MN with D_{tip} = 25μm, L = 0.7mm, and E = 3GPa at K = 0.7. B. Penetration study of glass MN with varying tip diameters. (i) Optical images of solid MNs fabricated using micropipette puller, with tip diameter of 5, 15, 24 and 37μm. Scale bar = 50μm. (ii) Influence of MN tip diameter on force at initial drop (human skin breakage). Mean and SD are shown (n=10, 6, 6, 5 from small to large tip respectively) * indicates significant difference between two groups with $p < 0.05$. (iii) Schematic explanation of phenomenon. For MN with tip diameter < ~80μm, shear force on the surface, which is proportional to r (two shaded areas on the surface), predominating force to compress skin underneath MN, which is proportional to r^2 (shaded area underneath the tissue). For tip diameter > 80μm, compression force gets predominant [81]. C. Influence of MN numbers/array (N) on insulin concentration in blood, assuming wedge-shaped MNs were applied for 4 hours [62]. D. Schematics showing effect of interspacing distance on activated antigen cells with (i) large, (ii) optimal, (iii) small interspacing distance. Optimal interspacing distance offered largest area exceeding saturation threshold.

Figure 2-7. Bug-inspired MN studies. A. True bug efferent system inspired microstructure. (i) SEM image of detail microstructure orientation on peritreme of *Tritomegas bicolor* [92]. Scale bar = 20μm(ii) Dimension of individual microstructure design and aligned microstructures. (iii) SEM side view of TPP printed microstructured MN. Scale bar = 50μm [93]. B. Honeybee inspired barbed MN system. (i) SEM image of worker honeybee stinger with barbs. Scale bar = 100μm [91]. (ii) Fabrication process of barbed MNs using magnetorheological drawing lithography, including formation of parent MNs on pillar tip through contacting, self-thinning and breakup, followed by drawing of pre-barbs and angle transferring to form final barbs. (iii) SEM image of honeybee inspired microbarbed MNs for improvement on tissue adhesion [94]. C. Mosquito proboscis inspired MN study. (i) Schematics of mosquito's proboscis composed of seven parts. (ii) CAD design of three-parts MN design, imitating two sets of maxillae and one labrum. (iii) SEM images of TPP printed mosquito proboscis inspired MNs (front and back view) [96].

Figure 2-8. Tooth-inspired MN studies. A. Limpet tooth inspired microfiber alignment MN system. (i) Optical image of fiber alignment within limpet tooth microstructure. (ii) magnetic field assisted alignment of iron nanoparticles into fiber-like bundle. (iii) SEM image of magnetic assisted 3D printed MN. Scale bar = 50μm [99]. B. Rear-fanged snake inspired MN system. (i) Schematic illustration of rear-fanged snake and its venom delivery system. Venom secreted from Duvernoy's gland flow through groovy snake fang into prey under capillary action. (ii) Schematic illustration of MN design in which narrow channels were created for cargo to be delivered from patch reservoir. (iii) SEM of top and side view of fabricated tri-, tetra-, penta- and hexa-grooved MNs. Scale bar = 100μm [101]. C. Shark tooth inspired inclined MNs for improved tissue adhesion. (i) Illustration of inclined shark teeth orientation. (ii) Schematic illustration of shark tooth inspired MN system for wound healing management. (iii) Optical image of casted shark tooth inspired MN (front and side view). Scale bar = 3mm [102].

Figure 2-9. Other bioinspired MN studies. A. Mantis foreleg inspired MN study for improved tissue adhesion. (i) Illustration of mantis foreleg with slanted serrated microbarbs. (ii) Illustration of attachment stability of two patches when placed upside down. Grey arrow shows that conventional perpendicular MN patch is prone to fall off whereas proposed serrated patch holds on firmly. (iii) Optical and SEM images of fabricated serrated MNs with 30^{o} and 90^{o}. Scale bar = 700μm / 200μm [103]. B. Eagle claw-inspired MN system for wound healing acceleration. (i) Illustration of eagle claw clamping mechanics. (ii) Schematic illustration showing that clamping MNs could tighten the wounded site and prevent dehiscence. (iii) SEM image of magnified MN tip. Scale bar = 200μm [104]. C. Octopus and mussel inspired adhesive MN for osteoarthritis treatment. (i) Schematic illustration of bioinspired multifunctional MNs with antibacterial and adhesive capabilities. Mussel byssus inspired adhesive PDA hydrogel was used as flexible base substrate while each MN was surrounded by a circle of octopus suction cup- inspired concave chamber. (iii) SEM image showing suction cup-inspired concave chamber surrounding a MN. Scale bar = 300μm [105].

Figure 2-10. Schematic illustration and working summary of basic 3D printing techniques [110].

Figure 2-11. Prior studies on 3D printing of MN system. A. MN fabrication using powder bed fusion (SLS and SLM). (i) Schematic illustration of basic PBF printing setup [108]. (ii) Cross section and top view of hollow MNs printed using selective laser micro melting (SLμM). Powder particles were shown to adhere on the shaft which were unable to remove. Scale bar = 200μm [121]. (iii) Optical images of stainless steel MNs after 3D printing (Top). Post treatment using electropolishing was employed in order to smoothen the surface and sharpen the tip region. Scale bar = 500μm [122]. B. MN fabrication using material extrusion (FDM). (i) Schematic illustration of basic FDM setup [108]. (ii) Conical PLA MNs printed using FDM which found to be sufficiently strong to penetrate skin. Optical and magnified SEM images of pre-MN pillar structure (left) and final

MN structure after KOH etching (right). Scale bar = 100µm, 200µm and 1mm respectively [123]. (iii) Sodium alginate (SA) / hydroxyapatite (HA) MNs fabricated using FDM printing and post stretching process for insulin delivery. Scale bar = 1mm [124]. C. MN fabrication using vat polymerization (SLA). (i) Schematic illustration of basic SLA printing setup [120]. (ii) SEM image of SLA printed cross-shaped MNs with larger drug loading surface for anticancer therapy. Scale bar = 1mm [125]. (iii) SEM image of SLA printed hollow bevel-tip MNs array for microfluidic integrated drug delivery system. Scale bar = 500µm [126]. D. MN fabrication using vat polymerization (DLP). (i) Schematic illustration of basic DLP printing setup [120]. (ii) DLP printed PEG-400 hydrogel MN for transdermal drug delivery. The array was printed with layer-to-layer 500ms exposure time. Scale bar = 200µm [127]. (iii) SEM image of hollow bevel MNs DLP printer using biocompatible resin for electrode integration and electrochemical sensing. Scale bar = 500µm [128]. E. MN fabrication using vat polymerization (TPP). (i) Schematic illustration of basic TPP printing operating mechanism. Two femtosecond lasers focus and cure from point to point. (ii) SEM image of TPP printed single MN for perforation and drug delivery of round window membrane. Scale bar = 200µm [129]. (iii) OVA and Poly(I:C) loaded CMC/trehalose MNs casted from TPP printed arrowhead MN template. Fluorescent microscope revealed distribution of both vaccine components within MN tip. Scale bar = 500µm [130].

Figure 2-12. Existing flexible wearables for drug delivery and biosensing. A. Flexible and stretchable multiplexed sensor (humidity, temperature and pressure sensing) where all electrodes are graphene-based material. (i) Schematic illustration of the 2x2 sensing elements and individual sensor pathway in stacking manner. (ii) Sensing capability of individual compartments under different stimuli [138]. B. Transdermal iontophoresis patch with self-powered biofuel cell for small molecule delivery. (i) Schematic illustration of the patch which composed of enzyme-modified carbon fabrics electrode, hydrogel loaded with biofuel and cargos and oxygen permeable medical tape, assembled with PDMS

frame. (ii) Iontophoresis assisted drug delivery mechanism. Biofuel cell generates ionic current from anode to cathode whereby driven electrophoretic diffusion of drugs into the skin. (iii) Mounting of assembled patch onto human arm [141]. C. Fully integrated patch for multiplexed *in situ* perspiration analysis, including data recording, post processing and wireless transmission onto phone application for display. (i) Schematic illustration of the array (including Na, K, glucose, lactate and temperature sensing). Block diagram shows signal transduction (orange), conditioning (green), post processing (purple) and transmission path (blue) to the mobile application. (ii) Compartment of integrated circuits. Red arrow indicates location of sensing region. (iii) Integrated flexible sensor array in wristband form [138]. D. Fingerprint like flexible three-axial tensile, slip force and temperature sensor fabricated using screen printing. (i) Schematic illustration of each sensor layers. (ii) FEM simulation to characterize structural deformation differences between touch and slip force applied. (iii) Optical image of the integrated fingerprint-like sensor. Scale bar = 1cm [139].

Figure 2-13. Prior studies on flexible MN system. A. Fabrication process of PLGA-PVP/VA based electro-drawn MN on flexible PDMS substrate for collagenase delivery. The process includes dipping flexible base substrates with PDMS pillar into water-in-oil emulsion containing collagenase solution, followed by pyroelectric crystal-induced-electric field assisted electro-drawing of MNs [143]. B. Reactive oxygen species (ROS)-responsive flexible MN system for acne vulgaris treatment. (i) Schematic illustration of the components and working mechanism. HA-based hydrogel and diatomaceous earth (DE) act as pus absorption pad while CDM as antibiotic for acne treatment is loaded into PVA MNs. (ii) Optical illustration of the fabricated flexible MN patch wrapping onto cotton stick for temporary usage [145]. C. Flexible MN electrode mesh array for wireless brain signal monitoring. (i) Schematic illustration of the design and geometry of flexible MN electrode array. The flexible base substrate is fabricated through UV lithography of polyimide while MNs are fabricated using SU-8 drawing lithography. (ii) Optical image of MN electrode array. Scale bar = 1mm

[148]. D. Flexible MN system with Miura-ori structured base substrate for biosensing with better ventilation and flexibility. (i) Fabrication process of the MN electrode array. After Miura-ori pattern was fabricated using micromachining tool, negative molds are fabricated using PDMS in which hard and soft epoxy resin are used as MN and base substrate material. Titanium and gold coating are used to improve conductivity of the MN electrodes. (ii) Optical image of the fabricated MN electrode array [150].

Figure 3-1. A. Schematic of preparing HA-Si solution and MN fabrication through micro-molding technique. B. Steel template and casted HA-based MN array [31]. Scale bar = 2mm.

Figure 3-2. Schematic illustration of nanoindentation process and important parameters [34]. A. General nanoindentation P-h curve of loading-unloading process and the parameters. B. Schematic illustration of unloading process and contact geometry between indenter and material surface.

Figure 3-3. Optical appearance of various HA-Si composite thin films. Scale bar = 1cm.

Figure 3-4. Morphological analyses of HA-Si MN. A. Optical image of various MNs with HA, HA-10vol%Si, HA-20vol%Si, HA-30vol%Si, HA-35vol%Si formulation (The black arrows indicate structural defect). Scale bar = 1mm. B. SEM image of MN tip morphologies at 1500x magnification. Scale bar = 10µm. C. SEM images of MN body morphologies at 800x magnification. Scale bar = 10µm.

Figure 3-5. TEM and EDS analysis of HA-20vol%Si. A. Microstructure of HA-Si matrix and pure HA matrix at higher magnification. (i) Silica network in HA-20 vol% Si matrix. Yellow bracket showed growth of silica NPs into network. Scale bar = 1µm/100nm. (ii) HA matrix region. Red bracket marked interconnected nanopores within the polymeric matrix. Scale bar = 100nm. B. Si

elemental mapping of HA-20 vol% Si using EDS mapping to show distribution of Si element throughout scanned area. Scale bar = 5µm. C. Point scan-EDS analysis of two pre-determined region on HA-20 vol% Si to determine elemental composition.

Figure 3-6. Chemical analysis (XRD) graphs of various HA-Si formulations

Figure 3-7. Nanoindentation tests of HA-Si thin films. A. Force-displacement curve of HA-Si samples. B. Modulus of HA-Si samples. C. Hardness of HA-Si samples. (* $p \leq 0.05$, ** $p \leq 0.01$, *** $p \leq 0.001$, ns = no significance)

Figure 3-8. Compression test of HA-Si MN in quantitative and qualitative manner. A. Schematic illustration of the compression setup and compressive force-%strain curve of HA-Si MN. B Schematic illustration of the bending test setup and optical images of representative groups (pure HA and HA-20 vol% Si) before and after penetrating PDMS bulk film. Scale bar = 500µm.

Figure 3-9. *In vitro* penetration test with bi-layered skin substitute. A. Schematic illustration of experimental setup with indication of successful penetration. Scale bar = 250µm. B. Normalized number of penetrations of various MNs. (*$p \leqslant 0.05$, **$p \leqslant 0.01$)

Figure 3-10. Degradation behavior of HA-Si MNs. A. Optical images of the HA-Si MNs dissolution progress. Scale bar = 500µm. B. Dissolution rate of various HA-Si MNs.

Figure 3-11. Drug release test of HA-Si MNs. A. Cargo release rate of HA-Si MNs loaded dye as high molecular weight model drug. B. Cargo release rate of HA-Si MNs, Insulin as commercial drug.

Figure 4-6. A. Three regions defined for in vitro penetration efficiency test as compared to full MN attached fractal cut patch. B. Schematic representation of gel extraction after patch administration onto bilayer elbow gel to quantify penetration depth of individual penetrated sites. C. Schematic representation of procedures to execute in vivo insulin delivery test

Figure 4-7. Computational modelling of RC, FC and FF base substrate. A. Assembly interaction of conformity test where a simplified spherical elbow model was pushed against three substrates, presented in strain contour graph. Scale bar = 1cm. B. Contact area (%) of three substrates against elbow model. C. Correlated penetration efficiency of three substrates applied onto spherical elbow model based on distance between individual subunits and projected sphere surface. D. Uniaxial stretching of FC and FF substrate with MN attachment at the centre of every subunit, presented in von Mises stress contour.

Figure 4-8. Fabrication process of RC, FC and FF MN patches. A. SEM images of 1x10 PLA and HA MN arrays. Scale bar = 100μm/10μm. B. Schematic representation of assembling process: casting, segmentation and reassembling. C. Optical image of segmented MNs. Scale bar = 1cm. D. Conceptual design and optical images of fabricated RC, FC and FF patches (from left to right). Scale bar = 1cm

Figure 4-9. Static and dynamic motion test of RC, FC and FF base substrate on human volunteers. A. Optical images of static test where casted silicon rubber elbow model RC, FC and FF MN patches were applied onto region 2 of the silicon rubber casted elbow model. B. Number of RC, FC and FF MNs penetration recorded at region 1 and region 2 of elbow model. C. Experimental procedures in dynamic motion test. RC, FC and FF patches were glued onto volunteer's elbow. Scale bar = 1cm. D. Normalized contact area (%) of RC, FC and FF base substrates after one cycle from extension to flexion position. Error

bars indicate standard deviation (n=10 for each substrate type). **p < 0.01 for contact area (%) of FC and FF substrates in flexion

Figure 4-10. In vitro penetration test in terms of contact condition using monolayer agarose elbow model. A. Schematic representation of experimental procedure and MN patches after the test. B. Penetration efficiency in terms of dissolution condition. **p < 0.01 for numbers of MNs that fully or partially penetrate the agarose mold across all types of patches

Figure 4-11. Top view and Z-stack confocal images of fluorescent dye in bilayer model penetrated by PLA MNs. Images categorized according to patch types (RC, FC or FF) and MN location (inner, middle or outer). Scale bar = 100μm

Figure 4-12. Penetration efficiency of RC, FC and FF MN patches based on positive correlation between penetration depth and patch conformity. Error bars indicate standard deviation (n=3 for inner region, n=5 for middle region, n=7 for outer region). **p < 0.01 for penetration depth of FC and FF outer MN patches

Figure 4-13. In vivo insulin delivery on mice using IP insulin injection, RC and FF substrates. A. Top view and side view of RC or FF MN patch application on mice. The mice were anesthetized at the moment. Scale bar = 0.5cm. B. Skin condition of mice back after RC and FF patch administration at endpoint (90 minutes). C. Normalized blood glucose reduction (%) of negative control, IP insulin injection, RC and FF insulin loaded MN patches. Black arrow indicates timepoint where insulin treatments were proceeded (30 minutes after glucose injection). D. Normalized amount of blood glucose reduced (%) at the first 30 minutes and 30-60 minutes after insulin treatment. IP injection and FF patch at first 30 minutes showed drastic blood glucose reduction rapid dissolution of HA MNs whereas NC and RC showed no significant difference

Figure 4-14. Fabrication and characterization of flexible fractal cut MN patch using DLP printing. A. Schematic illustration of two-step multi-material printing of flexible MN patch. B. Structural characterization of SUV substrate and MN integrated array. (i) Optical image of stretched SUV FF base substrate. Scale bar = 1cm. (ii) SEM image of single SUV FF subunit, and (iii) magnified view of red bracket. Scale bar = 100/10µm. (iv) Optical image of DLP printed FF MN patch. Scale bar = 1cm. (v) SEM image of single two-step printed MN on single FF subunit, and (vi) magnified view of SUV/plasGRAY interface. Scale bar = 1000/10µm

Figure 4-15. A. Interlayer adhesion force between plasGRAY and SUV tensile coupon. (i) Schematics and optical image of rigid-soft-rigid sandwich tensile coupon[46]. Scale bar = 1cm. (ii) Stress-strain curve of interlayer adhesion tensile coupon fabricated using DLP and glue/tape. B. In vitro penetration test of DLP printed RC and FF MN patches on monolayer agarose elbow model. (i) Optical images of dye loaded RC and FF MN patch for penetration test. Scale bar = 5mm. (ii) Number of MN penetration (30MNs/array). C. High customizability of FF design. (i) Variation in size. (ii) Variation in subunit geometry. (iii) Heterogeneity of MNs on single array through combination of different drug formulation/MN material. All scale bar = 1cm

Figure 4-16. Improvement of DLP printed MN geometry through synergistic approaches. A. Effect of antialiasing on MN geometry. (i-iii) MN fabricated without anti-aliasing. Scale bar = 500 / 100µm. (iv-vi) MN fabricated with optimized antialiasing through Matlab algorithm. Scale bar = 500 / 100µm [52]. B. Effect of printing orientation (0^o and 45^o). The optical and SEM images show preliminary result using commercial plasGRAY resin as MN material. (i) Schematic illustration of orientation setup using same MN design and printed samples (bottom). Scale bar = 5mm. (ii) SEM image of conical MN array printed in 0^o angle and magnified view of tip region (~20µm). Scale bar = 100 / 10µm. (iii) SEM image of conical MN array printed in 45^oangle and magnified view of

tip region (~10μm). Scale bar = 100 / 10μm. C. Effect of chemical etching (KOH). SEM images show preliminary result using biocompatible acrylated epoxidized soybean oil-based resin. (i) Schematic illustration of etching process. (ii) SEM image of pyramidal MN before and after 5M KOH etching for 13 hours. Scale bar = 100μm. (iii) SEM image of conical cylindrical MN before and after 5M KOH etching for 13 hours. Scale bar = 100μm.

Figure 5-1. Result summary of proposed research. At individual level, silica network was incorporated into low molecular weight hyaluronic acid (HA) through sol-gel conversion under acidic condition. Fabricated HA-Si MNs showed superior penetration capability and prolonged structural stability in water. Next, the wearability issue of existing flexible microneedle system was then addressed through introduction of kirigami-like fractal cut (FF) pattern into base substrate design. Both computational and experimental approaches have proven FF to have superior skin conformity, drug delivery efficacy and reduction of hard-soft interfacial delamination.

Figure 5-2. Fundamental study on MN geometrical effect through experiment and simulation. A. Definition of geometrical parameters to address, namely total height (1. tip region, and 2. pillar support), tip diameter, tip angle, base diameter and tip-to-tip interspacing distance. B. Meshed numerical model of single MN insertion into bilayer skin model to predict mechanical interaction during MN insertion. Material data input is identical to experimental setup for cross-checking purpose. Scale bar = 20μm

Figure 5-3. Drug loaded MN printing using DLP printer. A. Schematics of DLP resin mixed with PEGDA (blue), TPO photoinitiator (green) and cargo (pink). B. Schematic illustration of DLP printing setup. C. Removal of printed array from build platform and potential applications such as ocular, arm and torsol drug delivery. D. Schematic illustration of cargo delivery upon sensing environmental stimuli while maintaining overall MN structure [15].

Figure 5-4. Schematic illustration of proposed highly flexible MN-based glucose sensor. The MN system comprises of 2x2 segmented MNs subunit, disposable test strip containing glucose oxidase (GOx) and 3D printed flexible TPA base substrate integrated with conductive silver pathway. After attaching Gox test strip onto backing layer of meHA based MNs, they are attached onto individual subunits of printed FF base substrate to form final MN patch. Computational model in chapter 4 proven its high conformity onto complex geometry like elbow [25].

Abbreviations

2PP/TPP	Two-photon polymerization
3D printing	Three-dimensional printing
AAPBA	Acrylamidophenylboronic acid
ABAQUS	Finite-element Computer Code
ABS	Acrylonitrile- butadienestyrene
AHP-3	Acetyl-hexapeptide-3
BFC	Biofuel cell
BG	Blood glucose
BSA	Bovine serum albumin
$CaCl_2$	Calcium chloride
CAD	Computer-aided Design
CAGR	Compound annual growth rate
CCK-8	Cell counting kit-8
cGel/cHA	Crosslinked gelatin/ crosslinked hyaluronic acid
CMC	Carboxymethyl cellulose
CMOS	Post-complementary metal-oxide-semiconductor
CNT	Carbon nanotube
COVID-19	Coronavirus disease 2019
CPT	Cisplatin
CVD	Chemical vapor deposition
DED	Direct energy deposition

DIL	1,1'-Dioctadecyl-3,3,3',3'-Tetramethylindocarbocyanine Perchlorate
DIW	Direct ink writing
DLP	Digital light processing
DMEM	Dulbecco's Modified Eagle's medium
DMLS	Direct metal laser sintering
DNA	Deoxyribonucleic acid
DRIE	Deep-reactive ion etching
ECG	Electrocardiogram
EDS	Energy dispersive spectroscopy
EHD	Electro-hydrodynamic
FC	Flexible and continuous
FDA	U.S. Food and Drug Administration
FDM	Fused deposition modeling
$FeCl_3$	Iron chloride
FEM	Finite element modeling
FF	Flexible and fractal cut
FITC	Fluorescein isothiocyanate
GO_x	Glucose oxidase
HA	Hyaluronic acid
HCl	Hydrochloric acid
hEGF	Human epidermal growth factor

$HF\text{-}HNO_3$	Hydrofluoric acid-nitric acid
HMN	Hollow microneedle
hMTS	Hollow Micro-Structured Transdermal System
HNA	Hydrofluoric, nitric and acetic acid
IM	Intramuscular
IP	Intraperitoneal
IPA	Isopropanol
ISE	Ion-selective electrode
ISF	Interstitial fluid
IU	Insulin unit
IV	Intravenous
KOH	Potassium hydroxide
LCD	Liquid crystal display
meHA	Methacrylated hyaluronic acid
MN	Microneedle
MPP	Multiphoton polymerization
NDF	Normal human dermal fibroblast
NIPAM	N-isopropylacrylamide
NP	Nanoparticle
OCT	Optical Coherence Tomography
PBF	Powder bed fusion
PDA	Polydopamine

PDMS	Polydimethylsiloxane
PEDOT: PSS	Poly(3,4-ethylenedioxythiophene) polystyrene sulfonate
PEG	Poly (ethylene glycol)
PEGDA	Poly (ethylene glycol) diacrylate
PET	Polyethylene Terephthalate
pHEMA	Poly (2-hydroxyethyl methacrylate)
PI	Polyimide
PLA	Poly (lactic acid)
PLGA	Poly-lactide-co-glycolide
PMMA	Poly (methyl methacrylate)
PoC	Point of care
PU	Polyurethane
PVA	Polyvinyl alcohol
PVP	Polyvinylpyrrolidone
PZT	Lead zirconate titanate
RC,	Rigid and continuous
rhGH	Recombinant human growth hormone
SA	Sodium alginate
SC	Stratum corneum
SCI	Web of Science
SD rat	Sprague Dawley rat
SD	Standard deviation

SEM	Scanning electron microscopy
Si	Silica
SiO_2	Silicon dioxide (silica)
SLA	Stereolithography (technique)
SLM	Selective laser melting
SLS	Selective laser sintering
STL	Stereolithography (file)
SUV	Stretchable UV curable elastomer
TEM	Transmission electron microscopy
TEOS	Tetraethyl orthosilicate
TMAH	Tetramethylammonium hydroxide
TPO	Diphenyl (2,4,6- trimethylbenzoyl) phosphine oxide
TTDS	Transdermal drug delivery system
USD	US dollar
UV	Ultra-violet
VA	Vinyl acrylate
VP	Vat polymerization
XRD	X-ray diffraction

Summary

Increasing needs of painless, self-administrable and readily available home healthcare applications have driven the advancement of transdermal drug delivery system (TDD), aiming to replace current therapeutic and health monitoring schemes that require physical attendance and sophisticated process. Microneedle (MN) technology as third generation TDD system has been exploited in many bio-functional applications such as transdermal drug delivery and biosensing due to its greater skin disruption in minimal invasive manner as compared to previous generations that have molecular size limit and with needs of external power supply. MN device is designed in patch form with a collection of microscale-needles attachment as this allows simultaneous breaching of skin barrier in wider area for drug delivery and biosensing purposes. An ideal MN system should allow consistent and uniform penetration over target skin region especially when human skin is curved at most body areas while viscoelastic in nature. MN patch that failed to conform effectively onto target site could lead to under-desired therapeutic outcome and poor signal recording. Moreover, current MN systems are designed for finger-pressing administration therefore often in miniatured size, limiting the adaptability for most protein and peptide delivery dosage. To date, these issues have not been addressed effectively, hindering global commercialization of MN technology. Inspired by brilliant evolution of ancient fish armour system which has shown co-existence of rigidity and flexibility, we have found that they possess great similarities with the ideal MN system from micro- to macroscale aspects.

Therefore, in this thesis, I mainly focus on improvement on penetration efficiency of individual MN tips through 1) mechanical reinforcement at micro-scale (Chapter 3) and 2) adaptative tip configuration of flexible MN substrates depending on surface geometry at macro-scale (Chapter 4). Particularly, in this thesis, rapid dissolving biopolymer low molecular weight hyaluronic acid (HA) was used for dissolving MN (DMN) systems due to its high dissolution rates and abundant availability in human body naturally with reasonable drug loading

capabilities. However, the degradable polymer-based MN systems often experience significantly reduced transdermal penetration, especially when polymers have intrinsically weak mechanical strength as compared to other non-biodegradable materials like metal. Therefore, first, an *in situ* precipitation of silica network in HA matrix was proposed to improve intrinsic mechanical strength and improved physiological stability during administration of MN patches. Silica is a widely used bioactive additive with rapid physiological decay rate. Optimization of silica content in HA matrix was first studied through structural characterization to ensure minimal morphological defects in fabricated MN. Moreover, chemical analyses were used to characterize micro-structure and distribution of silica network in HA matrix. The HA-Si MNs fabricated demonstrated improved penetration efficiency and slight effect on dissolution behavior to pure HA MNs. Moreover, no cytotoxicity was found in the optimized HA-Si sample, indicating that the proposed hybridization of bioactive additive was encouraging.

Moreover, MN system comprises of tip region and base substrate where flexible and continuous base substrates have been proposed in previous studies to address skin conformity issue of traditional MN systems with rigid base substrate. However, existing flexible MN system only offers bidirectional flexibility, therefore not yet able to address conformity issues at movable joint regions like elbow. Furthermore, upscaling of MN patch dimension is expected in future market in order to resolve issue of limited drug loading and skin coverage for biosensing of wider body areas. Therefore, in this project, a kirigami-based auxetic fractal cut pattern was introduced into the flexible base substrate design, resembling that of wavy patterned fish tissue. Numerical and experimental evaluations have demonstrated significant improvement in terms of contact stability, complex skin geometry coverage, penetration depth and insulin delivery. These tests were designed and compared among traditional rigid, flexible continuous and proposed flexible fractal cut patch. Moreover, novel two-step fabrication of proposed fractal cut MN patch using DLP printing was

accomplished with high precision, lower production time/cost and promising functionality by exploiting working principle of DLP printing. Finally, customizability of FF MN patch in terms of patch size, subunit shape design and heterogeneity of MN material-drug formulation were displayed and proven to be a promising platform for diverse biomedical applications.

The two approaches presented in this thesis have shown to be the key aspects to consider when designing an ideal MN patch with excellent penetration efficiency, high drug loading and skin coverage, in micro- and macroscopic perspectives. With further development of such flexible MN system, MN technology will soon to be adopted in more therapeutic and biosensing applications, finally bringing revolution to the biomedical fields as a pain-free and multipurpose healthcare tool.

Chapter 1

Introduction

Market value of transdermal drug delivery in recent years has grown rapidly due to its outstanding performance in biomedical field and expected to be promising substitute over conventional hypodermic needles. Among all, microneedle as the latest generation TTDS has shown its potential not only as cosmetics products, but also a great candidate in drug delivery and diagnostic application. However, limited volume and poor skin conformity have hindered the commercialization of microneedle (MN) technology. Therefore, improvement of its contact and penetration efficiency should be considered to advance MNs development in biomedical application. This chapter introduces concept of microneedling, general working principle and bottleneck of current MNs technology. The objectives of the thesis are proposed as the potential solution for MNs technology. Finally, the organization of thesis is also demonstrated.

1.1 Background

In 2021, the overall global transdermal drug delivery system market size reached USD 6.4 billion, mainly driven by the increasing predominance of various chronic diseases which require regular drug administration for a long term. Although it is still attributing for relatively small segment in the whole drug delivery system market, it is observed to gain increasing attention over the decade on account of many advantages (good patience compliance, minimal damage and adverse effect) given by TTDS over other drug delivery method (oral and hypodermic injection). According to a market report [1], this market will grow at a stable CAGR of 3.7% for the next 5 years due to the continuous growing prevalence of chronic diseases along with increased aged population and environmental pollution. Since conventional drug delivery methods, including oral medications show lower efficacy despite excessive drug dosage due to the well-known hepatic first pass effect, the increasing demand for new generation therapeutic methods carries the momentum of the market growth for transdermal drug delivery systems which are pain-free, self-administrable, site-specific, and efficacious. For instance, in the case of diabetes, blood glucose monitoring and administration of insulin must be done occasionally by the injection with a hypodermal needle. However, the frequent injection with needles increases patient's discomfort and pain along with high infection transmission besides producing a large volume of medical wastes. In addition, recent outbreak of COVID-19 causes the need for periodical vaccination due to rapid mutation of virus. Worsening climate changes and industrial pollutions should prepare us to expect more epidemic or even pandemic like COVID-19 in the following decades. Current medical system still highly dependent on trained clinicians' hypodermic vaccine administration which requires to schedule and queue for appointment. Thus, due to significantly rising patient preference for autonomous and pain-free vaccine/drug administration, the adoption rate of transdermal drug delivery systems in a typical form of adhesive skin patches increased undoubtedly.

Among emerging transdermal therapeutic systems, microneedle (MN) patches are one of key drivers in the market[3-5]. As shown in **Figure 1-1A**, number of literatures related to MN study has increased notably according to Web of Science (SCI) data base, which in turn proven the prospective commercialization of MN technology with strong market acceptance[6]. Traditionally, MN patches have been developed in order to 1) reduce discomfort or soreness by reducing the needle size up to a few micrometers and due to an injection by a hypodermal needle and to 2) improve efficacy of drug delivery into a target area with or without biosensors. In contrast to the conventional transdermal therapy which often relies on the barrier performance of stratum corneum, MNs can physically penetrate the barrier tissue layer regardless of the barrier conditions associated with thickness, composition, and humidity of skin, varied by patients and even body regions. On the other hand, conventional procedure for disease diagnoses often requires sophisticated laboratory testing (extraction of sample, disease biomarker identification and quantification) which could narrow patients' therapeutic window when acquisition of result take up hours to days. Therefore, a rapid and sensitive point of care (PoC) diagnostics tool is preferable especially dealing with onset of acute disease or emergencies like heart attack[7]. Along with the advancement of MN technology for drug delivery, scientists have also discovered capability of MNs in clinical diagnostic and health monitoring since the trend of developing near-real time glucose monitoring using microneedle device in early 2000s[2, 8]. **Figure 1-1B** shows the existing platforms for MN-based diagnostic which function in different mechanisms: 1) Analyte capture for biomarker identification; 2) Biofluid extraction for *in vitro* analysis; 3) Biofluid extraction for real time/near real time electrochemical analysis, mainly subjected to the type of MN chosen[9, 10]. A typical MN patch includes arrays of micro-scale needles with tip diameter of 5-100 μm which don't cause any significant pain during the penetration and total length up to 1.5 mm like the mosquito proboscis (~1.5 to 2 mm in length and 20 to 40 μm in diameter)[3]. Noted that the individual MN of the patch is at least

three times slenderer than the smallest 30 gage hypodermic needle with an outer diameter of 320 μm. Now, this technology is approaching to the commercialization phase, challenging more advanced clinical trials and commercial-scale manufacturing.

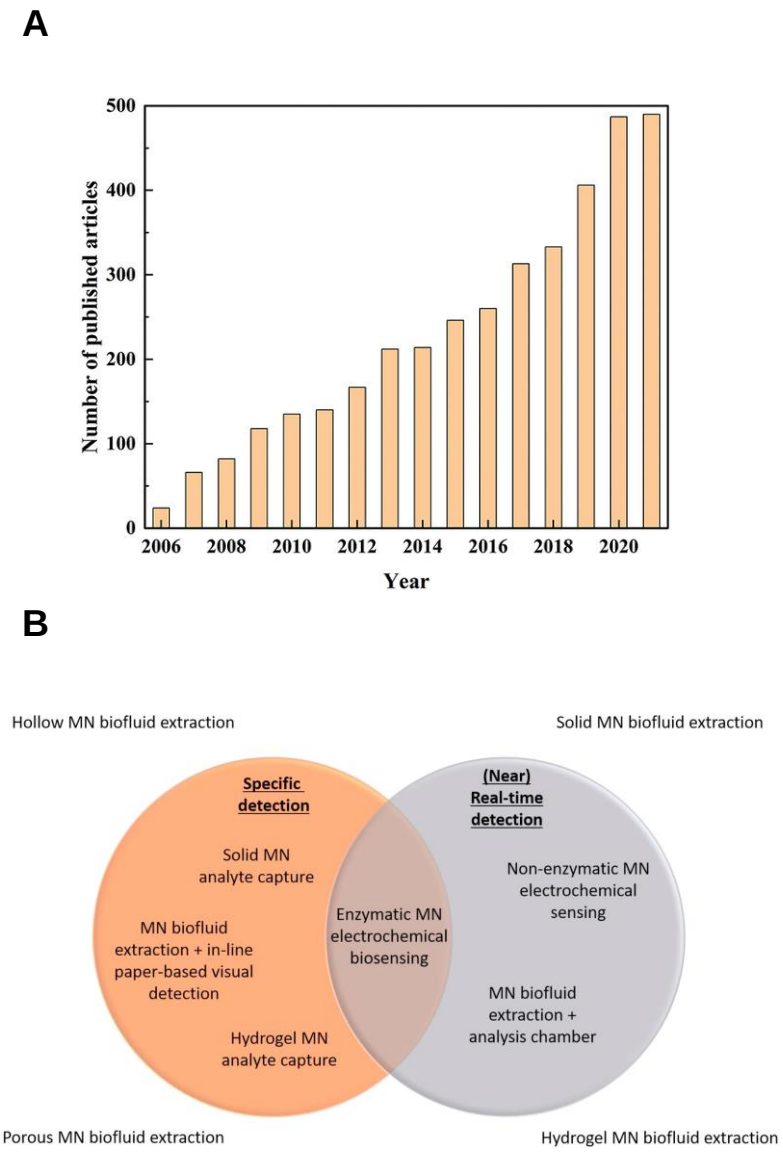

Figure 1-1. A. Diagram of MN-related literatures published from 2006-2021 [1]. B. Venn diagram of PoC diagnostic mechanisms and relationship between current MN diagnostic platforms [9].

For the realization of successful adoption of MN patches in the healthcare industry, effective and scalable manufacturing is needed[3-5]. For lab-scale manufacturing, depending on materials, either etching or casting methods have been widely used for the fabrication of microneedles. Wet and dry etching are common for hard and rigid materials such as silicon and stainless steel where bulk wafer will be placed in chemical etchants like HNA solution (hydrofluoric, nitric and acetic acid)[11] or plasma environment to allow reactive ion etching[12]. However, non-dissolvable material like silicon is brittle and prone to break during skin insertion which often causes inflammation and formation of abscess. Although efforts have been made to develop biocompatible nano-porous silicon (PSi)[13] with drug loading capability[14], density of the pore channels are limited to maintain sufficient penetration strength such that drug loading capacity remain as the crucial challenge to overcome. Polymers are the most trending category of MN material in current stage because of their superior biocompatibility, low cost and kinetic flexibility to engineer[15]. Casting method is to pour liquid polymeric solution into a negative silicone mold produced by the counterpart positive metal mold and cures into solid state through various treatment. Disposable and degradable MN patches are often made of polymers; thus, the casting method is more common for lab-scale manufacturing. The conventional micro-molding method for fabrication of microneedle patches can be easily translated into large-scale production for commercialization. In parallel to the advances of MN patches in the labs, large-scale manufacturing has already been launched by commercial facilities of several companies (e.g., 3M, Raphas, Micron Biomedical)[3, 16] where their respective MN fabrication methods are shown in **Figure 1-2**.

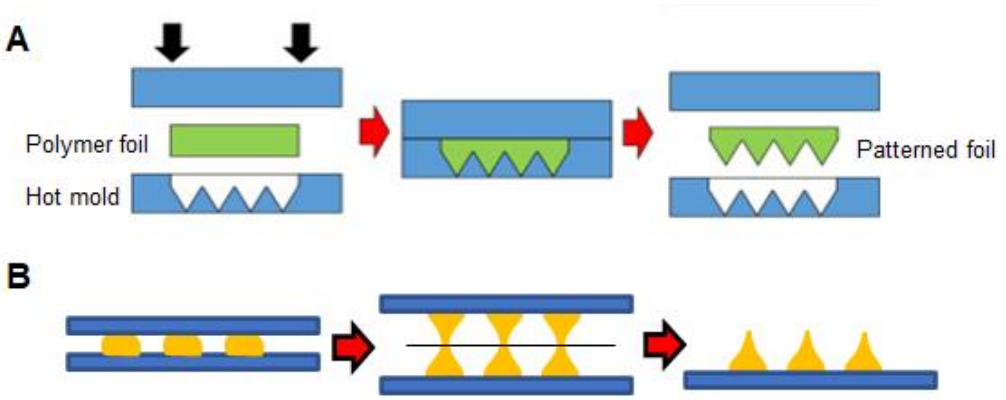

Figure 1-2. Large-scale fabrication of MN patches by A. an embossing method (3M) and B. a droplet-borne air blowing method (Raphas) [2, 17, 18].

However, the current molding method usually produce a "microneedle structure" with a single polymeric material. Since MNs should penetrate the multi-layered skin tissue, sufficiently higher stiffness of MN tips than that of the human skin is one of key requirements when a MN system is designed. Thus, in most cases, MN patches produced by the casting method are intrinsically rigid. During MN administration, that the penetration efficiency of MNs per area is often assumed to the same for all the MN tips. However, depending on the location of individual MNs with respect to the applied skin area, the penetration efficiency should be varied. The main reason is that our skin is not flat but curved, hyperelastic and inhomogeneous, whereas the MN patch is flat, stiff, and elastic, and relatively homogeneous. Some local regions of human skin should be relatively stiffer than other regions, and under the same loading, the MN tips, which need to penetrate the relatively stiffer regions, cannot go as deep as other MNs, especially for rapid dissolving polymers like hyaluronic acid which has limited mechanical properties to overcome skin resistance. Also, after unloaded, the highly reversible skin surface goes back to the undeformed state, then the applied MNs have varied penetration depths as shown in **Figure 1-3A**. Then, each MN should have different drug delivery efficiency, reducing the reliability of drug administration. Therefore, in depth understanding of MN geometrical

effect like shape, length, tip radius and needle to needle interspacing distance should be considered so that penetration efficiency of each MN can be maximized regardless of localized stiffness variation across target skin site. During the process, other factors like structure integrity and drug loading capacity should not be compromised since sharper or finer geometries often reflect as smaller surface area or volume even though they can breach skin barrier relatively easier.

In most scenario, a MN patch needs to cover a significantly large skin surface in order to maximize efficacy of drug delivery. Also, depending on a type of drugs, some MN patches are required to be placed on the skin area for prolonged drug or substance release. Then, a contact stability problem occurs like bandages. Since all manufacturing processes with soft and flexible substrates are based on flat geometry, the resultant devices need to be deformed for being applied on the human skin with various intrinsic curvatures[17-20]. As a result, the induced pre-stress conditions of the soft deformable membrane-type devices often initiate cracks at the device-human skin interface, leading to interfacial delamination and detachment of the device at the end. In particular, wearable devices, covering large skin surface areas (e.g., face or joint regions of the human body), significantly induce these interfacial problems (**Figure 1-3B-D**). Moreover, individual patients require the different amount of drug dosage depending on their health condition and disease progression. As one of drug delivery systems, MNs should meet various dosage requirements through their packaging. The current manufacturing approaches cannot address this customized packaging option in a consistent and sustainability manner. For instance, to increase or decrease the total amount of loaded drug per MN patch, two options may be possible. One is to change the drug concentration of liquid solutions and the other is to keep the same drug concentration, while changing the number of MNs per patch. However, either would increase the complication of production lines, leading to the reduced cost competition and production efficiency.

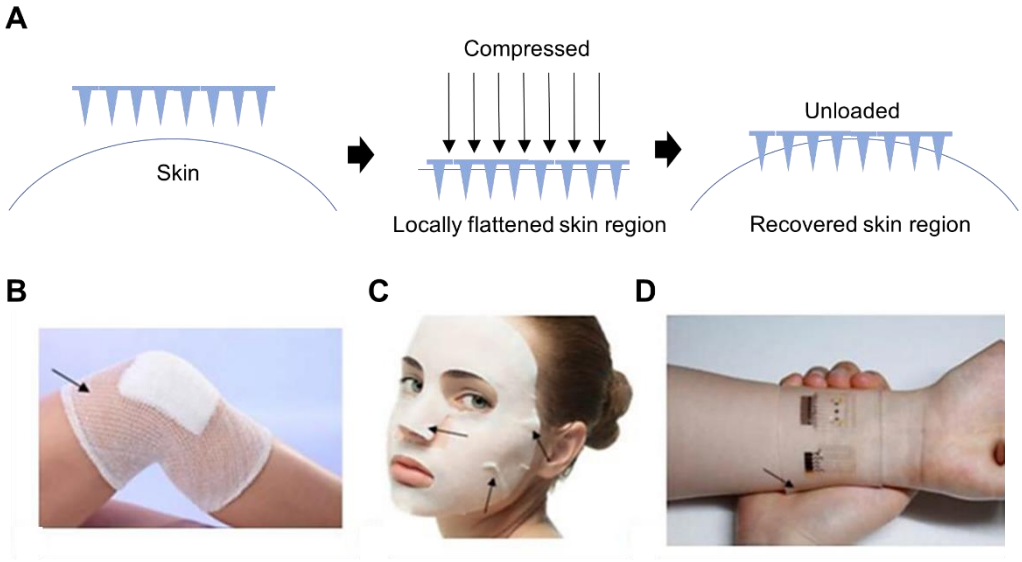

Figure 1-3. Existing conformity issue in flexible wearables. A. Illustration of conventional rigid MN patch on human skin before and after loading. B. stretchable knee bandage [19]; C. cosmetic facial mask [20]. D. conformal electronics [21] (The arrows indicate delamination or contact problem of the products).

1.2 Objectives and Scope

The ultimate goal of this research is to develop an ideal polymeric microneedle patch that provides uniform and consistent penetration of individual microneedles over target skin region with complex surface curvatures and large surface areas, allowing improved drug delivery efficacy and intended therapeutic outcome. Natural flexible armour systems often appear continuous, behaving as a seamless and comprehensive defence line to their organisms[21-26]. However, surprisingly, most of them consist of segmented articulating armour sub-units having evolved over millions of years to achieve a balance between protection and mobility, to maximize survivability of the species in their specific environments. Such biological exoskeletons, like human skin, consisting of multi-layered mineralized tissue with sensory and circulation systems, must fulfil

various performance requirements such as dissolution prevention, thermal and hydration regulation, mechanical protection, healing and regeneration, and growth[21, 22, 27, 28].

. In this context, there are great similarities between proposed ideal microneedle patch and natural flexible exoskeletal systems (e.g. fish armour [29]), summarized as shown in **Table 1-1**. Inspired by fish armour systems which are conformable, adaptive, flexible but rigid and responsive, multi-scale design approaches of natural segmented armour into flexible microneedle systems are proposed, as shown in **Figure 1-4**.

Table 1-1. Comparison between fish armour and an ideal microneedle patch[21, 22, 26, 27]

	Fish armour	**Ideal microneedle patch**
Unit	Fish scale	Microneedle
Unit property	Tough and rigid for protection	Sharp and rigid for penetration
	Sensing for regulation	Sensing and monitoring for controllable drug release
Assembly	Flexible and conformable through articulating multiple fish scales	Flexible and conformable through connecting microneedles
	Full body coverage by the sufficient number of scale units	Full coverage of a target area by adding or subtracting the number of microneedles

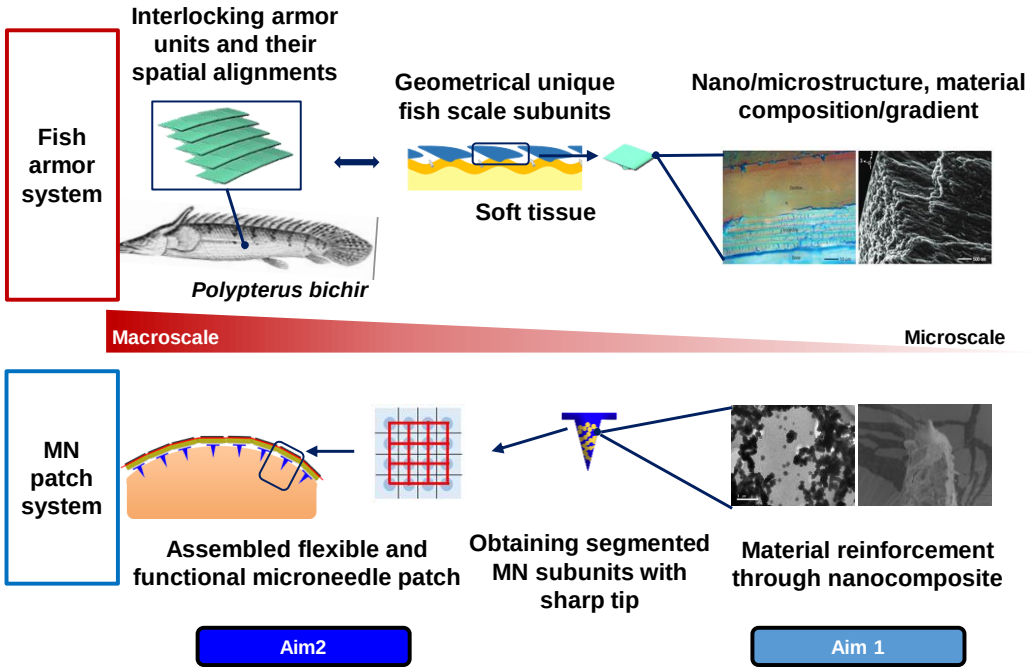

Figure 1-4. Schematics of flexible MN system inspired by natural armour system in multiscale manner [26]. By adapting the design from macroscale (spatial alignment of scale subunits on groovy patterned tissue) to microscale (composite-like material of individual fish scale) characteristics of ancient fish armour system, an ideal MN system with great skin adaptability and functionality can be achieved.

At microscale level, mechanical reinforcement of existing biodegradable microneedle system was proposed to ensure uniform and reliable penetration of individual microneedles during skin administration. In this case, low molecular weight biopolymer hyaluronic acid (HA) was chosen due to its excellent biocompatibility and frequent adaption by researchers in various biomedical field. Following objectives have been proposed:

- Reinforce low molecular weight HA with nanofiller and optimize the formulation to achieve mechanically strengthened matrix with good morphological consistency
- Fabricate microneedle through micro-molding method with comparable geometrical dimension as non-reinforced HA MNs

- Evaluate mechanical properties, drug release kinetics and biocompatibility of reinforced samples

At macroscale level, every microneedle should be able to penetrate consistently into human skin especially on curved surfaces like joint areas. Development of flexible and patterned microneedle patch has been proposed to address wearability issue of existing flexible continuous microneedle patch. This study aims to:

- Set up simulation model using ABAQUS to visualize deformation and stress distribution on selected patterned substrate during stretching
- Fabricate fractal cut substrate using 3D printer with appropriate STL design and dimension to act as flexible base of MN patch
- Segment HA-based MN array fabricated from micromolding technique to allocate onto least deformation spot on flexible base subunit
- Obtain surface conformity and drug delivery efficiency of conventional rigid, flexible continuous and proposed flexible patch through *in vitro* and *in vivo* evaluation

1.3 Overview and organization

This thesis reviews recent research regarding MN technology and proposes three approaches to address low drug loading capacity and penetration efficiency of polymeric MN system. The organization of the dissertation is shown in **Figure 1-5**.

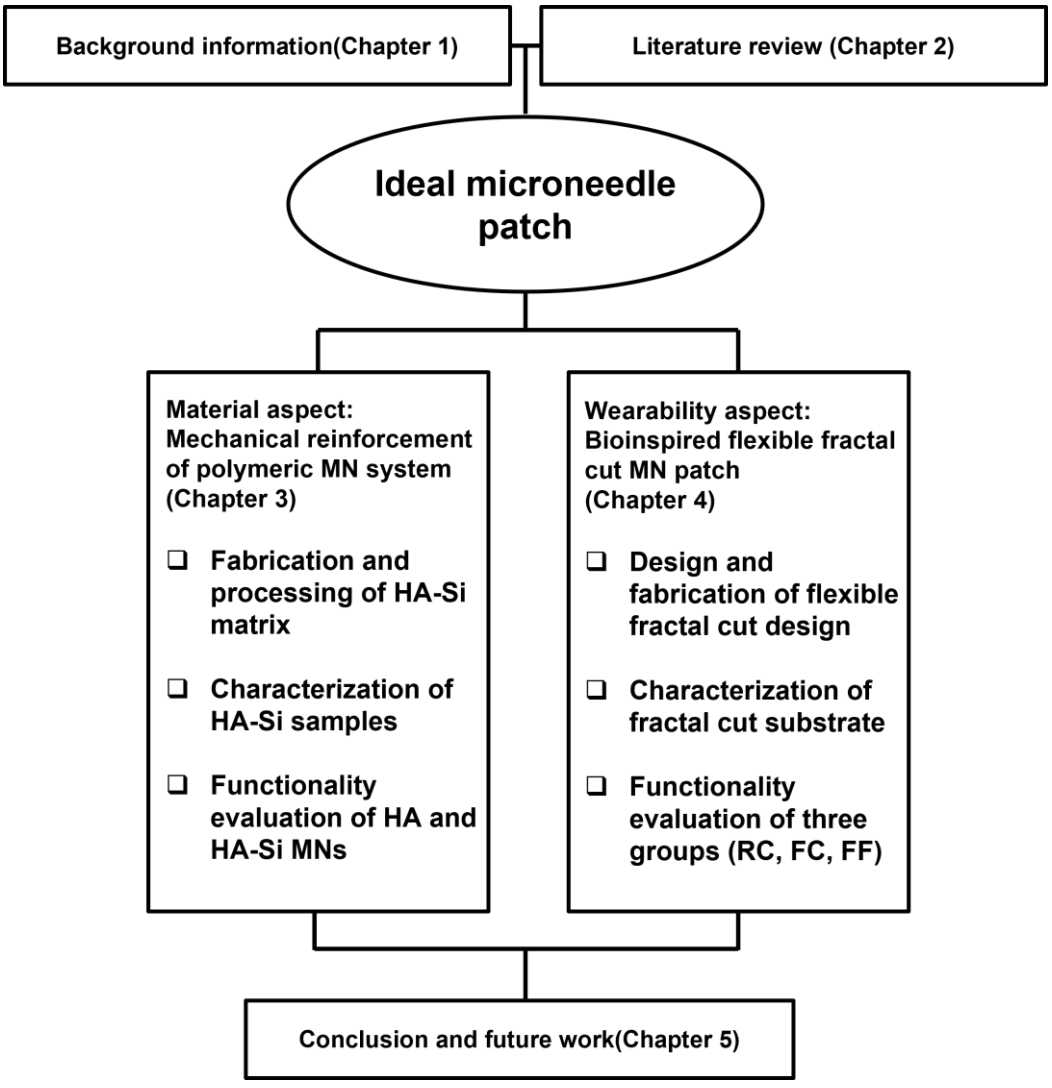

Figure 1-5. Diagram of thesis organization. This thesis addresses commercialization challenges encountered by rapid dissolving HA-based MN system that generally has low drug loading capacity and poor penetration efficiency. It reports two approaches inspired by nature to resolve the issue, which target material, and skin conformity respectively.

Chapter 1 provides background information of transdermal drug delivery, microneedle technology and its main applications. Biopolymer as one of the most trending materials for lab scale MN manufacturing was introduced and current bottleneck of MN technology was demonstrated.

Chapter 2 summarizes the existing MN technologies. First of all, transdermal drug delivery was introduced in which importance of MN technology was emphasized and compared with conventional drug delivery systems and previous generations of transdermal drug delivery technologies. The general requirements of MN were discussed, along with the introduction of four main MN categories: hollow, solid, coated and dissolving MN system. The characteristics of each system were reviewed and presented with several representative studies. Geometrical design of both individual MN and array was shown to be the crucial factor affecting penetration capability of MN system, thus each geometrical parameters were reviewed and discussed using several related studies. Among all, tip sharpness, length and density of the MN patch are the key factors according to the studies since these would extensively affecting MN insertion force, drug delivery volume and patience compliance which are the key element of defining penetration efficiency[30]. Additionally, bioinspired MN studies were reviewed where the research rationale and key findings were presented. 3D printing technologies have been widely explored in MN fabrication due to its manufacturing scalability and design flexibility. General processes of 3D printing techniques were discussed in terms of applicability in MN fabrications where FDM, SLA, DLP and TPP have the most interest in MN fabrication due to their resolution and material compatibility. Therefore, several 3D printed MN studies were reviewed based on these techniques. Flexible electronics are the current trend in healthcare industry due to their portability and prospective applicability in continuous health monitoring. Biomedical applications of these flexible wearables were reviewed. Lastly, MN system based on flexible substrates were presented based on continuous and patterned substrates. The literature review provides a guideline for the development of new

MN system to address key issues that hindered commercialization of MN technology.

Chapter 3 describes a new composite system based on medical grade low molecular hyaluronic acid (HA) for MN fabrication via micro-molding technique. A widely reported bio-reinforcement material, silica nanoparticle (Si NPs) is introduced to reinforcement HA matrix via *in situ* acidic sol-gel reaction of silica precursor tetraethyl orthosilicate (TEOS)[31, 32]. The fabrication and precipitation processes were validated by casting of composite thin film, tensile specimen and 10x10 MN array. In order to characterize precipitation of SiO_2 NPs in HA matrix after drying, transmission electron microscopy (TEM) was employed. Morphological properties were characterized and compared through optical image and scanning electron microscopy (SEM) to determine optimal silica concentrations for MN fabrication. Other chemical analysis like point scan energy dispersive spectroscopy (EDS) was used to verify elemental composition of HA-Si matrix locations. Moreover, mechanical properties like tensile strength and compressive strength, degradation and drug release kinetics, biological properties of HA-Si compositions were compared across different HA-Si volume ratio.

Chapter 4 reports a new flexible MN patch via hybridization approach of 3D printing and micro-molding method. A fractal cut design is adapted into the study to substitute conventional flexible continuous design of base substrate. First, a ABAQUS simulation model of rigid continuous, flexible continuous and fractal cut patterned substrate were created with experiment-retrieved mechanical properties. Contact conformity of these groups against spherical substrate was examined and compared, which then correlated as penetration efficiency. Strain behavior of these groups were characterized to determine potential tip delamination during stretching and verify appropriate location of tip displacement. Skin conformity of 3D printed fractal cut substrates were examined with 3D printed human elbow model and human volunteers in comparison of

conventional rigid and flexible continuous substrate. Lastly, functionalities like penetration and insulin delivery efficiency were evaluated using casted single-layered agarose elbow model and normal mice model respectively.

Chapter 5 summarizes key findings from previous chapters. According to the findings, we conclude that penetration efficiency of rapid dissolving MN system can be improved through material and skin conformity aspect such that uniform penetration and reliable drug delivery of MN system can be achieved. Finally, four future works are proposed to provide guidelines on further optimization of the proposed system. 1) fundamental study on MN geometrical effects, 2) large-scale and cost-effective DLP printing methods for MN systems, 3) development of 3D printing methods for flexible and cargo loaded hydrogel-based MN patch is also proposed and 4) electrochemical glucose monitoring of flexible MN systems.

References

1. *Transdermal Drug Delivery: Global Markets*. 2021, BCC Publishing Staff: BCC Research
2. Chinnadayyala, S.R., K.D. Park, and S. Cho, *Editors' Choice—Review—In Vivo and In Vitro Microneedle Based Enzymatic and Non-Enzymatic Continuous Glucose Monitoring Biosensors.* ECS Journal of Solid State Science and Technology, 2018. **7**(7): p. Q3159-Q3171.
3. Prausnitz, M.R., *Engineering Microneedle Patches for Vaccination and Drug Delivery to Skin.* Annu Rev Chem Biomol Eng, 2017. **8**: p. 177-200.
4. Larrañeta, E., et al., *Microneedle arrays as transdermal and intradermal drug delivery systems: Materials science, manufacture and commercial development.* Materials Science and Engineering: R: Reports, 2016. **104**: p. 1-32.
5. Kim, Y.-C., J.-H. Park, and M.R. Prausnitz, *Microneedles for drug and vaccine delivery.* Advanced Drug Delivery Reviews, 2012. **64**(14): p. 1547-1568.
6. Wang, R., et al., *Recent Advances in Polymer Microneedles for Drug Transdermal Delivery: Design Strategies and Applications.* Macromolecular Rapid Communications, 2022. **43**(8): p. 2200037.
7. Ahn, C.H., et al., *Disposable smart lab on a chip for point-of-care clinical diagnostics.* Proceedings of the IEEE, 2004. **92**(1): p. 154-173.
8. Takeuchi, K. and B. Kim, *Functionalized microneedles for continuous glucose monitoring.* Nano Convergence, 2018. **5**(1): p. 28.
9. Dixon, R.V., et al., *Microneedle-based devices for point-of-care infectious disease diagnostics.* Acta Pharmaceutica Sinica B, 2021. **11**(8): p. 2344-2361.
10. Ng, K.W., et al., *The diagnostic potential of microneedles in infectious diseases.* Precision Nanomedicine, 2020.
11. Hamzah, A.A., et al., *Optimization of HNA etching parameters to produce high aspect ratio solid silicon microneedles.* Journal of Micromechanics and Microengineering, 2012. **22**(9): p. 095017.
12. Laerme, F., et al., *Bosch deep silicon etching: Improving uniformity and etch rate for advanced MEMS applications*. 1999. 211-216.
13. Hernandez-Montelongo, J., et al., *Nanostructured porous silicon: The winding road from photonics to cell scaffolds. A review.* Frontiers in Bioengineering and Biotechnology, 2015. **3**.
14. Haidary, S.M., E.P. Córcoles, and N.K. Ali, *Nanoporous Silicon as Drug Delivery Systems for Cancer Therapies.* Journal of Nanomaterials, 2012. **2012**: p. 830503.
15. Faraji Rad, Z., P.D. Prewett, and G.J. Davies, *An overview of microneedle applications, materials, and fabrication methods.* Beilstein J Nanotechnol, 2021. **12**: p. 1034-1046.
16. Duan, D., et al., *Enhanced delivery of topically-applied formulations following skin pre-treatment with a hand-applied, plastic microneedle array.* Curr Drug Deliv, 2011. **8**(5): p. 557-65.
17. *PrimaNet® Net Tubular Bandage*. Cited 15/06/2022; Available from: https://www.primareltd.com/product/primanet-net-tubular-bandage/.
18. *Beauty Heaven. Reviews and Rewards*. Cited 15/06/2022; Available from: https://www.beautyheaven.com.au/skin-care/face-masks/superhero-face-masks.

19. *Tamicare. Cozyflex™*. Cited 15/06/2022; Available from: https://www.tamicare.com/cosyflex.
20. Alec. *British PhD student 3D prints on inflatable substrate to create artificial muscles*. 2015; Available from: http://www.3ders.org/articles/20150622-british-phd-student-3d-prints-on-inflatable-substrate-to-create-artificial-muscles.html.
21. Yang, W., et al., *Natural flexible dermal armor.* Adv Mater, 2013. **25**(1): p. 31-48.
22. Bruet, B.J.F., et al., *Materials design principles of ancient fish armour.* Nature Materials, 2008. **7**(9): p. 748-756.
23. Connors, M.J., et al., *Three-dimensional structure of the shell plate assembly of the chiton Tonicella marmorea and its biomechanical consequences.* Journal of Structural Biology, 2012. **177**(2): p. 314-328.
24. Liu, K. and L. Jiang, *Bio-inspired design of multiscale structures for function integration.* Nano Today, 2011. **6**(2): p. 155-175.
25. Spoerk, M., et al., *Anisotropic properties of oriented short carbon fibre filled polypropylene parts fabricated by extrusion-based additive manufacturing.* Composites Part A: Applied Science and Manufacturing, 2018. **113**: p. 95-104.
26. Song, J. *Multiscale materials design of natural exoskeletons : fish armor*. 2011.
27. Zhu, D., et al., *Structure and Mechanical Performance of a "Modern" Fish Scale.* Advanced Engineering Materials, 2012. **14**(4): p. B185-B194.
28. Song, J., et al., *Quantitative microstructural studies of the armor of the marine threespine stickleback (Gasterosteus aculeatus).* Journal of Structural Biology, 2010. **171**(3): p. 318-331.
29. Song, J., C. Ortiz, and M.C. Boyce, *Threat-protection mechanics of an armored fish.* J Mech Behav Biomed Mater, 2011. **4**(5): p. 699-712.
30. Johnson, A.R., et al., *Single-Step Fabrication of Computationally Designed Microneedles by Continuous Liquid Interface Production.* PLOS ONE, 2016. **11**(9): p. e0162518.
31. Yang, Y., et al., *Silica-Based Nanoparticles for Biomedical Applications: From Nanocarriers to Biomodulators.* Accounts of Chemical Research, 2020. **53**(8): p. 1545-1556.
32. Gerstenberg, M., et al., *Modular Hydrogel−Mesoporous Silica Nanoparticle Constructs for Therapy and Diagnostics.* Advanced NanoBiomed Research, 2022. **2**(3): p. 2100125.

Chapter 2

Literature review

An ideal MN system should be capable of delivering designated drug dosage in reliable manner. Therefore, individual MN should be robust enough to penetrate viscoelastic human skin while the base substrate could sufficiently be conformal to human curved surface to ensure uniform penetration of every MNs. This chapter introduces basic MN types, materials and respective fabrication methods to gain insight of choosing appropriate MN category that could fulfil desired biomedical purpose. The key factors determining penetration capability of individual MNs are material composition, geometrical design and interaction between MNs on the base substrate. Therefore, the geometrical parameters of tip and array designs are discussed, and previous studies on bio-inspired MN systems are reviewed. In recent decades, 3D printing of MN system has emerged as a promising platform due to its customizability. Basic 3D printing techniques and MN studies are explored. Finally, prior studies on flexible MN studies are reviewed, along with up-to-date flexible wearable technologies to show potential application of MN-based sensors in the future.

2.1 Transdermal drug delivery and microneedles

Drug delivery is a process of introducing pharmaceutic substances in the form of existing compounds or other xenobiotics to designated site of action within an organism, with the purpose of achieving therapeutic effect[1]. Study of their pharmacodynamics and pharmacokinetics are essential to utilize the properties for better efficacy and safety without compromising patient's compliance. Numerous drug carrier formulations aim to improve effectiveness of drug delivery have been developed and investigated over decades, for example liposomes, albumin microspheres, soluble bio-polymers, protein-DNA conjugates and hydrogel among others[2]. Depending on their favorable aspects and limitations, respective routes of administration are then implemented as to accomplish the adequate therapeutic outcome. Major routes of interest include oral administration, intramuscular or intravenous injection, inhalation through pulmonary circulation and transdermal delivery for systemic effect[3]. For treatment of typical human diseases, oral and hypodermic injection are more clinically favorable due to their simplicity and outstanding bioavailability. However, while these conventional drug administration methods are widely utilized, they still possess non-negligible problems to be resolved[4]. For orally administrated drugs, undesirable metabolic destruction by liver and intestinal wall often decreases amount of drug reaching the bloodstream despite of their noninvasive characteristics. On the other hand, although hypodermic injection allows direct delivery of drug into bloodstream with determined concentration reliably and rapidly, pain and higher risk of infections are usually accompanied with throughout the treatment[5]. As a potential alternative to oral delivery and hypodermic injection, transdermal drug delivery has been an attention topic in research studies due to its improved patient's compliance and localized drug profile. A variety of topical formulations which were to be placed on the systemic therapy have been explored over the years, starting from the first scopolamine patch which was approved by United states in 1979 for its effectiveness to treat motion sickness. Due to the selective permeability of skin, especially stratum

corneum which acts as a formidable transport barrier at the outermost skin layers, transdermal drug delivery systems are still tapered off at its scope due to the limited drug compatibility[4].

From there, first-generation transdermal delivery system has progressed slowly from small scale, low dose lipophilic drug to second- and third-generation drug delivery system that expands its applicability through modification of skin permeability, improving drug uptake and its consequent medical impact, in chemical and combination of physical approach respectively. Microneedles, a representative third generation drug delivery system have showed promising efficacy on permeabilizing epidermis physically by piercing with micro-scale needles and deliver drug with a self-administrable manner[6]. With its assuring capability of skin penetration, microneedles-assisted drug delivery candidates can be small molecules like calcein or large compounds such as protein and DNA[6-8]. Several advances in microneedle design and formulations have moved it towards a standalone drug delivery system that involved various development in fabrication methods and applications.

2.2 Classification of microneedle system

2.2.1 General requirements of microneedle

General skin anatomy must first be understood before expanding the discussion to the general design rule of microneedle system. Human skin consists of three layers, namely epidermis, dermis, and hypodermis, each with respective functions. Structures like blood vessel, lymphatics and nerve systems only exists underneath epidermis layer which implies that any penetration occurs in epidermis will not trigger pain receptor and damage blood vessel. Thickness of epidermis can varies from 500 μm to 1500 μm at different locations on the body[9] therefore as a superior counterpart of hypodermic microneedle in terms of improved patient's compliance, microneedles are fabricated at a micro scale length ranging from 150 to 1500μm, depending on the site of administration and consideration of drug properties and dosage. Expectation on microneedles with

painless penetration was proven by Gill *et al.* where microneedles administration has a pain scoring of 5% to 37% as compared to hypodermic injection with varying dimensions like tip angle, length, width and numbers of microneedles present on an array[10].

2.2.2 Types of microneedles

Microneedle (MN) can be fabricated by great variety of materials and fabrication depending on the desired application. In general, it can be categorized into four main types: hollow, solid, coated and dissolving MNs, as shown in **Figure 2-1**. Each array is made as a collection of needles to increase as much area of contact with interstitial area after penetration such that more interactions like drug release or biofluid extraction can be done in one go despite limited volume single microneedle tip provides. Among them, polymeric MN system has gained great attention in drug delivery studies due to their versatility in material programming and release kinetics. In the following section, characteristic, advantages, disadvantages and compatible materials of each MNs type will be further discussed and summarized in **Table 2-1.**

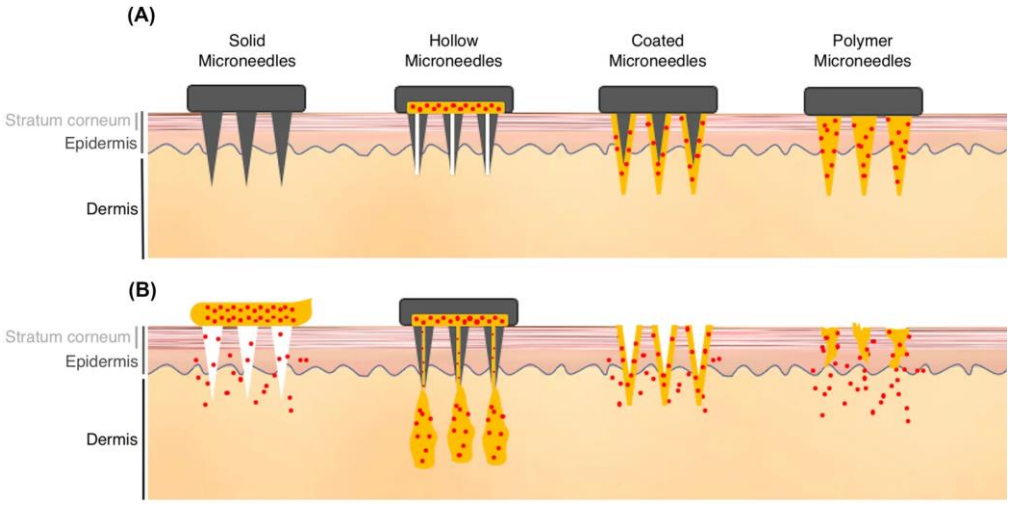

Figure 2-1 Basic types of MN and its mechanisms. A. Basic MN types with drug loading method. B. Release or drug delivery mechanism of respective MN types [34].

2.2.2.1 Hollow MN

Hollow MNs system consists of a chamber or cavity within the MN body and bore at the tip region, which is almost geometrically identical to that of hypodermic needles. Due to its high drug loading capability, it is reported to be used for vaccine, protein or other high molecular weight molecules[11]. Drugs can be filled into the empty space in advance and to be released upon insertion into skin. Li and the coworkers fabricated sharp silicon hollow microneedles with 5μm tip radii through deep-reactive ion etching (DRIE) for biofluid extraction[12]. The cavities were first fabricated through modified DRIE from the base side, having depth ranging from 30μm to >300μm which aimed to be exposed on the side of the MN. The photoresist coatings were then applied on the frontside to form MNs in pillar form and eventually sharpened using isotropic etching. Interestingly, release kinetics of drug loaded HMN is highly tunable through manipulation of hole diameter and drug formulation, depending on design intent, whether to release rapidly or in a controlled manner over time. In particular, Aoyagi *et al.* proposed fabrication of in-plane PLA MNs through heat casting of PLA pellets on potassium hydroxide (KOH) and tetramethylammonium hydroxide (TMAH) etched bulk silicon for blood extraction purpose[13]. Excimer laser with various power were then characterized in order to form either trench on the side or thin hole all-through the tip with diameter of 10, 20 and 50μm. Each design was testified for their capillary action-driven blood extraction capability, potentially provides alternative option for accurate blood glucose level measurement for diabetes. Also, flowrate of the loaded substance delivery can be controlled by specially designed device such as pressure actuator to achieve desired therapeutic outcome, as shown in **Figure 2-2**. For example, Bolton *et al.* reported hollow silicon microneedle system with integration of syringe pump to allow active delivery of fluorescent dye into human breast tissue[14]. The silicon hollow microneedle array with 1157μm length bore were first fabricated via three-step etching. The patch was then mounted to FITC loaded medical syringe and proved to penetrate

stratum corneum of human breast skin successfully. Further tests also proved successful detection of DIL fluorescent dye in porcine skin with constant flow rate of 10µLmin^{-1}[14-18].

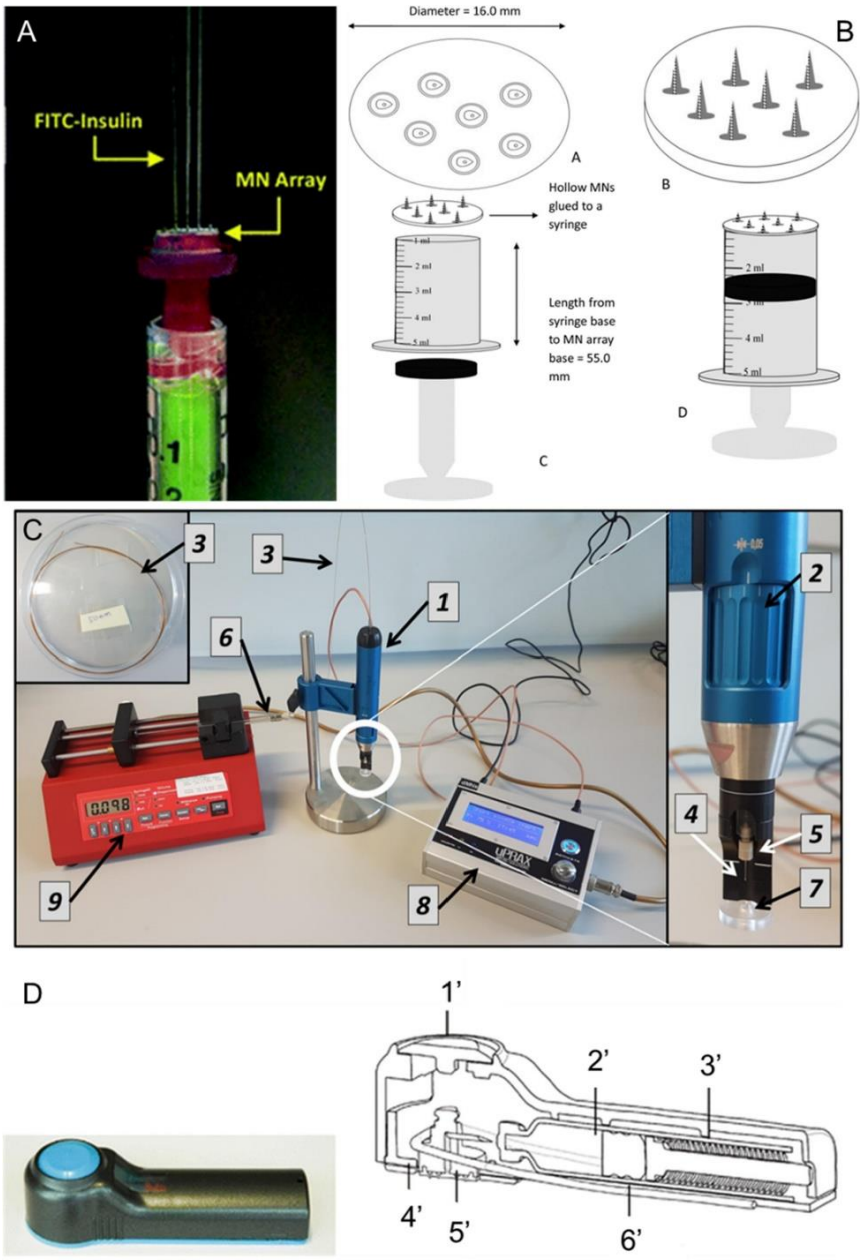

Figure 2-2 Examples of pressure-actuated device designed for hollow MN drug delivery system. A. Experiment setup of hollow MN attached to FITC-loaded syringe[27]. B. Illustration of hollow MN integrated modified syringe[29] C. Digitally controlled hollow MN injection system (DC-hMN-iSystem)[30]. D. Hollow Micro-structured Transdermal System (hMTS) and respective components [31]. Retrieved from Review [28].

However, hollow MN system has progressively became less attractive than solid MN due to disadvantages such as complicated fabrication processes, weaker strength due to tip design, heavy technical design and potential clogging or leakage of the channel[19].

2.2.2.2 Solid MN

Various research on MN technology has been studied over the decades ever since the first proposed solid MN made of silicon in the 1990s. Due to issue like biocompatibility and MNs mechanical resistance, many have then tried to investigate more versatile materials like metal, polymers and inorganic compounds[20]. In contrast to other MN types that could perform drug release subsequently upon insertion, traditional solid MN system is characterizable with its principle of "poke and patch" where no material residue degradation involved throughout the process and external drug reservoir in cream or patch form were to be administrated after transient formation of MN-induced microchannels. Therefore, strong material like glass, silicon, metal or non-degradable polymers are typical material of interest as they serve the best purpose in penetration[21, 22]. For instance, Pradeep *et al.* reported fabrication of high aspect ratio solid silicon MN through wet etching. The team optimized TMAH etching process by mix-and-matching factors like TMAH concentrations, etching duration, temperature and size of photoresist mask (**Figure2-3A**). They found that crucial factor of obtaining high aspect ratio MN is prominent etching rate in vertical direction than that of lateral direction. Through precise control over described factors, they have successfully fabricated MN with height-base ratio of 1.43 and tip radius of 0.20μm with ultimate tensile strength 52.2 times higher than skin[23]. However, the team did not include any biological test after the fabrication which is highly necessary since high aspect ratio of such fine and brittle MN could break due to misuse of insertion technique and remain as residual, causing tissue damage to applied site since silicon is not biocompatible. On the other hand, metal MN is not often studied as drug delivery device since high resolution fabrication of metal MN includes laser ablation which is

extremely costly and time ineffective. Instead, metal MN made of stainless steel is often used as high-resolution positive template for micro-molding technique or substrate in MN-skin interaction study. For example, Gupta *et al.* studied resealing process of human subjects' skin barrier upon MN insertion using electrical impedance spectroscopy. In plane stainless steel with various length, thickness, base width and MNs per array were prepared and studied on volar forearms of human subjects (**Figure 2-3B**). They found that micro-channels created by MN recovered within 2 hours if there is no occlusion while 3-40 hours are required depending on MN geometry if insertion site is covered. This result indicates that drug loaded in external reservoir can be effectively delivered without permeation concern since the occlusion can effectively slow down skin resealing process[24].

Recent years, polymers have received increasing attention as solid MN material candidate due to better material versatility and economically effective fabrication process. It can be further categorized into non-dissolving material like poly(lactic acid) (PLA) or Poly(methyl methacrylate)(PMMA) and chemically crosslinked biopolymer like hydrogel[25, 26]. Major fundamental difference between these two is that hydrogel-forming MN is water-absorbable thereby allows matrix swelling and facilitate drug permeation whereas non-dissolving polymer can only serve as pretreatment of skin similar to traditional solid MN material. For example, Donnelly *et al.* developed "super swelling" hydrogel MN system made of crosslinked PEG10,000, combining with ibuprofen sodium or ovalbumin loaded external lyophilized wafers for various drug delivery characterization (**Figure2-3C**). Their results showed prospective opportunity hydrogel MN- external drug reservoir configuration for drug and vaccine delivery[27]. To note, hydrogel MN system is also suitable for ISF extraction, which have also been reported in many studies[28-30].

2.2.2.3 Coated MN

At some point, coated MN is developed as the optimized design of solid MN due to its capability to release drug subsequently upon tissue contact. It is in general a solid MNs with a layer of drug formulation coated on individual tip body. Typical techniques to apply the layer are though dip-coating, spray coating or ink-jet printing among others[31]. For example, Ameri *et al.* successfully coated recombinant human growth hormone (rhGH) onto titanium MN through dip-coating on a roller drum[32, 33]. The thickness of the coating can be precisely controlled through number of dipping cycles (**Figure 2-3D**). *In vivo* dissolution test showed positive result as alternative platform for current rhGH hypodermic injection. However, some have introduced toxic chemicals like surfactant or thickening agent to ensure maximized drug coating thickness, which would potentially affect biocompatibility of the system[25]. Moreover, drug loading capacity of coated MN is still significantly lower than other MN types due to limit surface area for coating. Increasing thickness of the coating will also bring negative effects to the system such as compromised tip sharpness and overall mechanical strength[31]. Vaccination has shown to be an effective strategy in preventing death and severe illness against infectious diseases or pandemics. Recent needs of effective vaccination system have driven employment of MN system into the market since it provides numerous advantages over current clinical system, for example biohazardous waste reduction, self-administrable, and higher thermostability outside of cold supply among others, which potentially could improve global vaccination coverage especially those resource-limited regions[34]. Since vaccine doses are usually smaller compared to protein and peptides, many studies have investigated vaccine delivery efficacy and storage stability with coated MNs[35-37].

2.2.2.4 Dissolving MN

Dissolving MN is the branched subgroup from the development of solid and coated MN which have been the major focus in MN drug delivery technology due to its high material versatility and great flexibility in various functionalization. Dissolving MN systems are made of soluble or bio-degradable materials in which the matrix will slowly degraded along with the loaded contents, by implication able to act as an indicator of drug delivery completion (Dissolving MN is the branched subgroup from the development of solid and coated MN which have been the major focus in MN drug delivery technology due to its high material versatility and great flexibility for various functionalization[38, 39]. Dissolving MN systems are made of soluble biodegradable materials in which the matrix will be gradually degraded along with the loaded contents where no case of skin infection has been reported thus far. Due to excellent biocompatibility subsequent drug release upon insertion, dissolving MN is considered better than other types[40]. It can be further classified into rapid or slow dissolving MN systems where rapid dissolving MN can be fabricated using biopolymers like low molecular weight hyaluronic acid or sugars like maltose and sucrose[41]. For example, Lee *et al.* proposed drawing lithography fabrication of maltose-based microneedle patch for delivery of hydrophilic ascorbic acid-2-glucoside and niacinamide and proven to be delivered within 20 minutes[42]. On the other hand, slow dissolving microneedle system can be fabricated using polymers like PLA or PLGA which release within days to weeks[43]. Besides material aspect, factors like geometry and mechanical properties could also affect penetration performance of dissolving MN. Mechanical strength of biodegradable polymers is generally low as compared to silicon and metal MN, therefore often causing non-uniform or incomplete MN dissolution and lead to under-desired therapeutic level[44-46]. For example, Park *et al.* reported release rate controlled PLGA MN system for transdermal drug delivery where less than 10% of total mass of cargo was allowed to be loaded onto the MN before the system failed to penetrate the substrate effectively

(**Figure 2-3E**)[47]. Rationally, this could be one of the reasons why MN technology is still receiving low adoption rate in the market despite of advanced development over decades.

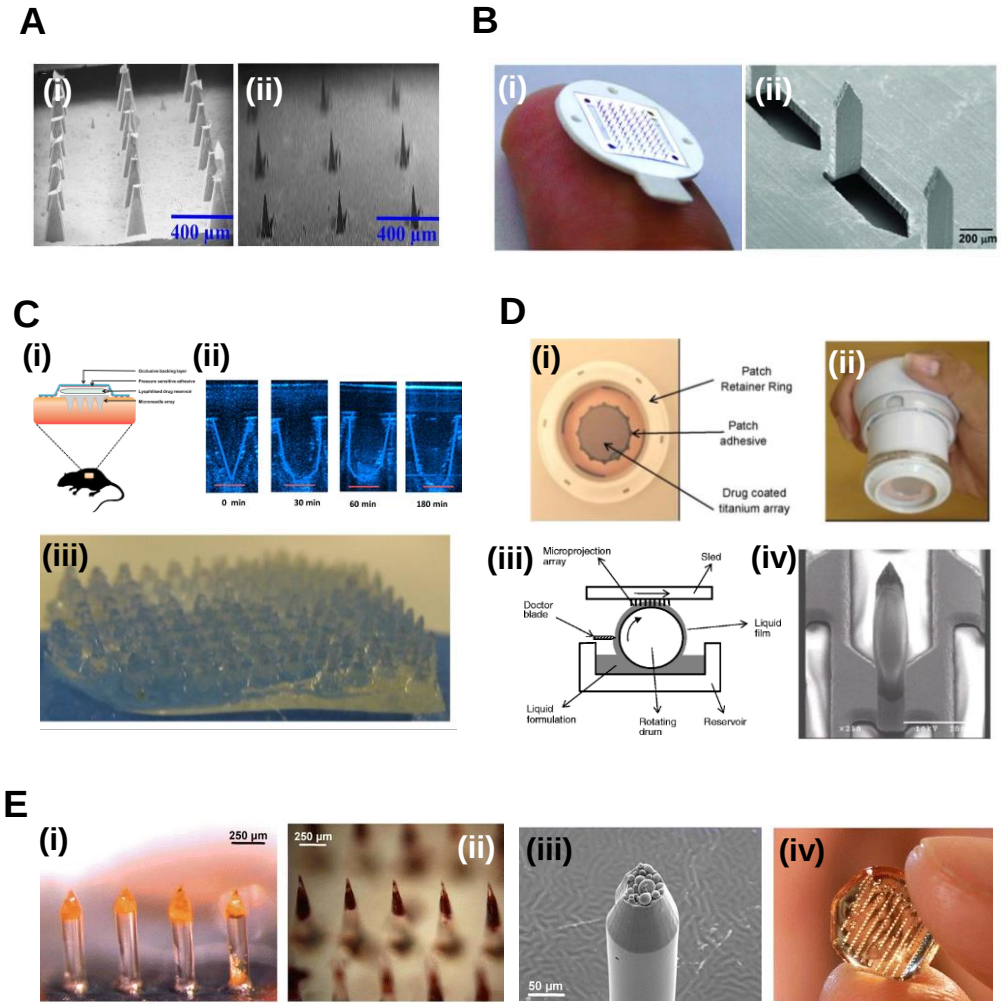

Figure 2-3 A. SEM images of solid silicon MN. (i) 3 x 6 array of solid Si MNs with SiO_2 layer for wet etching. (ii) Final solid Si MNs after 165 minutes etching[23]. Scale bars = 400µm. B. In plane stainless steel MNs for skin insertion. (i) Optical micrograph of 50 MNs array. (ii) SEM of a section of 50 MNs array[24]. Scale bar = 200µm. C. *Ex vivo and in vivo* swelling behavior of "super swelling" MN. (i) Schematics of experimental setup to evaluate *in vivo* cargo delivery on rat. (ii) False color image of the MNs swelling profile over 3 hours period using OCT on *ex vivo* porcine skin. Scale bar = 300µm (iii) Optical morphology of super swelling MN upon removal from rat skin after 24 hours insertion, showing that all MNs remained intact[27]. D. Coated MN drug delivery system. (i) Zosano-Pharma (ZP) with MNs in applicator ring. (iI) ZP-patch press fit onto applicator. (iii) Schematics of rhGH dip coating using roller drum[32]. (iv) SEM front view of individual rhGH coated MN[33]. Scale bar = 200µm. E. Drug loaded dissolving MNs with different shapes. (i) Optical image of bevel-tip MN and (ii) tapered-cone MNs made of PLGA and calcein encapsulation. Scale bar = 250µm. (iii) PLA microparticles exposed from the PLGA MN tip. Scale bar = 50µm. (iv) 20x10 array of PLGA MNs [47].

Table 2-1 Comparison of various MN types

Types	Characteristics	Advantages	Disadvantages	Material	Applications
Hollow	Holes at tip region or all through tip body Empty region to be filled with drug or as pathway for biofluid extraction	High drug loading volume Easy to control drug release kinetics or flowrate through hole shape	Complicated design and fabrication processes Low material versatility due to strength required More prone to tip breakage due to tip design Risk of clogging	Silicon Metal [48-51]	Disease diagnosis through biofluid extraction Drug delivery through cavity filling
Solid	Creating micro-channels for drug to be delivered in separate step Fabricated by strong material No loss in MN material after penetration	Amount of drug dosage not limited Simple fabrication process High mechanical strength	Requires two administration steps More prone to wound infection	Silicon Metal Polymers [6, 24, 52]	Drug delivery and cosmetics though external drug reservoir Disease diagnosis through hydrogel MN
Coated	Drug loading via various coating techniques Drug release upon penetration	Rapid drug release Able to choose strong material to facilitate penetration	Lesser drug loading Potential loss of drug due to shearing	Silicon Metal Polymers [53-57]	Drug and vaccine delivery
Dissolving	Encapsulation of drug in matrix Engineerable degradation profile Biodegradable	Biocompatible One step administration Efficient delivery of macromolecule	Requires optimization for different formulation Slower drug release Drug compatibility (hydrophilic/phobic)	Polymer [11, 58, 59]	Drug and vaccine delivery Cosmetics supplement

2.3 Geometry of MN

Due to viscoelastic nature of human skin, most of the functionalized MNs will undergo deformation upon administration, affecting penetration efficiency and resulting therapeutic effect. Geometrical design of MN arrays therefore must be carefully considered such that they could demonstrate sufficient strength under mechanical stresses (e.g. buckling force, bending force and skin resistance) acting on the tip during skin penetration with minimal failure[60]. Many have reported various determining factors through computational or experimental approach[61-63] which include shape, tip height and array density among others, as illustrated in **Figure 2-4.** To be noted that the intention of such manipulation is to maximize drug delivery efficacy through microneedle system with minimal side effect (**Table 2-2**). However, manipulation of single parameter often results in complication in other aspects. For example, increasing tip height enhances cargo loading capacity, but deeper penetration could result in pain which in turn compromise patient's compliance[10]. Therefore, obtaining effective range of every design parameter is important and can be done through detailed performance comparison and tradeoff analysis[64]. In the following section, we will focus on how previous studies characterize impact of different design parameters on drug delivery efficacy.

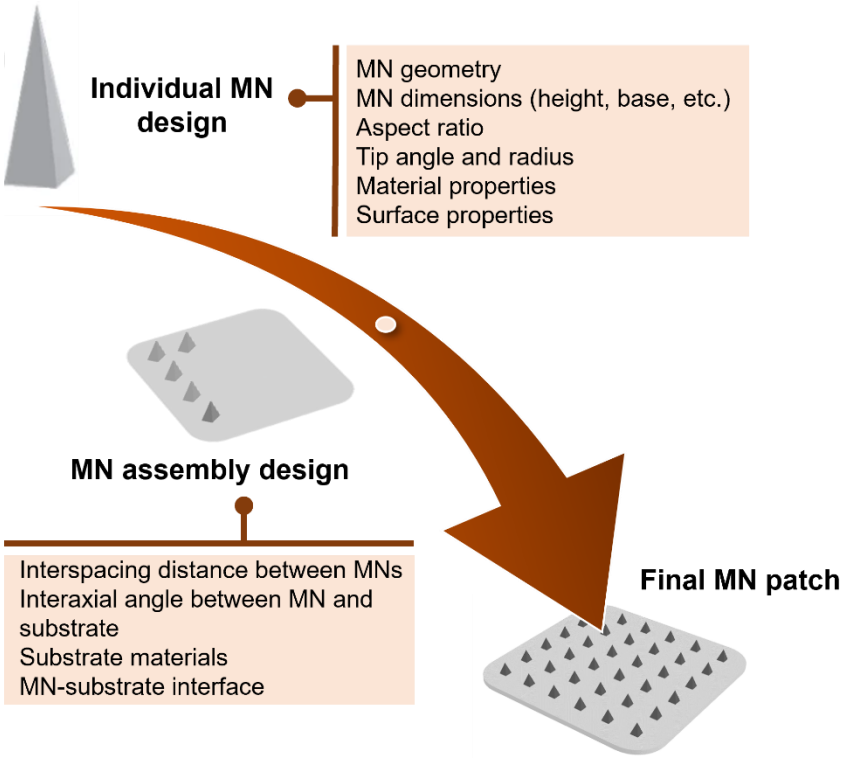

Figure 2-4. Hierarchy of MN system in the perspective of Individual tip design and MN assembly design. Parameters of individual MN design should be well aligned such that the MN can penetrate human skin with low insertion force. Design of MN assembly should ensure uniform and consistent performance of assembled tips, which includes parameters like MN alignment (orientation of neighboring MN) and base substrate design. Optimization of these levels form the final MN patch.

2.3.1 Common design of MN

An ideal MN should insert into skin effectively with minimal or no bulking or fracture, which could be influenced by strength of individual MN and insertion force to apply the MN patch. For example, overall MN strength can be synergically determined by material composition, height to base aspect ratio and MN shape, whereas tip radius, tip angle, number and density of the patch showed dominating impact over minimal insertion force required. Although geometrical design suggest insignificance to strong material like stainless steel, geometrical design of biocompatible materials with lower mechanical properties should be carefully considered. To categorize, common design rule of MN patch can be

split into individual tip design which includes shape, tip radius, tip height and aspect ratio while density and number of MN on each patch fall under array design.

Table 2-2. Relationship between microneedle design parameters to various factors affecting MN delivery efficacy.

MN design parameters	Strength	Drug loading	Treated Area	Penetration depth	Targeted cells	Release rate
Needle shape	✓	✓	×	✓	×	×
Tip height	✓	✓	×	✓	×	✓
Aspect ratio	✓	✓	×	✓	×	✓
Patch size	×	✓	✓	✓	✓	×
Interspacing distance	×	✓	×	✓	✓	×
Composition	✓	✓	×	×	×	✓

2.3.1.1 Tip design

Shape

Various MN fabrication methods have been proposed over the decades along with various design of MN shapes depending on application and fabrication limitation of respective techniques[64] as shown in **Figure 2-5A**. MN shape can directly affect stress and strain distribution within MN structure that induced by skin reaction force during insertion which contribute to MN fracture strength. Volume or surface area of MN could varies depending on the shape where optimal MN shape could effectively increase drug loading capacity. Penetration process can be generalized into two steps: skin breakage and shaft insertion. Under same administration force, penetration depth of various MN shapes can differ due to shearing of MN shaft design against tissue during insertion. The shapes can be further classified into in-plane and out-of-plane designs which

could be differentiated through the orientation between longitudinal axes and its substrate[65]. In-plane MN refers to the design where longitudinal axis of the MN is in parallel with its base substrate. It is usually used for chip-integrated biofluid analysis where micro-notches are built on the MN surface through laser-ablation or etching[12, 66]. The extraction of biofluid can be achieved through capillary action of the built microchannels. For example, Mamun *et al.* presented fabrication of in-plane silicon MN for biomarker extraction and analysis. In-plane Si MN arrays with 1 and 5 MNs/ array was fabricated via deep reaction ion etching (DRIE) where the wedge-shaped MN tips were further sharpened through selective chemical etching of HF-HNO_3 mixture[67]. The penetration capability of fabricated Si MN arrays was evaluated through *in vitro* chicken breast penetration and computational buckling simulation. The team has proven effective penetration capability of fabricated in-plane Si MN arrays which were to be integrated with post-complementary metal-oxide-semiconductor (CMOS) sensor for biomarker analysis. Silicone is the major material used for the fabrication of in-plane MN due to its compatibility with dry/wet etching method and lower manufacturing cost of etching compared to laser ablation of stainless steel. It is advantageous in terms of dimensional flexibility since the length and shape of MNs can be easily controlled through etching properties. However, there could only be a limited number of MNs on a single array which constrained its application in drug delivery[68]. Besides that, post-processing is required to further improve tip sharpness of the MN system since etching of in-plane MN system is often anisotropic[68].

On the other hand, longitudinal axis of out-of-plane MN is perpendicular to its base substrate so more MNs can be fitted on one array. This design is suitable for drug delivery as more micro-channels can be created on skin upon insertion so higher concentration of loaded substances can be delivered simultaneously. Typical out-of-plane MN system for drug delivery are in pyramidal and conical shape[69], with or without heighted base (obelisk and conical cylinder) which are all geometrically symmetry. Such design is

advantageous during skin insertion since stress and strain development within the MN structure against substrate resistance can be uniformly distributed as compared to traditional beveled tip that resembles shape of hypodermic needle. Thanh and the co-workers have developed computational model of polymeric based pyramidal and beveled MN to investigate optimal design for whole blood collection[70]. They found that both critical buckling load and maximum bending force exhibited by pyramidal MN were significantly higher than that of beveled tip. The simulated results were further validated through aluminum plate-penetration test where pyramidal MN had significantly higher failure force than beveled tip with 2.74N and 0.46N respectively (**Figure 2-5C**). Although polymeric beveled tip appeared to have weaker performance as compared to polymeric pyramidal MN, it still possesses outstanding advantages when fabricated using strong materials like silicon or stainless steel for hollow MN biofluid application. As sample extraction rate is essential in biomarker analysis, beveled tip offers greater flexibility in hole diameter design to adapt to different purposes whereas cavity design of hollow symmetrical MN is limited since the cavity is often placed on the MN tip. Large cavity design might lead to blunter tip and compromise aspects like penetration force and patient compliance.

Another study regarding to the comparison of immunization efficacy between conical, conical cylinder, pyramidal and hexagonal pyramidal MN were proposed by Li *et al.* In this study, *in vitro* Sprague Dawley (SD) rat skin insertion tests of aforementioned geometries showed that conical MN had the best skin insertion ratio among all as high as 97.8%, followed by hexagonal pyramidal (76.2%), pyramidal (49.6%) and conical cylinder MN (38.8%)[71]. Interestingly, volume ratio of conical: pyramidal: hexagonal pyramidal MN were shown to be 100:64:83 which means that not only conical MN can effectively penetrate the skin, maximum drug loading capacity of conical shape dissolving MN also showed superiority over other mentioned shapes. Finally, i*n vivo* study of ovalbumin loaded MNs showed better immunization effect as compared to that of hypodermic needle injection, suggesting that vaccine delivery through DMNs

can be a promising alternative in the future market. Moreover, Loizidou *et al.* have also shown that mechanical properties of pyramidal MNs can be affected by the number of vertices in the polygon base[72]. In this study, three types of pyramidal MNs (triangular, square and hexagonal) were investigated computationally in terms of critical load factors and von Mises stress. A higher critical load factor(k) indicates higher required load to reach buckling (unstable) while lower von Mises stress indicates less likelihood to yield. According to the result, higher number of vertices displayed higher k value and lower von mises stress (**Figure 2-5D**) which in turn proven that hexagonal had the best mechanical strength among all (hexagonal > rectangular > triangle).

Recently, irregular shape like arrowhead was proposed as a potential solution to existing limitation of biodegradable dissolving MN like incomplete penetration depth and insufficient strength. An array with blunt shafts attached to base substrate can first be prepared using strong material like stainless steel or PLA. Next, individual blunt shafts can then be jointed to drug loaded polymeric solution in standard micro-mold MN wells which will act as the tip region. Interface between blunt shaft and tip region can be coated with highly water-soluble polymers like PVA which act as adhesive layer such that the blunt shaft can be easily detached from the tip region upon skin insertion[73]. Due to this tip-shaft separable characteristic, different formulation can be prepared on the same patch to achieve desired therapeutic regimen. For example, Chen *et al.* proposed an arrowhead MN system with basal-bolus insulin regimen which aimed to cover three-meal-based postprandial glucose excursions in one patch (**Figure 2-5B**)[74]. Gelatin(gel), crosslinked gelatin (cGel) and cGel/hyaluronic acid mixture (cGel/cHA) with different drug release kinetics were used to load different types of insulin (short-, intermediate- and long-acting insulin) which expected to regulate blood glucose levels at pre-determined timepoints. Separable arrowhead MN benefits long term drug release in this study such that PLA as supporting shaft could provide sufficient strength for the insulin-loaded tip region to penetrate effectively and to be removed after then so only tip regions

will stay in human skin, reducing risk of patch detachment from normal movements. Results showed that integrated arrowhead MN designs were able to respond to intraday- elevations of blood glucose level in diabetic rats.

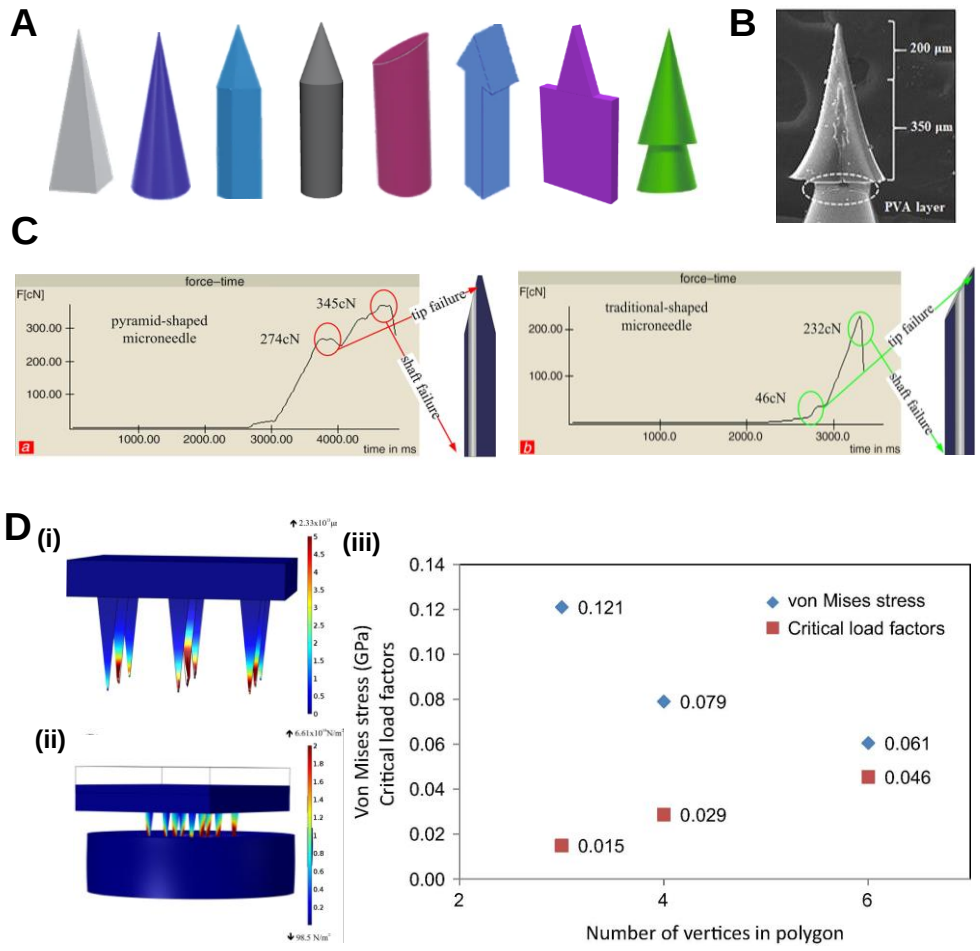

Figure 2-5 MN geometrical studies on shape effect. A. Common MN shape designs where studies showed that strength, drug loading capacity and penetration depth can be affected by MN shape [65]. B. SEM image of fabricated arrowhead cGel-cHA MN tip with PLA support shaft [74]. C. Fracture test result (force-displacement) of pyramidal cylindrical and bevel-tip SU-8 MNs. D. COMSOL FEM model of 3x3 MNs array under 5N axial force from the base in terms of (i) buckling mode and (ii) surface von Mises stress. (iii) Effect of facets in polygon on fracture strength, presented in von Mises stress (GPa) and critical load factors.[72]

Aspect ratio

Aspect ratio of MN refers to the length ratio between tip height and base diameter which should be crucially considered as it determines mechanical integrity and drug loading capacity of individual MN, especially for low mechanical strength biodegradable MN in coated and dissolving MN systems. For instance, Park *et al.* developed a mathematical model to analyze relationship between aspect ratio of single MN to failure force. Two mathematical formulas were employed, namely Euler's formula[72] which used to analyze elastic-like buckling of long MN (high aspect ratio) and Johnson's formula[75] which used for inelastic-like failure mode of short MN (low aspect ratio)[76]. This study demonstrated that under appropriate experimental setup (end fixity k = 0.7), data acquired from both formulas aligned well with experimental PLGA conical MN axial test. According to the results (**Figure 2-6A**), longer MN exhibited lower failure force, showing higher risk of buckling under same compressive load (>1000μm) whereas wider base diameter showed higher failure force due to greater mechanical stability. They concluded that aspect ratio of 12:1 or below and material with Young's modulus more than 3GPa were recommended for MN design. Findings in another study well aligned with these findings[77]. Rationally, increased MN length leads to higher volume available for drug loading and more effective drug permeation to deep dermis layer where capillaries present[78, 79]. However, reaching deep dermis layer would potentially induce pain receptor which have been shown in a study[10]. The study showed that tip length had the most dominant effect on pain as much as 7-fold increase in pain with 3-fold increase in MN length. In the same study, MN tip angle and base diameter did not show significance on pain score. A review literature suggested that minimum pain is induced when MN length is less than 750μm[80].

Tip sharpness

While studies tend to employ large force or high velocity during skin insertion to ensure effective penetration of MN array and compensate resolution limitation for fabricating less optimal MN tip sharpness, many have overlooked

the fact that tip sharpness, or tip diameter is the main factor deciding insertion force of individual MN tip. During MN application, skin will first undergo deformation and indentation before breakage happens. Smaller tip diameter with steeper tip region will influence lesser skin area upon contact, such that localized deformation can occurs predominantly over global deformation, causing skin fracture with lesser energy wastage[81]. Römgens *et al.* reported their findings in monitoring penetration process of glass MN with various tip diameters (**Figure 2-6B(i)**)[81]. They found that there was a linear relationship between tip diameter (5-37μm) and force required to break superficial layer of human skin (20-167mN) which suggested that sharper MN tip can induce skin breakage easier. The team concluded that tip diameter lesser than 15μm is preferable for vaccine delivery. **Figure 2-6B(iii)** showed their explanation regarding to the phenomenon where for tip diameter lesser than 80μm, force to stretch skin surface dominates force to compress skin underneath the MN and vice versa for tip diameter larger than 80μm. Similar tendency was reported by Davis *et al.*[82] and Park *et al.*[77] where linear relationship were observed between tip-skin interfacial contact area and insertion force. However, tip sharpness can also decrease structural strength of tip region which could cause undesired buckling or breakage if the material has low mechanical properties like biodegradable polymers.

2.3.1.2 Array design

Single MN has very limited drug loading volume or capacity to create microchannel that is sufficient to achieve minimal therapeutic efficacy thus MN system is usually designed as 2-D array with a collection of single MNs attached and arranged in specific orientation. Many studies have reported efficiency related factors of MN array design which will be discussed in following sections.

Size of MN patch (number of MNs)

Generally, MN array is fabricated in dimension of 0.5cm^2 to 1cm^2 as it is designated for self-administration therefore small dimension is preferred. For

coated and dissolving MN system, drug loading volume is often determined by the number of MNs present on the array therefore it is necessary to understand how increase of MNs can affect penetration behavior during application. For example, a study has investigated on how MN geometry effect would affect maximum insulin concentration in blood through mathematical framework[62]. Effect of having 50 to 500 MNs per array were calculated and plotted as shown in **Figure 2-6C**. Pharmacokinetic model used was as follow:

$$Vb\frac{dCb}{dt} = \left(\frac{dQ}{dt}\right)Sa - KeCbVb, \text{ [62]}$$

where Vb is the volume distribution in blood, dCb/dt is the change of insulin concentration into skin, dQ/dt is the penetration rate of insulin across skin, Sa is the surface area of MN patch, Cb is the insulin concentration in blood and Ke is the elimination rate constant. According to the model, effective surface area of MN patch and insulin concentration in blood has a linear relationship, therefore linear increase of insulin concentration in blood were observed as number of MNs increased. While some other studies have also proven higher drug permeability with increase of MN number on single array[83, 84], insertion force should be considered as well. Since interfacial contact area increases, higher force is expected in order to ensure full penetration of every individual MN, heightened the risk of incomplete penetration if insufficient force is exerted. The administration with more MN numbers will cause more severe pain as well[10]. Moreover, while keeping interspacing distance of MN to be constant, increase of MN number will inevitably increase overall patch size. Human skin is curved and flexible therefore contact between MN patch with rigid substrate could be problematic. Even though Ripolin *et al.* proposed flexible substrate for larger MN patch application, uneven force distribution across entire area could cause inconsistent MN penetration and drug dosing[85].

Interspacing distance

Increase of drug loading volume not only could be achieved by various approaches as mentioned before, but also appeared to be reasonable by increasing MN density on a limited area of substrate (fitting more MNs on the patch while patch dimension remains unchanged). However, studies have shown that a phenomenon called "bed of nails" tends to occur in high MN density patch [61, 86-88]. For example, Römgens *et al.* proposed a computational model to predict antigen diffusion and internalization of vaccine loaded MNs with various array design which includes interspacing distance, MN length and base diameter[88]. Efficiency of immune response in this study was defined by the proportion of antigens taken up by cells and number of antigen-presenting cells (APC) in epidermis and dermis. The process of antigen kinetics (release, diffusion and activation) was described by PDE developed by the team themselves[89]. Number of activated APCs were normalized and plotted as function of interspacing distance (0.25-4mm) as shown in **Figure 2-6D**. Saturated threshold (0.1-0.5) refers to the minimum amount of antigen required to activate the immunization. The result showed similar tendency in which higher number of activation cells occurred at higher interspacing distance until reaching maximum. For $\theta = 0.5$, optimal interspacing distance of 1mm and 1.5mm gave maximum number of APCs in epidermis and dermis respectively. Above the optimal distance, APCs showed constant value below maximum. This indicates that optimization of interspacing distance is crucial depending on the desired penetration depth and drug delivery intended. Another study[86] has reported that lesser normal stress was observed on the MN tip during penetration when interspacing distance increased, which in turn proven that resistance of penetration decreases when interspacing distance increases[90].

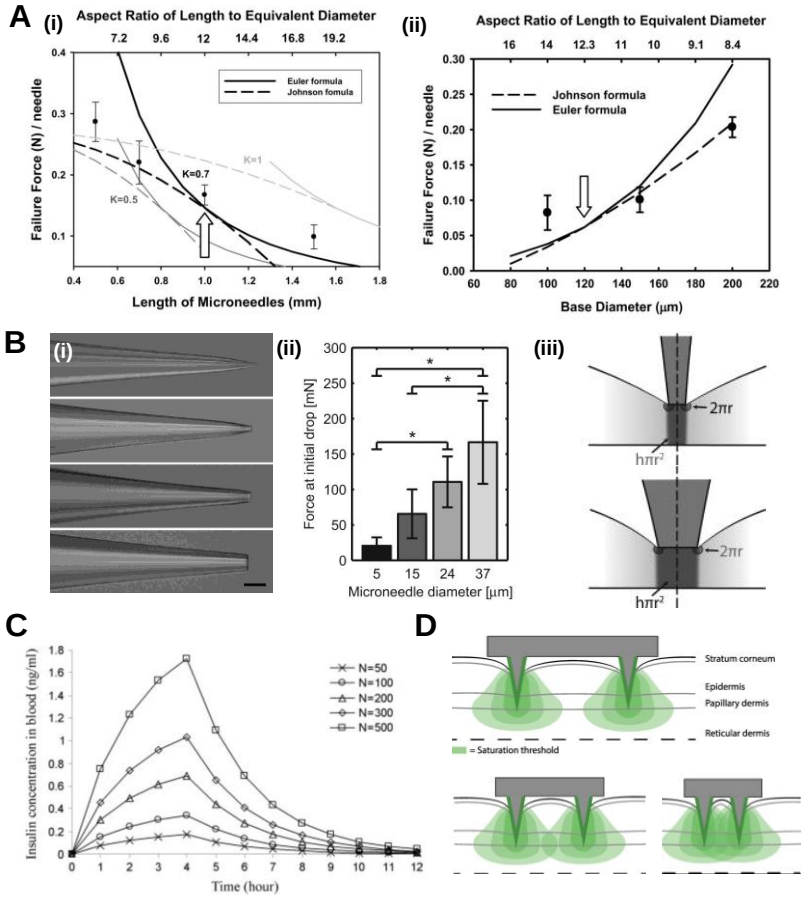

Figure 2-6. Geometrical studies on aspect ratio, tip sharpness and array density. A. Experimental and numerical predicted failure force of MN: (i) with D_{tip} = 25μm and D_{base} = 200μm, as a function of MN length and end fixity factor K(0.5, 0.7 and 1.0).[76] (ii) MN with D_{tip} = 25μm, L = 0.7mm, and E = 3GPa at K = 0.7. B. Penetration study of glass MN with varying tip diameters. (i) Optical images of solid MNs fabricated using micropipette puller, with tip diameter of 5, 15, 24 and 37μm. Scale bar = 50μm. (ii) Influence of MN tip diameter on force at initial drop (human skin breakage). Mean and SD are shown (n=10, 6, 6, 5 from small to large tip respectively) * indicates significant difference between two groups with $p < 0.05$. (iii) Schematic explanation of phenomenon. For MN with tip diameter < ~80μm, shear force on the surface, which is proportional to r (two shaded areas on the surface), predominating force to compress skin underneath MN, which is proportional to r^2 (shaded area underneath the tissue). For tip diameter > 80μm, compression force gets predominant [81]. C. Influence of MN numbers/array (N) on insulin concentration in blood, assuming wedge-shaped MNs were applied for 4 hours [62]. D. Schematics showing effect of interspacing distance on activated antigen cells with (i) large, (ii) optimal, (iii) small interspacing distance. Optimal interspacing distance offered largest area exceeding saturation threshold.

2.3.2 Bioinspired design of MN

Besides aforementioned artificial geometry design of MN system, bio-inspired MN studies have shown great functionality as MN geometrical designs, fulfilling biomedical applications like wound healing, drug delivery, drug loading and tissue adhesion mechanisms among others. Natural bio-microneedle in general possesses ingenious penetration properties with low insertion force, high mechanical integrity, high tissue adhesion and excellent biocompatibility[91]. Due to their complex and multi-functional geometries, conventional fabrication methods like etching or hot embossing will not be able to accurately duplicate micro-scale details of the design thus 3D printing has been employed in these studies to facilitate fabrication of bio-inspired MN design[46]. In the following section, some bio-inspired MN studies will be reviewed and discussed. More studies with interesting mechanism and functional achievements are summarized in **Table 2-3**.

2.3.2.1 Bug-inspired MN

Inspired by the scent gland secretion mechanism of a true bug (Heteroptera) that has unique wrinkles or microstructures aligned along the secretion channel for unidirectional and passive fluid transport, Hischen *et al.* abstracted microstructures of selected European true bugs into individual 3D microstructure for repetitive ablation on technical surfaces (steel, PMMA, PDMS etc.) (**Figure 2-7A(i)**)[92]. Following which, Plamadeala *et al.* adapted the microstructure design and proposed fabrication of pyramidal MN with microstructured surface through ornamentation[93]. **Figure 2-7A(ii)** illustrates conceptual design of the surface ornamented pyramidal MN tip fabricated via two-photon polymerization (2PP) to achieve microscale geometry with such omnidirectional complexity while maintaining high resolution (**Figure 2-7A(iii)**). In addition, honeybee stinger-inspired MN were developed to address weak tissue adhesion of MN patch during administration. Structurally, the stinger rod has a length of ~1.1mm and ultra-sharp tip angle of 33^{o}. where microstructured

barbs are found to be distributed evenly along the stinger (**Figure 2-7B(i)**) which effectively decrease insertion force while drastically improved tissue adhesion with 70 times larger in magnitude than smooth needles [91]. Chen *et al.* reported fabrication of honeybee-inspired MN system through novel magneto-rheological drawing lithography (MRDL)[94] with iron particles dispersed uniformly in epoxy novolac resin at designated ratio to prepare a curable magneto-rheological fluid (CMRF) (**Figure 2-7B(ii)** and **2-7B(iii)**). Although high-resolution barbed MN was fabricated with excellent functionality, complicated processes were required to obtain single MN, which made feasibility of complete MN patch and mass production questionable. Asides from tree bug and honeybee, mosquito proboscis-inspired biopsy needle was proven to reduce local tissue deformation and global organ displacement during biopsy, assuring effective target tissue sample acquisition for cancer diagnosis[95]. Adapting from this mechanism, Suzuki *et al.* expand the design on hollow MN application[96-98]. The MN was fabricated as a bundle of two parts, a pair of maxillae (with harpoon-shaped notches) and one labrum (extract fluid through capillary action) using ultra-precision 3D laser lithography and printer compatible resin (**Figure 2-7C(ii)** and **2-7C(iii)**)[96]. Again, the fabrication processes are sophisticated while parameters like notch shape, size and vibration source also are not optimized yet. Still, this interesting concept could potentially benefit blood collection procedure of chronic disease patients in painless and minimal invasive manner.

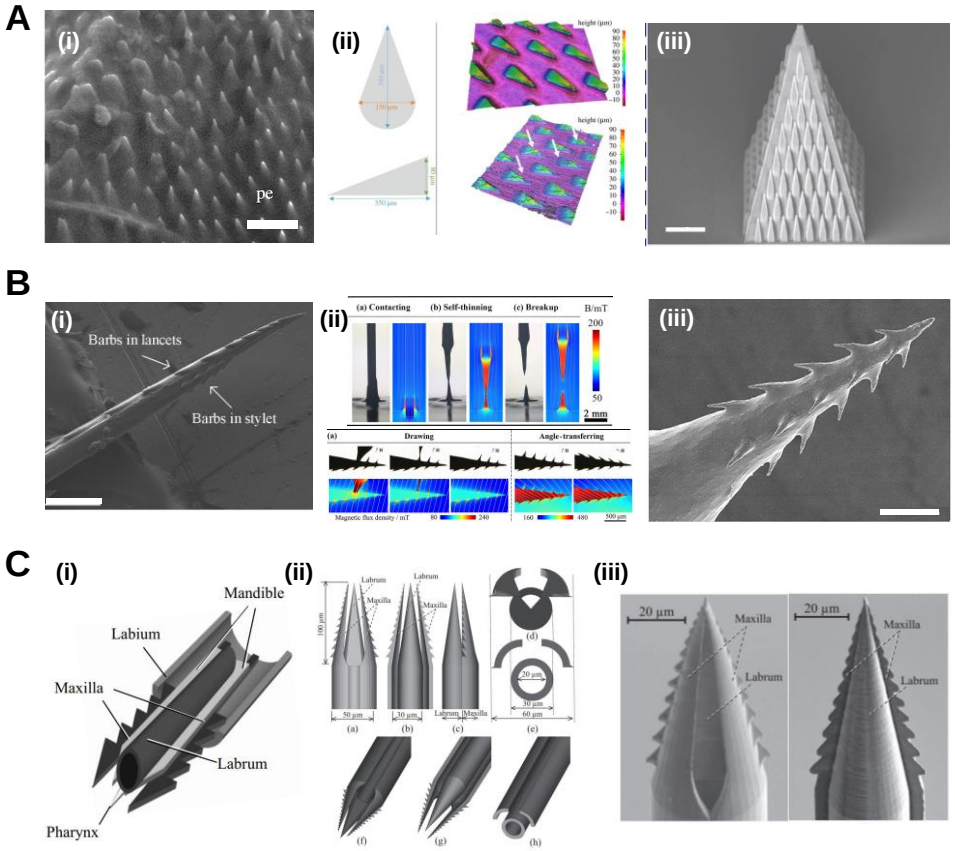

Figure 2-7. Bug-inspired MN studies. A. True bug efferent system inspired microstructure. (i) SEM image of detail microstructure orientation on peritreme of *Tritomegas bicolor* [92]. Scale bar = 20µm(ii) Dimension of individual microstructure design and aligned microstructures. (iii) SEM side view of TPP printed microstructured MN. Scale bar = 50µm [93]. B. Honeybee inspired barbed MN system. (i) SEM image of worker honeybee stinger with barbs. Scale bar = 100µm [91]. (ii) Fabrication process of barbed MNs using magnetorheological drawing lithography, including formation of parent MNs on pillar tip through contacting, self-thinning and breakup, followed by drawing of pre-barbs and angle transferring to form final barbs. (iii) SEM image of honeybee inspired microbarbed MNs for improvement on tissue adhesion [94]. C. Mosquito proboscis inspired MN study. (i) Schematics of mosquito's proboscis composed of seven parts. (ii) CAD design of three-parts MN design, imitating two sets of maxillae and one labrum. (iii) SEM images of TPP printed mosquito proboscis inspired MNs (front and back view) [96].

2.3.2.2 Tooth-inspired MN

Besides geometrical uniqueness, the material structure reinforcement phenomenon in biological organisms have been analyzed such that it could be implemented as engineering solutions[99]. For example, limpet tooth that has been reported in literatures as the strongest material found in nature, with tensile strength values up to 6.5GPa. Through observations in micro- and nanoscale, researchers have realized that this remarkably high tensile strength of limpet tooth results from distinctive orientation of high aspect ratio geothite nanofibers in the protein matrix. These mineral nanofibers were found to occupy approximately 80% of the total volume in mature tooth, aligning in parallel to the surface (**Figure 2-8A(i)**)[100]. Li *et al.* adapted the concept and proposed fabrication of limpet tooth inspired MN with aligned iron-nanoparticles bundles embedded in the matrix using magnetic assisted 3D printing (**Figure 2-8A(ii) &(iii)**)[99]. Also, front-fanged snakes' venom injection mechanism resembles traditional hypodermic needles and hollow MNs which deliver drug through hollow channel. With high pressure actuator, this could potentially be implemented into MN system to allow rapid and effective drug delivery. However, external pressure (through pump or actuator) is required and would be costly and ineffective in timely manner with the risk of cavity clogging[98]. Therefore, Won *et al.* adapted venom injection mechanism of rear-fanged snakes where venoms tend to be delivered passively without pressure-driven mechanism by designing fang-inspired MN with tri-, tetra-, penta- and hexa-grooves in contrast to original mono-groove structure of rear-fanged snake, providing multiple flow path and allow drug delivery occurs more rapidly (**Figure 2-8B**)[101]. These multi-grooved MNs (MG-MN) were fabricated via backside exposure lithography using biodegradable PEG-DA with sufficient mechanical strength to penetrate skin effectively. Furthermore, a shark tooth-inspired MN dressing(**Figure 2-8C**) for multi-functional wound management purpose was proposed by Guo *et al*. [102]. Shark teeth are flat and inclined in general which allow shark to bite and hold the prey firmly. By mimicking such structure, MN

dressing was able to provide strong skin adhesion throughout the treatment. In addition, the microfluidic channel incorporated at the back of the MN dressing can analyze biomarker at wound site to monitor progress of wound healing. Mxene-based electrocircuits were integrated aside with the microfluidic channel to act as motion sensor such that undesired stretching of wound area can be tracked and facilitates effective healing.

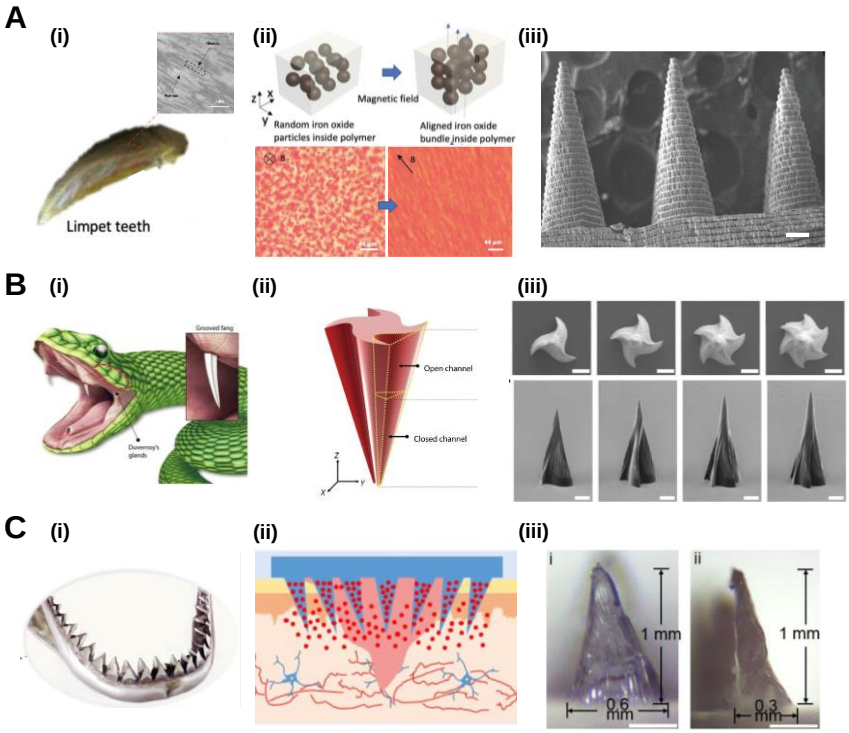

Figure 2-8. Tooth-inspired MN studies. A. Limpet tooth inspired microfiber alignment MN system. (i) Optical image of fiber alignment within limpet tooth microstructure. (ii) magnetic field assisted alignment of iron nanoparticles into fiber-like bundle. (iii) SEM image of magnetic assisted 3D printed MN. Scale bar = 50µm [99]. B. Rear-fanged snake inspired MN system. (i) Schematic illustration of rear-fanged snake and its venom delivery system. Venom secreted from Duvernoy's gland flow through groovy snake fang into prey under capillary action. (ii) Schematic illustration of MN design in which narrow channels were created for cargo to be delivered from patch reservoir. (iii) SEM of top and side view of fabricated tri-, tetra-, penta- and hexa-grooved MNs. Scale bar = 100µm [101]. C. Shark tooth inspired inclined MNs for improved tissue adhesion. (i) Illustration of inclined shark teeth orientation. (ii) Schematic illustration of shark tooth inspired MN system for wound healing management. (iii) Optical image of casted shark tooth inspired MN (front and side view). Scale bar = 3mm [102].

Table 2-3 Summary of various bio-inspired MN studies

Inspiration source	Application	Summary of findings	Ref
European True bug / Efferent system	Improvement of drug loading consistency for transdermal drug delivery	Microstructures were fabricated through ornamentation Oriented microstructures directed drug flow unidirectionally towards MN tip Provided promising design as bio-inspired drug coating method	[93]
Worker honeybee / Stinger	Improvement of tissue adhesion for transdermal drug delivery / disease diagnosis	Both MN and barbs were fabricated through magnetic field assisted lithography Pull-out force of bioinspired MN was 2.6 times higher than barbless MN	[94]
Mosquito / Proboscis	Improvement of MN insertion force for transdermal drug delivery / biopsy sampling	Three-in-one bundled (maxillae and labrum) MN was fabricated through 3D laser lithography Alternative vibratory motion of maxillae significantly reduced insertion resistance Blood sample was successfully extracted through capillary action for analysis	[96]
Limpet / Tooth	Mechanical enhancement of polymeric matrix through nanoscale fibers	Iron nanoparticles were aligned as bundled filament within MN matrix through external magnetic ring Optimal concentration of 2.5% aIOs MN showed no buckling and higher mechanical strength as compared to pure polymer and rIOs MN Mice studies showed painless administration of aIOs MN patch	[99]
Rear-fanged snake / Fang	Drug delivery through open conduits created on MN surface from drug reservoir	Multi-grooved PEGDA MNs were fabricated through backside exposure lithography All MNs were robust enough for skin penetration Rapid cargo delivery of 15seconds were achieved using penta-grooved MN Ovalbumin delivery showed effective protection against influenza virus in mice and guinea pigs	[101]
Shark / Tooth	Tissue adhesion for wound healing	Flat and inclined shark tooth inspired MN templates were fabricated through laser engraving of tilted and stretched PDMS Motion sensor and microfluidic channel were integrated onto the patch for efficient wound healing tracking and management	[102]

		Delivery of hEGF showed superior healing progress as compared to controls	
Mantis **/** **Forelegs**	Tissue adhesion for transdermal drug delivery (**Figure 2-9A**)	Conical and inclined mantis acicular foreleg inspired MN templates were fabricated through using oriented ferrofluid droplets and external magnet Casted silk fibroin-PEGDA MN patch showed excellent tissue adhesion under the presence of external force and rotation Delivery of glucocorticoid showed enhanced therapeutic effect on imiquimod-induced psoriasis in mice	[103]
Eagle **/** **Claw**	Tissue adhesion for wound healing	Liquid metal was encapsulated into MN patch through novel stack-molding technique (**Figure 2-9B**) Casted eagle-claw inspired MNs effectively anchored onto linear wound site while pulling wounds closer to prevent dehiscence Liquid metal connected to external power supply provides 2V/cm electric field to the wound site and proven to accelerate wound healing rate as compared to controls	[104]
Mussel or octopus **/** **Byssi or tentacles**	Tissue adhesion for transdermal drug delivery (**Figure 2-9C**)	Mussel-octopus inspired MN was fabricated using PEGDA-alginate as MN, adhesive PDA-gelatin as base with six suction cup-like structure surrounding each MN The integrated MN showed excellent skin adhesion in dry, wet or under external stress (bear object >240 times of their mass) MN showed to be antibacterial and promote cartilage healing with decreased fibrosis	[105]

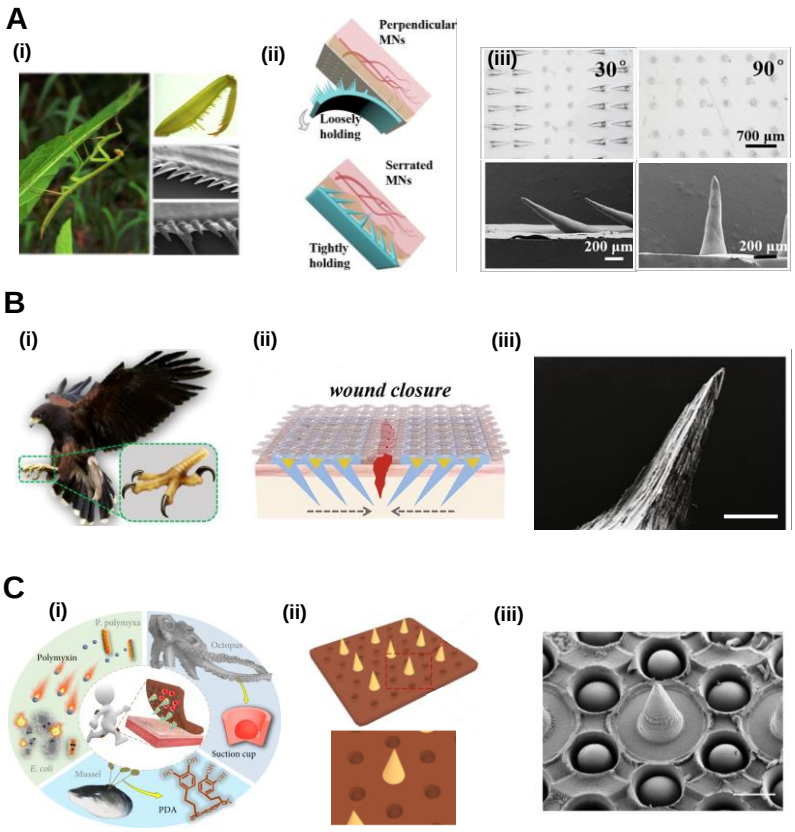

Figure 2-9. Other bioinspired MN studies. A. Mantis foreleg inspired MN study for improved tissue adhesion. (i) Illustration of mantis foreleg with slanted serrated microbarbs. (ii) Illustration of attachment stability of two patches when placed upside down. Grey arrow shows that conventional perpendicular MN patch is prone to fall off whereas proposed serrated patch holds on firmly. (iii) Optical and SEM images of fabricated serrated MNs with 30^{o} and 90^{o}. Scale bar = 700µm / 200µm [103]. B. Eagle claw-inspired MN system for wound healing acceleration. (i) Illustration of eagle claw clamping mechanics. (ii) Schematic illustration showing that clamping MNs could tighten the wounded site and prevent dehiscence. (iii) SEM image of magnified MN tip. Scale bar = 200µm [104]. C. Octopus and mussel inspired adhesive MN for osteoarthritis treatment. (i) Schematic illustration of bioinspired multifunctional MNs with antibacterial and adhesive capabilities. Mussel byssus inspired adhesive PDA hydrogel was used as flexible base substrate while each MN was surrounded by a circle of octopus suction cup- inspired concave chamber. (iii) SEM image showing suction cup-inspired concave chamber surrounding a MN. Scale bar = 300µm [105].

2.4 3D printing technology for MN fabrication

Numerous MN fabrication methods have been developed over decades, including hot embossing[65], dry or wet etching[23], droplet-borne air blowing method[106], lithography[50] and micromolding among others. While these fabrication methods have been widely proposed in various research studies, they still possess technical restrictions in terms of scalability, customizability and cost effectiveness[20]. Although micromolding technique is compatible with wide variety of polymeric material and able to fabricate MN rapidly in low cost manner, master template customization is costly and labor-intensive therefore still problematic especially for geometrical studies of MN and precise imitation of complex bio-inspired MN shapes as mentioned in the last section.

Additive manufacturing, or 3D printing offers layer-by-layer manufacturing of 3D model with high reproductivity, structural versatility and operational simplicity at micro- or nano-scale precision[107, 108]. According to ASTM F2792-12a, classification of 3D printing includes extrusion-based, photopolymerization-based, material jetting, powder-based and two other processes[109, 110]. Since the first FDA approval of 3D printed drug Spritam® in 2015[111], there has been an explosive growth of 3D printing technology in biomedical applications which advanced revolution of biomedical field towards customizable and personalized therapy. Each 3D printing technique has its own intrinsic limitation in terms of resolution, build volume, equipment cost and biocompatibility. Depending on the printing method, they can be employed for different biomedical purposes, for example laboratory instruments, diagnostic probes, tissue engineering, microfluidic chip, drug carrier or disease model used in researches[112]. In the following section, we will first review basic working principle of commonly used 3D printing techniques and discuss on their applicability on MN printing.

2.4.1 Common 3D printing techniques for biomedical application

2.4.1.1 Powder based 3D printing

Powder based 3D printing includes powder bed fusion (PBF), binder jetting and directed energy deposition (DED). These techniques are commonly used for thermoplastic polymers and metal/alloy 3D printing at high speed and high output volume[109]. PBF in general uses powder bed feedstock mechanisms wherein powdered materials were to be spread flatly on the building platform under heat sources like laser, electron beam or infrared lamp. The layered printing can be achieved by scanning heat sources across designated locations, bringing temperature of scanned areas to reach their glass transition temperature and bond together into solid layer. The building platform is then lowered by piston where another layer of powder will be spread on top of the solid layer via roller before subsequent printing[113]. In contrast to PBF, binder jetting replaces heat source with binding adhesive agent to hold the powdered material together in layer-by-layer manner. After printing, additional infiltrant substance or heat treatment will be introduced to improve mechanical properties of the printed parts[114]. However, binder jetting printed objects are usually brittle, therefore not suitable for functional purpose like transdermal drug delivery. DED on the other hand utilizes powder injection through nozzle to deposit and thermally bond powdered material from scratch or addition on workpiece. Therefore, DED is usually employed for part repair or structural modification[109].

Among all powder-based printing processes, only selective laser sintering (SLS) under PBF and binder jetting are more widely used in biomedical applications as dental and anatomical model due to poor accuracy and material pools of DED printing in general[115]. Main commercial materials used for SLS are polyamides, Alumide and rubber-like materials[116]. Recently, great efforts were made to expand applicability of SLS towards biomedical applications. Biocompatible materials like hydroxyapatite-based composites, polyvinyl alcohol, poly (L-lactide) have been reported to be SLS compatible biomaterial

for porous scaffold printing in tissue engineering[113]. Besides that, metals, bio-ceramics were also considered for personalized modelling of fracture implants and prosthetics purpose. In general, resolution of powder-based 3D printing is highly dependent on the powder particles size which usually lies between 58-180μm[114] and laser beam diameter. Due to intrinsically high porosity and surface roughness of SLS printing in addition to the large powder size, powder-based 3D printing has not been reported for microneedle fabrication.

2.4.1.2 Material jetting

Material jetting works similar to that of binder jetting where inkjet print head was used to position the jetting and disperse the material in layer-by-layer fashion[112]. However, in this method, polymeric material in liquid formulation will be jetted directly on the building platform to shape the structure and therefore supporting substrate is necessary for fabrication of complex overhang objects. Material jetting has been widely used in biomedical applications like scaffold printing and MN drug coating. Biocompatible photopolymers like alginic acid and gelatin can be used as bioink jetting of scaffold[117]. However, due to requirement of low viscosity ink and weak adhesion between printing layers, material jetting has not been reported in fabrication of MN structure[112]. Still, attributed to its controllable dispersion rate and precise positioning, many studies have proven that material jetting printing could facilitate uniform drug coating on MNs.

2.4.1.3 Extrusion based 3D printing

Extrusion based 3D printing is one of the most common printing processes that have been utilized in 3D printing manufacturing due to its ease of use and wide material adoption. In general, extrusion-based printing uses pneumatic actuator or mechanical screw to force melted polymer or semi-liquid viscous material extruded out through a nozzle or needle onto a building platform. Printed parts then required to be cured with various mechanisms, including thermal-, chemical- or photo-crosslinking depending on the material properties. Deposition rate, printing speed and coordinates in X, Y, Z directions are

controllable through computational command to obtain well-printed construct without disconnection or overlapping between filaments and layers[118]. Before the print, one should characterize printability of the ink in terms of viscosity, temporal and thermal stability such that these printed layers could be well extruded throughout the printing sequence and become self-supporting before next printing layer. As for printing of complex geometry, supporting bath or substrate are necessary especially those with curve and shell-like structures, i.e. freeform printing.

Typical extrusion-based technologies are fused deposition modelling (FDM) and direct ink writing (DIW). Main difference between these two are the material and presence of heating element. FDM is compatible with thermoplastics that requires melting process, for example poly(lactic acid) (PLA) and acrylonitrile-butadienestyrene (ABS). Heating process of FDM will adversely affect polymeric structure and cell viability during bioprinting of cell-laden hydrogel. In addition to this, hydrogel material is usually existing as viscous liquid so it could not provide self-supporting and form filament during the printing without curing process. Therefore, printing of hydrogel is usually done with DIW, which is more compatible with hydrogel material, colloidal suspensions and organic ink among others[119]. Resolution of extrusion-based printing is mainly affected by intrinsic rheological properties of ink (capability to hold filament diameter upon extrusion), print head velocity and nozzle or orifice diameter where these printing techniques have been reported to have low resolution(~100μm) and poor mechanical properties.

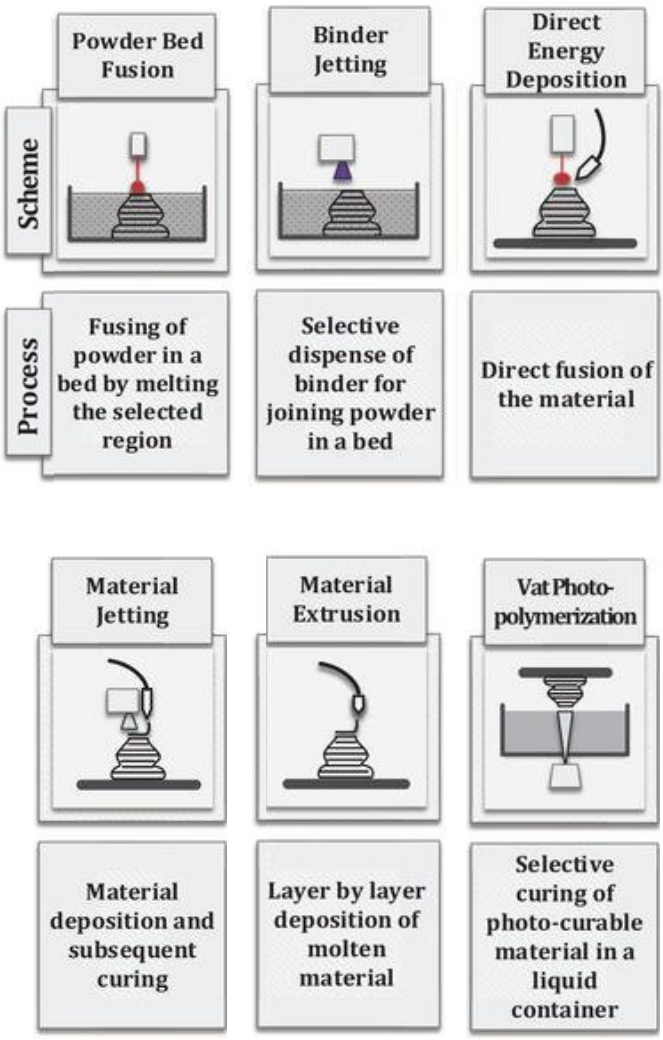

Figure 2-10. Schematic illustration and working summary of basic 3D printing techniques [110].

2.4.1.4 Vat polymerization-based 3D printing

Vat polymerization (VP) utilizes laser, UV or visible light to selectively cure liquid photopolymer that hosts in a vat into 3D constructs in layer-by-layer fashion. VP-based 3D printing methods use either top-down or bottom-up configuration of building platform. Top-down systems will have their printing stage submerged in the vat with exactly one layer printing thickness below the photopolymer surface. The light source on top would then be projected onto the

printing stage and initiates polymerization of the photopolymer such that adjacent polymer chains at the scanned area can be crosslinked and form the first 2D pattern. The printing stage would then move downwards until it reaches subsequent one layer thickness for next layer printing. This step will be repeated until full 3D model is printed. On the other hand, bottom-up approach will have the building platform submerged as deep to the vat bottom so that the light source placed under the vat can be projected through optically clear vat bottom and polymerizes the scanned area on the building platform. The platform would then lift for a layer-thickness distance to continue the next print. Two configurations work equally well when the construct has a uniform aspect ratio (height vs width) but when the CAD model is longer, delamination or crack formation between layers would be expected in bottom-up printing due to insufficient strength to counter gravitational force. On the other hand, when CAD model has a larger surface area, inhomogeneity or formation of void would be expected in top-down printing if the printed layers does not submerge consistently through the one-layer thickness recovery of uncured photopolymer after every subsequent Z-movement and before next layer printing.

One example of VP is stereolithography (SLA). SLA is one of the first few 3D printing technologies that has been launched in the market. It uses a laser of UV light (typically at 325nm) to operate where the source will move across building platform in point-to-point raster scan mode to cure the construct layer-by-layer. SLA was widely used in biomedical applications like scaffold printing since it offers high throughput procedure. However, SLA has been reported to have drawback of limited material choice, expensive, poor mechanical strength, low biocompatibility and time consuming where over-exposure of high-power UV would damage encapsulated cells during printing. Recently, micro-stereolithography (μ-SLA) has been proposed to address long printing time of SLA and limited resolution of DLP which will be discussed next. It comprises of LCD with photomask where individual pixels of LCD will project 2D pattern of

particular layer onto the resin such that the entire layer could be scanned and cured at once.

Digital light processing (DLP) works similar as SLA but instead of laser-UV light, it uses visible light range of wavelength[120]. Scan mode of DLP works the same as μ-SLA where image of the entire layer will be projected at once onto the building platform, effectively shorten building time as compared to SLA. Biocompatible materials like PEGDA and GelMA were reported to be used for DLP hydrogel bioprinting. Due to rapid printing of DLP, it has been utilized in printing patients' anatomical model for surgical preparations.

Multiphoton polymerization (MPP), in particular two-photon polymerization (2PP) is an emerging laser-based printing method that allows printing of complex structure within nanoscale. It comprises of two femtosecond infrared laser sources that could excite photo-initiator of single focal point and initiate polymerization only at that point. Through direct laser writing from point to point, TPP could produce 3D model without needs of supporting substrate with 100nm lateral resolution and 300nm axial resolution which benefits printing that requires nano-scale precision. Due to the reduction of needs for post-treatment like etching, polishing or post curing which often associated in other techniques, 2PP has been extensively used in various industries especially biomedical fields with wide variety of biomaterials (i.e. bioceramics, water-soluble polymers, composites).

2.4.2 Example and applications of 3D printed MN

In previous section, various mechanisms of basic 3D printing techniques were briefly reviewed and discussed to gain understanding of their respective limitations and potentials in MN fabrication, the summary of various 3DP features and their applicability in MN fabrication are tabulated in **Table 2-4**. Although powder-based 3D printings are compatible with strong materials like metals and alloys, poor biocompatibility and low microscale resolution of the products have hindered their applicability in MN fabrication. In fact, only two

studies have reported fabrication of MN using powder-based printing. For instance, Gieseke *et al.* reported their fabrication of hollow MN using selective laser micro-melting (SLM) which claimed to have higher resolution than that of SLS printing[121]. The fabricated MN is as shown in **Figure 2-11A(ii)**. Cylindrical stainless steel hollow MN with 160µm inner diameter was shown to have undesired particle adhesion on the surface, causing severe surface roughness that could not be resolved through proposed post treatments. In another study, solid MN was fabricated via direct metal laser sintering (DMLS) using the same material[122] (**Figure 2-11A(iii)**). In this study, electropolishing was employed as post treatment to smoothen the surface while further improving tip radius of the sintered MN. Although both surface roughness and tip radius were improved, undesired reduction in height was observed. To date, other processes like FDM, SLA, DLP and 2PP are of high interest in MN fabrication studies due to relatively better biocompatibility and resolution. Few studies will be reviewed in terms of respective fabrication processes.

2.4.2.1 Fused deposition modeling (FDM)

Although FDM has been widely reported to be excellent technique as controlled release drug carrier, patient-customized drug with respect to physiological factors (age, body weight, severity of disease etc.), low resolution due to limited availability of fine nozzles restraining their feasibility in MN fabrication. To address the issue, Luzuriaga *et al.* proposed post-etching process as conjunct technology to FDM[123]. In this study, biodegradable thermoplastic poly(lactic acid) (PLA) was used. Due to limited nozzle size with 0.35µm, screening of suitable MN shape was investigated and realized that only cylindrical MN could penetrate *in vitro* and *ex vivo* skin model after chemical etching. Degradation rate of PLA was mainly affected by strength of acidity or alkalinity, therefore high concentration potassium hydroxide (KOH) was used as the etching solution and the etched MN was as shown in **Figure 2-11B(ii)**. Although penetration test in this study verified penetration capability of etched PLA MN, non-uniform morphology of the MN would cause non-consistency in

terms of drug coating volume and mechanical integrity when apply to different skin conditions. Similar study was reported by Wu *et al.* where parametric studies of printing and etching condition were investigated to resolve PLA interfacial detachment issue during chemical etching[124]. In this study, printing conditions like nozzle and printing stage temperature were carefully optimized to facilitate stable welding of interfacial PLA layers with lesser void formation. Under optimal chemical etching conditions, PLA MNs with micron scale were also achieved (**Figure 2-11B(iii)**). The tissue adhesion capability and rhodamine B delivery efficiency of different MN structures (straight or inclined) were proven to be efficient using *in vitro* porcine skin penetration test.

2.4.2.2 Stereolithography (SLA)

Commercially available resins are often used in SLA based MN fabrication due to low adaptability of SLA technique to typical photopolymers like PEGDA and GelMA that used in research studies. For example, Uddin *et al.* proposed cross-shaped coated MN for anticancer drug delivery[125]. Cross-shaped was chosen to address limited drug volume of conventional shape and commercially available class I biocompatible resin was used (**Figure 2-11C(ii)**). Hydrophobic drug cisplatin (CPT) encapsulated in rapid dissolving hydrophilic polymer was successfully coated onto 3D printed MN through inkjet printing. *In vitro* penetration showed uniform penetration of cross-shaped MN into porcine skin while compression test showed sufficient force for skin penetration as well. Finally, *in vivo* studies showed successful tumor inhibition effect of CPT on Balb/c nude mice with epidermoid tumor. In another study, hollow MN integrated with multi-microfluidic channels was proposed to enable combinational therapy using simultaneous delivery of multiple drugs (**Figure 2-11C(iii)**)[126]. In this study, Yeung *et al.* investigated shape effect like conical, pyramidal and bevel tip of hollow MN to obtain optimal geometry for painless device, including improvement of finite SLA resolution (140μm) by changing printing orientation angle of MNs at 0^o, $\pm45^o$ and 90^o. They realized that 45^o printing with bevel tip MN had the best performance in parafilm penetration with

tip radius improved from 50µm to 25µm. *Ex vivo* delivery of different dyes through three inlets presented on the microfluidic compartment using microfluidic-MN integrated device showed promising capability of simultaneous dye delivery in which relative concentration of respective solutes can be controlled through input flow rate from the inlets.

2.4.2.3 Digital light processing (DLP)

Due to high printing speed and wider variety of material choice in reasonable range of resolution (~25µm), DLP has been widely reported in MN fabrication studies. For example, Yao *et al.* reported DLP printing of PEGDA400- hydrogel MN for transdermal drug delivery [127](**Figure 2-11D(ii)**). Printed MNs showed tip diameter of ~20µm with length of ~800µm. Rhodamine B was successfully loaded onto the MN through passive diffusion by soaking in the dye solution for 24 hours. Both penetration test and dye release test showed that printed MN has proper functionality. Besides fabrication of solid MN, some studies have also shown potential of DLP printed MN in diagnostic setup. For example, Miller *et al.* proposed the integration of DLP printed hollow MN with carbon fiber electrode for electrochemical sensing[128]. In the study, biocompatible class 11a resin, E-shell 200 was used as the photopolymer to fabricate pyramidal bevel hollow MN with ~1030µm height, ~1120µm base diameter and ~375µm bore diameter. The integrated device comprises of two layers, bottom layer consists of PMMA block substrate with carbon fiber secured in the laser drilled holes. Second layer consists of the printed hollow MN array where the carbon fibers were positioned within the MN bore to assure that extracted biofluid can directly in contact with the electrode (**Figure 2-11D(iii)**). Electrochemical analysis showed that the carbon fibers were able to response to various concentration of hydrogen peroxide and recognize presence of ascorbic acid by selective oxidation reaction.

2.4.2.4 Two-photon polymerization (2PP)

2PP technique offers design flexibility with high compatibility with variety of photopolymers therefore has been regarded as the most popular 3D printing technology in biomedical applications. For MN fabrication, owing to its capability to fabricate high resolution construct in nanoscale, it has been reported for MN fabrication in direct or indirect method. For instance, Aksit *et al.* reported ultrasharp 2PP printed single MN for perforation of round window membrane and improved drug diffusion[129]. Commercial biocompatible IP-S resin was used for direct laser writing of conical cylindrical solid MN where the tip diameter and base diameter were observed to be 1µm and 100µm respectively (**Figure 2-11E(ii)**). The MN base was designed with a cavity to allow attachment onto commercial 23-gauge syringe during cochlea perforation where some holes on the side were also implemented into the design to effectively reduce printing time. *Ex vivo* perforation test using RWM harvested from guinea pig showed successful penetration with only ~1.19mN insertion force and ~95.6µm perforation length. Potential multi-perforation was shown to be feasible through printing of multiple MNs on the array, suggesting design and manufacturing flexibility of the method. In another study, 2PP was used to fabricate arrowhead-MN templates for micro-molding technique. Balmert *et al.* have introduced Ovalbumin and polyinosinic-polycytidylic acid sodium salt (Poly(I:C)) into micro-mold casted CMC/trehalose hydrogel MN for immunization purpose [130](**Figure 2-11E(iii)**). Interestingly, instead of mixing drug into polymeric solution for casting, the team first coated biocargos into the wells through spin-casting. This could allow the drug mixture to be concentrated at tip region while not producing complications like drug wastage or drug inhomogeneity in MN matrix. Cutaneous vaccination with multicomponent-loaded MN showed higher immune response induced than that of traditional IM injection.

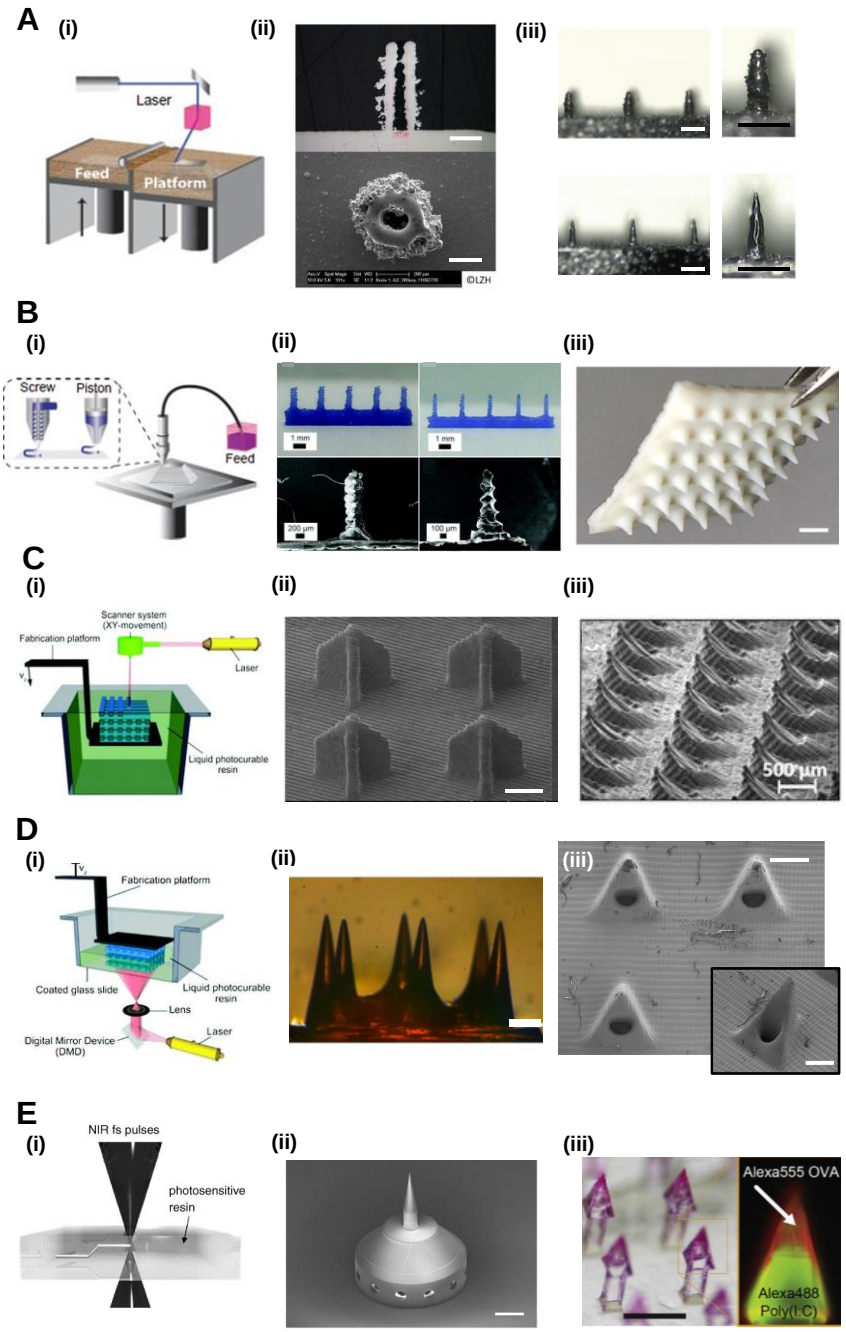

Figure 2-11. Prior studies on 3D printing of MN system. A. MN fabrication using powder bed fusion (SLS and SLM). (i) Schematic illustration of basic PBF printing setup [108]. (ii) Cross section and top view of hollow MNs printed using selective laser micro melting (SLµM). Powder particles were shown to adhere on the shaft which were unable to remove. Scale bar = 200µm [121]. (iii) Optical images of stainless steel MNs after 3D printing (Top). Post treatment using electropolishing was employed in order to smoothen the surface and sharpen the tip region. Scale bar = 500µm [122]. Continue in next page.

Figure 2-11 B. MN fabrication using material extrusion (FDM). (i) Schematic illustration of basic FDM setup [108]. (ii) Conical PLA MNs printed using FDM which found to be sufficiently strong to penetrate skin. Optical and magnified SEM images of pre-MN pillar structure (left) and final MN structure after KOH etching (right). Scale bar = 100µm, 200µm and 1mm respectively [123]. (iii) Sodium alginate (SA) / hydroxyapatite (HA) MNs fabricated using FDM printing and post stretching process for insulin delivery. Scale bar = 1mm [124]. C. MN fabrication using vat polymerization (SLA). (i) Schematic illustration of basic SLA printing setup [120]. (ii) SEM image of SLA printed cross-shaped MNs with larger drug loading surface for anticancer therapy. Scale bar = 1mm [125]. (iii) SEM image of SLA printed hollow bevel-tip MNs array for microfluidic integrated drug delivery system. Scale bar = 500µm [126]. D. MN fabrication using vat polymerization (DLP). (i) Schematic illustration of basic DLP printing setup [120]. (ii) DLP printed PEG-400 hydrogel MN for transdermal drug delivery. The array was printed with layer-to-layer 500ms exposure time. Scale bar = 200µm [127]. (iii) SEM image of hollow bevel MNs DLP printer using biocompatible resin for electrode integration and electrochemical sensing. Scale bar = 500µm [128]. E. MN fabrication using vat polymerization (TPP). (i) Schematic illustration of basic TPP printing operating mechanism. Two femtosecond lasers focus and cure from point to point. (ii) SEM image of TPP printed single MN for perforation and drug delivery of round window membrane. Scale bar = 200µm [129]. (iii) OVA and Poly(I:C) loaded CMC/trehalose MNs casted from TPP printed arrowhead MN template. Fluorescent microscope revealed distribution of both vaccine components within MN tip. Scale bar = 500µm [130].

Table 2-4 Summary of the 3D printing applicability on MN fabrication

Methods	Materials	Resolution (µm)	Advantage	Disadvantages	refs
Powder bed fusion	Powder of metal, alloy, polymers	20-250	High output volume Large surface area High mechanical strength in SLM Certain biocompatibility for scaffold printing	Low resolution for MN fabrication Slow printing speed Porosity and high surface roughness (SLS) Expensive due to high power and temperature	[112-114]

Binder jetting	Powder of Ceramics, polymers (PLA)	100	Fast printing speed Lower energy required Allows multi-material printing through powder mixing	NA	[112, 114, 115]
Direct energy deposition	Powder of metal, alloy, polymer	250	High mechanical strength High throughput	NA	[112]
Fused deposition modeling	Thermoplastic polymers like PLA, ABS, Nylon, PEI	>50	High printing speed Easy to operate Low cost	Limited material for MN fabrication Low resolution for MN fabrication Danger for biopolymers or cells due to high temperature	[112]
Direct ink writing	Hydrogel materials Viscous liquid polymers	>50	Suitable for bioprinting Wide variety of material choice	Low resolution for MN fabrication Clogging of nozzle or orifice Viscosity pairing is required	[119]
Stereo-lithography	Commercial resins like acrylates and epoxides	10	High resolution Smooth surface	Limited biodegradable materials Slow printing speed Poor biocompatibility and limited mechanical strength	[112]
Digital Light processing	Commercial resins like acrylates	25-100	Fast printing speed	Limited mechanical strength	[112]

	and epoxides Biomaterials like PEGDA and GelMA		Moderate resolution for MN fabrication Smooth surface Low resin volume (bottom-up configuration)		
Two photon polymerization	Acrylates (commercial or research biomaterial)	0.1-5	Ultra-high resolution for MN fabrication Material and design versatility	High cost Slow printing speed as compared to DLP	[112, 131]

2.5 Flexible epidermal device

Since the launch of silicon-based semiconductor technology in 1950s[132], development of low cost, compact and light-weighted integrated circuits (IC) have driven the advancement of electronics in various field and eventually leads to the transformation of every possible information in our daily life into digitized data, including news, music, historical documents, or even medical records. Ubiquitous access to internet and wireless connections have urged the development of information technology since traditional rigid silicon-based electronic devices could not been able to fulfil demand of the great majority, especially healthcare technology. For example, common household medical devices like electronic sphygmomanometer, blood glucose meter, electrocardiogram (ECG) monitor were too bulky and rigid to be brought along and hindered possibility to achieve real-time monitoring of comprehensive bioinformation[133]. In recent years, there is a growing demand for flexible wearable technologies to address electronic-skin interfacial mismatch of traditional medical electronics with rigid packaging[134]. Moreover, continual increase in medical cost due to aging-related chronic diseases have encouraged evolution of passive treatment towards proactive prevention and diagnosis of disease at their early stage[133].

Human skin functions not just as a sensory organ but also a great indicator of our health condition. Useful information like temperature, pressure and biochemical cues can be detected and extracted in non-invasive manner[135]. For example, fever or inflammation of localized area could be predicted through body temperature. Mechanical forces such as muscle movement, cardiovascular extraction could be related to physiological signals like blood pressure or pulse. Sweat or biofluid contains pH and chemical compositions like protein, glucose, various ions and minerals concentration that could aid in disease diagnosis and health monitoring[135]. Following sections will review some biomedical purposes of flexible wearables in terms of sensing modalities, followed by prior studies on flexible microneedle systems.

2.5.1 Flexible wearable sensors

2.5.1.1 Force sensor

Traditional force sensors are often heavy because of the metal and semiconductor materials therefore limited their applicability in flexible device. In contrast, flexible sensors in general are fabricated using carbon-based materials, metal nanomaterials and liquid metals with elastomer substrates which offers excellent conductivity while retaining good stretchability and conformity. In general, the sensing mechanisms can be divided into resistive sensor, capacitive sensor and piezoelectric sensor. Resistive sensor converts resistance change into electrical signal, which mainly caused by geometrical change of sensing element, gap change between nanowires or change in interlayer contact resistance. For example, Yamade *et al.* proposed a carbon nanotube (CNT) strain sensor for the detection of human motion[136]. In this study, singled-walled CNT (SWCNT) thin films were aligned side by side with 1mm overlap onto a stretchable elastomer substrate and perpendicular to that of strain direction. IPA was used to flatten the aligned thin films to the PDMS and eventually forming densely packed SWCNT bundles with strong adhesion to PDMS substrate

through van der Waals interaction. During stretching, the films fractured into gaps and islands with some portions remained interconnected. Such change in filament orientation caused resistance change with respect to stretch ratio. Such flexible and thin sensor has been successfully integrated onto stockings, bandages and gloves and managed to detect motion change during movement, breathing and typing[136]. In another study, lead zirconate titanate (PZT) nanoribbons have been incorporated in between metal electrodes to fabricate sensing element that act as both mechanical actuator and sensor[137]. Such ultrathin conformal modulus sensor was able to quantify skin viscoelasticity under quasi-static and dynamic conditions through strong van der Waals force driven skin adhesion. The integrated device that placed directly on lesions of basal cell carcinoma patient has successfully mapped skin modulus difference between normal and pathologized area spatially.

2.5.1.2 Electrochemical sensor

Electrochemical sensor utilizes chemical reaction occurs between sensing material and target analyte to detect existence or amount of analyte. Physiological condition can be obtained through analyzing changes in sensor's electrical properties. Regular glucose monitoring is essential for diabetic patients to maintain normal metabolism. Chen *et al.* proposed electrochemical sensing of glucose level in interstitial fluid (ISF) through non-invasive flexible biosensor. Subcutaneous electrochemical twin channel (ETCs) was produced by attaching paper battery directly on skin, enabling effective penetration of hyaluronic acid and induce reverse iontophoresis of glucose from intravascular vessels towards skin surface. Glucose then infiltrated into immobilized glucose oxidase (GOx) layer, initiating redox reaction and current acquisition. Clinical trials on human subjects showed comparable measurement as compared to commercial glucose meter. Also, Gao *et al.* proposed multiplexed biosensor that able to perform *in situ* detection of glucose, lactate, sodium, potassium and temperature of the sweat, in the form of wristband (**Figure 2-12A(iii)**) and headband[138]. **Figure 2-12A(i)** showed design and algorithm of the working principle. In this study, glucose and

lactate were detected through immobilization of glucose and lactate oxidase on chitosan film while K^+ and NA^+ were detected through ion-selective electrode (ISE), coupled with PEDOT:PSS as ion-to-electron transducer(**Figure 2-12A(ii)**). Results showed simultaneous detection of aforementioned analytes where the datas were also wirelessly transmitted onto mobile application through integration with a flexible printed circuit board (FPCB)[138].

2.5.1.3 Multifunctional sensor

The ultimate goal of flexible epidermal sensor is to perform multifunctional sensing for comprehensive healthcare monitoring and therefore many studies have tried to fit two or more sensing mechanisms in single biosensor array. In general, multi-functional sensor can be achieved through stacking or lamination of different sensing elements on top of each other. For example, Harada *et al.* fabricated triaxial sensor that could detect tactile force, friction force and temperature simultaneously for artificial skin application [139] (**Figure 2-12B**). In this study, nine "pixels" were fitted onto a flexible polyester substrate. Each pixel comprises of four strain sensor and a temperature sensor in which tactile force and friction force can be identified separately through reading of strain difference between four strain sensors. To reduce manufacturing cost, the components were prepared through screen printing of different conductive ink. The fingerprint-like structure represented the sensor resolution where it has shown promising functionality in imitating human skin through various tests. Another study proposed by Ho *et al.* showed integration of three separate sensors (humidity, temperature and pressure) in the matrix[140]. All components on the sensor array were fabricated using graphene-based materials. The configuration of sensor array is as shown in **Figure 2-12C** where the assembly of array was done by stacking and lamination of three sensor arrays. Reduced graphene oxide, graphene oxide and CVD-graphene electrodes were used as sensing element of temperature, humidity and pressure sensor respectively, either through spraying or sandwiching. Results shown that each sensor responded with high sensitivity while integration of three did not affect functionality of the individuals.

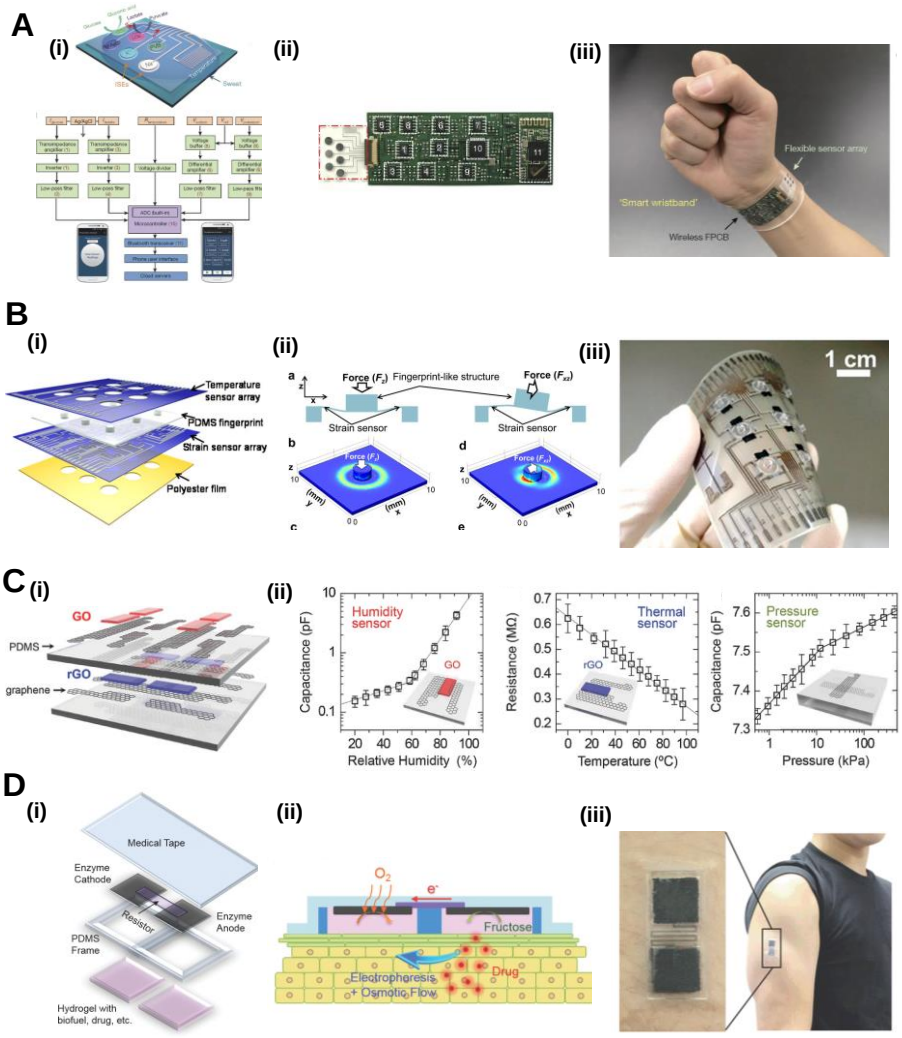

Figure 2-12. Existing flexible wearables for drug delivery and biosensing. A. Flexible and stretchable multiplexed sensor (humidity, temperature and pressure sensing) where all electrodes are graphene-based material. (i) Schematic illustration of the 2x2 sensing elements and individual sensor pathway in stacking manner. (ii) Sensing capability of individual compartments under different stimuli [138]. B. Transdermal iontophoresis patch with self-powered biofuel cell for small molecule delivery. (i) Schematic illustration of the patch which composed of enzyme-modified carbon fabrics electrode, hydrogel loaded with biofuel and cargos and oxygen permeable medical tape, assembled with PDMS frame. (ii) Iontophoresis assisted drug delivery mechanism. Biofuel cell generates ionic current from anode to cathode whereby driven electrophoretic diffusion of drugs into the skin. (iii) Mounting of assembled patch onto human arm [141]. Continue in next page.

Figure 2-12. C. Fully integrated patch for multiplexed *in situ* perspiration analysis, including data recording, post processing and wireless transmission onto phone application for display. (i) Schematic illustration of the array (including Na, K, glucose, lactate and temperature sensing). Block diagram shows signal transduction (orange), conditioning (green), post processing (purple) and transmission path (blue) to the mobile application. (ii) Compartment of integrated circuits. Red arrow indicates location of sensing region. (iii) Integrated flexible sensor array in wristband form [138]. D. Fingerprint like flexible three-axial tensile, slip force and temperature sensor fabricated using screen printing. (i) Schematic illustration of each sensor layers. (ii) FEM simulation to characterize structural deformation differences between touch and slip force applied. (iii) Optical image of the integrated fingerprint-like sensor. Scale bar = 1cm [139].

2.5.2 Flexible device for drug delivery

First generation of transdermal drug delivery offers non-invasive and painless drug delivery. However, delivery of large molecules with molecular weight >400Da has been reported to be inefficient which leads to invention of second generation TDD system with development of penetration enhancer which aims to improve skin permeability for better delivery efficiency, through chemical substance or external energy source[135]. For example, Ogawa *et al.* proposed iontophoresis patch powered by oxidation of biochemical fuels to generate mild electric current[141]. Enzymatic biofuel cell (BFC) uses enzyme as electro-catalyst which can oxidize biosafe fuels like sugars through reduction of environmental O_2 (**Figure 2-12D**). In this study, enzyme-modified carbon fabrics (CFs) and fructose were used as BFCs and biofuel respectively while PEDOT/PU was also integrated onto the patch as mechanically flexible resistor to eliminate voltage fluctuations during dynamic motion. Successful delivery of ascorbyl gluocoside and rhodamine B were shown which provided promising alternative of self-powered flexible iontophoresis transdermal drug delivery patch without external power supply[141].

2.5.3 Prior studies on flexible MN system

MN is the third-generation transdermal drug delivery system that offers superior drug delivery efficiency than previous generations despite efforts like sonophoresis, iontophoresis and penetration enhancers have been proposed to improve skin permeability, attributed to its self-administrable nature without needs of clinical expertise's supervision. As reported previously, majority of MN devices are fabricated with rigid substrate, mostly monolithic with tip material since it could significantly reduce the manufacturing burden for commercial scalability purpose. Moreover, self-administration of MN patch is designed for finger-pressing therefore dimension of the array has been limited to 0.5-1.5cm, presuming complete and uniform skin penetration. However, MN application site during therapeutic or biosensing application is not necessarily to be flat which may lead to uneven penetration and bring adverse effect on the device performance. For instance, long term drug delivery or health monitoring may take hours to days where the MN patch should be attached firmly throughout the window. Rigid nature of the MN patch may cause delamination or detachment during motion and therefore induce relative displacement, inaccurate measurement, under-desired drug dosage and noticeable pain.

Introducing flexibility to the substrate could potentially address the issue. Various MN-related studies have discovered ways to fabricate flexible MN device for therapeutic or diagnosis purpose. In the following section, few studies will be reviewed in terms of design, including flat and continuous flexible substrate and patterned flexible substrate.

2.5.3.1 Continuous substrate

Flexible substrate in MN fabrication is required to be compatible with microfabrication of MN tip while maintaining overall flexibility for skin conformity. Therefore, typical flexible materials like PDMS, PVA, PET and biocompatible polymers like meHA, PU and CMC are used[142]. These

substrates have been proven to be compatible with MN fabrication methods like micro-molding, etching, lithography and 3D printing among others.

For example, Onesto *et al.* fabricated PLGA-PVP/VA MNs encapsulated with collagenase through emulsion for rapid protein release[143]. In this study, flexible PDMS was first casted using PMMA replica molding. Collagenase was encapsulated in various concentration of PLGA-PVP/VA solution through water-oil emulsion where PVP/VA act as PLGA substitute to promote rapid release profile. The drug loaded MN was fabricated using electro-drawing. Briefly, after PDMS substrate with pillars were casted, drug loaded droplets were formed on the pillars through dipping. Electro-hydrodynamic (EHD) force was then applied onto the drops through pyroelectric crystals to form MN shape (**Figure 2-13A**). Results showed penetration of flexible MN substrate onto *in vitro* dermis model[143]. Similar fabrication method was reported by Vecchione *et al.* where PLGA MN with different drug formulations were electro-drawn on a flat PDMS substrate. Instead of dipping PDMS pillar into polymeric solution, drug formulations were directly dripped onto a flat flexible PDMS substrate such that customization of different loading substances on single MN array can be achieved[144]. In another study, biomaterial hyaluronic acid (HA) has been used as the flexible base substrate material. Zhang *et al.* fabricated reactive oxygen species (ROS)-responsive MN system for anti-acne therapy wherein antibiotic CDM was loaded in the ROS-PVA MN tip[145]. After drying of tip region, methacrylated-HA (meHA) loaded with diatomaceous earth (DE) was casted as flexible base substrate (**Figure 2-13B**). In addition to its flexibility, m-HA/DE acted as compartment to absorb pus or other purulent discharges which was proved to promote wound healing. *In vivo* acne treatment on mice showed promising wound healing effect.

Besides therapeutic purpose, flexible continuous MN patch was also reported in biosensing studies due to its painless and minimal invasive skin insertion, improving electrode contact with physiological environment without needs of skin preparation and conductive gel pre-treatment. For example, Lozano

et al. proposed microneedle electrode with flexible backing substrate for ECG and EEG recording[146]. In this study, conductive MN was fabricated by dispersing 72R carbon black powder in biocompatible resin for micromolding. Flexible substrate was then casted on top with mixture of polyurethane/epoxy/carbon black hybrid polymer mixture. Results showed that the MN electrode array has comparable impedance as compared to conventional setup with wet electrode which suggested a promising alternative over traditional electrode. Another study proposed by Lee *et al.* showed promising pH sensing of polyaniline deposited flexible MN array in peripheral artery disease model[147]. To fabricate pH sensing MN, epoxy siloxane was fabricated through sol-gel process where the mixture was poured into negative mold to form MN shape. Polyaniline was then electrochemically deposited on the MN tips. Spin-coated PDMS was used as the flexible base substrate where Ag/AgCl was deposited as reference electrode with paralyne coating on top as passivation layer. The casted MN and plasma treated PDMS substrate were assembled via covalent bond. The flexible pH sensing MN array showed promising capability on reading pH distribution in PAD rat model.

2.5.3.2 Patterned substrate

While flexible continuous substrate showed promising skin conformity of small MN patch in drug delivery and biosensing applications, few studies have proposed patterned flexible design to further improve flexibility of MN system, providing prospective concept for future development on larger MN patch which could potentially resolve drug loading limitation of current MN system. For example, Xiang *et al.* designed flexible MN electrode with mesh substrate to effectively conform on different locations of brain for wireless neural signal acquisition (**Figure 2-13C**)[148]. The polyimide (PI) mesh substrate was first produced by UV lithography, followed by gold tracing via lift-off process. A 4x4 SU-8 MN electrodes (400~3000μm) were fabricated on top of the UV-lithography made SU-8 pillar using drawing lithography where they realized that the length of MN can be controlled by adjusting diameter of SU-8 pillars. A gold

layer was then sputtered on the MN for electrical conduction. Implanted flexible MN electrode array on curved surface of SD rats' brain showed successful recording of neural signals which provided promising platform for continuous neural activity monitoring[148]. In another study, Miura-ori pattern[149] was introduced into a flexible substrate to allow two-directional in plane flexibility for ECG and EMG recording (**Figure 2-13D**)[150]. To precisely engrave Miura-ori pattern and positioning of MN electrodes on acrylic mold, numerical controlled milling machine was employed. After PDMS negative mold was casted with acrylic mold, two types of biocompatible epoxy resin were used for fabrication of MN tips (hard) and flexible substrate (soft). Titanium and gold coating were then sputtered on the Miura-ori MN electrode (M-MAE) to improve conductivity of the system. Electronic skin impedance (EII) and flexibility test suggested superior performance of M-MAE as compared to wet Ag/AgCl electrode, flexible dry electrode and flexible MAE without Miura-ori pattern, in terms of signal stability and lower impedance during bending. *In situ* EMG and ECG recording also suggested superior signal stability and functionality[150].

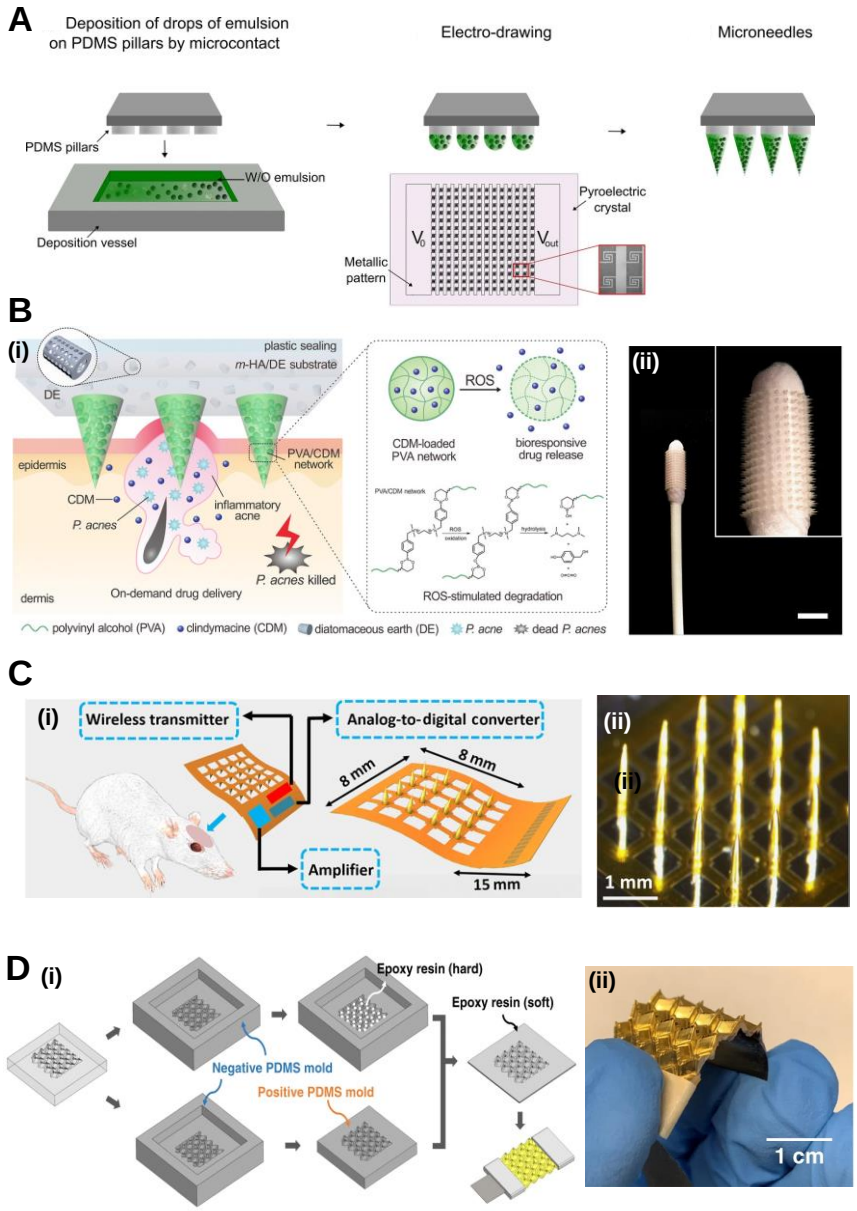

Figure 2-13. Prior studies on flexible MN system. A. Fabrication process of PLGA-PVP/VA based electro-drawn MN on flexible PDMS substrate for collagenase delivery. The process includes dipping flexible base substrates with PDMS pillar into water-in-oil emulsion containing collagenase solution, followed by pyroelectric crystal-induced-electric field assisted electro-drawing of MNs [143]. B. Reactive oxygen species (ROS)-responsive flexible MN system for acne vulgaris treatment. (i) Schematic illustration of the components and working mechanism. HA-based hydrogel and diatomaceous earth (DE) act as pus absorption pad while CDM as antibiotic for acne treatment is loaded into PVA MNs. (ii) Optical illustration of the fabricated flexible MN patch wrapping onto cotton stick for temporary usage [145].

Figure 2-13 C. Flexible MN electrode mesh array for wireless brain signal monitoring. (i) Schematic illustration of the design and geometry of flexible MN electrode array. The flexible base substrate is fabricated through UV lithography of polyimide while MNs are fabricated using SU-8 drawing lithography. (ii) Optical image of MN electrode array. Scale bar = 1mm [148]. D. Flexible MN system with Miura-ori structured base substrate for biosensing with better ventilation and flexibility. (i) Fabrication process of the MN electrode array. After Miura-ori pattern was fabricated using micromachining tool, negative molds are fabricated using PDMS in which hard and soft epoxy resin are used as MN and base substrate material. Titanium and gold coating are used to improve conductivity of the MN electrodes. (ii) Optical image of the fabricated MN electrode array [150].

2.6 Challenges of current MN technology and implication of research

Transdermal drug delivery system, in particular MN system is an emerging platform for high efficiency peptide, protein or large therapeutic substances delivery with minimal invasion, preventing potential wound infection and low patient compliance associated with conventional oral delivery and hypodermic injection. Various class of MN types and features have been discussed and reviewed in this chapter to provide insight of MN development where it has been shown to be not just a great candidature for drug delivery, but also an effective tool in diagnostic setup. Moreover, geometrical design of MN can also affect functionality of the system, offering design flexibility to address different aspect of biomedical applications, either with artificial or bio-inspired framework. Under this context, 3D printing platform has shown its effectiveness in substituting conventional MN fabrication while benefiting its advancement towards commercialization. Different 3D printing techniques have also been explored where applicability of corresponding methods in MN fabrication were reviewed and compared in terms of material, cost and resolution. Application of existing flexible wearables and MN studies showed that introduction of substrate flexibility expanded possibility of what MN system could offer in the future biomedical field. On the basis of previous studies, a few approaches to address current limitation of MN system were proposed.

First, painless and rapid delivery of therapeutic substances or vaccination antigen can be potentially achieved by MN system by using dissolvable biopolymer such that the administration can be done within minutes while the whole patch can be bio-degraded without leaving undesired medical waste. However, rapid dissolving polymers possess critical drawback such as low intrinsic mechanical strength, not to mention high drug loading could further reduce polymeric density and leads to uneven skin insertion and under-desired dosage. Therefore, rapid dissolving biopolymer should be mechanically reinforced while maintaining its biocompatibility since the entire polymeric matrix were to be released into physiological environment. Inspired by limpet-tooth where introduction of additional agent provides enhancement mechanically, a hybridization of rapid dissolving biopolymer and bioactive-additive were proposed in Chapter 3 of this thesis.

Secondly, drug loading capacity and uniform penetration of MN array remained problematic for majority of drug type especially when long term drug release is designated. While increasing density of MN on limited dimension can cause “bed of nails” effect, majority of current flexible MN system only offers bi-directional flexibility. Therefore, significant upscaling of patch dimension to increase drug loading capacity is impractical since it will induce contact problem, considering that complexity of human skin curvature is more than bidirectional. External drug reservoir could be potential solution to this, but only for drugs in liquid form. Lyophilized drug formulation was reported to be more compatible with MN system for commercialization because of lower transportation and cold storage cost. Moreover, biosensing application of MN technology is limited by its dimension such that stacking of compartments for multifunctional sensor design could compromise flexibility of the overall patch. Therefore, a 3D printed, patterned and flexible MN substrate design were proposed to allow omni-directional skin conformity, expanding design freedom of flexible MN system in Chapter 4 of this thesis.

Reference

1. Tiwari, G., et al., *Drug delivery systems: An updated review.* Int J Pharm Investig, 2012. **2**(1): p. 2-11.
2. Morimoto, Y. and S. Fujimoto, *Albumin microspheres as drug carriers.* Crit Rev Ther Drug Carrier Syst, 1985. **2**(1): p. 19-63.
3. Homayun, B., X. Lin, and H.J. Choi, *Challenges and Recent Progress in Oral Drug Delivery Systems for Biopharmaceuticals.* Pharmaceutics, 2019. **11**(3).
4. Prausnitz, M.R. and R. Langer, *Transdermal drug delivery.* Nature Biotechnology, 2008. **26**(11): p. 1261-1268.
5. Gulati, N. and H. Gupta, *Parenteral drug delivery: a review.* Recent Pat Drug Deliv Formul, 2011. **5**(2): p. 133-45.
6. Kim, Y.-C., J.-H. Park, and M.R. Prausnitz, *Microneedles for drug and vaccine delivery.* Advanced Drug Delivery Reviews, 2012. **64**(14): p. 1547-1568.
7. Chabri, F., et al., *Microfabricated silicon microneedles for nonviral cutaneous gene delivery.* Br J Dermatol, 2004. **150**(5): p. 869-77.
8. Gill, H.S. and M.R. Prausnitz, *Coating formulations for microneedles.* Pharm Res, 2007. **24**(7): p. 1369-80.
9. Yousef, H., M. Alhajj, and S. Sharma, *Anatomy, Skin (Integument), Epidermis*, in *StatPearls*. 2022, StatPearls Publishing
10. Gill, H.S., et al., *Effect of microneedle design on pain in human volunteers.* The Clinical journal of pain, 2008. **24**(7): p. 585-594.
11. Waghule, T., et al., *Microneedles: A smart approach and increasing potential for transdermal drug delivery system.* Biomedicine & Pharmacotherapy, 2019. **109**: p. 1249-1258.
12. Li, Y., et al., *Fabrication of sharp silicon hollow microneedles by deep-reactive ion etching towards minimally invasive diagnostics.* Microsystems & Nanoengineering, 2019. **5**(1): p. 41.
13. Aoyagi, S., et al., *Laser fabrication of high aspect ratio thin holes on biodegradable polymer and its application to a microneedle.* Sensors and Actuators A: Physical, 2007. **139**(1): p. 293-302.
14. Bolton, C.J.W., et al., *Hollow silicon microneedle fabrication using advanced plasma etch technologies for applications in transdermal drug delivery.* Lab Chip, 2020. **20**(15): p. 2788-2795.
15. Cárcamo-Martínez, Á., et al., *Hollow microneedles: A perspective in biomedical applications.* International Journal of Pharmaceutics, 2021. **599**: p. 120455.
16. Burton, S.A., et al., *Rapid intradermal delivery of liquid formulations using a hollow microstructured array.* Pharm Res, 2011. **28**(1): p. 31-40.
17. Ryan, E., et al., *Microneedle-mediated transdermal bacteriophage delivery.* Eur J Pharm Sci, 2012. **47**(2): p. 297-304.
18. van der Maaden, K., et al., *Novel hollow microneedle technology for depth-controlled microinjection-mediated dermal vaccination: a study with polio vaccine in rats.* Pharm Res, 2014. **31**(7): p. 1846-54.
19. Aldawood, F.K., A. Andar, and S. Desai, *A Comprehensive Review of Microneedles: Types, Materials, Processes, Characterizations and Applications.* Polymers (Basel), 2021. **13**(16).
20. Larrañeta, E., et al., *Microneedle arrays as transdermal and intradermal drug delivery systems: Materials science, manufacture and commercial development.* Materials Science and Engineering: R: Reports, 2016. **104**: p. 1-32.

21. Ma, G. and C. Wu, *Microneedle, bio-microneedle and bio-inspired microneedle: A review*. Journal of Controlled Release, 2017. **251**: p. 11-23.
22. Hu, Z., et al., *Solid and hollow metallic glass microneedles for transdermal drug-delivery*. Applied Physics Letters, 2020. **116**(20): p. 203703.
23. Pradeep Narayanan, S. and S. Raghavan, *Solid silicon microneedles for drug delivery applications.* The International Journal of Advanced Manufacturing Technology, 2017. **93**(1): p. 407-422.
24. Gupta, J., et al., *Kinetics of skin resealing after insertion of microneedles in human subjects.* J Control Release, 2011. **154**(2): p. 148-55.
25. Tariq, N., M.W. Ashraf, and S. Tayyaba, *A Review on Solid Microneedles for Biomedical Applications*. Journal of Pharmaceutical Innovation, 2021.
26. Donnelly, R.F., et al., *Hydrogel-Forming Microneedle Arrays for Enhanced Transdermal Drug Delivery.* Adv Funct Mater, 2012. **22**(23): p. 4879-4890.
27. Donnelly, R.F., et al., *Hydrogel-Forming Microneedles Prepared from "Super Swelling" Polymers Combined with Lyophilised Wafers for Transdermal Drug Delivery.* PLOS ONE, 2014. **9**(10): p. e111547.
28. Caffarel-Salvador, E., et al., *Hydrogel-Forming Microneedle Arrays Allow Detection of Drugs and Glucose In Vivo: Potential for Use in Diagnosis and Therapeutic Drug Monitoring.* PLOS ONE, 2016. **10**(12): p. e0145644.
29. Zheng, M., et al., *Osmosis-Powered Hydrogel Microneedles for Microliters of Skin Interstitial Fluid Extraction within Minutes.* Advanced Healthcare Materials, 2020. **9**(10): p. 1901683.
30. Xu, N., et al., *Swellable PVA/PVP hydrogel microneedle patches for the extraction of interstitial skin fluid toward minimally invasive monitoring of blood glucose level.* Analyst, 2022. **147**(7): p. 1478-1491.
31. Haj-Ahmad, R., et al., *Microneedle Coating Techniques for Transdermal Drug Delivery.* Pharmaceutics, 2015. **7**(4): p. 486-502.
32. Ameri, M., S.C. Fan, and Y.F. Maa, *Parathyroid hormone PTH(1-34) formulation that enables uniform coating on a novel transdermal microprojection delivery system.* Pharm Res, 2010. **27**(2): p. 303-13.
33. Ameri, M., et al., *Human Growth Hormone Delivery with a Microneedle Transdermal System: Preclinical Formulation, Stability, Delivery and PK of Therapeutically Relevant Doses*. Pharmaceutics, 2014. **6**(2): p. 220-34.
34. Wang, F.Y., et al., *Transdermal drug delivery systems for fighting common viral infectious diseases.* Drug Deliv Transl Res, 2021. **11**(4): p. 1498-1508.
35. Choi, I.J., et al., *Live Vaccinia Virus-Coated Microneedle Array Patches for Smallpox Vaccination and Stockpiling.* Pharmaceutics, 2021. **13**(2).
36. Kim, Y.C., et al., *Stability kinetics of influenza vaccine coated onto microneedles during drying and storage.* Pharm Res, 2011. **28**(1): p. 135-44.
37. Ameri, M., P.E. Daddona, and Y.F. Maa, *Demonstrated solid-state stability of parathyroid hormone PTH(1-34) coated on a novel transdermal microprojection delivery system.* Pharm Res, 2009. **26**(11): p. 2454-63.
38. Zhao, X., et al., *Tip-loaded fast-dissolving microneedle patches for photodynamic therapy of subcutaneous tumor*. Journal of Controlled Release, 2018. **286**: p. 201-209.
39. Shim, W.S., et al., *Role of Polyvinylpyrrolidone in Dissolving Microneedle for Efficient Transdermal Drug Delivery: In vitro and Clinical Studies.* Bulletin of the Korean Chemical Society, 2018. **39**(6): p. 789-793.

40. Guillot, A.J., et al., *Microneedle-Based Delivery: An Overview of Current Applications and Trends.* Pharmaceutics, 2020. **12**(6).
41. Zhang, N., et al., *Dissolving Polymer Microneedles for Transdermal Delivery of Insulin.* Front Pharmacol, 2021. **12**: p. 719905.
42. Lee, K., C.Y. Lee, and H. Jung, *Dissolving microneedles for transdermal drug administration prepared by stepwise controlled drawing of maltose.* Biomaterials, 2011. **32**(11): p. 3134-3140.
43. Lee, C., et al., *Optimization of Layered Dissolving Microneedle for Sustained Drug Delivery Using Heat-Melted Poly(Lactic-Co-glycolic Acid).* Pharmaceutics, 2021. **13**(7).
44. Lee, J.W., et al., *Dissolving microneedle patch for transdermal delivery of human growth hormone.* Small, 2011. **7**(4): p. 531-9.
45. Chen, M.C., et al., *Fully embeddable chitosan microneedles as a sustained release depot for intradermal vaccination.* Biomaterials, 2013. **34**(12): p. 3077-86.
46. Makvandi, P., et al., *Engineering Microneedle Patches for Improved Penetration: Analysis, Skin Models and Factors Affecting Needle Insertion.* Nano-Micro Letters, 2021. **13**(1): p. 93.
47. Park, J.H., M.G. Allen, and M.R. Prausnitz, *Polymer microneedles for controlled-release drug delivery.* Pharm Res, 2006. **23**(5): p. 1008-19.
48. Kim, K., et al., *A tapered hollow metallic microneedle array using backside exposure of SU-8.* J. Micromech. Microeng, 2004. **14**: p. 597-603.
49. Davis, S.P., et al., *Hollow metal microneedles for insulin delivery to diabetic rats.* IEEE Trans Biomed Eng, 2005. **52**(5): p. 909-15.
50. Mishra, R. and T.K. Bhattacharyya, *Chapter 16 - MEMS-based hollow microneedles for transdermal drug delivery*, in *Drug Delivery Devices and Therapeutic Systems*, E. Chappel, Editor. 2021, Academic Press. p. 325-344.
51. Sanjay, S.T., et al., *Controlled Drug Delivery Using Microdevices.* Curr Pharm Biotechnol, 2016. **17**(9): p. 772-87.
52. Nair, K.J., *Micro-injection moulded microneedles for drug delivery*. 2016.
53. Kwon, K.M., et al., *Microneedles: quick and easy delivery methods of vaccines.* Clin Exp Vaccine Res, 2017. **6**(2): p. 156-159.
54. Duong, H.T.T., et al., *Microneedle arrays coated with charge reversal pH-sensitive copolymers improve antigen presenting cells-homing DNA vaccine delivery and immune responses.* Journal of Controlled Release, 2018. **269**: p. 225-234.
55. Gill, H.S. and M.R. Prausnitz, *Coated microneedles for transdermal delivery.* J Control Release, 2007. **117**(2): p. 227-37.
56. Li, J., et al., *Microneedle Patches as Drug and Vaccine Delivery Platform.* Curr Med Chem, 2017. **24**(22): p. 2413-2422.
57. Ullah, A., C.M. Kim, and G.M. Kim, *Porous polymer coatings on metal microneedles for enhanced drug delivery.* Royal Society Open Science. **5**(4): p. 171609.
58. Dang, N., T.Y. Liu, and T.W. Prow, *Chapter Seventeen - Nano- and Microtechnology in Skin Delivery of Vaccines*, in *Micro and Nanotechnology in Vaccine Development*, M. Skwarczynski and I. Toth, Editors. 2017, William Andrew Publishing. p. 327-341.

59. González-Vázquez, P., et al., *Transdermal delivery of gentamicin using dissolving microneedle arrays for potential treatment of neonatal sepsis.* J Control Release, 2017. **265**: p. 30-40.
60. Aggarwal, P. and C.R. Johnston, *Geometrical effects in mechanical characterizing of microneedle for biomedical applications.* Sensors and Actuators B: Chemical, 2004. **102**(2): p. 226-234.
61. Römgens, A.M., et al., *Predicting the optimal geometry of microneedles and their array for dermal vaccination using a computational model.* Computer Methods in Biomechanics and Biomedical Engineering, 2016. **19**(15): p. 1599-1609.
62. Al-Qallaf, B., D.B. Das, and A. Davidson, *Transdermal drug delivery by coated microneedles: geometry effects on drug concentration in blood.* Asia-Pacific Journal of Chemical Engineering, 2009. **4**(6): p. 845-857.
63. Davidson, A., B. Al-Qallaf, and D.B. Das, *Transdermal drug delivery by coated microneedles: Geometry effects on effective skin thickness and drug permeability.* Chemical Engineering Research and Design, 2008. **86**(11): p. 1196-1206.
64. Johnson, A.R., et al., *Single-Step Fabrication of Computationally Designed Microneedles by Continuous Liquid Interface Production.* PLOS ONE, 2016. **11**(9): p. e0162518.
65. Jin, C.Y., et al., *Mass producible and biocompatible microneedle patch and functional verification of its usefulness for transdermal drug delivery.* Biomed Microdevices, 2009. **11**(6): p. 1195-203.
66. Li, Y., et al., *In-plane silicon microneedles with open capillary microfluidic networks by deep reactive ion etching and sacrificial layer based sharpening.* Sensors and Actuators A: Physical, 2019. **292**: p. 149-157.
67. Mamun, A.A., et al., *Design and evaluation of in-plane silicon microneedles fabricated with post-CMOS compatible processes.* Sensors and Actuators A: Physical, 2022. **336**: p. 113407.
68. Mamun, A.A. and F. Zhao, *In-Plane Si Microneedles: Fabrication, Characterization, Modeling and Applications.* Micromachines (Basel), 2022. **13**(5).
69. Ahmed Saeed Al-Japairai, K., et al., *Current trends in polymer microneedle for transdermal drug delivery.* Int J Pharm, 2020. **587**: p. 119673.
70. Le Thanh, H., et al., *Optimal design of polymer-based microneedle for improved collection of whole blood from human fingers.* Micro & Nano Letters, 2014. **9**(10): p. 644-649.
71. Li, Y., et al., *Dissolving Microneedle Arrays with Optimized Needle Geometry for Transcutaneous Immunization.* European Journal of Pharmaceutical Sciences, 2020. **151**: p. 105361.
72. Loizidou, E.Z., et al., *Evaluation of geometrical effects of microneedles on skin penetration by CT scan and finite element analysis.* Eur J Pharm Biopharm, 2016. **107**: p. 1-6.
73. Chu, L.Y. and M.R. Prausnitz, *Separable arrowhead microneedles.* Journal of Controlled Release, 2011. **149**(3): p. 242-249.
74. Chen Bo, Z., et al., *A basal-bolus insulin regimen integrated microneedle patch for intraday postprandial glucose control.* Science Advances. **6**(28): p. eaba7260.

75. *Dynamic Loading*. Formulas for Stress, Strain, and Structural Matrices, 2004: p. 451-518.
76. Park, J.H. and M.R. Prausnitz, *Analysis of Mechanical Failure of Polymer Microneedles by Axial Force.* J Korean Phys Soc, 2010. **56**(4): p. 1223-1227.
77. Park, J.H., et al., *Tapered conical polymer microneedles fabricated using an integrated lens technique for transdermal drug delivery*. IEEE Trans Biomed Eng, 2007. **54**(5): p. 903-13.
78. Avcil, M. and A. Çelik, *Microneedles in Drug Delivery: Progress and Challenges.* Micromachines (Basel), 2021. **12**(11).
79. Uppuluri, C.T., et al., *Microneedle-assisted transdermal delivery of Zolmitriptan: effect of microneedle geometry, in vitro permeation experiments, scaling analyses and numerical simulations.* Drug Dev Ind Pharm, 2017. **43**(8): p. 1292-1303.
80. Mansoor, I., et al., *Microneedle-Based Vaccine Delivery: Review of an Emerging Technology.* AAPS PharmSciTech, 2022. **23**(4): p. 103.
81. Römgens, A.M., et al., *Monitoring the penetration process of single microneedles with varying tip diameters.* Journal of the Mechanical Behavior of Biomedical Materials, 2014. **40**: p. 397–405.
82. Davis, S.P., et al., *Insertion of microneedles into skin: measurement and prediction of insertion force and needle fracture force.* J Biomech, 2004. **37**(8): p. 1155-63.
83. Park, J.-H., M.G. Allen, and M.R. Prausnitz, *Biodegradable polymer microneedles: Fabrication, mechanics and transdermal drug delivery.* Journal of Controlled Release, 2005. **104**(1): p. 51-66.
84. Gardeniers, H.J.G.E., et al., *Silicon micromachined hollow microneedles for transdermal liquid transport.* Journal of Microelectromechanical Systems, 2003. **12**(6): p. 855-862.
85. Ripolin, A., et al., *Successful application of large microneedle patches by human volunteers.* Int J Pharm, 2017. **521**(1-2): p. 92-101.
86. Olatunji, O., et al., *Influence of array interspacing on the force required for successful microneedle skin penetration: theoretical and practical approaches.* J Pharm Sci, 2013. **102**(4): p. 1209-21.
87. Yan, G., et al., *Evaluation needle length and density of microneedle arrays in the pretreatment of skin for transdermal drug delivery.* Int J Pharm, 2010. **391**(1-2): p. 7-12.
88. Römgens, A.M., et al., *Predicting the optimal geometry of microneedles and their array for dermal vaccination using a computational model.* Comput Methods Biomech Biomed Engin, 2016. **19**(15): p. 1599-609.
89. Römgens, A.M., et al., *A theoretical compartment model for antigen kinetics in the skin.* European Journal of Pharmaceutical Sciences, 2016. **84**: p. 18-25.
90. Zhang, Y.-h., S. A. Campbell, and S. Karthikeyan, *Finite element analysis of hollow out-of-plane HfO2 microneedles for transdermal drug delivery applications.* Biomedical Microdevices, 2018. **20**(1): p. 19.
91. Ling, J., et al., *Effect of honeybee stinger and its microstructured barbs on insertion and pull force.* J Mech Behav Biomed Mater, 2017. **68**: p. 173-179.
92. Hischen, F., et al., *The external scent efferent system of selected European true bugs (Heteroptera): a biomimetic inspiration for passive, unidirectional fluid transport.* Journal of The Royal Society Interface, 2018. **15**(140): p. 20170975.

93. Plamadeala, C., et al., *Bio-inspired microneedle design for efficient drug/vaccine coating.* Biomedical Microdevices, 2019. **22**(1): p. 8.
94. Chen, Z., et al., *Additive Manufacturing of Honeybee-Inspired Microneedle for Easy Skin Insertion and Difficult Removal.* ACS Applied Materials & Interfaces, 2018. **10**(35): p. 29338-29346.
95. Li, A.D.R., et al., *Mosquito proboscis-inspired needle insertion to reduce tissue deformation and organ displacement.* Sci Rep, 2020. **10**(1): p. 12248.
96. Suzuki, M., et al., *Fabrication of Microneedle Mimicking Mosquito Proboscis Using Nanoscale 3D Laser Lithography System.* International Journal of Automation Technology, 2015. **9**: p. 655-661.
97. Suzuki, M., T. Takahashi, and S. Aoyagi, *3D laser lithographic fabrication of hollow microneedle mimicking mosquitos and its characterisation.* International Journal of Nanotechnology, 2018. **15**: p. 157.
98. Makvandi, P., et al., *Bioinspired microneedle patches: Biomimetic designs, fabrication, and biomedical applications.* Matter, 2022. **5**(2): p. 390-429.
99. Li, X., et al., *Limpet Tooth-Inspired Painless Microneedles Fabricated by Magnetic Field-Assisted 3D Printing.* Advanced Functional Materials, 2021. **31**(5): p. 2003725.
100. Barber, A.H., D. Lu, and N.M. Pugno, *Extreme strength observed in limpet teeth.* Journal of The Royal Society Interface, 2015. **12**(105): p. 20141326.
101. Bae, W.-G., et al., *Snake fang–inspired stamping patch for transdermal delivery of liquid formulations.* Science Translational Medicine, 2019. **11**(503): p. eaaw3329.
102. Guo, M., et al., *Shark Tooth-Inspired Microneedle Dressing for Intelligent Wound Management.* ACS Nano, 2021. **15**(9): p. 15316-15327.
103. Zhang, X., et al., *Bio-inspired clamping microneedle arrays from flexible ferrofluid-configured moldings.* Science Bulletin, 2019. **64**(15): p. 1110-1117.
104. Zhang, X., et al., *Claw-inspired microneedle patches with liquid metal encapsulation for accelerating incisional wound healing.* Chemical Engineering Journal, 2021. **406**: p. 126741.
105. Zhang, X., et al., *Bioinspired Adhesive and Antibacterial Microneedles for Versatile Transdermal Drug Delivery.* Research, 2020. **2020**: p. 3672120.
106. Wu, L., et al. *Shadow mask assisted droplet-born air-blowing method for fabrication of dissoluble microneedle*. in *2017 IEEE 12th International Conference on Nano/Micro Engineered and Molecular Systems (NEMS)*. 2017.
107. Economidou, S.N. and D. Douroumis, *3D printing as a transformative tool for microneedle systems: Recent advances, manufacturing considerations and market potential.* Advanced Drug Delivery Reviews, 2021. **173**: p. 60-69.
108. Egorov, V., et al., *Evolution of 3D Printing Methods and Materials for Electrochemical Energy Storage.* Advanced Materials, 2020. **32**(29): p. 2000556.
109. Chin, S.Y., et al., *Powder-Based 3D Printing for the Fabrication of Device with Micro and Mesoscale Features.* Micromachines, 2020. **11**(7).
110. Perrot, A. and S. Amziane, *3D Printing in Concrete: General Considerations and Technologies*. 2019. p. 1-40.
111. Detamornrat, U., et al., *The Role of 3D Printing Technology in Microengineering of Microneedles.* Small, 2022. **18**(18): p. 2106392.
112. Rahmani Dabbagh, S., et al., *3D-Printed Microneedles in Biomedical Applications.* iScience, 2021. **24**.

113. Mazzoli, A., *Selective laser sintering in biomedical engineering.* Medical & Biological Engineering & Computing, 2013. **51**(3): p. 245-256.
114. Awad, A., et al., *Advances in powder bed fusion 3D printing in drug delivery and healthcare.* Adv Drug Deliv Rev, 2021. **174**: p. 406-424.
115. Salmi, M., *Additive Manufacturing Processes in Medical Applications.* Materials (Basel), 2021. **14**(1).
116. *3D printing - Additive*. Available from: https://make.3dexperience.3ds.com/processes/powder-bed-fusion.
117. Boland, T., et al., *Drop-on-demand printing of cells and materials for designer tissue constructs.* Materials Science and Engineering: C, 2007. **27**: p. 372-376.
118. Placone, J.K. and A.J. Engler, *Recent Advances in Extrusion-Based 3D Printing for Biomedical Applications.* Adv Healthc Mater, 2018. **7**(8): p. e1701161.
119. Jang, T.S., et al., *3D printing of hydrogel composite systems: Recent advances in technology for tissue engineering.* Int J Bioprint, 2018. **4**(1): p. 126.
120. Yu, X., T. Zhang, and Y. Li, *3D Printing and Bioprinting Nerve Conduits for Neural Tissue Engineering.* Polymers, 2020. **12**: p. 1637.
121. Gieseke, M., et al., *Additive Manufacturing of Drug Delivery Systems.* Biomedizinische Technik. Biomedical engineering, 2012. **57**.
122. Krieger, K.J., et al., *Development and Evaluation of 3D-Printed Dry Microneedle Electrodes for Surface Electromyography.* Advanced Materials Technologies, 2020. **5**(10): p. 2000518.
123. Luzuriaga, M.A., et al., *Biodegradable 3D printed polymer microneedles for transdermal drug delivery.* Lab on a Chip, 2018. **18**(8): p. 1223-1230.
124. Wu, L., et al., *Optimization of the fused deposition modeling-based fabrication process for polylactic acid microneedles.* Microsystems & Nanoengineering, 2021. **7**(1): p. 58.
125. Uddin, M.J., et al., *3D printed microneedles for anticancer therapy of skin tumours.* Mater Sci Eng C Mater Biol Appl, 2020. **107**: p. 110248.
126. Yeung, C., et al., *A 3D-printed microfluidic-enabled hollow microneedle architecture for transdermal drug delivery.* Biomicrofluidics, 2019. **13**(6): p. 064125.
127. Yao, W., et al., *3D Printed Multi-Functional Hydrogel Microneedles Based on High-Precision Digital Light Processing.* Micromachines, 2020. **11**(1).
128. Miller, P.R., et al., *Integrated carbon fiber electrodes within hollow polymer microneedles for transdermal electrochemical sensing.* Biomicrofluidics, 2011. **5**(1): p. 013415.
129. Aksit, A., et al., *In-vitro perforation of the round window membrane via direct 3-D printed microneedles.* Biomed Microdevices, 2018. **20**(2): p. 47.
130. Balmert, S.C., et al., *Dissolving undercut microneedle arrays for multicomponent cutaneous vaccination.* J Control Release, 2020. **317**: p. 336-346.
131. Faraji Rad, Z., P.D. Prewett, and G.J. Davies, *High-resolution two-photon polymerization: the most versatile technique for the fabrication of microneedle arrays.* Microsystems & Nanoengineering, 2021. **7**(1): p. 71.
132. Gu, Y., et al., *Mini Review on Flexible and Wearable Electronics for Monitoring Human Health Information.* Nanoscale Research Letters, 2019. **14**(1): p. 263.
133. Cheng, M., et al., *A review of flexible force sensors for human health monitoring.* J Adv Res, 2020. **26**: p. 53-68.

134. Liu, Y., M. Pharr, and G.A. Salvatore, *Lab-on-Skin: A Review of Flexible and Stretchable Electronics for Wearable Health Monitoring.* ACS Nano, 2017. **11**(10): p. 9614-9635.
135. Lee, E.K., M.K. Kim, and C.H. Lee, *Skin-Mountable Biosensors and Therapeutics: A Review.* Annual Review of Biomedical Engineering, 2019. **21**(1): p. 299-323.
136. Yamada, T., et al., *A stretchable carbon nanotube strain sensor for human-motion detection.* Nature Nanotechnology, 2011. **6**(5): p. 296-301.
137. Dagdeviren, C., et al., *Conformal piezoelectric systems for clinical and experimental characterization of soft tissue biomechanics.* Nature Materials, 2015. **14**(7): p. 728-736.
138. Gao, W., et al., *Fully integrated wearable sensor arrays for multiplexed in situ perspiration analysis.* Nature, 2016. **529**(7587): p. 509-514.
139. Harada, S., et al., *Fully Printed Flexible Fingerprint-like Three-Axis Tactile and Slip Force and Temperature Sensors for Artificial Skin.* ACS Nano, 2014. **8**(12): p. 12851-12857.
140. Ho, D.H., et al., *Stretchable and Multimodal All Graphene Electronic Skin.* Advanced Materials, 2016. **28**(13): p. 2601-2608.
141. Ogawa, Y., et al., *Organic Transdermal Iontophoresis Patch with Built-in Biofuel Cell.* Advanced Healthcare Materials, 2015. **4**(4): p. 506-510.
142. Huang, D., et al., *Recent advances on fabrication of microneedles on the flexible substrate.* Journal of Micromechanics and Microengineering, 2021.
143. Onesto, V., et al., *Engineered PLGA-PVP/VA based formulations to produce electro-drawn fast biodegradable microneedles for labile biomolecule delivery.* Progress in Biomaterials, 2020. **9**(4): p. 203-217.
144. Vecchione, R., et al., *Electro-Drawn Drug-Loaded Biodegradable Polymer Microneedles as a Viable Route to Hypodermic Injection.* Advanced Functional Materials, 2014. **24**(23): p. 3515-3523.
145. Zhang, Y., et al., *ROS-Responsive Microneedle Patch for Acne Vulgaris Treatment.* Advanced Therapeutics, 2018. **1**(3): p. 1800035.
146. Lozano, J. and B. Stoeber. *Microspike Array Electrode with Flexible Backing for Biosignal Monitoring*. in *2019 IEEE SENSORS*. 2019.
147. Lee, W., et al., *Conformable microneedle pH sensors via the integration of two different siloxane polymers for mapping peripheral artery disease.* Science Advances. **7**(48): p. eabi6290.
148. Xiang, Z., J. Liu, and C. Lee, *A flexible three-dimensional electrode mesh: An enabling technology for wireless brain–computer interface prostheses.* Microsystems & Nanoengineering, 2016. **2**(1): p. 16012.
149. Schenk, M. and S.D. Guest, *Geometry of Miura-folded metamaterials.* Proceedings of the National Academy of Sciences, 2013. **110**(9): p. 3276-3281.
150. Hou, Y., et al., *Miura-ori structured flexible microneedle array electrode for biosignal recording.* Microsystems & Nanoengineering, 2021. **7**(1): p. 53.

Chapter 3

Hyaluronic acid-silica hybrid microneedles for enhanced penetration efficiency and drug delivery capability

Dissolving microneedle (DMN) system offers excellent patient compliance, biocompatibility, and flexibility of functionalization to adapt into various therapeutic intents, in contrast to conventional routes of drug administration like oral and hypodermic injection. Low molecular weight hyaluronic acid (HA) as one of the typical biodegradable materials for DMN fabrication has been proven to perform better in terms of penetration capability when compared to high molecular weight hyaluronic acid. However, the overall mechanical strength of HA-DMNs is still insufficient to penetrate human skin effectively unlike other strong materials such as silicon and metal. Furthermore, high drug loading in the polymeric matrix would decrease matrix density and affect MN performance to a greater extent. Therefore, this chapter introduces an in-situ precipitation of silica nanoparticles (SiNPs) into the HA matrix using silica precursor to enhance the mechanical performance of the HA-based DMN system. Hybridization of silica network is demonstrated in which mechanical performance and penetration capability are evaluated using in vitro skin model. Potential adverse effect on morphological properties, drug release kinetics and biocompatibility of HA-Si MNs are compared to the pure HA MN. The proposed composite MN platform has shown great potential in large scale fabrication of biocompatible and high penetration efficiency rapid drug delivery system.

3.1 Introduction

As discussed in Chapter 2, transdermal drug delivery system and microneedle have served as a more favorable avenue for therapeutic purpose, and among other basic types of MN, dissolving MN system have been readily selected in transdermal drug delivery due to their superior compatibility with macromolecules and hydrophilic drugs[1, 2]. Dissolving MN system was first proposed in 2005 where biodegradable material PLA, PGA and PLGA were used for microneedle fabrication through simple micro-molding technique to address limitations like expensive and complex fabrication of conventional solid MN system[3]. In addition, key practical advantages of dissolving MN over solid MN and coated MN are effective reduction of biohazardous medical wastes like sharps, controllable formulation to allow tailored drug delivery, and most importantly, excellent biocompatibility to prevent activation of immune response[4]. Therefore, an ideal dissolving MN system should be biodegradable and mechanically robust to adapt to needs for high drug loading dosage. For this purpose, HA is a great option for rapid dissolving MN system as compared to other available biomaterials like PLA or PVP since its strong water binding ability helps the fast hydration of the applied area and eases delivery of large molecules into dermis and diffusion into systemic circulation[5].

Hyaluronic acid (HA), also known as hyaluronan, is one of the most abundant natural substances to be found in many parts of the human body, extensively available in articular cartilage and synovial fluid with varying forms and biological properties[6]. It is a linear, non-sulfated glycosaminoglycan formed by alternative repeating disaccharides D-glucuronic acid and N-acetyl-D-glucosamine (linked via β-1,3 and β-1,4 glycosidic bond) which exists as a macromolecule ranging from 10kDa to 8000kDa depending on the species[7]. Attributed by its excellent water retention capability and other hydrodynamic characteristics, HA plays a key role in physiological processes such as assembly of extracellular matrix (ECM), cellular signaling and wound repair[8]. In

addition, HA has rapid turnover in the tissue from hours to days through several enzymatic processes[9] where some also reported rapid removal of intravenous injected HA from blood circulation, subjecting to its molecular weight[10]. Due to these unique characteristics, HA and its derivatives have been extensively studied and utilized as cosmetic products for skincare routine over many decades. The reason of having high biocompatibility, promising bioavailability and presence of multiple carboxylic acid and alcohol groups have driven HA to be a popular candidate as engineerable biomaterial in tissue engineering and therapeutic applications in recent years[7, 11-13]. In this context, molecular weight of HA is reviewed since studies have shown notable contrast of performances in applications[14, 15]. In particular, Chi *et al*. compared RhB delivery efficacy of HA MNs with three molecular weights (10k, 70k and 290kDa) using porcine skin and Franz diffusion cell where they concluded that 70kDa molecular weight HA best delivery efficacy amongst. In fact, 10kDa was found to exhibit higher mechanical strength therefore the optimal molecular weight should lie in between 10k and 70kDa to gain balance between penetration strength and drug delivery efficacy.

As discussed earlier, an ideal microneedle patch should assure full MN penetration into human skin to release reliable dosage of drug. While some have reported that pure HA dissolving MN has sufficient strength to penetrate skin, many studies have also proposed mechanical reinforcement of HA-based dissolving MN system through multipolymer mixing[16-18] or introduction of nanomaterial. This is due to variation of skin thickness and mechanical properties depending on age, race, gender and target site of the human body. For example, Kalra A *et al.* summarized various studies regarding to factors affecting skin's modulus where they concluded that effect of gender does not exhibit consistent relationship whereas skin hydration content is the dominating factor over other parameters[19]. Above suggests that global commercialization of MN technology still remains questionable since skin condition of different populations might vary significantly. On top of that, high loading of therapeutic

substances can also potentially cause mechanical impairment of MN due to lower matrix density. Therefore, mechanical reinforcement of MN addresses the concern since mechanically stronger MN should be more likely to adapt under different circumstances.

Bio-reinforcement material refers to additives that could enhance mechanical performance of base material without concern of triggering immune response, in contrast to conventional inorganic additives like strontium[20]. Most common bio-reinforcement materials can be naturally derived material like cellulose[21] or synthetic materials like graphene oxide[22], carbon nanotubes[23] and magnetic nanoparticles[24]. In consideration of microscale geometry, bio-reinforcement material in nanoparticle form and can serve the best purpose. Recently, silica-based nanoparticles (SiNPs) have drawn tremendous interest in biomedical applications as composite scaffold[25] or drug delivery carrier[26]. It has been approved by United State Food and Drug administration (FDA) as an biosafe additive in food industry[27]. By looking at the structural perspective, silica consists of silanol group, which is a good site of conjugating targeting ligand for target-specific or stimuli-responsive drug delivery[28, 29].

Hybridization of silica and hyaluronic acid-based system was previously reported in hydrogel fabrication. For instance, Vallés Lluch *et al.* proposed mechanical enhancement of high molecular weight hyaluronic acid (~1.6MDa) through physically mixing HA solution with pre-formed silica aggregates in sodium hydroxide (NaOH)[25]. Divinyl sulfone (DVS) was added as the chemical HA crosslinker prior to drying and residue washing. Incorporated silica within HA hydrogel enhanced mechanical properties of the overall structure and increased swelling capability of the system without compromising the cell viability. However, dispersion of nanoparticles in viscous polymeric matrix may be challenging using mixing method, likely to form particle agglomeration that would disrupt uniformity of the matrix. Therefore, Lee *et al.* proposed in situ precipitation of silica from precursor through sol-gel conversion [30].

Tetramethyl orthosilicate (TMOS) was used as the silica precursor to infiltrate 1,4-butanediol diglycidyl ether (BDDE)-crosslinked hyaluronic acid matrix in 70% ethanol. Hydrolysis was initiated through temperature elevation, where condensation of the deposited silica nanoparticles was subsequently triggered through multiple solvent-induced shrinkage processes. However, washing steps were necessary for these reported studies due to non-biosafe chemicals like NaOH (corrosive) and precursor TMOS (toxic methyl group as byproduct). As non-crosslinked low molecular weight HA chosen in our study, washing step must be eliminated to avoid destruction of structure during the process thus the preparation method was revised and improved in our study.

Herein, a new composite system based on low molecular hyaluronic acid (HA) for MN fabrication via micro-molding technique is reported. A widely reported bio-reinforcement material, silica nanoparticle (SiNPs) is introduced to reinforce HA matrix via *in situ* acidic sol-gel reaction of less toxic silica precursor tetraethyl orthosilicate (TEOS). Transmission electron microscopy (TEM) was employed to characterize precipitation of SiNPs in HA matrix after drying. Morphological properties were then characterized and compared through optical image and scanning electron microscopy (SEM) to determine optimal silica concentrations for MN fabrication. Other chemical analysis like point scan energy dispersive spectroscopy (EDS) was used to verify elemental composition of HA-Si matrix locations. Moreover, HA-Si samples have shown prolonged degradation and drug release kinetics directly proportional to silica content. The fabricated HA-Si sample also exhibited excellent mechanical properties and biological properties up to 20 vol% which confirmed 20 vol% as the optimal concentration for HA-Si rapid dissolving MN system. This approach provides a promising alternative to mechanically reinforce the rapid dissolving MN system effectively.

3.2 Materials and methods

3.2.1 Materials

Hyaluronic acid sodium salt (molecular weight ≈ 40-60kDa) was purchased from Zhonglan Industry, China. Tetraethyl orthosilicate (TEOS), hydrochloric acid (HCl) and human recombinant insulin were purchased from Sigma Aldrich (USA). Absolute ethanol was purchased from Aik Moh (Singapore). Poly(dimethylsiloxane) (Sylgard^{TM}184, Dow Corning) purchased from Dow Corning and agarose provided by NTU SBS store (Singapore) were used for the fabrication of PDMS-agarose skin substitute. FluoSphere^{TM} carboxylate-modified microsphere dye was purchased from Thermofisher (Singapore) Detection and quantification of insulin release profile were conducted using insulin ELISA kit purchased from CrystalChem (USA). All chemicals were used without further purification.

3.2.2 PDMS micromold casting

The PDMS micromold was fabricated using traditional micro-molding technique as reported in previous studies[2]. First, PDMS at a 10:1 w/w of prepolymer to curing catalyst ratio was mixed and poured into container with stainless steel master template **(Figure 3-1B)** (Micropoint Technology, Singapore) immobilized at the bottom[31] (10x10 array of MN which are in pyramidal shape with height of ~1000μm, interspacing distance of ~700μm and base width of ~300μm). The container was then stored under vacuum to remove bubble formation for 2 hours and cured overnight in 70^{o}C oven. Solidified PDMS mold with inverse patterns was used for the fabrication of HA-based polymeric MNs.

3.2.3 Preparation of HA / HA-Si specimen and MNs array

Silica sol was first prepared at a molar ratio of 5: 1: 0.02: 4.5 involving distilled water, TEOS, HCl in the presence of ethanol (**Figure 3-1A**). HA-Si solutions were synthesized by mixing 0 vol%, 10 vol%, 20 vol% , 30 vol% and

35 vol% of silica solution in semi-dissolved HA solution (60mg/ml) for 16 hours at 35^{o}C in sealed container. The mixtures were then placed under vacuum to remove micro-bubbles formation for 2 hours. To fabricate HA and HA-Si film, 5ml of degassed mixtures were poured into plastic molds with a dimension of 60mm x 15mm x 15mm and store for air drying under constant airflow and room temperature (RT). After 24 hours of drying process, formed films were carefully taken out and trimmed for corresponding evaluations. To fabricate HA and HA-Si MN patches, 0.5ml of HA and HA-Si solution were poured onto the PDMS mold and centrifuged (4000 rpm at 25^{o}C) for 10 minutes until the solutions were spun into the individual tip wells. Next, 0.2ml of the respective formulations were to be added onto the mold and act as supportive backing layer right after centrifuging and 6 hours after (in total of three layers) to achieve desirable thickness. The samples were then left air-dried overnight at room temperature and finally detached from the mold by bending the PDMS mold carefully. Schematics summarizing the processes are as follow:

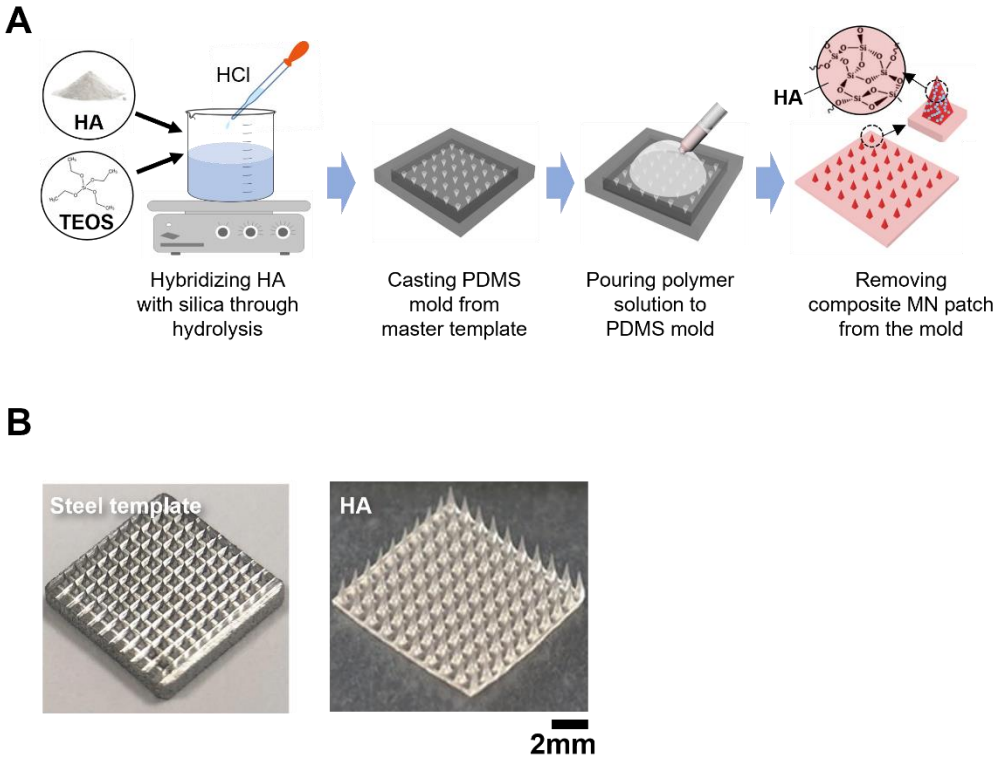

Figure 3-1 A. Schematic of preparing HA-Si solution and MN fabrication through micro-molding technique. B. Steel template and casted HA-based MN array [31]. Scale bar = 2mm.

3.2.4 Structural and chemical analyses of HA-Si specimens

The surface morphology and internal micro-structure of HA and HA-Si thin film were observed using field emission scanning electron microscopy (JSM-6700F, JEOL Techniques, Tokyo, Japan) and transmission electron microscopy (JEM-3010, JEOL Techniques, Tokyo, Japan). TEM specimens were prepared by diluting HA and HA-Si solutions in 1:1000 ratio and pouring onto a copper grid. TEM was then performed after overnight drying under constant air flow at room temperature. X-ray diffraction spectra of HA and HA-Si composites were also analyzed to determine their crystallinity by using single crystal X-ray Diffractometer (Smart APEX II SC-XRD, Bruker) at angle ranging from 20^{o} to 80^{o}. Surface elemental composition of HA-Si thin film have been investigated in order to visualise the distribution of Si and its derivatives on the surface by using

energy dispersive spectroscopy (EDS) with spot analysis function equipped on the aforementioned FESEM equipment.

3.2.5 Mechanical assessments of HA-Si system

3.2.5.1 Nanoindentation of HA-Si thin film

All nanoindentation tests were carried out using a Nano Indenter G200 (KLA Corporation, Milpitas, CA, USA) equipped with a Berkovich tip. A minimum of 10 indentations were performed on each HA or HA-Si film with a peak load of 0.5 mN and loading/unloading rate of 1 mN/s. The resulting maximum penetration depths are always below 1 μm for all the samples, which are significantly smaller than 10% of the film thickness (0.3 mm or above) so as to ensure valid measured results free from the influence of substrate.

The Young's modulus (E) and hardness (H) were obtained according to Oliver-Pharr method[32]. Briefly, the method utilizes load-displacement (P-h) curve from one cycle of loading- unloading indentation test to measure E and H of the testing material (compatible for elastic-plastic material)[33]. Three key quantities to obtain from experimental curve are maximum displacement (h_{max}), maximum load (P_{max}) and stiffness of upper portion of unloading curve (S) (**Figure 3-2A**). Due to elasticity of material, the surface tends to recover after complete unloading of indenter (Berkovich tip) where the final displacement is defined as h_s [34]. **Figure 3-2B** illustrates the unloading process and the parameters involved. Several relationships can then be introduced to calculate E:

$$M = \frac{\sqrt{\pi}}{2} * \frac{S}{\sqrt{A}} = \frac{E}{(1-v)^2};\ h_s = \in \frac{P_{max}}{S};\ h_c = h - h_s;\ A = f(h_c);\ H = \frac{P_{max}}{A}\ [34]$$

where M is the indentation modulus which can be used to calculate elastic modulus E, v is the assumed poisson's ratio, $\in$ is the indenter geometry constant, h_c is the displacment from elastic recovery, A is the contact area which can be calculated by substituting h_c into standard area function of Berkovich tip, and H can be obtained by dividing maximum load by the contact area.

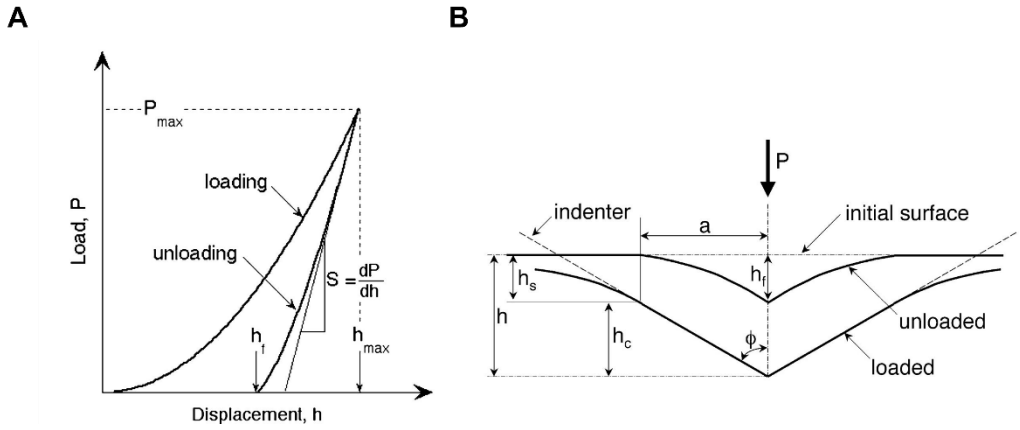

Figure 3-2. Schematic illustration of nanoindentation process and important parameters [34]. A. General nanoindentation P-h curve of loading-unloading process and the parameters. B. Schematic illustration of unloading process and contact geometry between indenter and material surface.

3.2.5.2 Bending test of HA-Si MNs on PDMS film

The bending test was performed on bulk silicone rubber Sylgard^{TM} 184 to investigate deformation resistance of composite microneedle against substrate reaction force. According to our preliminary finding, a PDMS base: catalyst ratio of 5:1 can represent hyperelastic behavior of human skin. After fabricating the PDMS thin film, 1x10 pure HA and 20vol%-Si MN patches were applied onto the thin film with constant force and the optical images before and after penetration were obtained.

3.2.5.3 Compression test of HA-Si MNs

Compressive force of fabricated composite microneedles in this study were also measured using a Instron 5543 material testing machine (Instron, USA). Briefly, 1x10 patch of HA or HA-Si microneedle was trimmed and attached to a rigid stainless steel station with adhesive tape and pressed by a pressure probe at 0.5 mm/s. Then the tensile meter recorded the force compressing the patches until 80% of its original thickness had been compressed.

3.2.6 Evaluation of functionality

3.2.6.1 *In vitro* penetration test of model drug loaded HA-Si MNs

Preparation of PDMS-agarose multilayered skin model

In order to determine how HA-Si composite system can improve MNs resistance against substrate penetration, a skin substitute made of PDMS-agarose hybrid system was used. 1.8wt% agarose powder and ultrapure water were poured into glass container before microwaving for 2 minutes at medium-high power. Immediately after dissolution, agarose solution was poured into a container to produce a 2mm thin agarose flat gel piece. After cooling in 4^{o}C fridge for 15 minutes, degassed 5:1 base to catalyst ratio of PDMS (Sylgards ™ 184) were then applied onto the gel piece to resemble elastic and water impermeable layer of stratum corneum. The gel piece was then placed in a 70^{o}C oven for 20 minutes and subsequently being transferred to fume hood for overnight curing under constant airflow.

Preparation of dye-loaded HA-Si MN and penetration test

2% of FluoSpheres™ was added to premixed HA or HA-Si solution. Similar to the previous HA MNs fabrication, 0.2ml of dye loaded HA or HA-Si solution were pipetted to cover tip wells and centrifuged at 4000rpm for 10 minutes. Excess HA was then scraped from the surface of the PDMS mold. Bare HA or HA-Si solutions were used for the second and third layers to ensure that only the MN tips contained fluorescent dye. After the second layers were applied, the molds were covered with foil and placed under constant airflow for approximately 6 hours before third layers were applied and the molds were covered with foil for complete drying in the fume hood overnight.

Each of the 10x10 MN arrays were trimmed into 6x6 arrays and attached onto a homemade applicator with adhesive tape before applying onto the multilayered skin model. After 30 seconds of administration, the arrays were removed from the gel piece and sent for observation under microscope.

3.2.6.2 Drug release test

Dissolution profile of HA-Si MN in PBS

1x10 HA-Si MN arrays of 0, 10, 20, 30 and 35 vol% were fabricated through micro-molding. Each MN patch was segmented using surgical blade to obtain single MN. The single MNs were attached onto homemade applicator and immersed into 5mL Dulbecco's phosphate buffered saline (dPBS, Thermofisher, USA) at room temperature (RT) for up to 2 minutes. At each predetermined timepoint, MN-attached applicator was lifted and excess moisture was carefully removed before placing under microscope. MN length remained on the array was recorded and measured using ImageJ software later.

Pseudo-drug release test

A drug release test using model drug, 2% Fluospheres^{TM} red fluorescent dye were loaded into 0%, 10% and 20% HA-Si composite solutions before casted into MNs array. 2mm 1.8wt% agarose gel were casted in a 3mm x 3mm petri dish to form a flat substrate for dye releasing intensity quantification using Zeiss LSM 800 confocal microscope (Zeiss, Germany). 3 time points (0, 5 and 10 seconds) have been chosen for this test where z stacks of 200 images taken from the penetrated locations. The images were merged using ImageJ software before measuring the intensity from each of the test groups.

Insulin release test in various time point

10μL of insulin was mixed with various concentrations of composite solution at 4^{o}C with gentle agitation for 2 minutes. The solutions were then placed in a vacuum container at 4^{o}C for 3 hours for degassing. After centrifuging at 4^{o}C, 4000rpm for 20 minutes, PDMS molds and petri dishes filled with insulin-composite solution were then placed in the vacuum container with 200g silica desiccating beads overnight for drying. On the following day, dried samples were dissolved fully in 4^{o}C DI water prior to test with a human insulin ELISA kit (CrystalChem, USA). On the other hand, 1 IU of insulin solution was loaded onto

various composite solutions at 4°C with gentle agitation for 2 minutes. The solutions were then stored in a vacuum container at 4°C for 3 hours for degassing. 0.2ml of various solutions were poured into the PDMS mold and centrifuged (4000rpm) for 20 minutes at 4°C. After second and third layer were applied, 200g of desicating beads were added into the container for sample drying overnight at 4°C. For the drug release test, the samples were immersed in 10ml deionized water at 4°C at predetermined time points of 10 seconds, 20 seconds, 30 seconds and 40 seconds. 10μL of samples were extracted for further dilution and the released amount of insulin were examined using ELISA kit.

3.2.7 Cytotoxicity test

Cytotoxicity of HA-Si extractables were evaluated using human normal dermal fibroblast (NDF) cultured in complete DMEM medium (high glucose with Glutamax™, Gibco, Thermofisher, USA) with 10% fetal bovine serum (FBS) and 1% penicillin and streptomycin (P/S) in a 37°C incubator with 5% CO_2 supply. The extractions were prepared by immersing UV-sterilized composite microneedles in complete DMEM culture medium at 37°C and 24 hours for full dissolution, with a proportion of 0.2g/ml, according to ISO 10993-12:2002 standard: "Sample Preparation and Reference Materials".

NDF cells were seeded at a density of 5000 cells per well onto 24-well tissue culture plates. 1ml cell culture medium was added during seeding procedure. After 24 hours seeding, bare culture medium were to be removed and replaced with extracted HA and HA-Si solution after 24 hours. Cells were then incubated for 24 hours and 72 hours. To assess cell viability, the wells were washed in multiple cycles with PBS carefully to remove composite solution and replenished with DMEM contained CCK-8 reagent (Sigma Aldrich, Singapore) at 100μL per well. The plate was then covered with aluminum foil and to be incubated for 3 hours. 100μL of aliquots were transferred to a 96 well plates as triplicates for absorbance measurement at 450 nm. Measured absorbance was normalized with control untreated NDF, defined as 100% viable.

Studies have also shown that medium viscosity is pertinent to cellular functions such as cell stretching and movement that related to cell growth. To reduce medium viscosity effect and establish comparable setup with control untreated cells, preliminary study of cell viability under various sample dilution were conducted. Briefly, extracted solutions with various viscosity were prepared by multiple 2-fold dilutions, from 100% undiluted groups to 4 times dilution groups with 6.25% concentration.

3.2.8 Statistical analysis

Each experiment was conducted with samples $n \geqslant 3$. All datas were presented in mean $\pm$ SD or otherwise as specified. Significances were accessed with one way analysis of ANOVA or student t-test to determine p value using Microsoft® Excel®. In all cases, p value <0.05 was considered statistically significant.

3.3 Results

3.3.1 Hybridization process of HA-Si system

Hyaluronic acid is a naturally occurring polysaccharide that are reported to be heat-sensitive, prone to undergo severe thermal degradation above 60^{o}C[35]. Sol-gel process of TEOS generally includes 1) hydrolysis of precursor into colloidal solution and 2) further condensation of hydrolyzed product, where these processes are known to be exothermic and could potentially elevates solution temperature during reaction[36]. Effective infiltration of silica precursor (TEOS) into HA matrix prior precipitation is essential whereby it helps to generate homogeneous distributed primary silica nanoparticles during hydrolysis and supports desired growth into constructive silica network through condensation thus simultaneous processes of HA powder dissolution and TEOS sol-gel reaction are proposed. After the silica sol was prepared, it was then added into HA powder with additional DI water to form final concentration of 60mg HA per mL solvent, presuming to act as water substitute at various weightage (0-35vol%). To make HA-Si compatible to be used as MN material, morphological properties of the dried HA-Si matrix should be carefully assessed since condensing and aggregation of silica networks could roughen the matrix surface and cause crack formation during drying[37, 38].

After the subsequent drying process, all composite films were removed from the container (**Figure 3-3**). As seen, HA-Si composite film had an increase in opaqueness with higher concentration of silica content. Surface roughness of the film also increased especially above 30% (v/v) TEOS addition, with a significantly visible non-uniform silica aggregation. Characterization of their stability and reproductivity will be presented in the further sections.

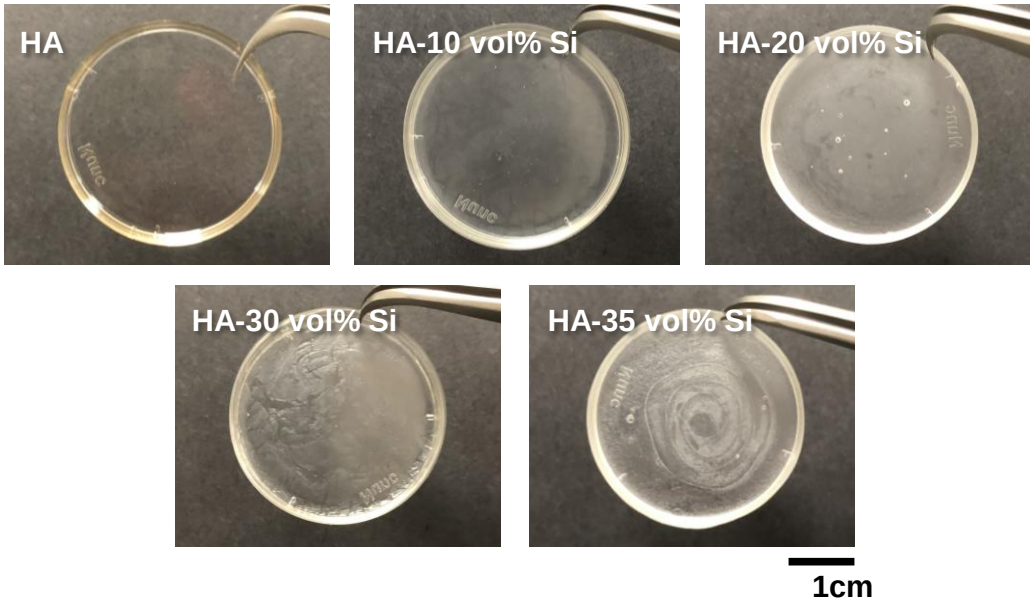

Figure 3-3. Optical appearance of various HA-Si composite thin films. Scale bar = 1cm.

3.3.2 Physical and chemical analyses of HA-Si system

Surface morphologies of various HA-Si MNs were observed in order to access how incorporation of silica network would affect consistency of casted MN as compared to that of pure HA (**Figure 3-4**). All MNs were dried and well-formed after removing from PDMS mold where every tips were intact on the base. From the optical appearance, MNs up to HA-20vol% Si showed consistent quality as compared to that of pure HA MNs. This tendency is consistent with casted films earlier on where samples up to 20vol% Si were observed to have minimal impact on surface roughness. Although HA-30vol% Si and HA-35 vol% Si MNs can also be casted with complete formation of array, they were observed to have relatively defective MN bodies which could potentially damage micro-integrity of the MN structure (**Figure 3-4A**).

Further characterization of MN morphologies were conducted using SEM. Tip region of MNs up to HA-20vol% Si case showed similar consistency and quality with tip radii ~10μm. The remaining MN tip region with high Si content showed severe distortion of geometry, especially the 35vol%Si case

where a teardrop-like aggregate was formed on the apex, causing increase in tip radius to ~16μm (**Figure 3-4B**). MN bodies showed similar trend where slight increase in roughness observed up to 20vol%-Si case. For HA-30vol% Si MN, rough surface was observed due to phase separation induced by inhomogeneous silica distribution. Besides that, increase in solution viscosity with higher silica content may cause difficulty to form designated MN tip shape during centrifuging. A greater extent of irregular silica distribution was observed in HA-35vol% Si case (**Figure 3-4C**).

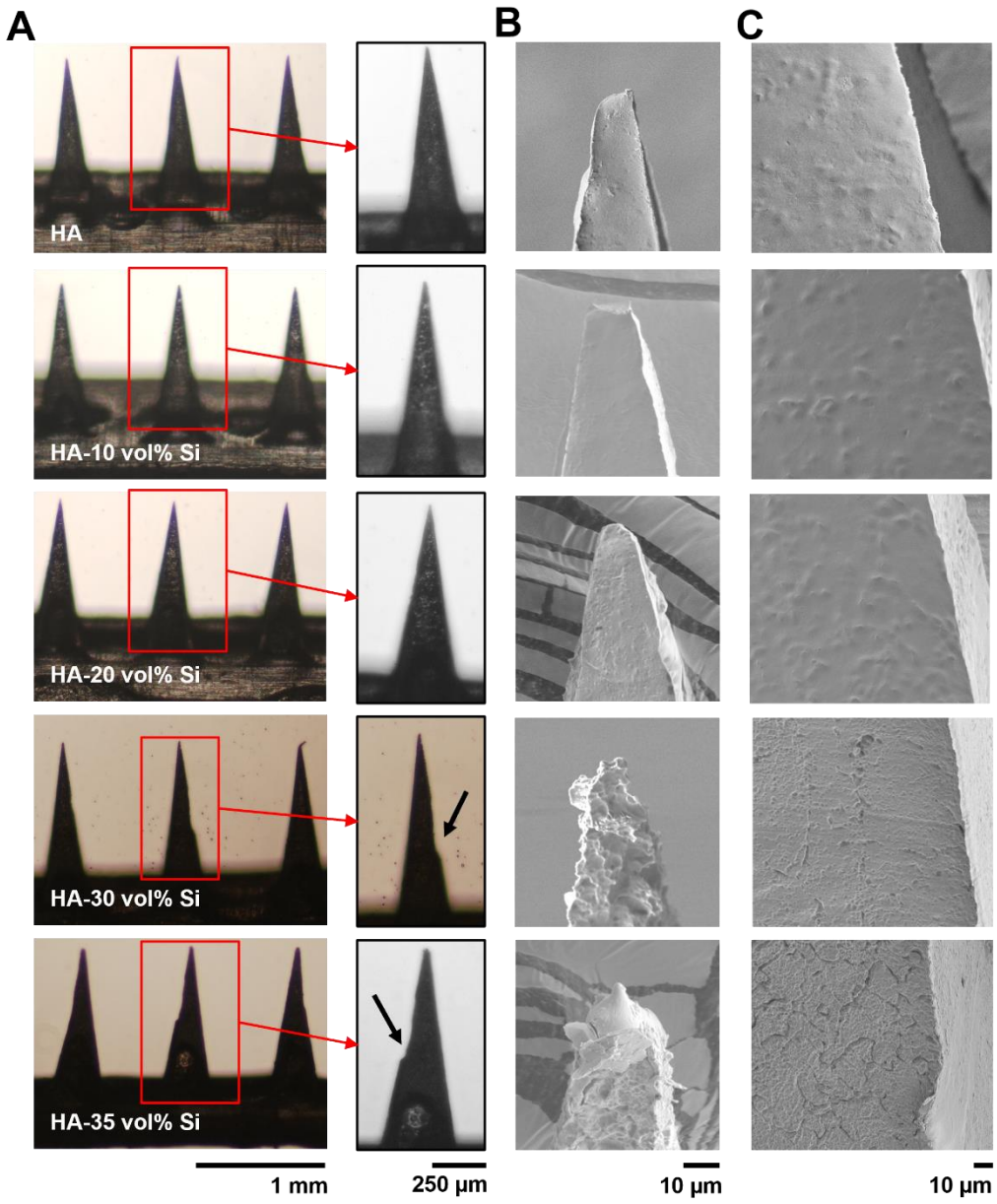

Figure 3-4. Morphological analyses of HA-Si MN. A. Optical image of various MNs with HA, HA-10vol%Si, HA-20vol%Si, HA-30vol%Si, HA-35vol%Si formulation (The black arrows indicate structural defect). Scale bar = 1mm. B. SEM image of MN tip morphologies at 1500x magnification. Scale bar = 10μm. C. SEM images of MN body morphologies at 800x magnification. Scale bar = 10μm.

Distribution of silica NPs in HA matrix was then investigated using TEM and EDS analysis (**Figure 3-5**). First, microstructure of the HA-Si polymeric matrix was visualised using TEM(**Figure 3-5A**). Take HA-20 vol% Si as reference, silica network was observed within the matrix which showed successful activation of sol-gel reaction. SiNPs were deposited and connected due to gelation with discrete sizes varying from 0.14-0.25μm. Pure HA matrix was also characterized with further magnification (bracketed in red), being observed to have nanoporous structure, with pore sizes varied from 25 nm to 230 nm in an interconnected manner.

Elemental mapping of HA-20 vol% Si confirmed existence of Si in the matrix which has shown to be somewhat homogeneous (**Figure 3-5B**). Additional point-scan EDS analysis was employed to analyze composition of HA-20 vol% Si at different locations. A flatter surface (region 1) was chosen to be location supposably having no SiNPs while a hump surface (region 2) was expected to have localized existence of SiNPs deposition. The composition in weight was measured and verified as tabulated in **Figure 3-5C**.

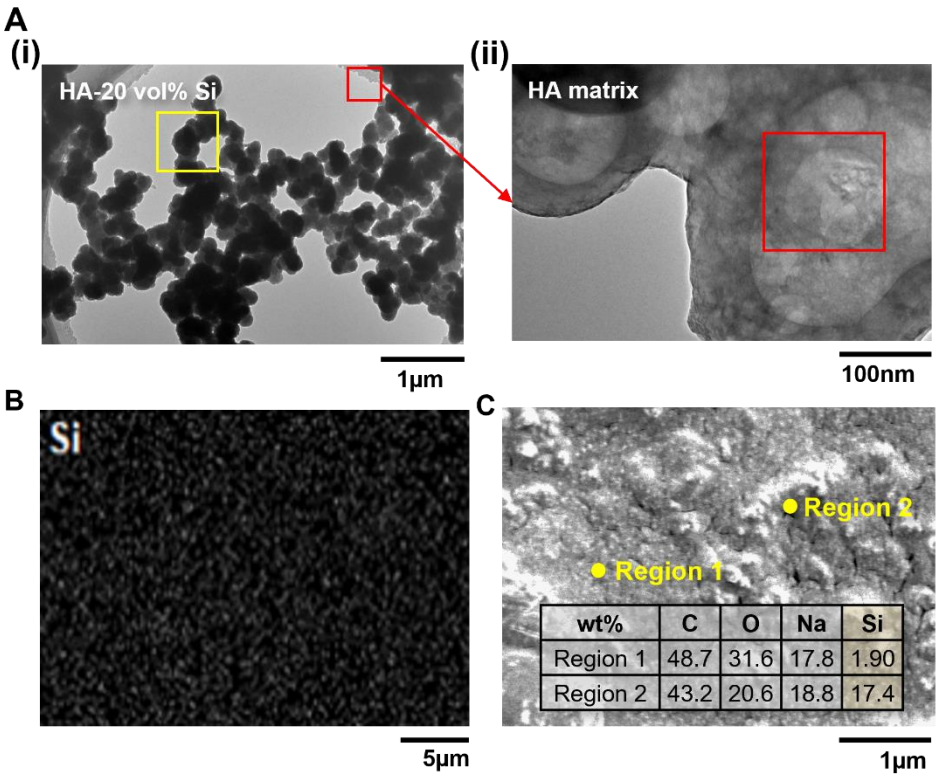

Figure 3-5. TEM and EDS analysis of HA-20vol%Si. A. Microstructure of HA-Si matrix and pure HA matrix at higher magnification. (i) Silica network in HA-20 vol% Si matrix. Yellow bracket showed growth of silica NPs into network. Scale bar = 1µm/100nm. (ii) HA matrix region. Red bracket marked interconnected nanopores within the polymeric matrix. Scale bar = 100nm. B. Si elemental mapping of HA-20 vol% Si using EDS mapping to show distribution of Si element throughout scanned area. Scale bar = 5µm. C. Point scan-EDS analysis of two pre-determined region on HA-20 vol% Si to determine elemental composition.

XRD graphs showed that HA in pure HA and its composites were all in poor crystallinity or amorphous state, being indicated by the non-distinct peaks at ~22^{o} (**Figure 3-6**). The broad peaks observed at 22^{o} in the graph also indicated amorphous state of silica in the composition.

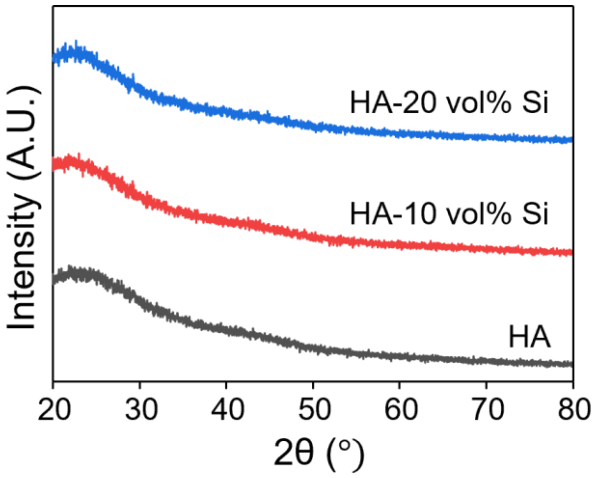

Figure 3-6. Chemical analysis (XRD) graphs of various HA-Si formulations

3.3.3 Mechanical properties

3.3.3.1 Nanoindentation of HA-Si as bulk film

In order to understand the impact of silica incorporation and surface morphology on the mechanical properties, the Young's modulus E and hardness H of both hyaluronic acid film and composite films were estimated through nanoindentation tests. The representative load–depth (P–h) curves can be seen in **Figure 3-7A**. At the same maximum load, the indentation penetration depth generally decreases with increasing silica content, indicating an increasing trend of hardness. The E and H values obtained by Oliver-Pharr method are plotted as a function of silica content in HA matrix in **Figure 3-7B** & **3-7C**. It is obvious that both E and H show significant enhancement with increasing silica content, up to ~196% in E and ~158% in H at 20 vol% as compared to the non-reinforced system. E and H shows insignificant increment with further increase in silica content above 20% and seemingly reach saturations. This may due to aggregation of silica NPs within HA matrix and eventually leads to inhomogeneous distribution of silica network. Another noteworthy feature is that the standard deviations of both values also become obviously larger as silica content increases (20 – 35 vol%), suggesting a higher surface inconsistency when silica nanoparticles aggregate. In general, E and H results are aligned with the optical

observation where higher silica content generates higher density of nanoparticles network and strengthen the polymeric matrix.

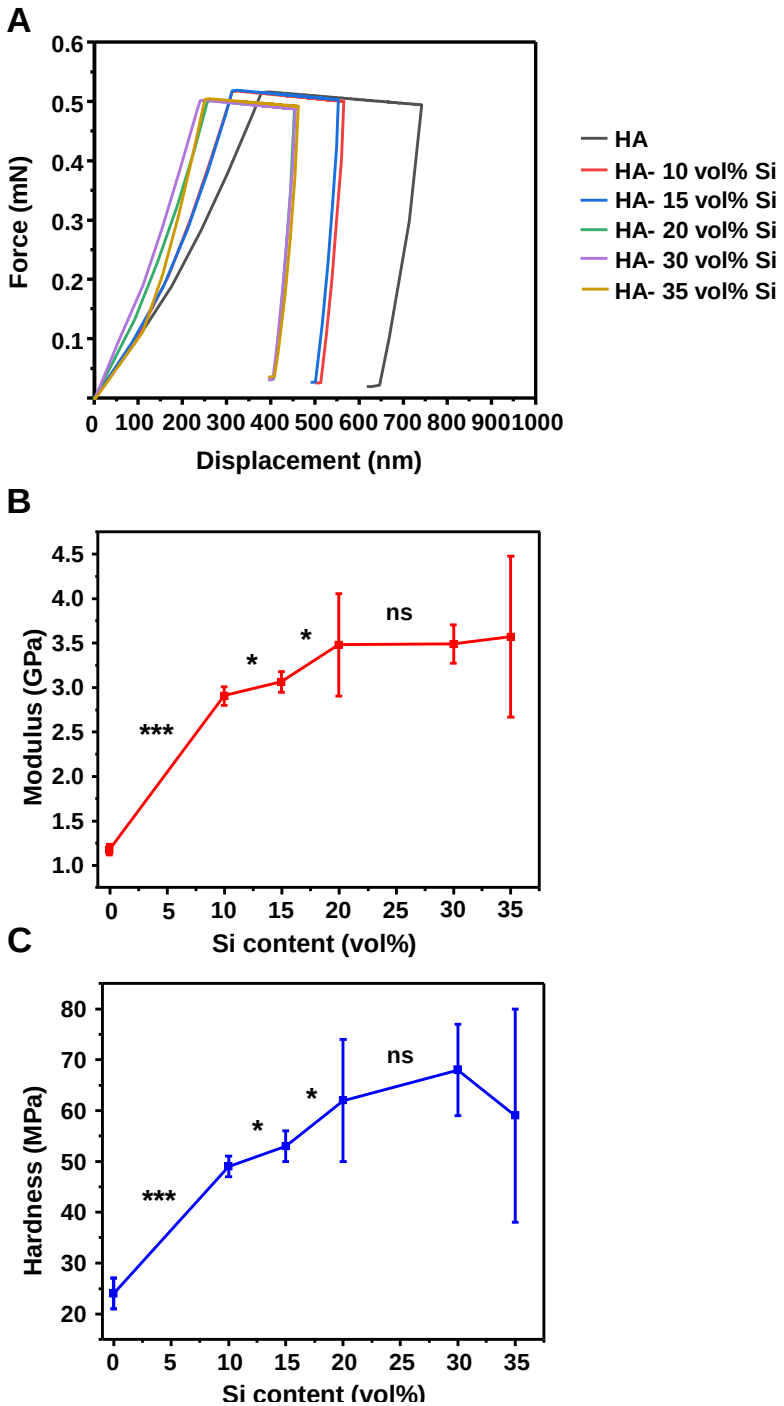

Figure 3-7. Nanoindentation tests of HA-Si thin films. A. Force-displacement curve of HA-Si samples. B. Modulus of HA-Si samples. C. Hardness of HA-Si samples. (* $p \leq 0.05$, ** $p \leq 0.01$, *** $p \leq 0.001$, ns = no significance)

3.3.3.2 Compression tests of HA-Si MNs

Penetration capability of HA-Si MNs were addressed in two approaches: quantitative measurement of penetration force using tensile meter as compared to pure HA MNs and quick observation using PDMS thin film to act as stratum corneum as shown in **Figure 3-8**. Steeper curves were observed in higher Si content up to HA-20vol%Si MN, suggesting that incorporation of silica did improve compressive strength of the system. However, this tendency was not observed in the HA-30 vol% Si case where it exhibited weaker compressive behavior than pure HA MN (**Figure 3-8A**). This finding is consistent with observation in morphological characterization where severe geometrical distortion was observed in samples with silica content above 30vol%. One of the possibilities that caused mechanical impairment could be the over-aggregated network in high Si content samples where structural inhomogeneity was introduced into the microstructure, potentially causing excess stress accumulation at the weaker spot of the matrix and failing prematurely.

Structural changes of HA-Si MNs in preliminary PDMS penetration test were shown in **Figure 3-8B.** Pure HA MN after unloading from PDMS film showed severe tip bending, suggesting that the tip region was ductile and deform upon contact with PDMS. Based on the measurement from ImageJ software, an average approximately 49% of MN length remained unbent. This remaining length of MN can then be dissolved in interstitial area and release the loaded drug. Presuming that the loaded drug is homogeneous in the MN matrix and the whole undeformed MN portion can fully penetrate the skin and dissolves, only 70% of the total dosage could be delivered into skin using pure HA MN(measurement from remaining volume). On the other hand, although slight reduction of MN length was observed in HA- 20vol% Si (27% in length), approximately 93% of the drug dosage could be delivered effectively into the skin based on theoretical calculation.

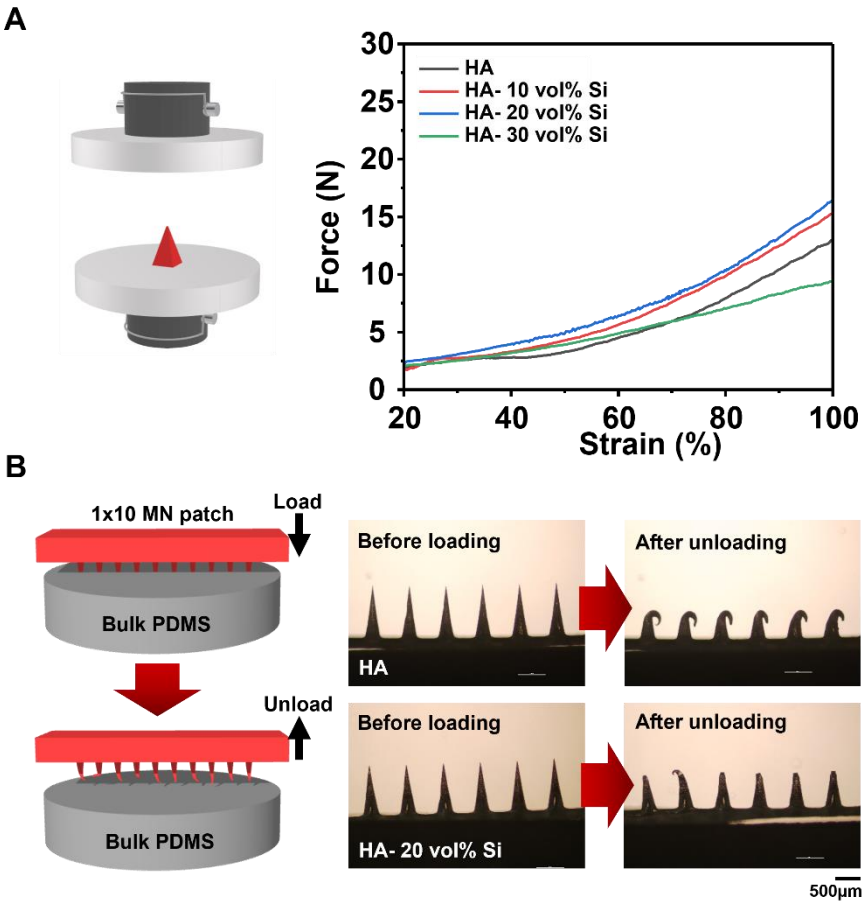

Figure 3-8. Compression test of HA-Si MN in quantitative and qualitative manner. A. Schematic illustration of the compression setup and compressive force-%strain curve of HA-Si MN. B Schematic illustration of the bending test setup and optical images of representative groups (pure HA and HA-20 vol% Si) before and after penetrating PDMS bulk film. Scale bar = 500µm.

3.3.4 Functionality evaluation

3.3.4.1 *In vitro* penetration test of HA-Si on bilayered skin model

To systematically evaluate how HA-Si hybridization improve penetration capability of MN system, HA-Si MNs were first tested using *in vitro* skin model penetration(**Figure 3-9**). Effective penetration of MN includes breaching of outermost skin layer, stratum corneum and epidermis therefore PDMS- agarose was proposed in this study to mimick multi-layered nature of human skin. In this

study, only locations observed with dye signal were considered as successful penetrations, as illustrated in **Figure 3-9A**. 10x10 MN patch were trimmed in this study due to rapid diffusion of fluorescent dye upon contact with agarose, therefore a smaller patch could give a more accurate data collection throughout. According to **Figure 3-9B**, normalized number of MNs penetration for pure HA, HA-10 vol% Si and HA-20 vol%Si were found to be 56.67 ± 4.71%, 76.67 ± 12.47% and 80 ± 8.17% respectively. In general, HA-Si MNs showed better penetration efficiency as compared to pure HA MN significantly ($p < 0.05$) with improvement over 20%. Interestingly, HA-10 vol% Si and HA-20 vol% Si MNs did not have statistical differences. Nonetheless, lower standard deviation observed in HA-20 vol% Si should be noted as indication of better consistency.

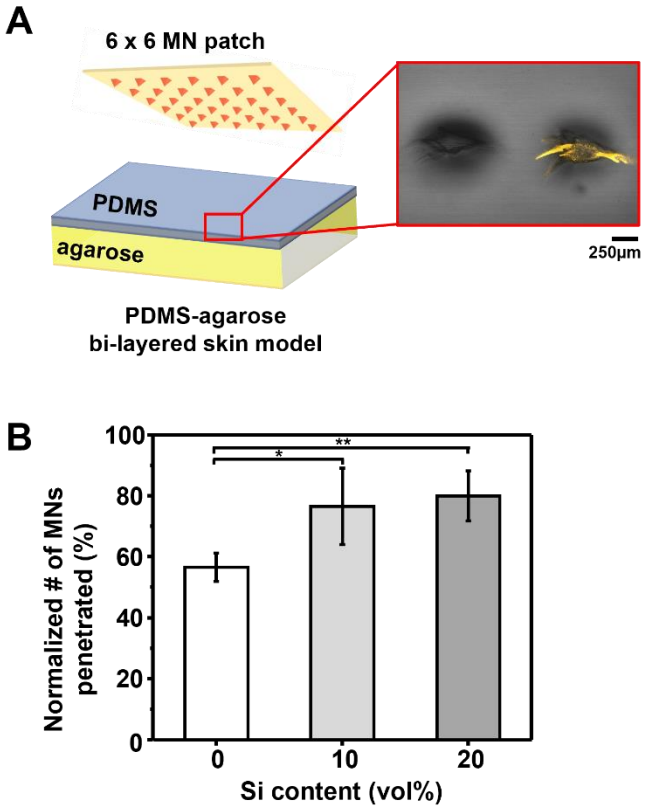

Figure 3-9. *In vitro* penetration test with bi-layered skin substitute. A. Schematic illustration of experimental setup with indication of successful penetration. Scale bar = 250μm. B. Normalized number of penetrations of various MNs. (*p ≤0.05, **p≤0.01)

3.3.4.2 Drug release test

Drug release kinetics of the HA-Si system as fully functional bio-degradable MN were characterized in three approaches. First, dissolution rate of HA-Si MNs were recorded and plotted as **Figure 3-10**. According to the graph, MN dissolution rate dropped with an increase in silica content up to HA-20vol% Si MN. Moreover, complete dissolution time of the MN extended from 60 seconds to 90 seconds as compared to pure HA. To be noted that HA-30vol% Si dissolved faster than that of HA-20vol% Si, but slower than that of pure HA and HA-10vol% Si case, at complete dissolution time of 80 seconds. This may due to structural imperfection as observed in SEM characterization (crack or phase separation etc.) where water get easily diffused into the matrix and led to faster degradation. As a consequence, HA-30vol% Si group had been excluded from the later studies.

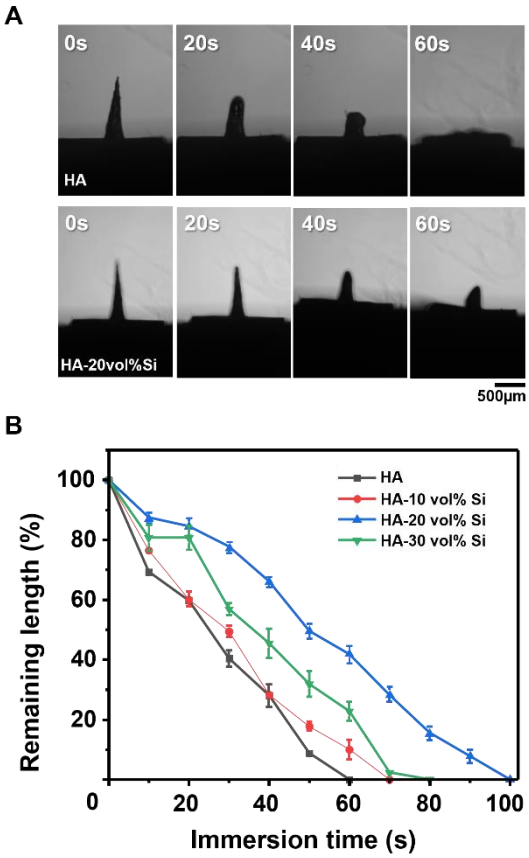

Figure 3-10. Degradation behavior of HA-Si MNs. A. Optical images of the HA-Si MNs dissolution progress. Scale bar = 500μm. B. Dissolution rate of various HA-Si MNs.

Fluosphere^{TM} is a carboxylate-modified fluorescent dye which has a molecular size of ~0.2µm. Therefore the quantitative measurement of the model drug intensity can be correlated as high molecular weight drug release rate (**Figure 3-11A)**. A rapid release of dye was observed in the pure HA samples as compared to the samples incorporated with silica. The tendency is consistent with dissolution test where HA-20vol%Si has the lowest dye intensity detection throughout due to slow and gradual degradation of matrix. Next, insulin as commercial therapeutic substance has been loaded onto various HA-Si MNs where drug release profile was investigated using a quantitative method. Human insulin ELISA assay was used to obtain insulin concentration during PBS immersion of composite microneedles in various time point where the amount of insulin was normalized to maximum amount of pure HA for better insight. According to **Figure 3-11B**, pure HA MN has a notably faster insulin release than that of HA-Si MNs. Interestingly, drug release kinetics of HA-10vol% Si and HA-20vol% Si were observed to be considerably similar.

Prior to the drug release study, a preliminary study of insulin compatibility was conducted in order to check whether the HA-Si system can potentially degrade loaded drug. No sign of signal reduction has been detected after 24 hours incubation with HA-Si in film and MN form. HA and HA-Si system were proved to be safe for insulin loading therefore drug release test were then proceeded.

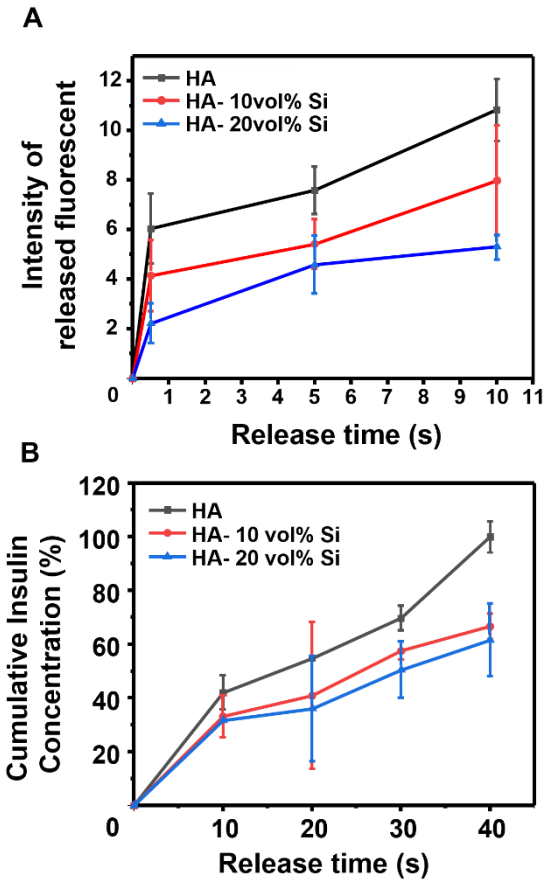

Figure 3-11. Drug release test of HA-Si MNs. A. Cargo release rate of HA-Si MNs loaded dye as high molecular weight model drug. B. Cargo release rate of HA-Si MNs, Insulin as commercial drug

3.3.5 Cytotoxicity test

HA-Si samples were extracted with DMEM full culture medium according to ISO standard for biocompatibility study. To evaluate effect of HA-Si extraction to medium viscosity, multiple 2-fold dilution were performed where extracted medium with no dilution and 4x dilution were compared with that of normal DMEM culture medium, as plotted in **Figure 3-12A** with shear rate from 0.01 to 100. For undiluted extracted medium(0.2g/ml), viscosity increased from ~3.5x10^5mPa.s (HA medium), ~4.2x10^5mPa.s (HA-10 vol%Si medium), ~7.9x10^5MPa.s (HA-20vol%Si medium) up to ~9.4x10^5mPa.s (HA-30 vol%Si medium)at low shear rate of 0.01s^{-1}. All undiluted samples showed significantly

higher viscosity in contrast to that of pure culture medium with ~1mPa.s, similar to reported value in literature[39]. On the other hand, viscosities at $0.1s^{-1}$ after 4x diluted showed to be ~63.8mPa.s (HA medium-D), ~178.5mPa.s (HA-10vol%Si medium-D), ~445.7mPa.s (HA-20vol%Si) and ~886.3mPa.s (HA-30 vol%Si) respectively.

Next, effect of medium viscosity on cell viability were evaluated through 2-folds serial dilutions of extracted medium up to 4x against positive control (PC) which was treated with normal culture medium. As a result, the pure HA group with 4x dilution showed comparable viability with untreated control NDF cells therefore 4x serial dilutions were chosen for studies onwards (**Figure 3-12B**).

On the other hand, NDF cells were also treated with silica solutions with various concentrations up to 30 vol% in DMEM medium to study their cell toxicity effect. According to the graph, slight declines were observed as silica content increased from 0% to 20% which can still be deemed as biocompatible. However, a sharp decline was observed from 30% onwards with $p \geq 0.05$, denoting inhibition of cell growth which may be due to excessive amounts of silica present. As acidic catalyst HCl was also introduced, decrease in pH could also contributed to the cell death [40](**Figure 3-13A**). HA-Si extracted cell mediums with 4x serial dilutions were then tested and the viability after 3 days were as shown in **Figure 3-13B**. HA-Si matrices with Si content below 30 vol% were found to be non-toxic since they were statistically insignificant.

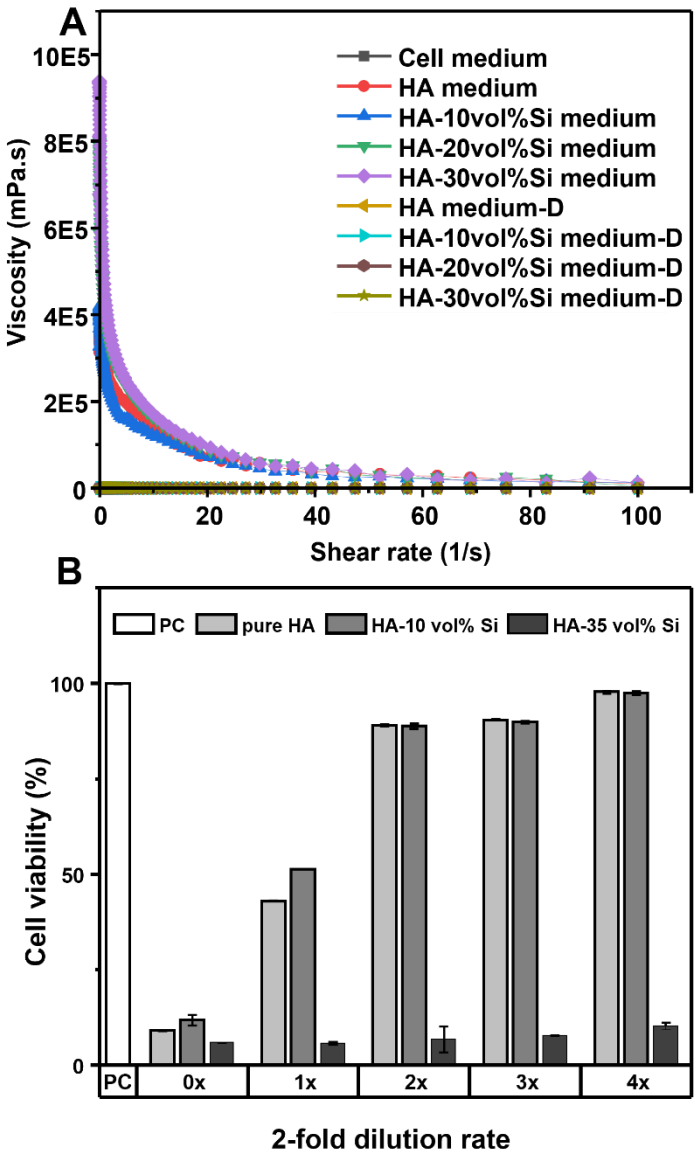

Figure 3-12. Preliminary studies to determine proper dilution of HA-Si extracted medium. A. Viscosity profile of various HA-Si extracted medium. B. Effect of medium viscosity to cell viability. Cell viability was quantified based on CCK-8 assay protocol.

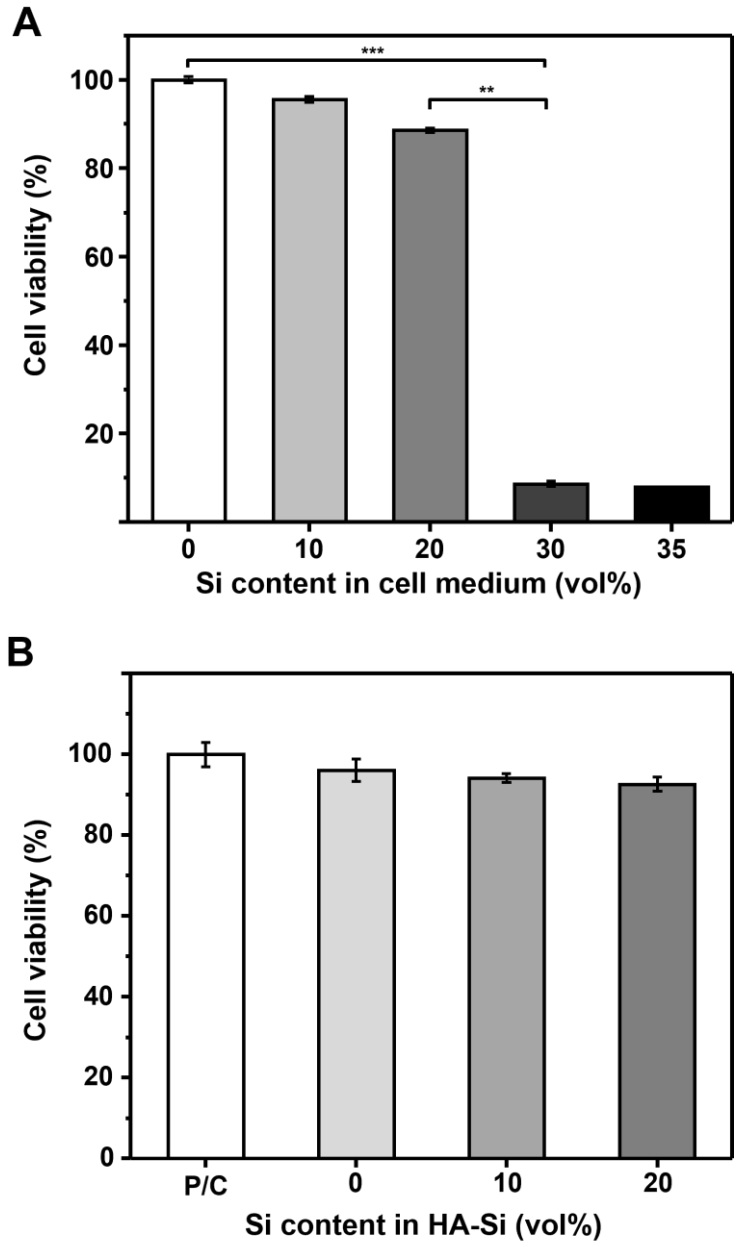

Figure 3-13. 3 days NDF proliferation study of various HA-Si samples. A. 3 days proliferation with silica solutions only; B. 3 days proliferation with HA-Si extracted mediums. All cell viability tests were conducted based on CCK-8 assay protocol (*$p \leq 0.05$, **$p \leq 0.01$, ***$p \leq 0.001$)

3.4 Discussion

Current hypodermic administration of drug and vaccines can be done within a minute therefore a material with rapid dissolution rate should also be preferable. Hyaluronic acid (HA) is a suitable material to address most requirements as mentioned, however still challenging for commercial acceptance due to relatively low mechanical strength with high drug dosage loading of biodegradable polymers in general [41]. Besides that, molecular weight of HA has been carefully chosen in this study as discussed in the introduction section. Therefore, our study has chosen 40k-60kDa molecular weight HA as the base material to ensure proper functionality of the pure HA MN case.

Bioactive fillers or additives are often introduced into polymeric systems as hybridization mediators to allow tunability of mechanical properties for different purposes. Hydroxyapatite, graphene oxide, bioactive glass and silica granules are the typical inorganic additives to date[22, 42, 43]. Among all, silica nanoparticle is one of the most suitable bioactive inorganic additives to use in our study, as proven in many studies[44, 45]. This is attributed by the capability of silicon ions to promote inflammatory cell recruitment and effectively induce wound-healing progression and collagen regeneration[46]. Finally, physiological degradation of silica was also proven to be non-toxic[47], making silica a promising candidate for polymeric reinforcement. However, mere dispersion of colloidal silica into HA matrix is unrealistic since pure HA matrix is viscous which could cause particles to agglomerate[48] and potentially obtain an inhomogeneous system. Therefore, a widely used silica precursor, TEOS, is chosen. Sol-gel reaction involves acidic or basic hydrolysis of silica precursors and condensation of hydroxyl groups into a network. Acidic catalyst HCl was used as acidic hydrolysis of TEOS was reported to have better-formed granules and to be condensed into linear polymer with weak crosslinked network, making it better for hybridization process, in contrast to smaller and highly branched structure through basic hydrolysis[49]. Ethanol as a common solvent has been added into the reaction and allows effective hydrolysis of TEOS into hydroxyl

groups. *In situ* precipitation of silica can be done in room temperature which is advantageous for heat sensitive biopolymers like HA. Slight elevation of temperature was to accelerate dissolution of HA, ensuring that condensation of silica network initiates after homogeneous formation of HA matrix.

According to optical appearance, HA-30vol% Si and HA-35vol% Si thin film showed significant increase in surface roughness where cloudy inhomogeneity was observed in HA-35vol% Si. This may be due to larger silica particle size formation of high TEOS concentration during sol-gel reaction and occupying more space in the HA matrix[50]. Moreover, denser gelation of higher TEOS concentration through condensation also caused highly aggregated silica networks, eventually affecting surface roughness of HA-Si morphology. This was further observed in SEM images of casted MN where poor quality and consistency of tip region were found. As viscosity plays an important role in micromolding technique, high viscosity of high concentration HA-Si could also affect proper settlement of solution into the tip wells and brings negative effect to the MN quality. From SEM images of MN bodies (**Figure 3-4C**), crack formations were also observed in HA-30vol%Si and HA-35vol%Si MNs. A common characteristic of air-drying method is volume shrinkage. Since brittleness can be introduced into the matrix as Si content increases [51], cracks were formed in HA-30vol%Si MN and above due to volumetric shrinkage during the drying process. This delamination of microstructure could potentially cause weaker mechanical behavior, which was confirmed in the MN compression test.

According to the XRD graph, the pattern of HA and HA-Si matrix showed no distinct peaks at determined locations (20-30^{o}), indicating amorphous state of both compositions, which are consistent with reported literatures[52, 53]. Worth to note that crystalline silica (Min-U-Sil) can be fatal and was found to be carcinogenic, causing silicosis and lung cancer[54] therefore characterization of silica crystallinity is important in development of biomedical devices.

Incorporation of silica was proven to improve mechanical properties of HA matrix in various test. There was no intended conjugative mediator introduced into the system, therefore interaction between HA and silica is through hydrogen bonding between silanol group and hydrophilic group on HA[25, 30, 55]. In addition, HA exists as a linear poly-chain of disaccharides which therefore able to form interpenetration with condensed silica networks physically even without crosslinking[46].

Interestingly, dissolution tendency of HA-Si in general was observed to be slightly different as compared to cargo release test. According to **Figure 3-10**, HA-20 vol% Si exhibit significantly slower degradation rate in terms of remained length, as compared to pure HA and HA-10vol%Si where 70% of MN length still remained on the array at 40 second time point (~30% for both HA and HA-10 vol% Si case). Yet from the cumulative insulin release graph, HA-10 vol% Si and HA-20 vol% Si showed similar insulin release rate throughout. This may be contributed by the higher number of molecular interactions between HA and silica in HA- 20 vol% Si case whereby MN could preserve its overall MN structure without undergo severe bulk fragmentation. But since HA is reported to be highly hygroscopic, moisture should infiltrate the whole MN network at the same rate. Consequently, diffusion rate of the loaded cargos in HA-10vol%Si and HA-20vol%Si MN were almost identical. Under this context, pure HA MN still displayed highest cargo release rate due to more rapid bulk fragmentation upon contact with water.

HA- 30 vol% Si and above showed consistently poor cell viability in 3-days proliferation test which indicates high toxicity to cells. Otherwise, pure HA, HA-10 vol% Si and HA-20 vol% Si demonstrated good cytocompatibility with no significant reduction in cell viability. This suggested that HA-Si is a bio-safe material that could be used in MN fabrication that fulfils fundamental requirement of dissolving MN development.

3.5 Conclusion

In this study, HA-based dissolving MN with enhanced mechanical properties and excellent biocompatibility were successfully fabricated by introducing an *in situ* bio-active inorganic nanoparticles through one step sol-gel reaction. Silica nanoparticles were first precipitated homogeneously in HA matrix from silica precursor TEOS, further condensed into silica network and form interpenetrating network of HA-Si matrix. The incorporation of silica networks gave minimal impact on surface morphology up to 20 vol%, suggesting good and consistent MN quality as compared to pure HA MN. Furthermore, the HA-Si system has shown to significantly enhance mechanical properties of HA up to HA-20 vol% Si concentration due to strong hydrogen bonding of Si-O and HA hydrophilic groups in both bulk and microneedle form. Functionality tests also showed improved penetration capability up to HA-20 vol% Si MN, aligning with the observation made in structural analyses. Cargo release tests showed unique dissolution and drug release kinetics of HA-Si, attributed by the interaction between HA and silica network. Finally, HA-Si up to 20vol%Si did not exhibit cytotoxicity. This platform provides a promising HA-based dissolving MN material to address commercialization hindrance of dissolving MN system.

References

1. Xu, Q., et al., *Rapidly dissolving microneedle patch for synergistic gene and photothermal therapy of subcutaneous tumor.* Journal of Materials Chemistry B, 2020. **8**(19): p. 4331-4339.
2. Dangol, M., et al., *Anti-obesity effect of a novel caffeine-loaded dissolving microneedle patch in high-fat diet-induced obese C57BL/6J mice.* J Control Release, 2017. **265**: p. 41-47.
3. Park, J.-H., M.G. Allen, and M.R. Prausnitz, *Biodegradable polymer microneedles: Fabrication, mechanics and transdermal drug delivery.* Journal of Controlled Release, 2005. **104**(1): p. 51-66.
4. Dang, N., T.Y. Liu, and T.W. Prow, *Chapter Seventeen - Nano- and Microtechnology in Skin Delivery of Vaccines*, in *Micro and Nanotechnology in Vaccine Development*, M. Skwarczynski and I. Toth, Editors. 2017, William Andrew Publishing. p. 327-341.
5. Du, H., et al., *Hyaluronic Acid-Based Dissolving Microneedle Patch Loaded with Methotrexate for Improved Treatment of Psoriasis.* ACS Applied Materials & Interfaces, 2019. **11**(46): p. 43588-43598.
6. Gupta, R.C., et al., *Hyaluronic Acid: Molecular Mechanisms and Therapeutic Trajectory.* Front Vet Sci, 2019. **6**: p. 192.
7. Burdick, J.A. and G.D. Prestwich, *Hyaluronic acid hydrogels for biomedical applications.* Adv Mater, 2011. **23**(12): p. H41-56.
8. Toole, B.P., *Hyaluronan: from extracellular glue to pericellular cue.* Nature Reviews Cancer, 2004. **4**(7): p. 528-539.
9. Laurent, T.C. and J.R. Fraser, *The properties and turnover of hyaluronan.* Ciba Found Symp, 1986. **124**: p. 9-29.
10. Mattheolabakis, G., et al., *Hyaluronic acid targeting of CD44 for cancer therapy: from receptor biology to nanomedicine.* J Drug Target, 2015. **23**(7-8): p. 605-18.
11. Allison, D.D. and K.J. Grande-Allen, *Review. Hyaluronan: a powerful tissue engineering tool.* Tissue Eng, 2006. **12**(8): p. 2131-40.
12. Kona, S., A.S. Wadajkar, and K.T. Nguyen, *6 - Tissue engineering applications of injectable biomaterials*, in *Injectable Biomaterials*, B. Vernon, Editor. 2011, Woodhead Publishing. p. 142-182.
13. Overstreet, D.J., H.A. Von Recum, and B.L. Vernon, *5 - Drug delivery applications of injectable biomaterials*, in *Injectable Biomaterials*, B. Vernon, Editor. 2011, Woodhead Publishing. p. 95-141.
14. Fallacara, A., et al., *Hyaluronic Acid in the Third Millennium.* Polymers (Basel), 2018. **10**(7).
15. Snetkov, P., et al., *Hyaluronic Acid: The Influence of Molecular Weight on Structural, Physical, Physico-Chemical, and Degradable Properties of Biopolymer.* Polymers (Basel), 2020. **12**(8).
16. Cheng, Z., et al., *Preparation and characterization of dissolving hyaluronic acid composite microneedles loaded micelles for delivery of curcumin.* (2190-3948 (Electronic)).
17. Shim, W.S., et al., *Role of Polyvinylpyrrolidone in Dissolving Microneedle for Efficient Transdermal Drug Delivery: In vitro and Clinical Studies.* Bulletin of the Korean Chemical Society, 2018. **39**(6): p. 789-793.

18. Sawutdeechaikul, P., et al., *Detachable dissolvable microneedles: intra-epidermal and intradermal diffusion, effect on skin surface, and application in hyperpigmentation treatment.* Scientific Reports, 2021. **11**(1): p. 24114.
19. Kalra, A. and A. Lowe, *An Overview of Factors Affecting the Skins Youngs Modulus.* Journal of Aging Science, 2016. **4**.
20. Grigoriadou, I., et al., *Evaluation of silica-nanotubes and strontium hydroxyapatite nanorods as appropriate nanoadditives for poly(butylene succinate) biodegradable polyester for biomedical applications.* Composites Part B: Engineering, 2014. **60**: p. 49-59.
21. Martwong, E., et al., *A Potential of New Untreated Bio-Reinforcement from Caesalpinia sappan L. Wood Fiber for Polybutylene Succinate Composite Film.* Polymers (Basel), 2022. **14**(3).
22. Yi, J., et al., *Graphene oxide-incorporated hydrogels for biomedical applications.* Polymer Journal, 2020. **52**(8): p. 823-837.
23. Wang, W., et al., *Carbon Nanotubes Reinforced Composites for Biomedical Applications.* BioMed Research International, 2014. **2014**: p. 518609.
24. Li, X., et al., *Limpet Tooth-Inspired Painless Microneedles Fabricated by Magnetic Field-Assisted 3D Printing.* Advanced Functional Materials, 2021. **31**(5): p. 2003725.
25. Vallés-Lluch, A., et al., *Hyaluronic Acid–Silica Nanohybrid Gels.* Biomacromolecules, 2013. **14**(12): p. 4217-4225.
26. M. Ways, T.M., et al. *Silica Nanoparticles in Transmucosal Drug Delivery*. Pharmaceutics, 2020. **12**, DOI: 10.3390/pharmaceutics12080751.
27. FDA. *Synthetic Amorphous Silica*. [cited 2022 06 December]; Available online: https://www.cfsanappsexternal.fda.gov/scripts/fdcc/index.cfm?set=GRASNotices&id=321].
28. Yang, Y., et al., *Silica-Based Nanoparticles for Biomedical Applications: From Nanocarriers to Biomodulators.* Accounts of Chemical Research, 2020. **53**(8): p. 1545-1556.
29. Gerstenberg, M., et al., *Modular Hydrogel−Mesoporous Silica Nanoparticle Constructs for Therapy and Diagnostics.* Advanced NanoBiomed Research, 2022. **2**(3): p. 2100125.
30. Lee, H.-Y., et al., *Strategy for Preparing Mechanically Strong Hyaluronic Acid–Silica Nanohybrid Hydrogels via In Situ Sol–Gel Process.* Macromolecular Materials and Engineering, 2018. **303**(9): p. 1800213.
31. Zheng, M., et al., *Osmosis-Powered Hydrogel Microneedles for Microliters of Skin Interstitial Fluid Extraction within Minutes.* Advanced Healthcare Materials, 2020. **9**(10): p. 1901683.
32. Kan, Q., et al., *Oliver–Pharr indentation method in determining elastic moduli of shape memory alloys—A phase transformable material.* Journal of the Mechanics and Physics of Solids, 2013. **61**(10): p. 2015-2033.
33. Li, H. and J.J. Vlassak, *Determining the elastic modulus and hardness of an ultra-thin film on a substrate using nanoindentation.* Journal of Materials Research, 2011. **24**(3): p. 1114-1126.
34. Oliver, W.C. and G.M. Pharr, *Measurement of hardness and elastic modulus by instrumented indentation: Advances in understanding and refinements to methodology.* Journal of Materials Research, 2004. **19**(1): p. 3.

35. Mondek, J., et al., *Thermal degradation of high molar mass hyaluronan in solution and in powder; comparison with BSA.* Polymer Degradation and Stability, 2015. **120**: p. 107-113.
36. Matsuoka, J., et al., *Heat of Reaction of the Hydrolysis-Polymerization Process of Tetraethyl Orthosilicate in Acidic Condition.* Journal of Sol-Gel Science and Technology, 2000. **19**(1): p. 661-664.
37. Lee, D.H., et al., *Superhydrophobic surfaces with near-zero sliding angles realized from solvent relative permittivity mediated silica nanoparticle aggregation.* Journal of Materials Chemistry A, 2014. **2**(40): p. 17165-17173.
38. Mohd Yusop, H., A.I.H. Mohd Ismail, and W.A.-O. Wan Ismail, *Preparation and Characterization of New Sol-Gel Hybrid Inulin-TEOS Adsorbent. LID - 10.3390/polym13081295 [doi] LID - 1295.* (2073-4360 (Electronic)).
39. Poon, C., *Measuring the density and viscosity of culture media for optimized computational fluid dynamics analysis of in vitro devices*. 2020.
40. Mackenzie, C.G., J.B. Mackenzie, and P. Beck, *The effect of pH on growth, protein synthesis, and lipid-rich particles of cultured mammalian cells.* J Biophys Biochem Cytol, 1961. **9**(1): p. 141-56.
41. Park, J.H., M.G. Allen, and M.R. Prausnitz, *Polymer microneedles for controlled-release drug delivery.* Pharm Res, 2006. **23**(5): p. 1008-19.
42. Fiorati, A., et al., *Bioactive Hydrogels: Design and Characterization of Cellulose-Derived Injectable Composites.* Materials (Basel), 2021. **14**(16).
43. Kołodziejska, B., A. Kaflak, and J. Kolmas, *Biologically Inspired Collagen/Apatite Composite Biomaterials for Potential Use in Bone Tissue Regeneration-A Review.* Materials (Basel), 2020. **13**(7).
44. Pan, F., et al., *pH-responsive silica nanoparticles for the treatment of skin wound infections.* Acta Biomaterialia, 2022. **145**: p. 172-184.
45. Quignard, S., et al., *Silica nanoparticles as sources of silicic acid favoring wound healing in vitro.* Colloids Surf B Biointerfaces, 2017. **155**: p. 530-537.
46. Song, E.H., et al., *Polyurethane-silica hybrid foams from a one-step foaming reaction, coupled with a sol-gel process, for enhanced wound healing.* Mater Sci Eng C Mater Biol Appl, 2017. **79**: p. 866-874.
47. Carvalho, G.C., et al., *Highlights in Mesoporous Silica Nanoparticles as a Multifunctional Controlled Drug Delivery Nanoplatform for Infectious Diseases Treatment.* Pharmaceutical Research, 2020. **37**(10): p. 191.
48. Sumi, D., et al., *Effect of colloidal silica dispersions on the properties of PDMS-colloidal silica composites.* Journal of Applied Polymer Science, 2012. **125**(S1): p. E515-E522.
49. Silva, C.R. and C. Airoldi, *Acid and Base Catalysts in the Hybrid Silica Sol–Gel Process.* Journal of Colloid and Interface Science, 1997. **195**(2): p. 381-387.
50. !!! INVALID CITATION !!! {}.
51. Jiao, J., X. Sun, and T.J. Pinnavaia, *Mesostructured silica for the reinforcement and toughening of rubbery and glassy epoxy polymers.* Polymer, 2009. **50**(4): p. 983-989.
52. Hamad, G., et al., *Physicochemical, Molecular and Functional Characteristics of Hyaluronic Acid as a Functional Food.* American Journal of Food Technology, 2017. **12**: p. 72-85.
53. Nallathambi, G., et al., *Effect of Silica Nanoparticles and BTCA on Physical Properties of Cotton Fabrics.* Materials Research, 2011. **14**: p. 552-559.

54. Skuland, T., et al., *Pro-inflammatory effects of crystalline- and nano-sized non-crystalline silica particles in a 3D alveolar model.* Particle and Fibre Toxicology, 2020. **17**(1): p. 13.
55. Theofanous, A., et al., *Antioxidant Hydrogen-Atom-Transfer to DPPH Radicals by Hybrids of {Hyaluronic-Acid Components}@SiO2.* Langmuir, 2022. **38**(40): p. 12333-12345.

Chapter 4*

Bioinspired flexible microneedle patches for improved adaptability and functionality

The emerging global attention on healthcare issues have urged the development of point-of-care technologies especially when continual increase of chronic disease cases and ageing population aggravated the burden of current medical system. Flexible-based MN system has shown its potential as a wearable device to achieve bio-functional applications, including transdermal drug delivery, biosensing and biofluid extraction in conformal and painless manner. However, challenges still remain as miniaturized size of current MN device limited its capability to perform high dosage drug delivery and diagnostic purposes with wider skin coverage. Moreover, current flexible substrate only offers bidirectional conformity such that skin areas with higher degree of complexity (elbow etc.) cannot be addressed. In this chapter, an ancient fish armour system-inspired composition of flexible MN system is proposed. The MN patch was fabricated by introducing a kirigami-based auxetic cut pattern into flexible base substrate, followed by integration of segmented MN subunits. The proposed MN system demonstrated significant enhancement in contact stability, skin penetration and drug delivery efficiency through numerical and experimental evaluations. Moreover, proof-of-concept of novel flexible MN patch fabrication using low-cost 3D printing is also presented. High customizability and improved performance of the proposed MN system have elevated applicability of MN technology in more diverse biomedical applications.

*This section filed technical disclosure (TD) substantially as Design and Fabrication Method of Flexible and Adaptive Microneedle Patches Thereof. Ref no: 2021-528.

4.1 Introduction

Skin is the largest and most available organ of human body which allows extraction or transport of molecules in various biofunctional applications which include drug delivery for therapeutic purpose, blood or biofluid extraction for diagnosis and health monitoring purpose[1-4]. Invasive parenteral routes such as intravenous and subcutaneous needle administration of therapeutic delivery and blood sample collection are still the primary consideration during clinical attendance up to now since drug delivery and acquisition of analytes through direct contact to blood circulation can be more effective[5]. However, invasive nature of parenteral needle administration brings discomfort and infection throughout the medical procedure, likely to cause delayed or avoidance of necessary medical attention. To note, statistics have indicated that more than 50% of children and 10% of adults are suffering from trypanophobia (needle phobia)[6]. Although efforts like capillary blood microsampling[7] which intended to draw minimal amounts of blood through intradermal prick were developed, they were still inevitably invasive enough to trigger pain receptors.

Continual increase of chronic disease cases and primacy of patient's welfare have encouraged development of non-invasive transdermal drug delivery and diagnostic techniques such that these purposes could be achieved without damaging skin barrier[8, 9]. From a global sense, advancement of transdermal drug delivery system can be generalized into three generations, from first generation systems that deliver drugs purely depending on molecular diffusion across multi-layered skin barrier with little or no permeation augmentor; through second generation that developed skin permeation enhancer for active or boosted passive transport of small molecules; to third generation that offers transport of relatively wider variety of drug types through stronger disruption to stratum corneum barrier[10]. Rationally, approaches to enhance skin permeation in second generation systems like Azone[11], sonophoresis[12] and iontophoresis[13] could only improve transport of small molecules while also reported to be associated with potential skin irritation[10], therefore displayed

minimal impact on self-administrable vaccination development and driven invention of more effective system, in this case, MN technology.

MN system comprises two parts, tip region which normally fabricated in a collection of 4-100 multi-needles, and a base substrate at the bottom to hold these MNs in predetermined orientation for self-administration purpose. Majority of MN systems however, were studied and developed based on rigid substrates where most of the time are monolithic with the tip material[14-16]. Hence, this may lead to interfacial contact issues where the MN array cannot conform well onto viscoelastic-like human skin with curved surfaces as shown in **Figure 4-1**. While delivery dosage or signal sensitivity of transdermal drug delivery and biosensing mainly depends on contact condition between MN tips region and penetrated skin site, poor skin conformity due to base rigidity would induce adverse effect on device performance like under-desired therapeutic outcome[17] and inconsistent signal recording. It is true that some acute applications only require MN administration on small area of skin or those with large curvature radii like chest or upper arm (ECG electrodes[18], vaccination[19, 20] etc.), which may show insignificant advantage of flexible substrate over rigid substrate. However, for long term applications like chronic wound healing[21] or health monitoring, rigid base substrate without flexibility and conformity may cause delamination or shearing of MN against the skin and lead to noticeable pain.

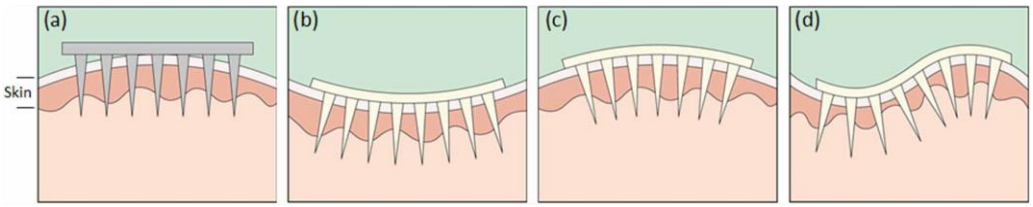

Figure 4-1 Comparison of skin contact condition. A. rigid substrate. B-D. Flexible substrate [22].

Flexible substrates have then been explored to address contact issue in various MN-related applications. Typical materials used for flexible substrate fabrications are silicone rubber, polyurethane, polyimide or biodegradable

materials like Poly(ethylene glycol) diacrylate(PEGDA), Polyvinyl alcohol (PVA) and polyvinylpyrrolidone (PVP)[22] where the MN arrays can be assembled either through direct formation of MN on these flexible sheets using lithography[23, 24] or to be casted as backing layer after casting MNs through micromolding[17, 25]. However, most flexible MN studies up to now are designed with flexible and continuous substrates which only offer effective bi-directional flexibility. Dimensional upscaling of MN patch is predictable in the future to increase drug loading volume for high dose drug delivery and expand skin coverage of biosensing devices for health monitoring purpose therefore could be inapplicable for higher degree of curvatures like elbow, knee joint and shoulder. In recent years, flexible and patterned substrates for MN fabrication have been gradually adapted in some applications that require complex conformity, for example neural signal recording on the brain[26] and long term ECG/EMG recording[18]. Still, the conformal capabilities of these designs were not studied systematically therefore their improvement over conventional flexible continuous substrates are still poorly understood.

To address the above problem, a base substrate that is highly flexible, conformal and not compromising penetration efficiency of the rigid MN tips is needed. Inspired by natural fish armour which possesses aligned segmented rigid fish scale units on a flexible patterned tissue[27], a flexible MN patch is adapted in the system where segmented individual MNs were to be assembled onto a kirigami-based auxetic fractal cut patterned substrate that able to conform omni-directionally onto human skin. Fractal cut design is basically segmenting a flat sheet into subunits with repeating hierarchy cut patterns and only connected through hinges such that these hinges could endure most of the high uniaxial or biaxial deformation while subunits can conform well onto surfaces[28, 29]. Due to its unique strain behavior, it has been wide explored in various highly-deformable devices like wearable battery[30], footwear support[31], tissue engineering[32] and strain sensor[33] among others. The conceptual design of bioinspired flexible MN patch is as shown in **Figure 4-2C**.

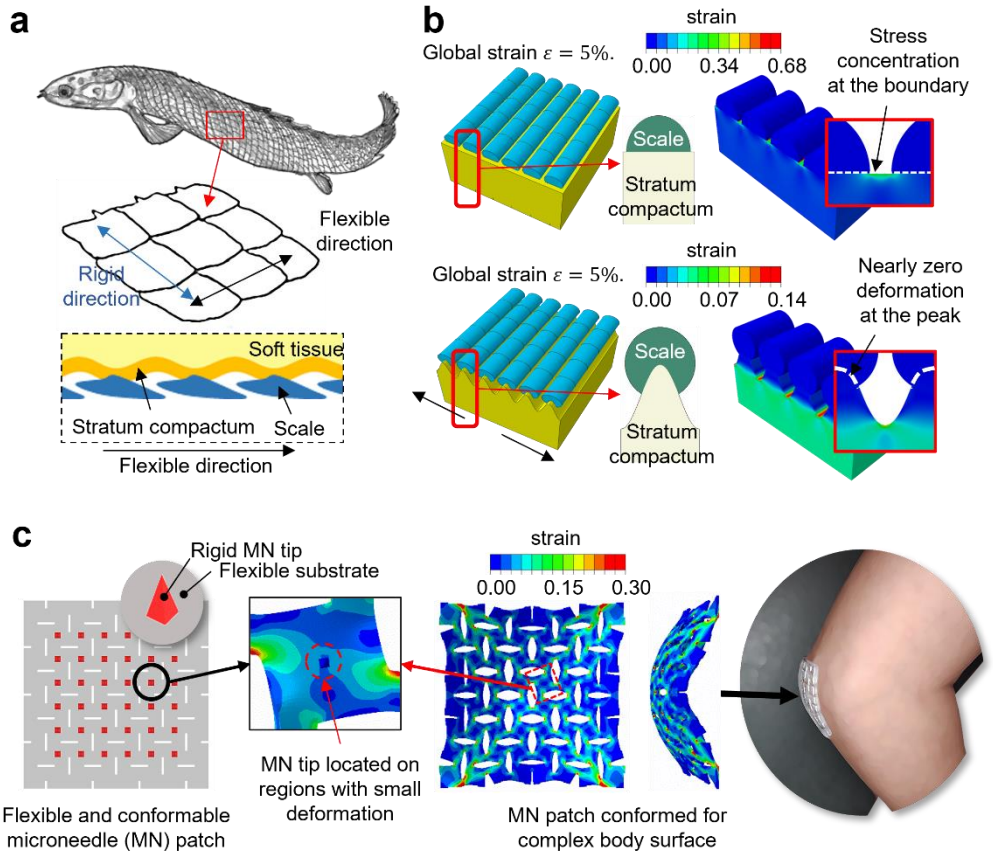

Figure 4-2 Fish armour inspired flexible patterned MN system. A. Fish scale alignment on a curvy and patterned tissue. B. FEM models showing deformation behavior and stress concentration of wavy tissues with segmented fish scale subunits[27]. C. Schematic representation of bioinspired flexible MN patch with omni-directional conformity and minimal MN delamination.

In this chapter, fabrication, characterization and evaluation of fractal cut MN patch is presented through computational and experimental approaches. First, the deformation mechanism of designed fractal cut substrate was predicted using finite element model (FEM) to find optimal location for MN allocation (low strain) such that minimal delamination of MN is expected during stretching. Potential soft-hard interfacial stress concentration was also visualized using FEM model where MNs were attached on predetermined location on the subunits, presenting in comparison to that of conventional rigid and flexible continuous substrate. Conformity of the substrates were also evaluated using simple elbow model so their penetration efficiency can be correlated. In experimental aspect,

three step fabrication of flexible MN patch is proposed, which includes preparation of flexible and rigid substrates through 3D printing, followed by segmentation of casted MNs, and finally assembled the parts into fully functional MN patch. To review functionality of this system, static and dynamic conformity test, *in vitro* conformity and penetration test, *in vivo* insulin delivery test were compared across three groups. Furthermore, by exploiting bottom up configuration of vat polymerization, two step multi-material printing of flexible substrate-MN tips can be achieved with high precision. Subsequently, adhesion force between MN and substrate were characterized after post processing to assure intactness of the soft-hard interface. On the whole, this method provides systematic characterization of highly flexible and conformal MN patch using hybrid fabrication of 3D printing and micromolding method to enhance penetration efficiency of existing MN platform through addressing skin contact stability issue.

4.2 Material and methods

4.2.1 Materials

Hyaluronic acid sodium salt (molecular weight ≈ 40-60kDa) was purchased from Zhonglan Industry (China). Poly (lactic acid) (3mm granule), human recombinant insulin, diphenyl(2,4,6-trimethylbenzoyl)phosphine oxide (TPO) and isobornyl acrylate (IBOA) were purchased from Sigma Aldrich (USA). Agilus 30 FLX935 photocurable resin was purchased from R&D technologies (USA) for polyjet printing of flexible base substrates while epoxy aliphatic acrylalte (EAA, Ebercyl 113) and aliphatic urethane diacrylate (AUD, Ebercyl 8413) were purchased from Allnex (Malaysia) for the development of DLP printable flexible substrate. Poly(dimethylsiloxane) (Sylgard^{TM}184) purchased from Dow Corning (USA) and agarose provided by Vivantis (Malaysia) were used for the fabrication of PDMS-agarose skin substitute. FluoSphere^{TM} carboxylate-modified microsphere (0.2µm) was purchased from Thermofisher (USA). Detection and validation of insulin presence in *in vivo* drug

delivery test was conducted using insulin ELISA kit purchased from CrystalChem (USA). All chemicals were used without further purification.

4.2.2 Computational modeling

Numerical simulations were conducted using 3D finite element modeling (FEM) in ABAQUS/Standard 2017®. As shown in **Figure 4-3A**, the fractal cut patch was designed with 8x8 subunits where adjacent subunits were connected by four alternatively repeating hinges at the corners with dimension of 1.7 x 0.25mm^2. The whole square patch was designed with side length of 4.24 cm which is dimensionally more than 3 times larger than that of conventional MN patch in order to evaluate conformity of such large patch on curved surfaces. Since typical flexible and stretchable materials usually exhibit rubber-like properties[34], the matrix material was assumed to follow classic neo-Hookean hyperelastic model wherein the coefficients were derived experimentally from elastic modulus of the polyjet material used. Briefly, strain energy density of neo-Hookean model is formulated as follow:

$$U = C_{10}\left(\left(J^{-\frac{1}{3}}\lambda_1\right)^2 + \left(J^{-\frac{1}{3}}\lambda_2\right)^2 + \left(J^{-\frac{1}{3}}\lambda_3\right)^2 - 3\right) + \frac{1}{D_1}(J-1)^2 \quad [34]$$

where U is the elastic strain energy per unit reference volume; λ_1, λ_2 and λ_3 are three principal stretches; and J is the total volume ratio in which $J = \lambda_1\lambda_2\lambda_3$. In the model, coefficients C_{10} and D_1 are material dependent therefore should be characterized prior to numerical calculation. They can be experimentally obtained via conversion from shear modulus G and bulk modulus K_b using relationship below:

$$C_{10} = \frac{1}{2}G; \quad D_1 = \frac{2}{K_b} \quad [35]$$

where G and K_b can be directly derived from elastic modulus E through formulas $G = E / 2(1 + \upsilon)$ and $K_b = E / 3(1 - 2\upsilon)$ [35]. Assuming that the material is incompressible, Poisson's ratio υ was selected to be 0.475 in this study. On the other hand, resolution and accuracy of the analysis is determined by size and

shape of the mesh. Therefore, global mesh size in this study was fixed based on hinge width (0.25mm), which was the smallest feature in the model so that deformation of the hinges can be considerably predicted without compromising computational cost. In addition, an adaptive mesh element of solid eight-node brick element with reduced integration (C3D8R) was applied for all parts.

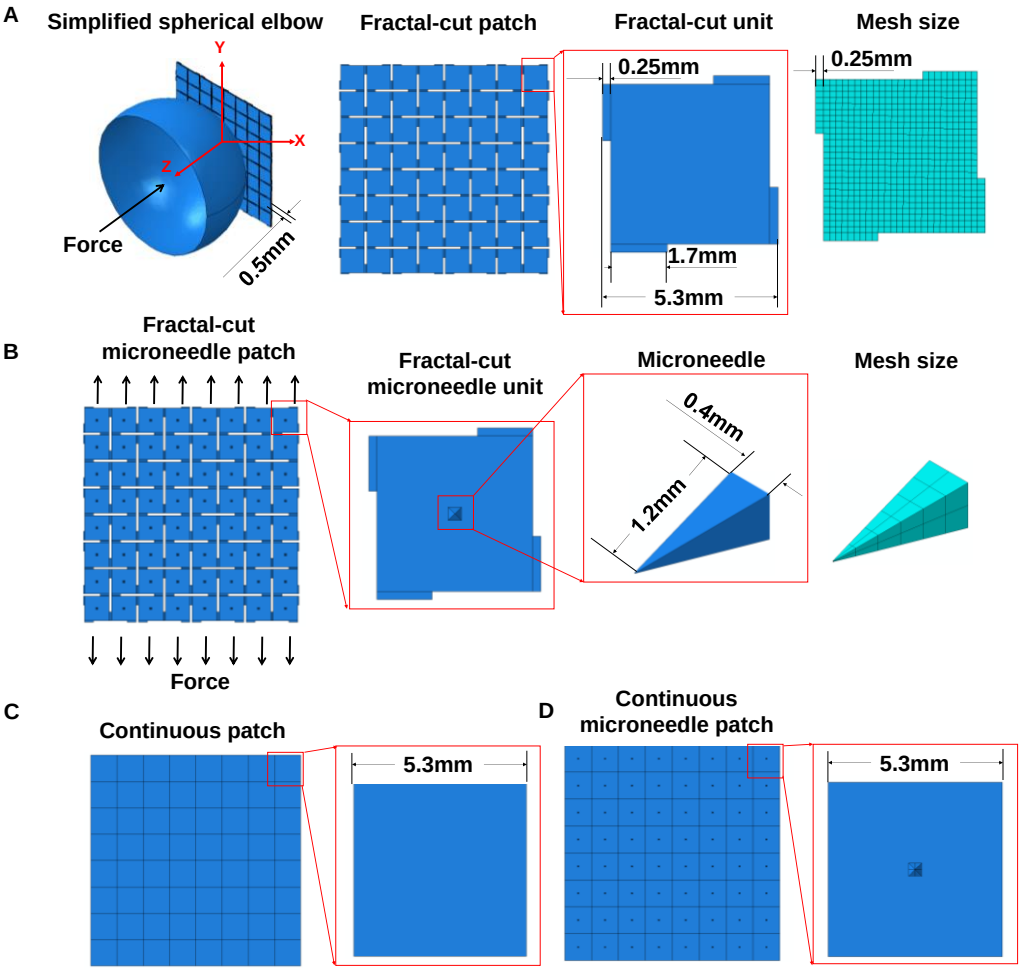

Figure 4-3 Schematic representation of FEM designs. A. Simplified elbow model (left), design of fractal cut patch, dimension of fractal cut subunit and indication of mesh size. B. In-plane stretching of flexible substrates (left), MN allocation, MN dimension and meshing. C. Illustration of 8x8 rigid and flexible continuous patches. D. Flexible continuous MN patch with MN allocations.

4.2.2.1 Conformity test on simplified elbow model

The actual human elbow has very complex convex profile, displaying a tremendous curvature changes in three-dimensional space[36]. Due to continuously varied morphing mode of human elbow which could cause difficulty in obtaining proper meshes, a simplified spherical analytical rigid model with radius of 24.9mm was proposed to mimick a young men's elbow in the largest curving angle. In this study, wrapping efficiency of conventional rigid continuous (RC), flexible continuous (FC) and flexible fractal cut (FF) patches onto the proposed simplified elbow model were compared. For fair comparison, all three substrates were modelled with the same dimension of 4.24 x 4.24 x 0.05cm^3 as reference to flexible fractal cut patch. FC and FF were assigned with the same material properties to characterize conformity difference with the presence of fractal cut design. On the other hand, hyaluronic acid (HA) was assigned as the rigid material to model RC base substrate where elastic modulus of 0.62GPa was obtained experimentally, assuming the Poisson's ratio to be 0.4. As illustrated in **Figure 4-3A and C**, four corners of all three substrates were fixed such that no displacements and rotations were allowed. Next, a reference point was defined at the top surface-centre position of the analytical rigid elbow model. A 0.4N force were then exerted onto the reference point in Z-axis towards the fixed substrates to mimick patch administration process. Wrapping or conformity efficiency of three substrates were presented as the total contact area between 64 subunits and simplified elbow model.

4.2.2.2 Effect of uniaxial stretching on MN attachment

Deformation experienced by flexible substrates during elbow conformity test were found to be composed of in-plane stretching and out-of-plane bending where stretching mode dominated the other. This may cause MN delamination when the adhesion force between rigid MN and flexible substrate is insufficient to overcome the interlaminar shear force induced by substrate stretching. Therefore, stretching deformation of MN attached flexible substrates (FC and FF) were studied where square pyramidal MNs with 1.2mm length and 0.4mm

base diameter were integrated at the center of all 64 subunits (**Figure 4-3B and D**). HA was assigned as the MN material with 6 meshes along the MN height axis. As illustrated in **Figure 4-3B**, in-plane deformation was simulated by applying uniform uniaxial force of 0.4N along one side while constraining displacement and rotation of the opposite side. The von Mises stress concentration was used as the indicator for any potential delamination. Briefly, if high von Mises stress (theoretical measure for yield fracture) is concentrated at location where MN and substrate are in contact, a higher chance of delamination is expected, vice versa.

4.2.3 Preparation of HA and PLA MNs array

Both HA and PLA MNs were prepared using micromolding technique as reported in chapter 3. Briefly, negative mold with 1x10 and 10x10 MNs were prepared by pouring PDMS in 1:10 w/w catalyst to prepolymer ratio into container immobilized with stainless steel MN templates. After degassing and overnight 70^{o}C curing, the solidified molds were trimmed and used for fabrication of MN arrays. HA MN was also fabricated as per discussed in chapter 3 where 60mg/ml of HA powder was fully dissolved in DI water before pouring into the negative mold. 0.5ml of HA solution was centrifuged at 4000rpm at 25^{o}C for 10 minutes until fully spun into individual tip wells. An additional 0.2ml HA solution was added into the wells after centrifuging to ensure no presence of hollow cavity in the wells after drying while having a sufficiently thin backing layer for the ease of segmentation procedure afterwards.

For the fabrication of PLA MNs, a pre-processing was proposed to obtain solid PLA MNs with thin backing layer. Briefly, the PLA pellets were placed on a glass slide and transferred to a heat vacuum oven at 200^{o}C for 1 hour. Subsequently, a ceramic weight (1.7kg) was pressed onto the melted PLAs for 2 hours until PLA thin films were formed. To extract the PLA thin films, a blade was used to carefully remove the adhered PLA films after overnight cooling of ceramic weight-PLA-glass slide at room temperature and pressure (rtp). The

extracted PLA thin films were then trimmed to fit exactly into the inverse pattern of 1x10 or 10x10 PDMS molds and were transferred to the 200^{o}C vacuum oven for 1 hours subsequently to melt the PLA thin films. Then, a -90kPa pressure was introduced into the oven for 2 hours such that the melted PLA could fill into individual wells to form MN shape while removing microbubbles formed in the array. Finally, the PLA MNs were removed from the molds after cooling.

4.2.4 Preparation of base substrates

To align with the computational model, three base substrates were prepared for experimental evaluation, namely rigid continuous (RC), flexible continuous (FC) and flexible fractal cut (FF) base substrate. FC and FF base substrates were prepared by polyjet printer Stratasys Objet 500 (Stratasys, USA) with rubber-like photopolymer (Agilus 30 FLX935). RC base substrate was prepared by trimming a bulk polypropylene (PP) board with ~1.5mm thickness which offered sufficient rigidity and appropriate ductility. All base substrates were prepared with dimensions of 4.24 x 4.24 x 0.15 cm^3 for fair comparison.

4.2.5 Assembling of rigid and flexible MN patches

To characterize substrate effect among three substrates, factors like MN material, MN design and allocation of MN (interspacing distance) were standardized across all groups, referencing that of FF base substrate. Biosafe adhesive glue was used to attach MNs onto predetermined locations with needle-to-needle interspacing distance of 5.3mm.

4.2.6 Preparation of elbow-shaped *in vitro* bilayer skin model

Three-dimensional contour of actual human elbow was chosen to represent complex curvature on human body for the conformity evaluation. The elbow morphology of a female volunteer was scanned using portable Structure Sensor Pro 3D scanner (Structure SDK, Occipital Inc., USA). The scanned object was in OBJ file extension which contained vertices' coordinates, vertices' directional vectors, texture mappings, and vertices' grouping for the formation of

polygonal faces. The OBJ file was then converted into STL format for the compatibility purpose for 3D printing using Blender software. Finally, the elbow model was 3D printed using selective laser sintering (SLS) printer EOS P396 (EOS, USA) with polyamide rigid white powder (PA2200). The casting mold was designed to have two parts, positive part with scanned elbow morphology and inverted negative parts with 3mm gap in between for material casting. To fabricate the bilayer skin model, 2.4wt% agarose was first dissolved in DI water through microwaving and poured into the negative casting mold subsequently. After covering with the positive casting mold, the enclosed molds were stored at 4^{o}C for 20 minutes until elbow-shaped gel was formed (**Figure 4-4**). Meanwhile,

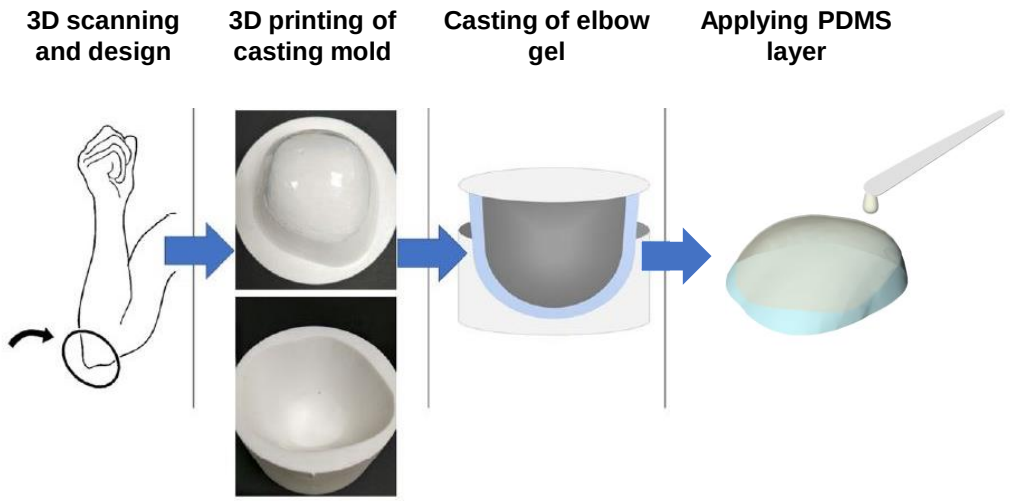

Figure 4-4 Schematic workflow to prepare elbow-shaped bilayer skin model

PDMS solution in 0.5:10 catalyst to prepolymer ratio was prepared and degassed. After the solidified gel was removed from the casting mold, 0.5ml PDMS solution was uniformly applied onto the gel surface to mimic stratum corneum (SC) layer. The PDMS-agarose elbow gel was then transferred to sealed container that quarterly filled with DI water to effectively cure PDMS layer at 70^{o}C while preventing excessive dehydration of agarose gel.

4.2.7 Functionality evaluation of fractal cut MN patches

4.2.7.1 Static and dynamic motion test

Objective of the static motion test was to evaluate conformity of RC, FC and FF MNs patch on human elbow model with different curvature ratios. Two regions were selected for this test where the curvature contours are as shown in **Figure 4-5**. To obtain information about the surface curvature, MATLAB was used to visualize the normal vectors on the STL surface from the scanned elbow image. An STL file is composed of triangular faces, each composed of three vertices x, y and z in the order defined by the right-hand convention. Then, the curvature of each triangular face can be defined in the following equation:

$$curvarture(x,y,z) = \frac{1}{R} = \frac{4A}{|x-y||y-z||z-x|}$$

where A is the area of the triangular face formed by the three vertices, x, y and z and |x-y| is the distance between points x and y. The curvature of each triangular face was calculated with MATLAB. Each MN patch was fabricated with 36 PLA MNs (6x6) while silicon rubber SE1700 (base: catalyst: mineral oil of 5: 0.2: 0.25) was casted as elbow substrate for testing due to high reusability. The number of MN subunits penetrated the silicon rubber layer were recorded and compared across three groups of MN patches.

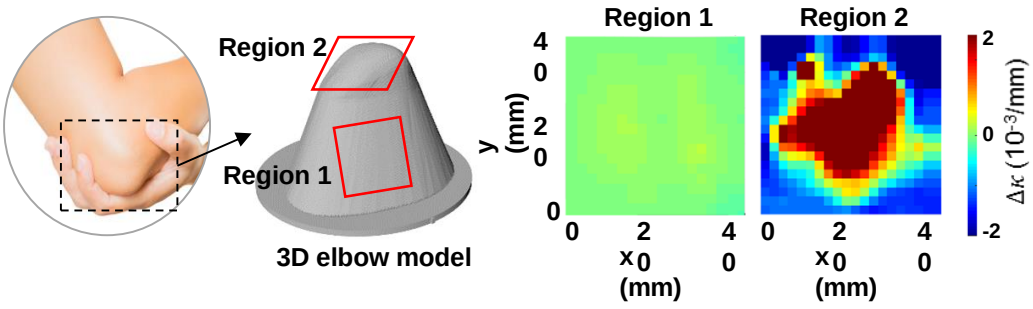

Figure 4-5 Selected regions for static and dynamic motion test. Contour of curvature variation was as shown on the right.

Dynamic motion test was conducted on elbows of 10 human volunteers with only base substrates due to the concern of sterilization and restriction of humane related experiments. Prior to the test, appropriate amounts of biosafe glue were applied onto each subunit of base substrates, presuming minimal patch detachment during extension and flexion motion of elbow. The base substrates were then applied onto the volunteers' elbow in extension position where olecranon was taken as the center reference point of the substrate positioning. Contact area between substrate and elbow was recorded as reference conformity where the same position was maintained for 10 minutes to assure proper attachment of the patch before bending their elbow to form 90^{o} angle (in flexion). After one cycle was completed, remaining areas of attachment were recorded and plotted as % contact area, normalized to 64 subunits.

4.2.7.2 *In vitro* penetration assessment

Penetration efficiency in terms of dissolution completion

RC, FC and FF MN patches were fabricated with 100 HA MNs/array where 1% Trypan blue was added into the HA matrix for better visual contrast during data acquisition. Monolayer 2.4wt% elbow-shaped agarose gel was casted and placed over the positive casting mold for mechanical support during MN patch administration. Each MN patch was applied onto the elbow gel for 3 minutes where the steepest corner was referenced for positioning the center of the patch. To differentiate different penetration conditions, each of the MNs were optically observed and sorted into non-, partially- and fully dissolved.

Penetration efficiency in terms of penetration depth

Furthermore, confocal microscope Zeiss LSM 800 (Zeiss, Germany) was employed to quantify penetration depth of MNs at different locations on the patch as this could provide better insight of the overall performance of a large MN patch with proposed substrate design. Bilayered elbow model was prepared and placed over positive casting mold for better handling as per discussed. As

illustrated in **Figure 4-6A**, A MN patch was categorized into inner, middle and outer regions such that penetration efficiency of different patch region could be compared and analyzed separately among three substrate designs. In this study, 4, 20 and 36 PLA MNs were attached onto inner, middle and outer region of all three base substrates respectively. Each patch was applied onto the PDMS-agarose model for 30 seconds before removal. Upon removal, all penetrated sites on the right column and bottom row were extracted for analysis (**Figure 4-6B**). To visualize the penetration depth, 2.5µL of 2% Fluospheres^{TM} dye was added onto each extracted gels for 3 seconds and wiped off afterwards to avoid signal saturation during imaging. Finally, the 3D morphology of penetrated sites was acquired through z stack scanning at 10µm interval and merged for depth measurement using ImageJ software.

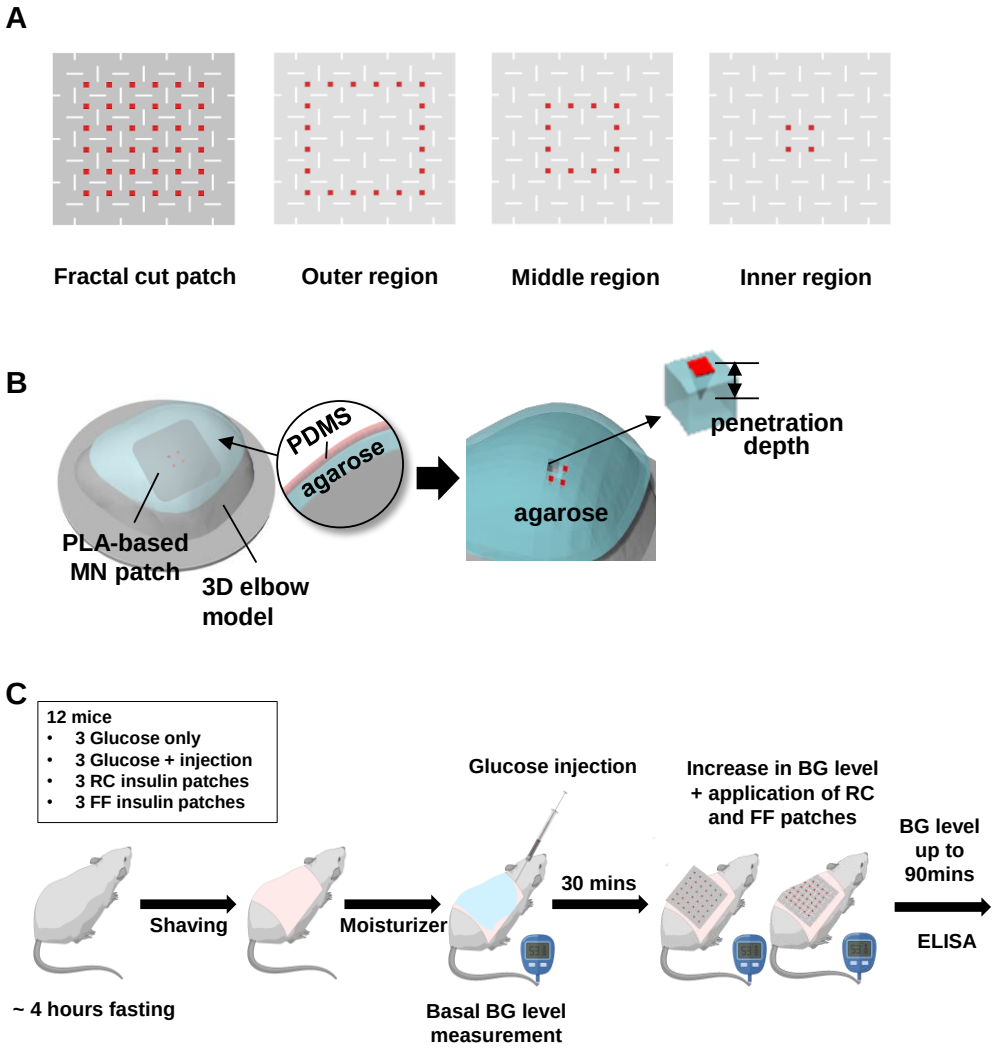

Figure 4-6 A. Three regions defined for *in vitro* penetration efficiency test as compared to full MN attached fractal cut patch. B. Schematic representation of gel extraction after patch administration onto bilayer elbow gel to quantify penetration depth of individual penetrated sites. C. Schematic representation of procedures to execute *in vivo* insulin delivery test

4.2.7.3 *In vivo* insulin delivery test

Preparation of insulin loaded HA MNs

In this study, insulin delivery of RC and FF base substrates were compared. Briefly, insulin solution was loaded into HA solution at 4^{o}C with gentle agitation for 2 minutes. The solutions were then stored in a vacuum

container at 4^{o}C overnight to eliminate microbubbles. 0.2ml of HA-insulin solution was transferred into the PDMS mold and centrifuged (4000rpm) for 5 minutes at 4^{o}C. Excess insulin-HA solution was scraped from the mold such that only the MNs region was loaded with insulin and avoided material wastage. The PDMS mold was stored at 4^{o}C for 1 hour before subsequent insulin-HA casting. A total of 7 insulin-HA layers were added, centrifuged and dried in desiccant chamber at 4^{o}C with 1 hour interval. After that, 0.2ml of pure HA solution was added to form thin backing layer. Throughout the casting and segmentation processes, insulin-HA MNs were stored at 4^{o}C to preserve its functionality.

Preparation of insulin loaded RC and FF MN patches

For the fabrication of insulin loaded MN patches, total of 6x6 subunits were attached with MNs. To ensure sufficient dose of insulin (1 IU) could be loaded onto the MN patch, each MN subunit was prepared with 4 MNs (in total of 144 MNs/array). Besides that, as the mice back was significantly narrower than that of the human elbow, the base substrates were scaled down with dimensions of 3 x 3 x 0.5 cm^{3}. The patches were applied onto the mice by stretching mice skin onto a rigid surface and with the help of a homemade applicator due to soft mice abdomen and elastic nature of mice skin. In addition, rigid supports made from polypropylene with length of two fractal cut subunits were attached to the back of the fractal cut substrates such that sufficient force can be exerted on the subunits to effectively penetrate insulin-loaded HA MNs during administration.

***In vivo* monitoring of blood glucose level and insulin on mice model**

The animal experiment was conducted on 6 weeks old C57BL/6 female mice where 12 mice were allocated for four experimental groups, including basal insulin group (no treatment), insulin injection group, RC and FF groups. As illustrated in **Figure 4-6C**, the mice were fasted for 4 hours before the test. Mice assigned for RC and FF were pre-shaved and anesthetized with isoflurane (Vetpharma, Spain) where 0.2ml of commercial moisturizer Nivea express

hydration body lotion (Nivea, Germany) were applied 30 minutes prior to topical application of MN patch to improve moisture content of the dorsal skin. Then, basal blood glucose (BG) levels of all mice were measured with commercial glucose meter Freestyle Optimum Neo (Abbott, USA) through blood extraction from mice tail veins. Subsequently, 0.4ml of 10% glucose solution was injected intraperitoneally into all mice. The change in blood glucose level was measured 30 minutes after the glucose injection. Then, intraperitoneal injection of 1U insulin and administration of insulin patches were executed to corresponding mice groups. BG level was measured every 30 minutes afterwards up to 90 minutes time point. At the endpoint, all mice were subjected to blood collection such that the existence of delivered human insulin can be verified using ELISA kit (**Figure 4-6C**).

4.2.8 Statistical analysis

Each experiment was conducted with samples $n \geqslant 3$. All datas were presented in mean $\pm$ SD or otherwise as specified. Significances were accessed with one way analysis of ANOVA or student t-test to determine p value using Microsoft® Excel®. In all cases, p value <0.05 was considered statistically significant.

4.3 Results and discussion

4.3.1 Computational model

In previous studies, drug loading volume in drug delivery and skin coverage in diagnostic setup were limited by MN patch dimension, which was intrinsically constrained by the rigidity of the base substrate. Even though base substrate flexibility was shown to improve uniform penetration of most existing MN systems, we hypothesized that MN systems with flexible and continuous base substrate is insufficient to adapt onto skin surfaces with higher degree of curvature variation, considering that increase of patch dimension is prospective in future MN market. Interestingly, groovy or wavy patterns were observed on fish skin tissues of ancient fish species at microscopic scale, providing high body flexibility for movement without inducing catastrophic structural deformation. Therefore, repeating hierarchy cut pattern was introduced into the flexible base substrate, which has displayed its pluripotency in development of new wearable technologies. An ideal flexible MN system comprises of two key criteria: 1) stretching and patch compliance onto skin surface; 2) patch adherence on skin during dynamic motion. However, excessive stretching of fractal cut substrate may cause out-of-plane bending and affect MN orientation angle, causing undesired complexity to skin penetration. Moreover, stretching of fractal cut could induce disruptive shearing force between MN and base substrate, inducing risk of MN delamination during dynamic motion.

To predict deformation behavior of fractal cut patch under stretching and its interaction with MN attachment, FE model was employed. First, the base substrates without MN attachment were used for stretching simulation. As shown in **Figure 4-7A**, a simplified elbow model was applied against RC, FC and FF base substrates at 0.4N where the strain distributions were mapped in contour graphs. High rigidity of RC material inhibited effective deformation of the substrate to conform against the sphere with less than 20% strain observed. For FC case, hyperelasticity of the material enabled stretching of substrate against

the spherical model where the strain was distributed uniformly throughout neighbouring subunits. The strain intensity was also observed to increase diagonally towards the pinned corners due to reaction force. For FF case, the side view revealed a higher degree of conformity under the same exerted force as compared to FC case which was attributed to the higher flexibility offered by the cut pattern. From the top view, most of the strain was observed to concentrate in the connecting hinges at the corners, inducing in-plane rotation with minimal strain (<10%) in the middle of individual subunit. Contact areas between substrates and spherical elbow model were plotted in **Figure 4-7B** where FF substrate exhibited the highest among all (~90%). 10% disconnection was mainly of those subunits at the edges which were constrained by the pinned corners, thus higher contact area should be expected with unpinned corners. Since spherical elbow was modelled as analytical rigid and no deformation was observed in RC substrate, the contact area for RC case was plotted as 0%, suggesting that the contact mode between them was merely point contact. On the other hand, although FC was modelled with hyperelastic properties, the graph only showed ~20% contact area. Because in most existing MN studies, ratio between skin curvature radius and patch dimension is high, presuming that MN patch were to be administered onto a flat surface. Therefore, this result indicates that at a low ratio of skin curvature radius: patch dimension (~0.6 in this study), poor conformity is expected with existing FC substrate design. Besides that, penetration efficiency of three substrates were also correlated based on the distance between centre point of each subunit (64 in total) and projected point on elbow model surface (**Figure 4-7C**). Penetration will be considered when distance between two points are less than 1mm (MN length). According to the graph, FF substrate had the highest penetration efficiency (~70%) among all, followed by FC substrate with ~35% and finally RC substrate with less than 10%, suggesting that fractal cut substrate effectively improved penetration efficiency of MN systems. Out-of-plane bending of subunits were not observed in FF

substrate under stretching, indicating that the MNs can penetrate substrate at proper angle.

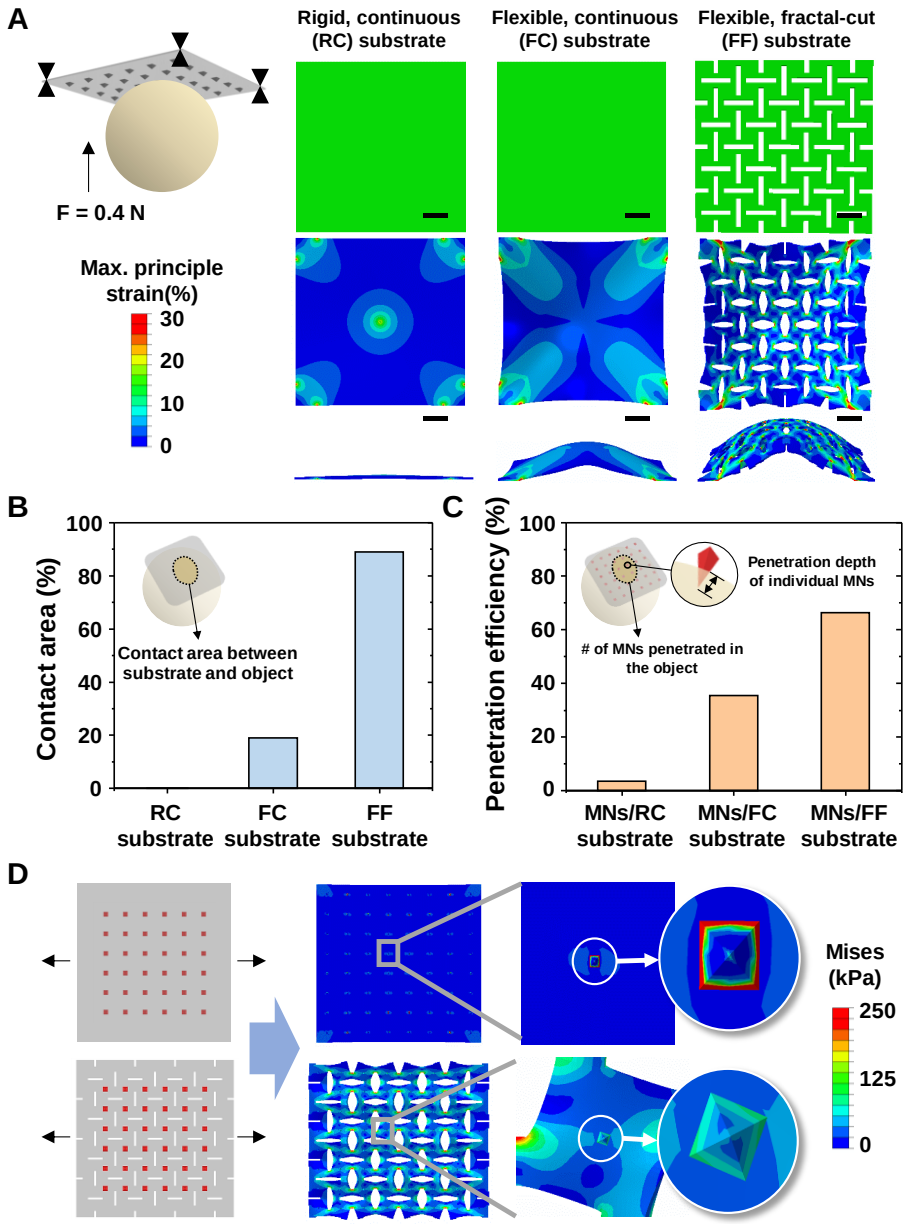

Figure 4-7 Computational modelling of RC, FC and FF base substrate. A. Assembly interaction of conformity test where a simplified spherical elbow model was pushed against three substrates, presented in strain contour graph. Scale bar = 1cm. B. Contact area (%) of three substrates against elbow model. C. Correlated penetration efficiency of three substrates applied onto spherical elbow model based on distance between individual subunits and projected sphere surface. D. Uniaxial stretching of FC and FF substrate with MN attachment at the centre of every subunit, presented in von Mises stress contour.

Deformation of individual subunits were further characterized by applying uniform uniaxial force of 0.4N along one side of FC and FF with the attachment of MNs (**Figure 4-7D**). Von Mises stress contour graphs showed high concentration of stress (~250kPa) around the base of MN tip on FC substrates. This is well aligned with the observation in previous study wherein the whole subunit tends to deform uniformly in FC base substrates. High shear stress induced between MN and FC base substrate has increased the risk of MN delamination with the increase of stretch rate, limiting stretchability of the system. On the other hand, most stress was observed to accumulate at the hinge region of FF substrate where less than 125kPa von Mises stress was observed around the base of the tip region. While most deformation occurred at the hinge regions, middle of the subunit had the least stress and stress accumulation, suggesting that MN attachment at the middle of each subunit enables the flexible MN system less likely to undergo interfacial delamination during patch stretching.

4.3.2 Fabrication of MN patches

Low molecular weight hyaluronic acid (HA) and poly(lactic) acid (PLA) are the typical biodegradable MN materials used in the development of rapid and long term dissolving MNs respectively. In the experimental section of our study, these MN materials were employed depending on experimental needs, both prepared using the same MN dimension of PDMS negative molds. **Figure 4-8A** showed SEM images of the casted PLA and HA MN arrays. Average dimension of PLA and HA MNs were as shown in **Table 4.1**. HA MNs had slightly lower dimensions due to inevitable volumetric shrinkage from air drying, yet not statistically significant to affect the functionality. As inspired by ancient fish armour where the co-existence of body flexibility and threat protection (rigid armour) are based on the alignment of individual fish scale subunits on the wavy tissue, the casted HA and PLA MN arrays were segmented using scalpel blade prior to patch assembling such that MN subunits were obtained. The assembling

procedure is as illustrated in **Figure 4-8B** which includes casting, segmentation and reassembling of segmented MNs onto substrate. Optical appearance of the segmented MN subunits and assembled RC, FC and FF MN patches were shown in **Figure 4-8C and D** where the interspacing distance of all substrates were marked carefully and fixed in reference to the FF subunits.

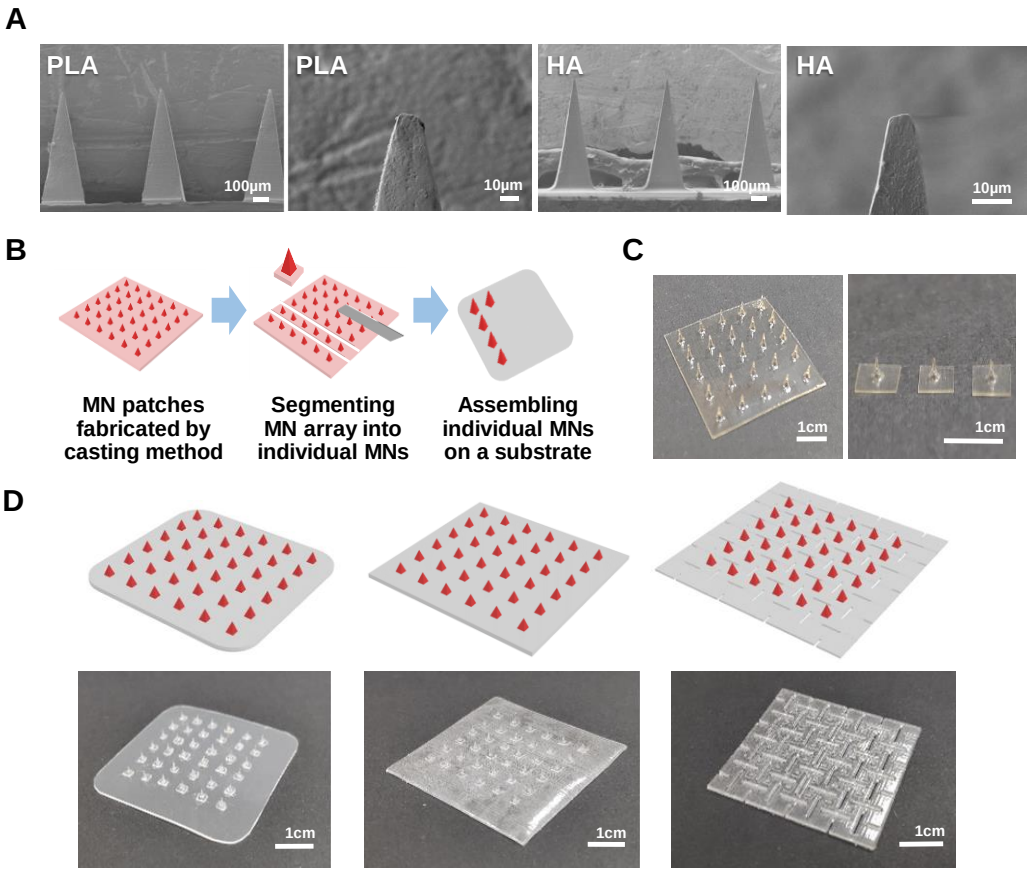

Figure 4-8 Fabrication process of RC, FC and FF MN patches. A. SEM images of 1x10 PLA and HA MN arrays. Scale bar = 100μm/10μm. B. Schematic representation of assembling process: casting, segmentation and reassembling. C. Optical image of segmented MNs. Scale bar = 1cm. D. Conceptual design and optical images of fabricated RC, FC and FF patches (from left to right). Scale bar = 1cm

Table 4-1 Dimensions of micromold casted PLA and HA MNs

Material	Length (μm)	Base diameter(μm)	Tip diameter(μm)
PLA	893.48 ± 7.65	303.26 ± 10.10	11.07 ± 2.09
HA	859.11 ± 2.06	295.16 ± 9.67	5.93 ± 0.57

4.3.3 Functionality evaluation of fractal cut MN patches

4.3.3.1 Static and dynamic motion test

According to **Figure 4-9A**, it was observed that RC patches had the least MNs penetrated in the PDMS layer for both regions due to poorest flexibility. As region 1 having a relatively simple curvature as compared to region 2, FC and FF patches showed similar conformity in region 1 however a larger variation in curvature led to significant difference in conformity, as reflected on the number of MNs penetrated in region 2 of FC and FF patches (**Figure 4-9B**).

Figure 4-9C has shown experimental procedures during dynamic motion test. Prior the test, the back surfaces of each base substrate were marked with 10x10 squares for assessment of contact area. After that, the volunteers faced their elbow upwards along with the base substrates applied with glue for 10 minutes until the glue dried completely. During the test, volunteers were asked to recover their elbow back to comfort position in extension. Subsequently, the volunteers slowly bent their elbow into flexion position (90^{o}). As human elbow radius and curvature varies from individuals, sub-areas adhering on the volunteers' elbow after bending were recorded as contact area remaining (%) as shown in **Figure 4-9D**. Full detachment of RC substrates were observed in flexion position while having the lowest contact area (%) in extension position as well due to the poor flexibility. Although FC was able to conform as well as FF substrate in extension position where the elbow surface was flattened, it still had lower area of contact in flexion position due to its limited flexibility. As a result, both static and dynamic tests showed superior performance of fractal cut design patches in terms of conformity on a complex geometry like human elbow. Even though the significantly enhanced contact stability of the FF substrate was successfully demonstrated through those tests, the penetration efficiency of MNs on the substrate wasn't directly evaluated. Thus, instead, the 3D elbow model consisting of bi-layered thin membranes were used for further MN assessments.

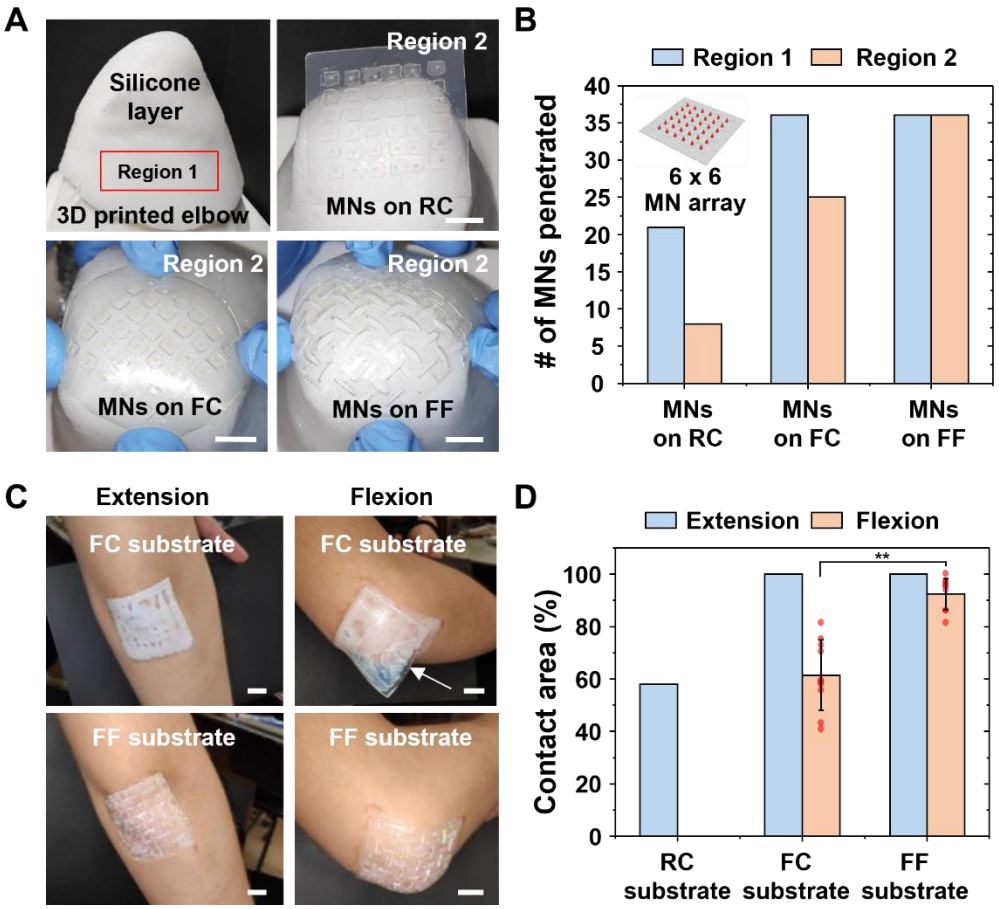

Figure 4-9 Static and dynamic motion test of RC, FC and FF base substrate on human volunteers. A. Optical images of static test where casted silicon rubber elbow model RC, FC and FF MN patches were applied onto region 2 of the silicon rubber casted elbow model. B. Number of RC, FC and FF MNs penetration recorded at region 1 and region 2 of elbow model. C. Experimental procedures in dynamic motion test. RC, FC and FF patches were glued onto volunteer's elbow. Scale bar = 1cm. D. Normalized contact area (%) of RC, FC and FF base substrates after one cycle from extension to flexion position. Error bars indicate standard deviation (n=10 for each substrate type). **p < 0.01 for contact area (%) of FC and FF substrates in flexion.

4.3.3.2 *In vitro* penetration assessment

Penetration efficiency in terms of dissolution condition

10 x 10 trypan blue loaded- HA MNs were attached onto RC, FC and FF patches to investigate their penetration efficiency in terms of dissolution

condition. Three levels of dissolution were defined where 'Fully' referred to complete dissolution of whole MN tip, 'Partially' referred to those MN that had remaining length after administration, and 'None' was for those MNs maintained their original length. Based on our previous studies, pure HA MNs were shown to be able to dissolve fully within a minute, therefore 3 minutes administration is sufficient for all MNs to dissolve fully depending on contact condition. According to **Figure 4-10**, less than 30% of MNs on RC patches were observed to penetrate the agarose elbow model due to their substrate rigidity. Among these, around 20 MNs located around the inner region of RC patches were shown to fully penetrate the agarose. On the other hand, although FC continuous (FC) patches were able to perform a certain degree of flexibility, ~20% of MNs were observed to penetrate partially while ~10% of all MNs were not in contact with the elbow model, suggesting insufficient flexibility from FC substrate design. On the other hand, more than 90% of all MNs on FF patches were shown to penetrate the agarose elbow model effectively and less than 5% of all MNs were not in contact with the gel. Interestingly, even though flexible fractal (FF) patches were able to conform well onto the elbow mold, slight portion of MNs (~10% of all MNs) were observed to penetrate the agarose mold partially, indicating that insertion angle of some MNs were not in normal (90^{o}) to the elbow surfaces due to mishandling during administration. During administration of FF patches, four corners of the patches were stretched with fingers to apply onto the substrate where forces exerted onto individual subunits may not be uniform, eventually affecting their contact condition.

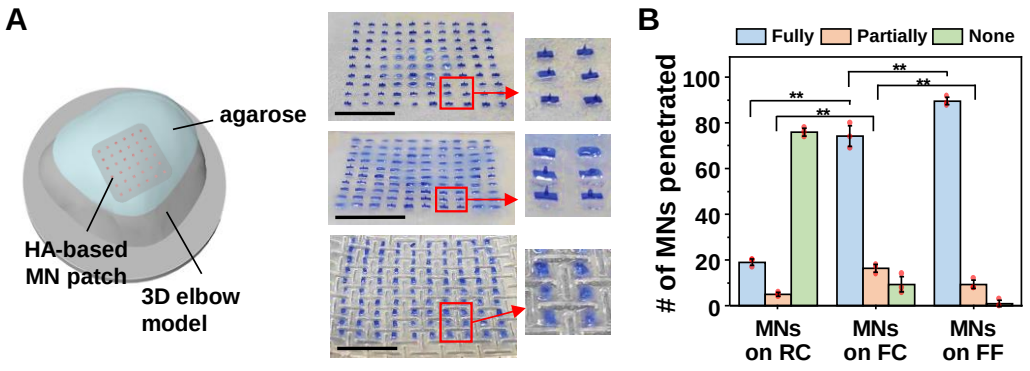

Figure 4-10 *In vitro* penetration test in terms of contact condition using monolayer agarose elbow model. A. Schematic representation of experimental procedure and MN patches after the test. B. Penetration efficiency in terms of dissolution condition. **p < 0.01 for numbers of MNs that fully or partially penetrate the agarose mold across all types of patches.

Penetration efficiency in terms of penetration depth

To effectively analyze and compare effect of substrate design on penetration efficiency, each substrate was further categorized into inner, middle and outer region where the penetration efficiency was presented in terms of penetration depth on PDMS-agarose bilayer elbow model as discussed earlier. In this study, PLA MN was used as the MN material due to highly sensitive requirement of transparency in confocal microscope. As HA MNs can rapidly dissolve in agarose model, debris from HA dissolution may scatters laser penetration and leads to inaccurate measurement. Therefore, PLA MN patches have served as the pre-treatment to create microchannels on the elbow gel and the depth of penetration holes were traced using fluorescent dye subsequently. **Figure 4-11** showed the top view and the merged Z-stack images of fluorescent dye traced PLA MNs penetration site. For RC case, penetrations were only observed in inner region. In contrast to previous study where HA MNs can be dissolved upon contact with highly hydrated monolayer agarose elbow model, both sufficient force and well aligned MN insertion angle are the key requirement in this study to effectively break PDMS layer for dye diffusion. Due to rigidity nature of RC base substrate, some MNs in the middle region went in contact with PDMS-agarose surface in a slanted angle, thus insufficient localized deformation was induced to cause fracture of PDMS layer. On the other hand, FC and FF MN patches showed penetration in both middle and outer region where inconsistency of penetration depth was observed for FC-middle region and FC-outer region groups. FF exhibited consistent penetration depth across three regions.

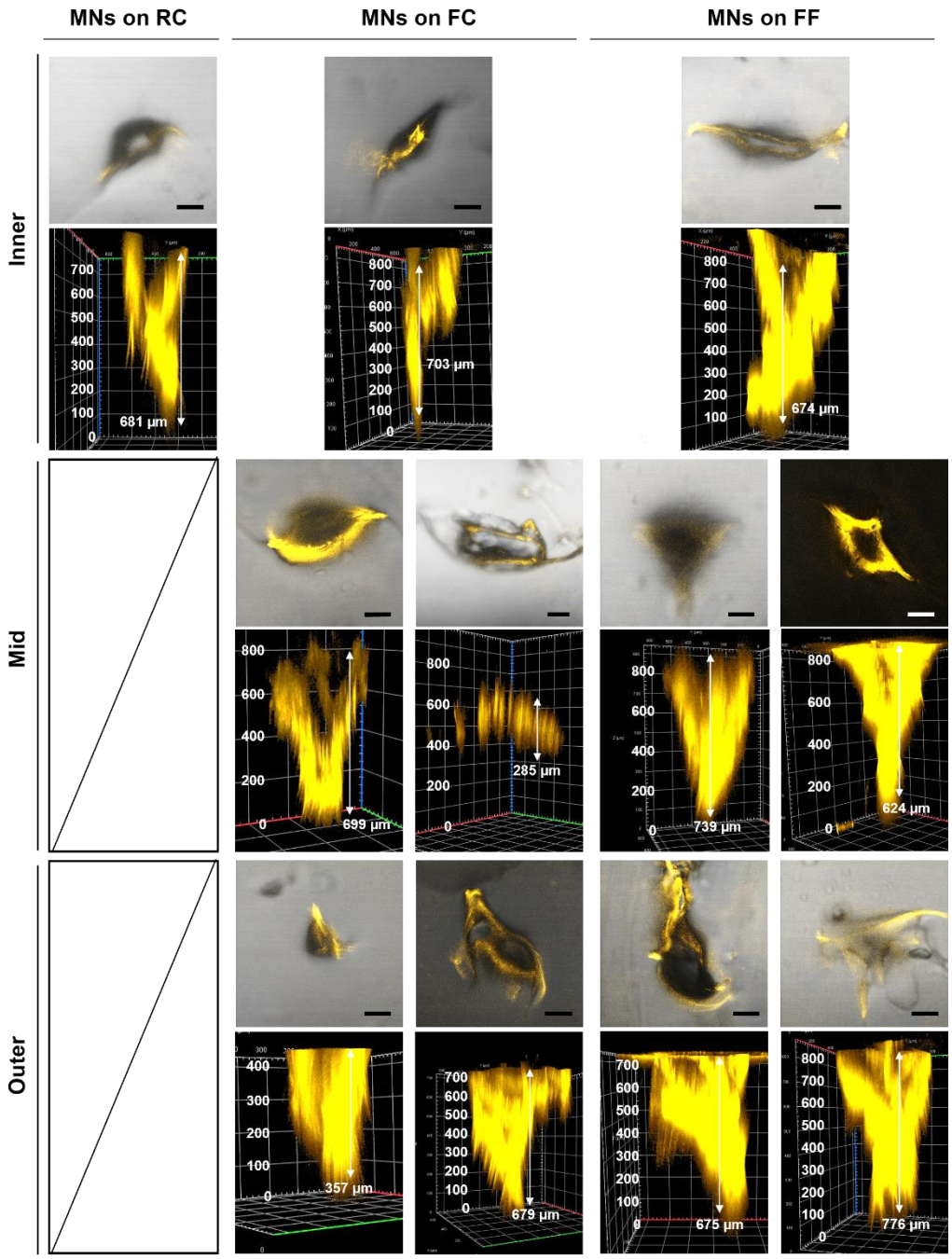

Figure 4-11 Top view and Z-stack confocal images of fluorescent dye in bilayer model penetrated by PLA MNs. Images categorized according to patch types (RC, FC or FF) and MN location (inner, middle or outer). Scale bar = 100µm

As shown in **Figure 4-12**, middle region samples of FC and FF were able to penetrate with depth ≥ 80%. Although ~10% depth difference and higher standard deviation were observed in FC case, FC and FF exhibited no statistical difference in penetration performance at the middle region. Still, MNs penetration at FF middle region should perform more consistently. For the outer region, FF exhibited slight drop in penetration depth as compared to inner and middle region, indicating that some MNs penetrated at a slightly slanted angle onto the elbow model. On the other hand, FC had a significant decline in penetration performance due to the limited flexibility and stretchability, reflected similarly to that of previous sections. To summarize, FF displayed the most consistent performance in terms of elbow model conformity and further evaluation of penetration depth, suggesting superior penetration efficiency than that of RC and existing FC substrates.

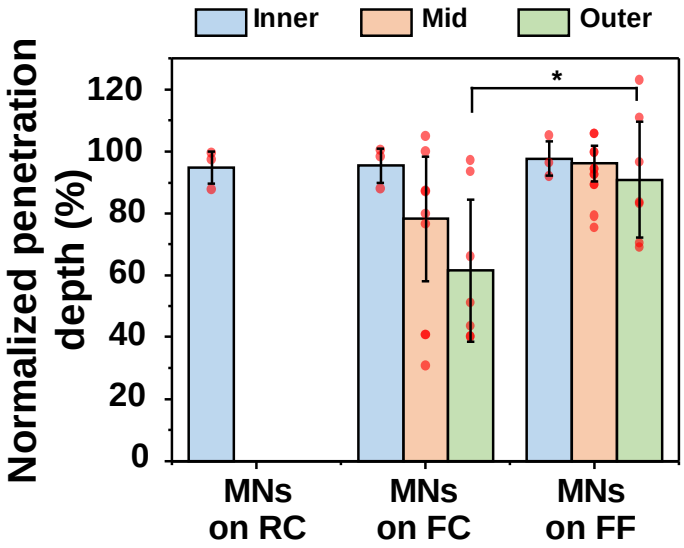

Figure 4-12 Penetration efficiency of RC, FC and FF MN patches based on positive correlation between penetration depth and patch conformity. Error bars indicate standard deviation (n=3 for inner region, n=5 for middle region, n=7 for outer region). **p < 0.01 for penetration depth of FC and FF outer MN patches.

4.3.3.3 *In vivo* insulin delivery test on mice

6 x 6 RC and FF base substrates with 4 MNs/subunit were prepared to delivery 1U insulin into mice to evaluate *in vivo* performance of proposed fractal cut substrate design. Effective MN administration of such large patch on mice skin is technically more challenging than that of human skin since human skin is firm and intactly adhere to the underlying tissues, whereas mice skin is loose and flexible[37-39]. Moreover, mice backspine offered very limited mechanical support during MN administration while excessive pressing force may injure the mice organ. Therefore, a 3cm x 3cm mice back area was pre-shaved and stretched out against rigid glass slide to provide sufficient mechanical support. Homemade applicator and polypropylene backing support were also introduced into the administration procedure to aid effective MN application of these large patches. After glucose injection and 30 minutes resting, RC and FF MN patches were applied onto the mice skin as shown in **Figure 4-13A**. From the side view, a large gap was clearly observed between RC substrate and curvy mice back, indicating insufficient conformity of the substrate onto mice skin. On the other hand, FF MN patch was observed to be conformal on the mice skin from the side view. The patches were applied onto the skin throughout the experiment until reaching the endpoint at 90minutes to imitate long term administration of MN patches. Upon endpoint, patches were removed from the mice back where top view of the penetration sites were as shown in **Figure 4-13B**. RC mice back only displayed partial penetration holes due to rigidity of the substrate thus failing to conform effectively onto curvy surface whereas FF mice back showed large area of penetration holes, suggesting better conformity exhibited by the flexible substrate.

Reduction in BG level was normalized to respective 0 minutes timepoint (30 minutes after the glucose injection) where all four experimental groups were plotted in **Figure 4-13C**. According to the graph, intraperitoneal (IP) insulin injection showed most effective BG level reduction at 30 minutes timepoint

(~80%) as expected due to direct contact of insulin with blood circulation. BG reduction of RC and FF at the same timepoint were shown to be ~40% and ~60% respectively. This indicates that insulin delivery of FF patches were more effective than that of RC, as reference to negative control group (no treatment). Compared to **Figure 4-13C** where the initial high glucose levels of all the treatment cases were normalized to be 100%, **Figure 4-13D** shows the reduction in glucose level, normalized by the normal glucose level, after insulin injection at two predetermined time duration, 30 mins and 60 mins. Since glucose was injected before insulin was treated, the glucose level was increased 2-3 times than its normal condition. Thus, during the initial 30 mins after insulin was introduced to the body, significant reduction in glucose was observed for all cases. Particularly, in case of IP insulin injection, reduction in glucose occurs abruptly by ~150%, pushing down the glucose level even below the normal condition within the 30 min duration. Interestingly, insulin delivered by FF exhibited rapid glucose reduction, recovering the original glucose level in the blood within 30 min. In case of RC, during the initial 30 min, the insulin delivery was almost negligible because the glucose reduction was comparable to that of the no treatment case. The delivered insulin from RC became more effective after 30 min, significantly reducing the glucose level compared with the no treatment case. From the previous *in vitro* results, we already confirmed that compared to FF, MNs of RC partially penetrated into the artificial tissue (**Figure 4-10 to 4-12**). Thus, MNs on FF more effectively delivered loaded insulin than those on RC, enabling recovery of glucose level within a short time being like the IP injection case. Moreover, still the insulin shock due to overdose of the direct insulin injection can be easily prevented by controlling the number of MNs[40, 41]. For both FF and RC, during the initial 30min, more mild glucose redcution was observed compared with the IP injection case, allowing insulin delivery to be kinectically controllable for minimal side effects.

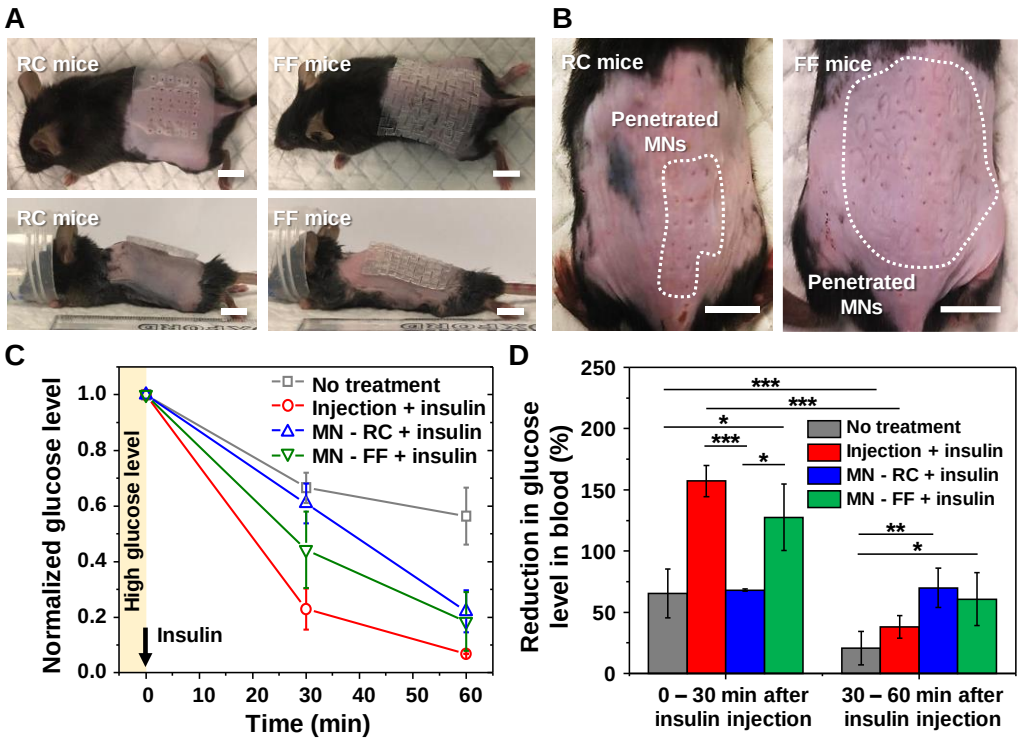

Figure 4-13 *In vivo* insulin delivery on mice using IP insulin injection, RC and FF substrates. A. Top view and side view of RC or FF MN patch application on mice. The mice were anesthetized at the moment. Scale bar = 0.5cm. B. Skin condition of mice back after RC and FF patch administration at endpoint (90 minutes). C. Normalized blood glucose reduction (%) of negative control, IP insulin injection, RC and FF insulin loaded MN patches. Black arrow indicates timepoint where insulin treatments were proceeded (30 minutes after glucose injection). D. Normalized amount of blood glucose reduced (%) at the first 30 minutes and 30-60 minutes after insulin treatment. IP injection and FF patch at first 30 minutes showed drastic blood glucose reduction rapid dissolution of HA MNs whereas NC and RC showed no significant difference.

4.3.4 Two-step fabrication of fractal cut patch using low cost 3D printing

Flexible fractal cut patch was shown to be a promising platform for transdermal drug delivery with improved conformity onto high curvature complexity surfaces like human elbow in previous studies. Yet, manufacturing cost, production time, scalability and regulatory framework are the key factors to consider during commercialization of MN technology[42]. With current

fabrication procedures of flexible fractal cut patch (casting, segmenting, reassembling), manual attachment of individual MN subunits may leads to contamination issues and batch-to-batch inconsistency due to human error. Moreover, drug stability due to prolonged exposure in air may also be affected through undesired oxidation and hydrolysis reactions[43] since reassembling step itself might take hours to complete. Therefore, an automated fabrication process is needed to enable efficient, highly precise, and customizable fractal cut MN patch in a drug-friendly environment.

3D printing MN fabrication is then a great candidate to date. As discussed in chapter 2, FDM, SLA, DLP and TPP are the key technologies that meet nano- to microscale resolution requirement of MN fabrication. Among them, digital light processing (DLP) has drawn our attention due to its considerable resolution, high material versatility, rapid prototyping and low cost characteristics. Therefore in this section, a novel multi-material printing of MN is reported in which flexible base substrate and assembling of individual MN subunits can be achieved with high spatial accuracy through sequential printing and vat switching. Evaluation of functionality will also be reported.

4.3.4.1 Fabrication and structural characterization of two-step printing

As proof of concept, a commercial resin plasGRAY was used as rigid MN material and a highly stretchable UV curable elastomer (SUV) was chosen for the printing of flexible base substrate. The SUV elastomer was prepared as per the protocol described by Patel *et al* [44]. Briefly, aliphatic urethane diacrylate (AUD) were first diluted in isobornyl acrylate (IBOA) before mixing to epoxy aliphatic acrylate (EAA) at 5:5 weight ratio at 70^{o}C. 2% w/w of photoinitiator TPO was then added to the mixture and covered in aluminium foil until fully dissolved. Before transferring to a detachable resin vat, the fully mixed SUV resin was left for cooling until room temperature. On the other hand, plasGRAY resin was used without further modification.

General fabrication process was as illustrated in **Figure 4-14A**. The printing stage of MAX X UV385 printer (ASIGA, Australia) performed the first calibration in which the build platform was adjusted until it reached the transparent window and set as zero position. After SUV resin vat was loaded, 10 x 6 FF base substrate with subunit length of 5.3mm and 0.5mm thickness, in addition to two sacrificial test strips on both sides were printed. The printed samples were then washed with isopropanol (IPA) to remove unreacted resin residual. The printed sample was adhered on the build platform throughout the washing process. Next, sacrificial test strips were extracted from the building platform for subsequent calibration. Since cured sample thickness could vary from batch to batch around 0.1-0.5mm, additional printing of test strips could provide accurate calibration to ensure the MN layer could be in good contact with the base substrate. The second calibration were performed similarly and measured thickness of base substrate was taken into account, which made the base substrate surface as zero position in this case. Subsequent printing started after switching to plasGRAY resin vat. The MN was designed to be conical shape, 1.2mm length, 0.6mm base diameter and 20μm tip diameter with 0.1mm backing layer. The printed FF MN patch was removed from the build platform after the print and post processed with 10 minutes sonication in IPA and 3 minutes UV curing.

Structural characterization of printed SUV FF base substrate and MN patch were shown in **Figure 4-14B**. The printed SUV FF base substrate was highly stretchable with in-plane rotation observed, similar to that of polyjet printed FF base substrate (**Figure 4-14B(i)**). Elastic modulus and elongation at break of SUV measured from tensile test was ~3 ± 0.04 MPa and ~200% which is comparable to literature values[44]. On the other hand, surface morphology of printed FF subunit was as shown in **Figure 4-14B(ii-iii)** where micro-roughness can be clearly seen in the magnified view. Two-step printed FF MN patch was as shown in **Figure 4-14B(iv)** where all MNs were successfully printed onto the designated centre of subunits. Interfacial surface between plasGRAY and SUV

were further characterized through SEM (**Figure 4-14B(v-vi)**). The interfacial adhesion was seen to be continuous, indicating that the thickness across the SUV base substrate was uniform thus all MNs could be well-printed.

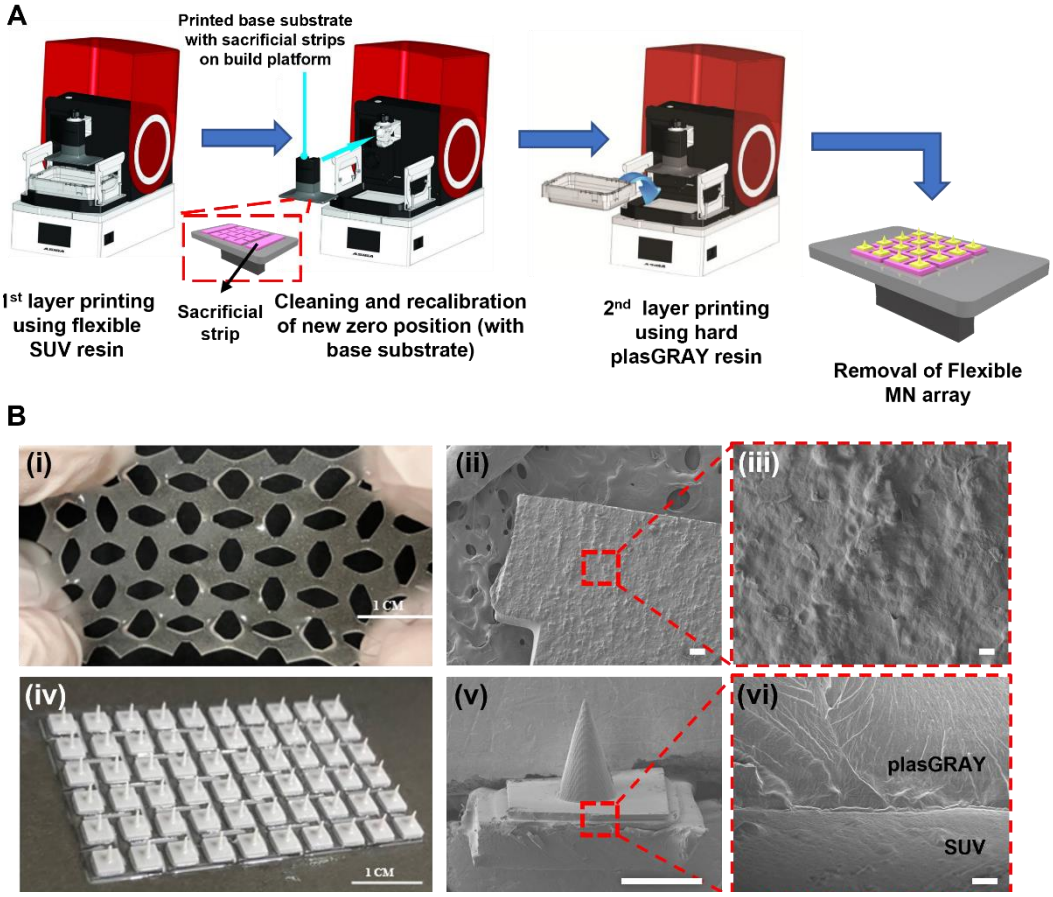

Figure 4-14 Fabrication and characterization of flexible fractal cut MN patch using DLP printing. A. Schematic illustration of two-step multi-material printing of flexible MN patch. B. Structural characterization of SUV substrate and MN integrated array. (i) Optical image of stretched SUV FF base substrate. Scale bar = 1cm. (ii) SEM image of single SUV FF subunit, and (iii) magnified view of red bracket. Scale bar = 100/10µm. (iv) Optical image of DLP printed FF MN patch. Scale bar = 1cm. (v) SEM image of single two-step printed MN on single FF subunit, and (vi) magnified view of SUV/plasGRAY interface. Scale bar = 1000/10µm.

4.3.4.2 Functionality tests and prospect of flexible fractal cut MN system

During conventional RC MN patch administration, we usually presume that the skin surface is sufficiently flat such that all MNs could penetrate in

normal direction. However, for flexible MNs patches which requires adaptation to bi- or omni-directional skin curvature complexity, MN delamination could occur in the case of mishandling (slanted insertion angle). Although proper patch application protocol and ultra-flexible patch like FF design could overcome the issue, it is still important to understand interfacial adhesion force between hard-soft materials since complex mix of shear and axial forces are expected to be exerted onto MNs due to dynamic movements in long term applications (slow drug release or *in situ* bioanalysis)[45]. To characterize the interlayer adhesion force, a rigid-soft-rigid sandwich tensile coupon was fabricated (**Figure 4-15A(i)**)[46, 47]. PlasGRAY blocks and SUV film were printed in dimensions of 5 x 5 x 10 mm^3 and 3 x 3 x 1 mm^3 respectively, either through two-step printing or adhered using tape and glue as reported in previous sections. Representative comparison graph of mechanical adhesion strength was as shown in **Figure 4-15A(ii)**. The sudden drop from the highest point indicates occurrence of failure where DLP printed coupons had a superior resistance with ~1.85MPa at 64% strain whereas lower strength of glue and tape was observed (~0.55MPa at 43% strain). To note that for DLP printed coupons, failure of SUV was observed with no occurrence of interfacial delamination, indicating that the adhesion strength between plasGRAY and SUV should be higher than this value. On the other hand, interfacial delamination of tensile coupons adhered with tape and glue was as expected. Constant stress of ~0.5MPa persisted due to gradual progression of delamination until complete failure was reached (~250%). The result was encouraging which offered a promising platform for rapid fabrication of highly flexible MN systems with photocurable MN material.

Finally, functionality comparison of DLP printed RC and FF MN patches with 30 MNs/array were conducted using monolayer agarose elbow model. For better visualization, trypan blue dye was spray-coated onto MNs through commercial mist spray. Selective plasma treatment was employed to improve hydrophilicity of the MNs by covering base substrates with 3D printed masks such that only MNs were exposed and plasma treated. Optical images of coated

RC and FF MN patches were shown in **Figure 4-15B(i)**. As expected, RC had a significantly lower number of MNs penetration due to its rigid nature, in contrast to FF with complete penetration (**Figure 4-15B(ii)**).

Another interesting application that the proposed MN patch fabrication process offers is the mix-and-match of MN and base substrate design (**Figure 4-15C**). Drug dosage and sensing coverage of applied skin site are often decided by the number of MNs present on single array where upscaling of FF base substrate is feasible without the need to increase array density and compromise MN penetration efficiency(**Figure 4-15C(i)**). By exploiting CAD modeling flexibility of 3D printing techniques, fractal cut patch can be designed not only in square or rectangular shape, but also polygons with various subunit designs, as presented in **Figure 4-15C(ii)** where triangle subunits assembled into hexagon-shaped fractal cut base substrate[28]. This allows adaptability of FF MN patches to serve different purposes and administration sites depending on the morphological limitation, offering engineering tunability for studies to optimize their respective FF-based MN system. For example, Xiang *et al.* proposed to use MN electrode array for *in situ* monitoring of brain neural activity[26]. They incorporated mesh design into base substrate to offer higher degree of flexibility in order to conform onto complex rat brain curved surfaces. However, the human brain was found to be in larger size and with more complex contours where mesh or square-FF design might not be able to address effective conformity. By using hexagon-shaped FF design that can undergo drastic deformation during stretching, the MN electrode array might be able to conform onto the brain surface with wide coverage, offering potential opportunity to record neural signals simultaneously from different brain regions in chronic disease monitoring or brain development. Besides that, mix-and match of several drug formulations in different MN materials are possible using the proposed fabrication process which is as shown in **Figure 4-15C(iii)**. Introduction of such heterogeneity into the MN system not only could provide simultaneous delivery of different drug formulations, but also be able to engineer drug release kinetics of various drugs

to achieve synergistic therapeutic outcome, similar to the concept Chen *et al.* have proposed[48].

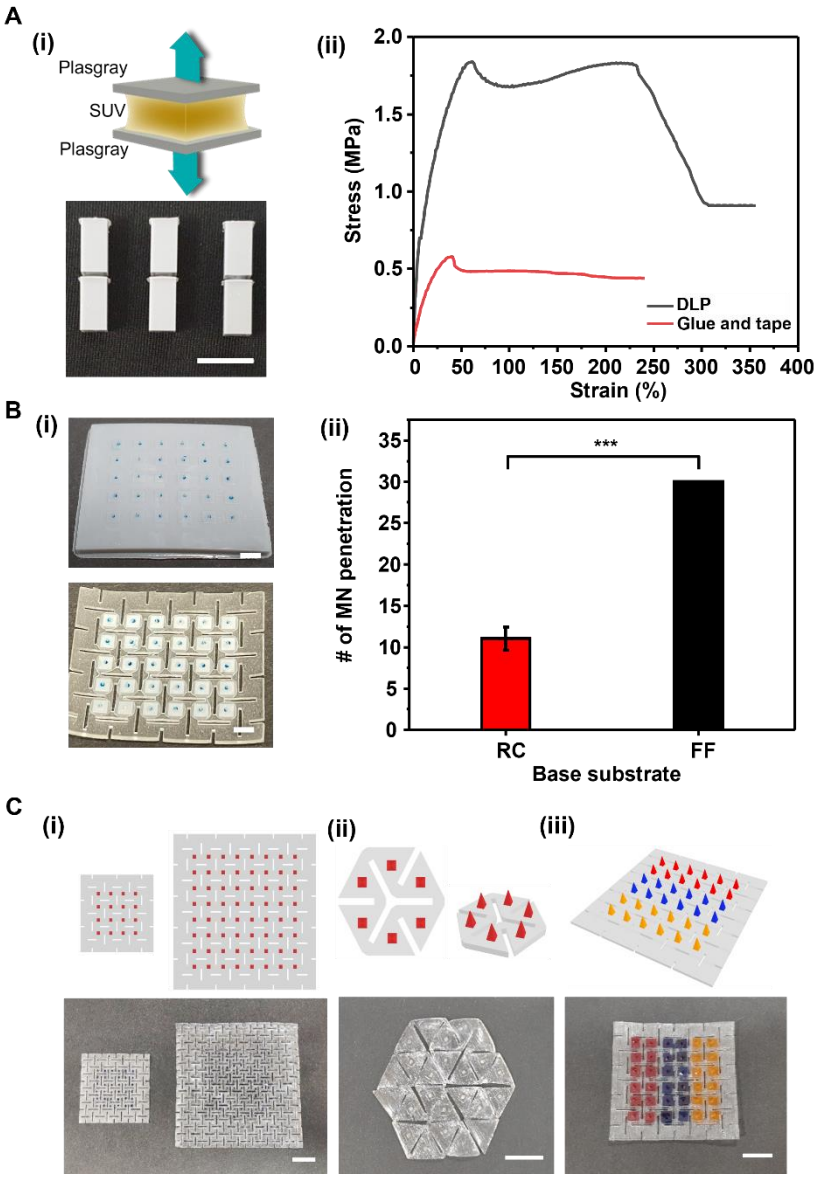

Figure 4-15 A. Interlayer adhesion force between plasGRAY and SUV tensile coupon. (i) Schematics and optical image of rigid-soft-rigid sandwich tensile coupon[46]. Scale bar = 1cm. (ii) Stress-strain curve of interlayer adhesion tensile coupon fabricated using DLP and glue/tape. B. *In vitro* penetration test of DLP printed RC and FF MN patches on monolayer agarose elbow model. (i) Optical images of dye loaded RC and FF MN patch for penetration test. Scale bar = 5mm. (ii) Number of MN penetration (30MNs/array). C. High customizability of FF design. (i) Variation in size. (ii) Variation in subunit geometry. (iii) Heterogeneity of MNs on single array through combination of different drug formulation/MN

4.4 Discussion

Additive manufacturing, or 3D printing is an emerging platform for highly customized and functional device in various fields including MN fabrication. Typical 3D printing method for MN fabrications is vat polymerization which includes SLA, DLP and TPP as reviewed in chapter 2. Among them, DLP printing has the most interest due to its low cost, rapid prototyping and wide biomaterial compatibility. Moreover, novel two-step printing of FF MN patch has shown its potential in fabricating fully functional MN patch with excellent skin conformity. However, existing DLP printers only come with X-Y resolution of ~20μm which has hindered applicability of fabricating ultrahigh resolution DLP printed MN or MN template as compared to SLA (~10μm) and TPP (~0.5μm). Besides that, undesired staircase-stepping effect has been observed on printed MN due to limited Z resolution of ~10μm, cutting off continuous features from layer to layer. In addition, common laser ablated MN template usually provides tip diameter of 5-10μm with smooth MN surface thus usually MN templates are fabricated through TPP with maskless and point-to-point curing characteristic. Therefore, post processing method could be a promising approach to further improve tip geometry and surface defects of DLP printed MN without compromising other aspects.

Prior studies on post processing treatment of 3D printed MN utilized irreversible hydrolysis of biopolymer via chemical etching in controlled manner. For instance, Luzuriaga *et al.* fabricated PLA pre-MN structures in seven shapes with 0.35mm nozzle diameter using FDM printing[49]. Tip region of the structures were then immersed in 5M KOH for 4 hours for selective etching. Subsequently, arrays were fully immersed into KOH solution for additional 5 hours to form the final structures. Similarly, Wu *et al.* printed PLA pre-MN structures with different incline angles[50]. Hydrolysis rate is known to be affected by various factors which include temperature and pH[51]. Therefore, effect of etchant concentration, stirring speed and temperature were studied. The

study has shown that increase of etchant concentration and temperature could effectively improve etching quality of the PLA MN with smooth surface and finer geometry. On the other hand, Johnson and Procopio proposed a novel approach to improve DLP MN printing through customization of light intensity exposure using algorithmic calculation[52]. By using optimization algorithms derived in MATLAB, anti-aliasing effect of imported build command successfully improved conical MN printing with smoother surface as compared to print without anti-aliasing and built-in anti-aliasing algorithm from the printer software (**Figure 4-16A**). These studies provided applicable guidelines to optimize printing quality of DLP MNs as micromolding template and functional drug delivery system.

Therefore, a study with cooperative efforts to improve MN quality printed with DLP technique can be further proposed. Both commercially available biocompatible resin and biopolymer PEGDA and meHA can be used to characterize effect of material composition on the optimization processes. A study has found that printing orientation could affect geometrical agreement between input model and actual geometry due to structural warpage induced by resin flow during building platform movement[53]. In this study, the materials will be prepared and printed in various angles from 0-45^{o} to obtain respective optimized printing orientations with minimal gravitational effect. Preliminary result of angled printing using commercial plasGRAY resin was as shown in **Figure 4-16B**. Printed MNs were then being chemically etched with common etchants like KOH, H_2SO_4 and acetone with various temperature and concentrations to further improve surface roughness of the MN body. In general etchants are of high toxicity, therefore multiple washing with DI water and ethanol should be proceeded, along with cell viability test to evaluate potential toxic residue (**Figure 4-16C**). Customizability of printing settings like velocity of build platform and light intensity will also be investigated. Finally, penetration efficiency will be further validated through *in vitro* and ex vivo studies.

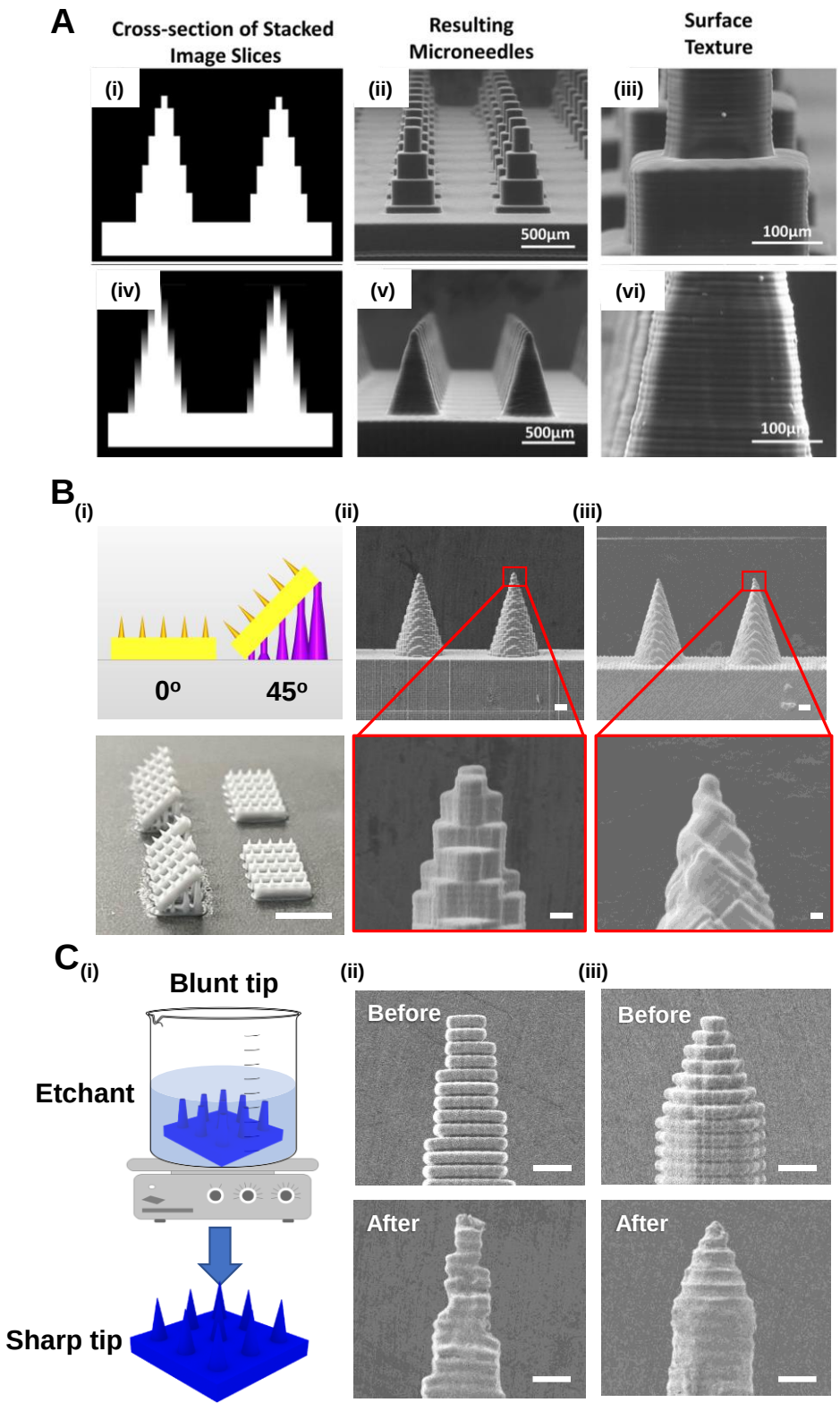
A
Cross-section of Stacked Image Slices
Resulting Microneedles
Surface Texture
(i)
(ii)
(iii)
500μm
100μm
(iv)
(v)
(vi)
500μm
100μm
B
(i)
(ii)
(iii)
0°
45°
C
(i)
Blunt tip
Etchant
Sharp tip
(ii)
(iii)
Before
Before
After
After

Figure 4-16. Improvement of DLP printed MN geometry through synergistic approaches. A. Effect of antialiasing on MN geometry. (i-iii) MN fabricated without anti-aliasing. Scale bar = 500 / 100µm. (iv-vi) MN fabricated with optimized antialiasing through MATLAB algorithm. Scale bar = 500 / 100µm [52]. B. Effect of printing orientation (0^{o} and 45^{o}). The optical and SEM images show preliminary result using commercial plasGRAY resin as MN material. (i) Schematic illustration of orientation setup using same MN design and printed samples (bottom). Scale bar = 5mm. (ii) SEM image of conical MN array printed in 0^{o} angle and magnified view of tip region (~20µm). Scale bar = 100 / 10µm. (iii) SEM image of conical MN array printed in 45^{o} angle and magnified view of tip region (~10µm). Scale bar = 100 / 10µm. C. Effect of chemical etching (KOH). SEM images show preliminary result using biocompatible acrylated epoxidized soybean oil-based resin. (i) Schematic illustration of etching process. (ii) SEM image of pyramidal MN before and after 5M KOH etching for 13 hours. Scale bar = 100µm. (iii) SEM image of conical cylindrical MN before and after 5M KOH etching for 13 hours. Scale bar = 100µm.

4.5 Conclusion

In this study, a fish armour-inspired flexible MN system was proposed with high skin conformity and penetration efficiency. A kirigami-based auxetic fractal cut pattern was introduced into existing flexible and continuous substrate to provide omni-directional flexibility. Deformation and conformity of RC, FC and FF base substrate was investigated through numerical simulation where FF was found to have the highest conformity onto simplified elbow model among all, followed by FC and RC as expected. Deformation of FF under stretching showed that most stress and strain were concentrated at the hinges which made the subunit free of deformation. This resulted in lesser MN delamination during stretching in contrast to FC where high stress accumulated at the base of the substrate, suggesting potential MN delamination if excessive stretching occurs. The designs of these base substrates were then converted into STL models for 3D printing. As inspired by fish armour which is composed of scale subunits, MNs were prepared by conventional micromold casting, followed by segmentation such that individual MN subunits were obtained. The segmented MN subunits were then reassembled onto three base substrate designs for functionality

evaluation. The incorporation of fractal cut design significantly improved skin conformity and penetration efficiency of the MN system in terms of contact stability, patch coverage, consistency of MN penetration and insulin delivery into mice. Novel two step-printing of the proposed flexible MN patch using low cost DLP printing also displayed a prospective outcome in fabricating a highly flexible MN system with high efficiency, high precision and design customizability. In particular, design flexibility of patch size, cut pattern and drug/material mix-and-match heterogeneity allowed diverse applications to explore using FF design. Taken together, the results suggest that ancient fish armour inspired flexible MN system could address limitations of existing flexible MN system encountered and provide a promising approach to advance commercialization of MN technology.

References

1. Roberts, M.S., *TARGETED DRUG DELIVERY TO THE SKIN AND DEEPER TISSUES: ROLE OF PHYSIOLOGY, SOLUTE STRUCTURE AND DISEASE.* Clinical and Experimental Pharmacology and Physiology, 1997. **24**(11): p. 874-879.
2. Niculescu, A.B., et al., *Blood biomarkers for memory: toward early detection of risk for Alzheimer disease, pharmacogenomics, and repurposed drugs.* Molecular Psychiatry, 2020. **25**(8): p. 1651-1672.
3. Cameron, J.M., et al., *Biofluid spectroscopic disease diagnostics: A review on the processes and spectral impact of drying.* J Biophotonics, 2018. **11**(4): p. e201700299.
4. Ganesh, A.N., et al., *Patient-centric design for peptide delivery: Trends in routes of administration and advancement in drug delivery technologies.* Medicine in Drug Discovery, 2021. **9**: p. 100079.
5. Kim, J. and O. De Jesus, *Medication Routes of Administration*, in *StatPearls*. 2022, StatPearls Publishing
6. McLenon, J. and M.A.M. Rogers, *The fear of needles: A systematic review and meta-analysis.* J Adv Nurs, 2019. **75**(1): p. 30-42.
7. Krleza, J.L., et al., *Capillary blood sampling: national recommendations on behalf of the Croatian Society of Medical Biochemistry and Laboratory Medicine.* Biochem Med (Zagreb), 2015. **25**(3): p. 335-58.
8. Lee, E.K., M.K. Kim, and C.H. Lee, *Skin-Mountable Biosensors and Therapeutics: A Review.* Annual Review of Biomedical Engineering, 2019. **21**(1): p. 299-323.
9. Lee, H., et al., *Device-assisted transdermal drug delivery.* Advanced Drug Delivery Reviews, 2018. **127**: p. 35-45.
10. Prausnitz, M.R. and R. Langer, *Transdermal drug delivery.* Nature Biotechnology, 2008. **26**(11): p. 1261-1268.
11. Jampilek, J. and K. Brychtova, *Azone analogues: classification, design, and transdermal penetration principles.* Med Res Rev, 2012. **32**(5): p. 907-47.
12. Newman, C.M. and T. Bettinger, *Gene therapy progress and prospects: ultrasound for gene transfer.* Gene Ther, 2007. **14**(6): p. 465-75.
13. Escobar-Chávez, J.J., et al., *The use of iontophoresis in the administration of nicotine and new non-nicotine drugs through the skin for smoking cessation.* Curr Drug Discov Technol, 2009. **6**(3): p. 171-85.
14. Rajabi, M., et al., *Flexible and Stretchable Microneedle Patches with Integrated Rigid Stainless Steel Microneedles for Transdermal Biointerfacing.* PLOS ONE, 2016. **11**(12): p. e0166330.
15. Li, J., et al., *Microneedle Patches as Drug and Vaccine Delivery Platform.* Curr Med Chem, 2017. **24**(22): p. 2413-2422.
16. Larrañeta, E., et al., *Microneedle arrays as transdermal and intradermal drug delivery systems: Materials science, manufacture and commercial development.* Materials Science and Engineering: R: Reports, 2016. **104**: p. 1-32.
17. Woodhouse, I., et al., *Flexible Microneedle Array Patch for Chronic Wound Oxygenation and Biofilm Eradication.* ACS Applied Bio Materials, 2021. **4**(7): p. 5405-5415.

18. Hou, Y., et al., *Miura-ori structured flexible microneedle array electrode for biosignal recording.* Microsystems & Nanoengineering, 2021. **7**(1): p. 53.
19. Choi, I.J., et al., *Live Vaccinia Virus-Coated Microneedle Array Patches for Smallpox Vaccination and Stockpiling.* Pharmaceutics, 2021. **13**(2).
20. Kim, Y.C., et al., *Stability kinetics of influenza vaccine coated onto microneedles during drying and storage.* Pharm Res, 2011. **28**(1): p. 135-44.
21. Holl, J., et al., *Chronic Diabetic Wounds and Their Treatment with Skin Substitutes.* Cells, 2021. **10**(3).
22. Huang, D., et al., *Recent advances on fabrication of microneedles on the flexible substrate.* Journal of Micromechanics and Microengineering, 2021.
23. Vecchione, R., et al., *Electro-Drawn Drug-Loaded Biodegradable Polymer Microneedles as a Viable Route to Hypodermic Injection.* Advanced Functional Materials, 2014. **24**(23): p. 3515-3523.
24. Onesto, V., et al., *Engineered PLGA-PVP/VA based formulations to produce electro-drawn fast biodegradable microneedles for labile biomolecule delivery.* Progress in Biomaterials, 2020. **9**(4): p. 203-217.
25. Lau, S., et al., *Multilayered pyramidal dissolving microneedle patches with flexible pedestals for improving effective drug delivery.* J Control Release, 2017. **265**: p. 113-119.
26. Xiang, Z., J. Liu, and C. Lee, *A flexible three-dimensional electrode mesh: An enabling technology for wireless brain–computer interface prostheses.* Microsystems & Nanoengineering, 2016. **2**(1): p. 16012.
27. Song, J., *Multiscale materials design of natural exoskeletons : fish armor.* 2012.
28. Cho, Y., et al., *Engineering the shape and structure of materials by fractal cut.* Proceedings of the National Academy of Sciences, 2014. **111**: p. 17390 - 17395.
29. Tang, Y., et al., *Design of Hierarchically Cut Hinges for Highly Stretchable and Reconfigurable Metamaterials with Enhanced Strength.* Advanced Materials, 2015. **27**(44): p. 7181-7190.
30. Kim, K.-B., et al., *Extremely Versatile Deformability beyond Materiality: A New Material Platform through Simple Cutting for Rugged Batteries.* Advanced Engineering Materials, 2019. **21**(7): p. 1900206.
31. Babaee, S., et al., *Bioinspired kirigami metasurfaces as assistive shoe grips.* Nature Biomedical Engineering, 2020. **4**(8): p. 778-786.
32. Pradhan, S., et al., *Biofunctional Silk Kirigami With Engineered Properties.* ACS Applied Materials & Interfaces, 2020. **12**(11): p. 12436-12444.
33. Wu, H., et al., *Stretchable, sensitive, flexible strain sensor incorporated with patterned liquid metal on hydrogel for human motion monitoring and human–machine interaction.* Journal of Materials Chemistry C, 2022. **10**(21): p. 8206-8217.
34. Bergström, J., *5 - Elasticity/Hyperelasticity*, in *Mechanics of Solid Polymers*, J. Bergström, Editor. 2015, William Andrew Publishing. p. 209-307.
35. Smith, M., *ABAQUS/Standard User's Manual, Version 6.9*. 2009, Providence, RI: Dassault Systèmes Simulia Corp.
36. Tan, W.S., et al., *Development of a new additive manufacturing platform for direct freeform 3D printing of intrinsically curved flexible membranes.* Additive Manufacturing, 2020. **36**: p. 101563.
37. Zomer, H.D. and A.G. Trentin, *Skin wound healing in humans and mice: Challenges in translational research.* J Dermatol Sci, 2018. **90**(1): p. 3-12.

38. Gerber, P.A., et al., *The top skin-associated genes: a comparative analysis of human and mouse skin transcriptomes.* Biol Chem, 2014. **395**(6): p. 577-91.
39. Wong, V.W., et al., *Surgical approaches to create murine models of human wound healing.* J Biomed Biotechnol, 2011. **2011**: p. 969618.
40. Ahad, A., et al., *Delivery of Insulin via Skin Route for the Management of Diabetes Mellitus: Approaches for Breaching the Obstacles.* Pharmaceutics, 2021. **13**(1).
41. Zhao, J., et al., *Microneedle-based insulin transdermal delivery system: current status and translation challenges.* Drug Delivery and Translational Research, 2021.
42. Mohannak, K. and L. Samtani, *A criteria-based approach for evaluating innovation commercialisation,* in *Proceedings of the DRUID Society Conference 2014*. 2014, DRUID Society: Denmark. p. 1-15.
43. Snape, T., A. Astles, and J. Davies, *Understanding the chemical basis of drug stability and degradation.* The Pharmaceutical Journal, 2010. **285**.
44. Patel, D.K., et al., *Highly Stretchable and UV Curable Elastomers for Digital Light Processing Based 3D Printing.* Advanced Materials, 2017. **29**(15): p. 1606000.
45. Lim, S.H., et al., *Geometrical optimisation of a personalised microneedle eye patch for transdermal delivery of anti-wrinkle small peptide.* Biofabrication, 2020. **12**(3): p. 035003.
46. Pittman, K. *Cost-Effective Adhesive Bonding for High Strength Assemblies*. 2017 [cited 2022 08 December]; Available from: https://www.engineering.com/story/cost-effective-adhesive-bonding-for-high-strength-assemblies?postID=13729.
47. Ando, M., M. Birosz, and S. Jeganmohan, *Surface bonding of additive manufactured parts from multi-colored PLA materials.* Measurement, 2020. **169**: p. 108583.
48. Chen Bo, Z., et al., *A basal-bolus insulin regimen integrated microneedle patch for intraday postprandial glucose control.* Science Advances. **6**(28): p. eaba7260.
49. Luzuriaga, M.A., et al., *Biodegradable 3D printed polymer microneedles for transdermal drug delivery.* Lab on a Chip, 2018. **18**(8): p. 1223-1230.
50. Wu, L., et al., *Optimization of the fused deposition modeling-based fabrication process for polylactic acid microneedles.* Microsystems & Nanoengineering, 2021. **7**(1): p. 58.
51. Rydholm, A.E., K.S. Anseth, and C.N. Bowman, *Effects of neighboring sulfides and pH on ester hydrolysis in thiol-acrylate photopolymers.* Acta Biomater, 2007. **3**(4): p. 449-55.
52. Johnson, A.R. and A.T. Procopio, *Low cost additive manufacturing of microneedle masters.* 3D Printing in Medicine, 2019. **5**(1): p. 2.
53. Yeung, C., et al., *A 3D-printed microfluidic-enabled hollow microneedle architecture for transdermal drug delivery.* Biomicrofluidics, 2019. **13**(6): p. 064125.

Chapter 5

Conclusion and future work

In this chapter, the works presented in previous chapters are emphasized and summarized. In addition, four topics that can be further explored are also proposed to provide guidelines on further optimization of the proposed system. Briefly, penetration efficiency of MN system is also found to be susceptible to various MN geometrical designs like length, tip radius and density of the array among others. Therefore, fundamental study on MN geometrical effects is proposed using low cost DLP printer where the penetration efficiency will be evaluated through numerical and experimental approaches. Next, Synergistic geometrical improvement of DLP printed flexible MN patch is proposed to provide low cost, highly customizable flexible MN fabrication platform with promising penetration efficiency. To further expand opportunities of DLP printing on MN fabrication, two-step printing of flexible and cargo loaded stimuli-responsive hydrogel-based MN patch is also proposed for smart drug delivery. Finally, applicability of fractal cut MN system will be explored in electrochemical glucose monitoring with the integration of silver-based conductive pathway and highly swellable hydrogel for rapid fluid extraction.

5.1 Conclusion

Transdermal drug delivery (TDD) system has been developed to offer alternative route of administration in pain-free, self-administrable, site-specific and efficacious manner, in contrast to conventional oral and parenteral delivery of protein and peptide. Majority TDD systems in current market are still first-generation device which only able to deliver small molecules through diffusion. Therefore, microneedle (MN) technology as third generation of TDD system has been widely studied over the decades since it provides greater skin disruption in minimal invasive manner thus suitable for large molecules delivery. MN device is designed in patch form with a collection of MN oriented on the substrate in an organized manner since this allows wider area of penetration and more rapid drug delivery into penetration site. An ideal MN system should provide consistent and excellent penetration efficiency over target skin region especially when human skin is viscoelastic in nature and having complex skin contour. MN patch failed to uniformly conform onto target skin site could lead to under-desired therapeutic outcome. Besides that, drug dosage and release kinetics are the key factors to consider in development of drug delivery system. MN patch is usually fabricated for self-administration through finger-pressing, therefore often encounter drug loading limitation due to small patch size. These are the main reasons why MN technology is still not yet able to be widely commercialized, as it failed to carry desired drug dosage and conform consistently onto curved skin surface for designated outcome. Inspired by ancient fish armour system which has shown great similarities to the proposed ideal MN system, this thesis aimed to improve penetration efficiency and drug loading volume of MN patch in material and flexibility aspect.

Common MN classifications and fabrication methods were discussed. Moreover, geometrical influence of MN design (as individual tip or as an array) was also reviewed in a comprehensive manner. This information will be helpful for the selection of suitable MN types, material and array design to fulfil desired

biomedical applications, including drug delivery and biosensing purpose. To effectively customize MN design, several 3D printing techniques for MN fabrications were reviewed. Prior studies on flexible wearables and MN system were investigated to provide better insight on bottleneck of current MN technology and potential applications that MN system could be explored on.

In material aspect, rapid dissolving biopolymer low molecular weight hyaluronic acid (HA) was chosen due to its capability in acute drug delivery, minimal biowaste production and high matrix drug loading capacity as compared to coated MNs. However, high drug loaded matrix could cause decline in matrix strength, especially when polymers have intrinsically weak mechanical strength as compared to other non-biodegradable materials like metal. Therefore, reinforcement of HA matrix was achieved through *in situ* precipitation of silica network with rapid physiological decay rate. Silica content in HA matrix were first studied through structural characterization to ensure minimal morphological defects during MN fabrication. In addition, chemical analyses confirmed deposition of silica NPs in HA matrix in a controllable manner. The HA-Si MNs fabricated demonstrated improved penetration efficiency and slight effect on dissolution behavior to pure HA MNs. Moreover, no cytotoxicity was found in the optimized HA-Si sample, indicating that the proposed hybridization of bioactive additive was encouraging.

As for flexibility aspect, a kirigami-based auxetic fractal cut pattern was introduced into the flexible base substrate design, resembling that of wavy patterned fish tissue. To predict deformation behavior of proposed FF design as base substrate, numerical simulation was employed where traditional rigid and flexible base substrate were compared as well. Result showed that FF base substrate provided highest conformity on simplified elbow model amongst. Next, experimental fabrication of RC, FC and FF MN patch were achieved through three steps: micromold casting of MN, segmentation of MN into subunits and reassembling on base substrate using biosafe glue. The functionality of three

substrates were compared in terms of contact stability, elbow model coverage, penetration depth and insulin delivery. All tests have suggested that FF improved penetration efficiency of MN system in contrast to traditional rigid and existing flexible continuous MN system. Moreover, novel two-step fabrication of proposed FF MN patch using DLP printing was accomplished with high precision, lower production time/cost and promising functionality by exploiting working principle of DLP printing. Finally, customizability of FF MN patch in terms of patch size, subunit shape design and heterogeneity of MN material-drug formulation were displayed and proven to be a promising platform for diverse biomedical applications.

In summary, this thesis presented a bio-inspired approach to address various challenges encountered for the commercialization of MN technology, including limited dosage capacity, skin coverage and size constraint (**Figure 5-1**). With further development of proposed flexible MN system, MN technology can be advanced towards personalized healthcare that requires customizable drug release profile with promising penetration efficiency. With the material and design flexibility, proposed flexible MN system can be adopted for diverse biomedical applications like disease diagnosis and biosensing in pain-free and minimal invasive manner.

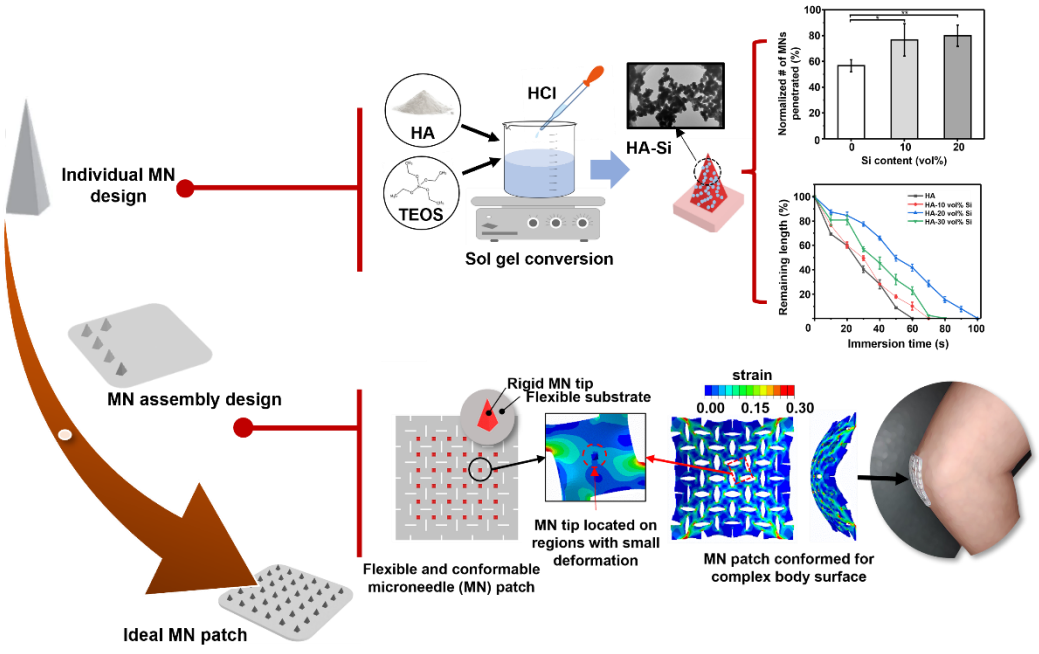

Figure 5-1. Result summary of proposed research. At individual level, silica network was incorporated into low molecular weight hyaluronic acid (HA) through sol-gel conversion under acidic condition. Fabricated HA-Si MNs showed superior penetration capability and prolonged structural stability in water. Next, the wearability issue of existing flexible microneedle system was then addressed through introduction of kirigami-like fractal cut (FF) pattern into base substrate design. Both computational and experimental approaches have proven FF to have superior skin conformity, drug delivery efficacy and reduction of hard-soft interfacial delamination.

5.2 Future work

5.2.1 Fundamental studies on microneedle geometrical design through experimental and computational model

Penetration efficiency of MN refers to the capability of particular MN system in penetrating application site uniformly using low insertion force so designated dosage can be delivered into target site painlessly. In chapter 3 and chapter 4, improvement of rapid dissolving MN system penetration efficiency were addressed in material and flexibility aspect. Yet, geometrical design of MN has not been considered in our studies to further optimize flexible fractal cut MN system that consist of MN allocation with large interspacing distance. Stress and strain distribution on individual MN during insertion onto curved skin surface should be investigated as well such that the interaction between MN and potential skin curvature-induced shear force exerted on the MN tip could be fundamentally understood.

In chapter 2, many studies have proven importance of geometrical design on drug delivery performance. Factors like shape, aspect ratio and tip radius have been widely studied. For example, Lim *et al.* investigated on relationship of MN patch curvatures, along with geometrical parameters like tip length, tip diameter and interspacing distance on mechanical strength and human skin penetration[1].

They found that complex mix of axial and shear force were exerted on MN tips when penetrating using different bending curvatures of MN patch, causing comprehensive change on skin penetration efficiency. Synergistic effect of patch curvature and geometrical parameters were considered during design of personalized anti-wrinkle eye patch where *in vitro* delivery of AHP-3 showed superior performance as compared to commercially available treatments. Besides that, computational model has been proven to be a promising platform to visualize deformation behavior of MN during skin insertion while act as theoretical reference to experimental data for cross validation. For instance, Olatunji *et al.* proposed a numerical model to predict deformation mode of sugar based dissolving MN depending on sugar composition[2]. They found that buckling force dominated during deformation and the order of buckling was proportional to Young's modulus of material composition.

Based on these studies, penetration efficiency of the flexible fractal cut MN patch can be further optimized by exploiting high design customizability of DLP printing technique and photopolymer. Mechanical properties of photopolymers can be tuned through varying duration of UV curing. While studies often presume MN should have sufficient mechanical strength to penetrate the skin, few studies have investigated skin-MN modulus ratio on penetration efficiency. By tuning post curing duration of DLP material[3], penetration capability of MN patch can be further understood through modulus ratio effect which could provide design guidance in the future MN material development in experimental and computational manner. Geometrical parameters like tip length, tip radius, tip angle, base diameter and interspacing distance will be studied using conical cylindrical MN shape such that various parameters can be individually varied without changing the others, providing thorough comparison of geometrical effects (**Figure 5-2A**). In previous studies, penetration efficiency was addressed based on penetration depth[4], bioavailability of delivered substance[5] and MN failure[6]. MN insertion force is also one of the crucial factors to date where insufficient application force may

also affect drug delivery efficiency. Therefore, both insertion force upon skin breakage and force progression during shaft insertion will be analyzed in this study to understand how shearing between MN shaft and tissue could affect penetration efficiency, using *in vitro* monolayered and bilayered skin model of agarose and parafilm-agarose as skin substitute[7, 8]. SEM will be employed to characterize printing accuracy of the printed MNs to ensure fair comparison across groups. The MN insertion behavior will be characterized using micro-tensile meter where number of successful penetrations will also be presented for bilayered model. Finally, computational analysis of the MN insertion process will be conducted using ABAQUS® software, which is a useful platform used for modeling and analysis of mechanical interactions through visualization of finite element analysis. **Figure 5-2B** has shown the proposed numerical model.

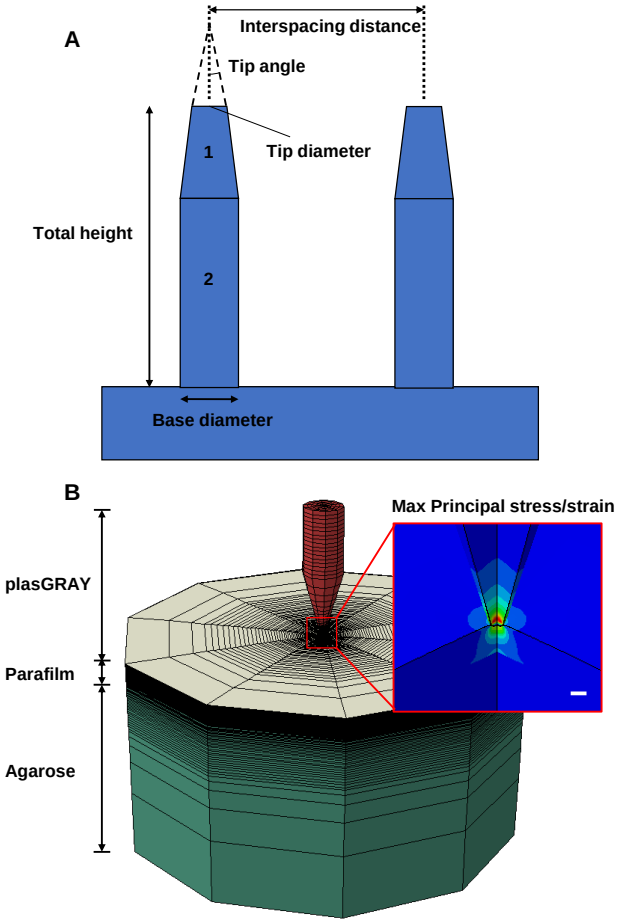

Figure 5-2. Proposed fundamental study on MN geometrical effect through experiment and simulation. A. Definition of geometrical parameters to address, namely total height (1. tip region and 2. pillar support), tip diameter, tip angle, base diameter and tip-to-tip interspacing distance. B. Meshed numerical model of single MN insertion into bilayer skin model to predict their mechanical interaction during skin penetration. Material data input is identical to experimental setup for cross-checking purpose. Scale bar = 20μm.

5.2.2 Fabrication and characterization of stimuli-responsive hydrogel-based flexible microneedle patch using low cost 3D printing

Stimuli-responsive hydrogels are capable of undergo structural or mechanical changes in response to endogenous cues in physiological environment like pH value, ions, enzymes among others, or exogenous triggers like light, ultrasound, electric field and others[9]. Due to their excellent engineerability, stimuli-responsive hydrogels are employed for various biomedical applications like drug delivery, biosensing, bionic device and tissue regeneration[10, 11]. In recent years, they have drawn extensive attention in MN technology to serve as high efficiency smart drug delivery and biosensing system. In chapter 4, multi-material DLP printing of MN patch has shown to be feasible, wherein the interfacial adhesion force between MN and flexible base substrate has been proven to be sufficiently strong such that no delamination would occurs during skin penetration. However, MN printed in the study was non-dissolvable polymer thus only suitable to delivery drug through coating. Penetration efficiency of coated MN is often affected by the coating thickness[12] therefore drug loading volume of the system is further restricted. Therefore, photocurable hydrogels are great candidates in this case since they offer great DLP printability and larger drug loading volume as compared to coated MN. Drug delivery functionality with promising skin conformity offered by flexible fractal cut patch can be further improved by stimuli-responsive hydrogel material for long term release, enabling advanced drug delivery mode like intraday blood glucose regulation.

Typical stimuli responsive hydrogel materials used in MN fabrication are PNIPAAM, PEGDA, meHA, PVA, and pHEMA among others[13]. For example, Shen *et al.* developed PBA-based glucose responsive hydrogel MN for smart drug delivery[14]. PNIPAAM/AAPBA/AGA hydrogel were fabricated where MBA act as crosslinker. When glucose concentration increases, AAPBA moieties was proven to form phenylborate ester bond with surrounding glucose thus leading to looser hydrogel network, weaker hydrophobicity association and release of loaded Rhodamine B. In another study, Avra *et al.* proposed 3D printing of diclofenac sodium loaded PEGDA MN using DLP printer[15]. The drug was directly dispersed in the resin vat along with PEGDA and photoinitiator where the MN was printed with 500µm height, 1000µm interspacing distance and 200µm base diameter. The drug release kinetic was shown to be controllable with respect to environmental pH and temperature (**Figure 5-3**).

Taking these as reference, meHA based stimuli-responsive hydrogel MN will be studied and developed to integrate flexible fractal cut patch for transdermal long term drug release[16]. Responsive mechanism of the HA-based hydrogel system will be first studied to optimize formulation of stimuli-responsive moiety and UV curing properties. Mechanical performance of the system will then be characterized to ensure sufficient penetration efficiency before integration of flexible substrate. Subsequently, two-step printing of HA-based MN structure and stretchable substrate will be studied where interfacial adhesive force should be evaluated to ensure minimal delamination. In addition, *in vitro* and *ex vivo* skin model will be employed under appropriate stimuli to validate functionality of the flexible MN system.

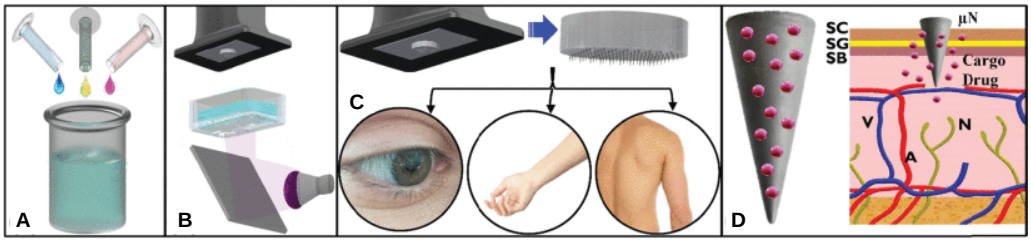

Figure 5-3. Drug loaded MN printing using DLP printer. A. Schematics of DLP resin mixed with PEGDA (blue), TPO photoinitiator (green) and cargo (pink). B. Schematic illustration of DLP printing setup. C. Removal of printed array from build platform and potential applications such as ocular, arm and torsol drug delivery. D. Schematic illustration of cargo delivery upon sensing environmental stimuli while maintaining overall MN structure [15].

5.2.3 *In situ* interstitial glucose monitoring using highly flexible hydrogel-based MN patch integrated with 3D printed conductive pathway

Medical burden intensified by the increase of epidermic and chronic diseases continue to underline the importance of prevention and early stage disease detection. Point-of-care technologies which originally designed as the adjunct tool to sophisticated central lab testing, have shown to provide high effective and low-cost healthcare delivery due to advancement of information technology in recent years[17, 18]. Flexible wearables for example, have made interaction between medical clinician and patients more intelligible, through near real time update of clinically useful bio-information without the need of physical contact. For example, traditional household blood glucose meter requires invasive blood collection and blood glucose analysis through device with rigid packaging which are controversial with patients[19]. Therefore, current trend is towards non- or minimal invasive detection and measurement blood glucose concentration with perspiration, tears and interstitial fluid (ISF)[20]. MN based glucose sensors are reported in many studies for promising interstitial fluid extraction tool in which hollow MN or hydrogel MN are usually used and shown to provide accurate measurement up to few days[21]. However, these MN systems are typically based on rigid or flexible continuous substrates that

provides insufficient conformity and contact stability at movable joint region during dynamic motion thus not suitable for long term skin application. In chapter 4, fractal cut base substrate has shown its potential in rapid insulin delivery with omni-directional conformity, however its applicability in diagnostic setup still not yet displayed. Therefore, a highly flexible MN patch with integrated glucose sensors can be useful and effective for *in situ* long term monitoring.

Up to date, MN-based glucose sensors are made of silicon or hydrogel such as meHA. For example, Sharma *et al.* fabricated glucose sensor by metallizing polycarbonate MNs with platinum and silver to act as working and reference electrodes respectively[22]. The Ag/AgCl reference electrode and Pt-based electrode were prepared by modifying silver paste coated MN with $FeCl_3$ to induce oxidation reaction while GOx was entrapped onto polyphenol functionalized Pt MN. Conductive wires attached on MN array were then connected onto external potentiostat for signal recording. In another study, Zheng *et al.* had developed an osmosis-powered meHA hydrogel MN patch with rapid fluid extraction rate by introducing maltose into meHA matrix as osmolyte. The glucose oxidase (GOx) solution was mixed with single-walled carbon nanotubes (SWCNTs) and deposited onto screen-printed conductive path micromachined using PET sheet. The MNs array were then integrated onto sensing region of the microfluidic like electronic glucose sensor [23]. A flexible and porous PDMS MN was also proposed by Tekeuchi *et al.* which aimed to resolve contact stability issue during dynamic motion of existing MN-based glucose sensor[24]. The porous PDMS MN array was fabricated by mixing salt in PDMS matrix and remove these salt particles after curing of micromold casted PDMS MNs array in DI water. To ensure sufficient strength and improve hydrophilicity of the tip region, hyaluronic acid (HA) was then coated onto the porous PDMS MNs to form the functional MN array. ISF infused from applied skin site was extracted by compressing the flexible array with certain force such that the fluid could be absorbed onto glucose test papers on the base substrate.

These studies provided guideline and inspiration for developing a highly flexible MN-based glucose sensor by exploiting 3D printing technology. In contrast to prior studies where the electrodes were prepared either by functionalizing MNs which required to regularly replenish depleted GOx, or by integrating MN patch onto bulky electronic chip, we proposed a novel meHA MN based-glucose sensor that integrates working electrode, reference electrode and counter electrode onto individual fractal cut subunits for improved flexibility and portability (**Figure 5-4**) [25]. Briefly, osmolyte-meHA MN arrays will be fabricated through micro-molding using 3D printing-customized template, followed by segmentation to obtain 2x2 MN subunits (for rapid fluid extraction). Next, FF base substrate with three sockets will be printed using flexible thermoplastic polyamide (TPA) due to its mass scalability and consistency. These sockets will then be deposited with silver-based conductive ink in which iron chloride oxidized AgCl will be added into reference electrode socket to form Ag/AgCl. As GOx tend to deplete after several cycles of test thus it will be fabricated as disposable strip which could be attached onto segmented meHA MN subunits before reassembling step, and to be disposed along with meHA MNs afterwards so the FF base substrate can be recycle and assembled with fresh GOx-MNs for subsequent tests. Functionality of the glucose sensor will be characterized using cyclic voltammetry (CV) and chronoamperometric (CA) equipment where successful electrochemical reading could be evaluated through oxidization and reduction peak behavior. Finally, *in vitro* penetration test and glucose measurement will be conducted on glucose-loaded agarose gel.

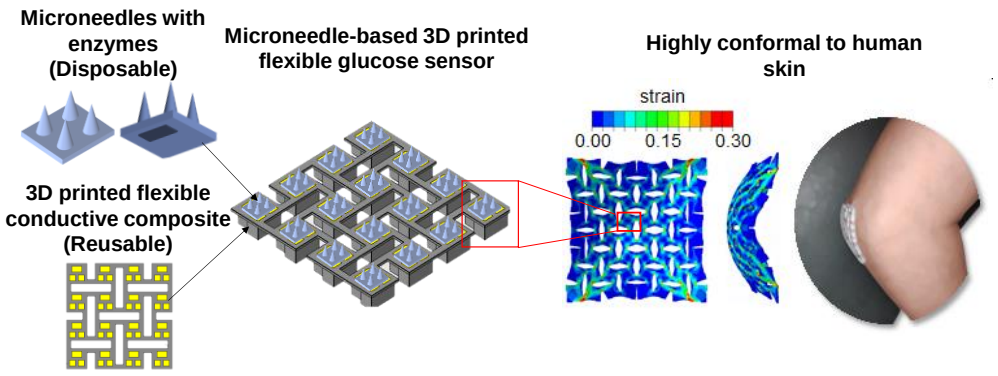

Figure 5-4. Schematic illustration of proposed highly flexible MN-based glucose sensor. The MN system comprises of 2x2 segmented MNs subunit, disposable test strip containing glucose oxidase (GOx) and 3D printed flexible TPA base substrate integrated with conductive silver pathway. After attaching Gox test strip onto backing layer of meHA based MNs, they are attached onto individual subunits of printed FF base substrate to form final MN patch. Computational model in chapter 4 proven its high conformity onto complex geometry like elbow [25].

References

1. Lim, S.H., et al., *Geometrical optimisation of a personalised microneedle eye patch for transdermal delivery of anti-wrinkle small peptide.* Biofabrication, 2020. **12**(3): p. 035003.
2. Olatunji, O., et al., *Influence of array interspacing on the force required for successful microneedle skin penetration: theoretical and practical approaches.* J Pharm Sci, 2013. **102**(4): p. 1209-21.
3. Lee, Y., et al., *Impact of UV curing process on mechanical properties and dimensional accuracies of digital light processing 3D printed objects.* Smart Structures and Systems, 2018. **22**.
4. Römgens, A.M., et al., *Monitoring the penetration process of single microneedles with varying tip diameters.* Journal of the Mechanical Behavior of Biomedical Materials, 2014. **40**: p. 397–405.
5. Al-Qallaf, B., D.B. Das, and A. Davidson, *Transdermal drug delivery by coated microneedles: geometry effects on drug concentration in blood.* Asia-Pacific Journal of Chemical Engineering, 2009. **4**(6): p. 845-857.
6. Park, J.H. and M.R. Prausnitz, *Analysis of Mechanical Failure of Polymer Microneedles by Axial Force.* J Korean Phys Soc, 2010. **56**(4): p. 1223-1227.
7. Makvandi, P., et al., *Engineering Microneedle Patches for Improved Penetration: Analysis, Skin Models and Factors Affecting Needle Insertion.* Nano-Micro Letters, 2021. **13**(1): p. 93.
8. Weimer, P., R.C. Rossi, and L.S. Koester, *Dissolving Microneedles Developed in Association with Nanosystems: A Scoping Review on the Quality Parameters of These Emerging Systems for Drug or Protein Transdermal Delivery.* Pharmaceutics, 2021. **13**(10).

9. Li, Z., et al., *Stimuli-responsive hydrogels: Fabrication and biomedical applications.* VIEW, 2022. **3**(2): p. 20200112.
10. Hu, L., et al., *Harnessing the Power of Stimuli-Responsive Polymers for Actuation.* Advanced Functional Materials, 2020. **30**(2): p. 1903471.
11. Chao, Y., Q. Chen, and Z. Liu, *Smart Injectable Hydrogels for Cancer Immunotherapy.* Advanced Functional Materials, 2020. **30**(2): p. 1902785.
12. Haj-Ahmad, R., et al., *Microneedle Coating Techniques for Transdermal Drug Delivery.* Pharmaceutics, 2015. **7**(4): p. 486-502.
13. Makvandi, P., et al., *Stimuli-responsive transdermal microneedle patches.* Materials Today, 2021. **47**: p. 206-222.
14. Shen, D., et al., *Glucose-responsive hydrogel-based microneedles containing phenylborate ester bonds and N-isopropylacrylamide moieties and their transdermal drug delivery properties.* European Polymer Journal, 2021. **148**: p. 110348.
15. Kundu, A., et al., *DLP 3D Printed "Intelligent" Microneedle Array (iμNA) for Stimuli Responsive Release of Drugs and Its in Vitro and ex Vivo Characterization.* Journal of Microelectromechanical Systems, 2020. **29**(5): p. 685-691.
16. Jo, Y.-J., et al., *Multi-stimuli responsive hydrogels derived from hyaluronic acid for cancer therapy application.* Carbohydrate Polymers, 2022. **286**: p. 119303.
17. Beyette, F.R., Jr., et al., *Point-of-Care Technologies for Health Care.* IEEE Trans Biomed Eng, 2011. **58**(3): p. 732-5.
18. Lee, E.K., M.K. Kim, and C.H. Lee, *Skin-Mountable Biosensors and Therapeutics: A Review.* Annual Review of Biomedical Engineering, 2019. **21**(1): p. 299-323.
19. Liu, Y., M. Pharr, and G.A. Salvatore, *Lab-on-Skin: A Review of Flexible and Stretchable Electronics for Wearable Health Monitoring.* ACS Nano, 2017. **11**(10): p. 9614-9635.
20. Lee, H., et al., *Enzyme-Based Glucose Sensor: From Invasive to Wearable Device.* Adv Healthc Mater, 2018. **7**(8): p. e1701150.
21. Jina, A., et al., *Design, development, and evaluation of a novel microneedle array-based continuous glucose monitor.* J Diabetes Sci Technol, 2014. **8**(3): p. 483-7.
22. Sharma, S., et al., *A pilot study in humans of microneedle sensor arrays for continuous glucose monitoring.* Analytical Methods, 2018. **10**(18): p. 2088-2095.
23. Zheng, M., et al., *Osmosis-Powered Hydrogel Microneedles for Microliters of Skin Interstitial Fluid Extraction within Minutes.* Advanced Healthcare Materials, 2020. **9**(10): p. 1901683.
24. Takeuchi, K., et al., *Flexible and porous microneedles of PDMS for continuous glucose monitoring.* Biomedical Microdevices, 2020. **22**(4): p. 79.
25. Song, J.T., W. S.;Tay, J. H. ;Lim, Y. H.;Zheng, M.;Xu, C., *A Highly Flexible Microneedle Patch System With An Integrated Glucose Sensor And A Method of Fabrication Thereof* I.P.O.o. Singapore, Editor. 2021: Singapore.

Appendix

List of patents

1. Song, J.; **Tay, J. H.**; Lim, Y. H.; Tan, W. S.; Zheng, M. & Xu, C. (**2021**). *Design and Fabrication Method of Flexible And Adaptive Microneedle Patches Thereof* (NTU Ref No. 2021-528). Intellectual Property Office of Singapore.
2. Song. J.; Tan, W. S.; **Tay, J. H.**; Lim, Y. H.; Zheng, M. & Xu, C. (**2021**). *A Highly Flexible Microneedle Patch System With An Integrated Glucose Sensor And A Method of Fabrication Thereof* (NTU Ref no. 2021-529). Intellectual Property Office of Singapore.

Conferences

1. Poster presentation. Improved Penetration Efficiency and Drug Delivery of Hydrogel Nanocomposite Microneedle Systems through *in situ* hybridization. 2022 AIChE Annual Meeting, Rockstars of Regenerative Engineering Conference – Chicago. 19-20th April 2021, Virtual.
2. Poster & oral presentation. Improved Penetration Efficiency and Drug Delivery of Hydrogel Nanocomposite Microneedle Systems through *in situ* hybridization. SingHealth Duke-NUS Scientific Congress 2021, Basic Science & Translational Research. 17-18th September 2021, Virtual.
3. Oral presentation. Bioinspired Flexible Microneedle Patches for Improved Transdermal Drug Delivery. 2021 Material Research Society Fall Meeting & Exhibit. 6-8th December 2021, Virtual.